



EUROPEAN  
COMMISSION

European  
Research Area

# Microstructural quantification of multi-phase steels (Micro-quant)

## **Interested in European research?**

**RTD info** is our quarterly magazine keeping you in touch with main developments (results, programmes, events, etc.). It is available in English, French and German. A free sample copy or free subscription can be obtained from:

Directorate-General for Research and Innovation  
Information and Communication Unit  
European Commission  
1049 Bruxelles/Brussel  
BELGIQUE/BELGIË  
Fax +32 229-58220  
E-mail: [research@ec.europa.eu](mailto:research@ec.europa.eu)  
Internet: <http://ec.europa.eu/research/rtdinfo.html>

**EUROPEAN COMMISSION**  
Directorate-General for Research and Innovation  
Research Fund for Coal and Steel Unit

*Contact: RFCS publications*  
*Address: European Commission, CDMA 0/178, 1049 Bruxelles/Brussel, BELGIQUE/BELGIË*  
*Fax +32 229-65987; e-mail: [rtd-steel-coal@ec.europa.eu](mailto:rtd-steel-coal@ec.europa.eu)*

# Research Fund for Coal and Steel

## Microstructural quantification of multi-phase steels (Micro-quant)

M. P. Aarnts, R. A. Rijkenberg, F. A. Twisk, D. Wilcox, M. J. Zuiderveld (¹),  
A. Arlazarov, D. Barbier, L. Germain, M. Gouné, A. Hazotte, D. Huin, B. Krebs (²),  
L. Barbé (³), J. Hagström, J. Komenda, S. Zajac (⁴),  
W. Bleck, M. Fischer, F. Gerdemann (⁵), F. Friedel, V. Marx (⁶),  
C. Commenda, E. Füreder, R. Hackl (⁷)

(¹) Corus Technology BV — PO Box 10000, 1970 CA IJmuiden, NETHERLANDS

(²) ArcelorMittal R & D (ARSA) — Voie Romaine, BP 30320, 57283 Maizières-lès-Metz Cedex, FRANCE

(³) Centre de Recherches Metallurgiques ASBL (CRM) — Technologiepark 903c, 9052 Zwijnaarde, BELGIUM

(⁴) Korrosions-och Metallforskningsinstitutet AB (KIMAB) — Drottning Kristinas väg 48,  
SE-114 28 Stockholm, SWEDEN

(⁵) Rheinisch-Westfälische Technische Hochschule Aachen — Intzestraße 1, 52072 Aachen, GERMANY

(⁶) ThyssenKrupp Steel AG — Kaiser-Wilhelm-Straße 100, 47166 Duisburg, GERMANY

(⁷) voestalpine Stahl GmbH — Voest-Alpine-Straße 3, Postfach 3, 4031 Linz, AUSTRIA

Contract No RFSR-CT-2006-00017  
1 July 2005 to 31 December 2009

### Final report

## **LEGAL NOTICE**

Neither the European Commission nor any person acting on behalf of the Commission is responsible for the use which might be made of the following information.

***Europe Direct is a service to help you find answers  
to your questions about the European Union***

**Freephone number (\*):**

**00 800 6 7 8 9 10 11**

(\*) Certain mobile telephone operators do not allow access to 00 800 numbers or these calls may be billed.

A great deal of additional information on the European Union is available on the Internet.  
It can be accessed through the Europa server (<http://europa.eu>).

Cataloguing data can be found at the end of this publication.

Luxembourg: Publications Office of the European Union, 2011

ISBN 978-92-79-21632-9

doi:10.2777/83656

ISSN 1831-9424

© European Union, 2011  
Reproduction is authorised provided the source is acknowledged.

*Printed in Luxembourg*

PRINTED ON WHITE CHLORINE-FREE PAPER

# Table of content

Table of content.....	3
Final summary .....	6
1 WP 1 Collection of samples and initial characterization.....	15
1.1 General objective .....	15
1.2 Task 1.1 Collection of samples.....	15
1.3 Task 1.2 Conventional light optical microscopy.....	15
1.3.1 HSLA grade 100.....	16
1.3.2 HSLA31415 steel .....	16
1.3.3 MoB LB steel.....	16
1.3.4 Dual Phase (DP) grade 600 .....	17
1.3.5 TRIP grade 700.....	17
1.3.6 Complex Phase (CP) grade 800.....	17
1.3.7 Complex Phase (CP) grade 1000.....	17
1.3.8 Martensitic steel (M) grade 1200.....	17
1.4 Task 1.3 Chemical analysis.....	18
1.5 Task 1.4 Mechanical testing.....	18
2 WP2 Definition of phases, phase constituents, and properties.....	19
2.1 General objectives.....	19
2.2 Task 2.1 - Definition of phases and phase constituents .....	19
2.2.1 Microstructural aspects AHSS.....	22
2.3 Task 2.2 - Development of a Classification Scheme .....	27
2.4 Task 2.3 - Definition of microstructural parameters and properties .....	29
2.4.1 Mean-free distance .....	29
2.4.2 Contiguity and network probability of secondary phase constituents .....	29
2.4.3 Continuity .....	30
3 WP3 Development of electron optical microstructural imaging and quantitative image processing.....	35
3.1 General objective .....	35
3.2 Task 3.1 Specimen preparation.....	35
3.2.1 Evaluation of standard specimen preparation methods for SEM imaging. ....	35
3.2.2 Special tint etchants containing heavy elements.....	35
3.2.3 Correlation between etching response and crystallographic orientation .....	35
3.2.4 Etch response, SEM morphology, EBSD phase identification and crystallographic orientation of RA.....	36
3.2.5 Evaluation of different specimen preparation methods for EBSD analysis .....	36
3.3 Task 3.2 Development of procedures for SEM imaging.....	38
3.3.1 Resolution and statistical considerations .....	38
3.3.2 Microstructural imaging based on SEM .....	38
3.3.3 Comparison of LOM / SEM and EBSD results of an identical sample area. ....	40
3.4 Task 3.3 Development of procedures for EBSD imaging.....	41
3.4.1 EBSD partitioning of phase constituents .....	41
3.4.2 Flow chart for EBSD analysis .....	42
3.4.3 Influence of measurement parameters .....	43
3.4.4 Applicability of grain reference orientation deviation (GROD).....	43
3.5 Task 3.4 Development of procedures for quantitative image analysis .....	43
3.5.1 Pixel-Based Analysis: QWin and AnalySIS.....	43
3.5.2 Context-Based Analysis: MicroGOP.....	45
3.5.3 Object-Based Analysis: eCognition.....	46
3.5.4 Combined IQ + KAM image analysis .....	47
4 WP 4 Morphological quantification of phases and phase constituents .....	49
4.1 General objective .....	49
4.2 Task 4.1 Volume fraction.....	49
4.2.1 General influences on analysis results .....	49
4.2.2 Correlation to mechanical properties.....	50

4.2.3	Comparison SE images / QBSD images.....	50
4.3	Task 4.2 Grain size (distribution) .....	50
4.3.1	General influences on analysis results.....	51
4.3.2	Line intercept analysis .....	51
4.3.3	Lower bainitic steel grade.....	51
4.3.4	Correlation to mechanical properties.....	52
4.4	Task 4.3 Ferrite-second phase boundary interface.....	52
4.4.1	General influences on analysis results.....	52
4.5	Task 4.4 Shape factor.....	52
4.6	Task 4.5 phase connectivity (mean free distance/continuity/contiguity).....	54
4.7	Task 4.6 Banding and clustering.....	54
4.7.1	ASTM Standard Practice (Designation: E 1268-99) <sup>[1]</sup> .....	54
4.7.2	Method based on progressive erosion <sup>[22]</sup> .....	54
4.7.3	Method based on meangreying <sup>[22]</sup> .....	55
4.7.4	Covariogram .....	55
4.7.5	Other basic methods .....	57
5	WP 5 Orientation and crystallographic characterization.....	59
5.1	General objective .....	59
5.2	Task 5.1 Effective grain size.....	59
5.3	Task 5.2 Distribution of boundary misorientation .....	59
5.4	Task 5.3 Lattice imperfection (defect density) .....	59
5.5	Task 5.4 Volume fraction of phases.....	60
5.6	Task 5.5 Additional parameters .....	60
5.6.1	Experimental.....	61
5.6.2	Results .....	61
5.7	Task 5.6 Texture .....	66
6	WP 6 Chemical characterization .....	67
6.1	General objectives.....	67
6.2	Task 6.1 Chemical segregation .....	67
6.2.1	Chemical segregation in DP steel .....	67
6.2.2	Chemical segregation in TRIP steel. ....	68
6.3	Task 6.2 Chemistry of inclusions / precipitates .....	69
6.3.1	Influence of the cut-off size of 1 or 2 µm on some basic quantification parameters.....	69
6.3.2	Indentification of: AlN or Al <sub>2</sub> O <sub>3</sub> ; TiN <sub>2</sub> or TiN and Ca <sub>(n)</sub> MnS <sub>(1-n)</sub> . ....	70
6.3.3	Quantification and classification of inhomogeneous inclusions.....	70
6.3.4	Inclusion/precipitates analysis in an industrial 1200M steel (Contribution KIMAB) ....	71
6.4	TASK 6.3 Chemistry of individual phases .....	72
6.4.1	Principles of Nano-SIMS.....	73
6.4.2	3D-analysis of bainitic structures in TRIP steel .....	73
6.4.3	SIMS study of carbon re-partitioning during tempering of martensite in DP steel .....	74
6.4.4	Investigations on boron state .....	74
6.4.5	Quantification of the micro-chemistry of martensite and ferrite in DP and TRIP.....	76
7	WP7 Nano scale mechanical testing.....	79
7.1	General objective .....	79
7.2	Task 7.1 Development of a nano-indentation approach.....	79
7.2.1	Conventional nano-indentation versus Continuous Stiffness Method.....	79
7.2.2	Empirical correlation between micro-Vickers and nano-hardness .....	82
7.2.3	Indentation-induced phase transformation .....	83
7.3	Task 7.2 Correlation between nano-hardness and phase properties.....	84
7.3.1	Nano-hardness of phase constituents in DP and TRIP steels .....	84
7.3.2	Relationship between composition and nano-hardness for ferrite .....	84
7.3.3	Relationship between composition and nano-hardness for martensite .....	85
7.4	Task 7.3 Retained austenite stability.....	86
7.4.1	Indentation-induced transformation of austenite and micro-crack formation in TRIP....	86
7.4.2	Lath-shaped and block-shaped retained-austenite in TRIP steel .....	88
8	WP 8 Validation of procedures .....	91
8.1	General objective .....	91

8.2	Task 8.1 Testing the reproducibility of procedures .....	91
8.3	Task 8.2 Testing the discriminative power of procedures in relation to mechanical properties .....	91
8.3.1	Phase fraction and phase (or grain) size in relation to mechanical properties for a DP series.....	92
8.3.2	Bainite and martensite volume fractions in relation to production properties (DP series).....	95
8.3.3	Phase fraction and phase (or grain) size in relation to mechanical properties (DP series).....	95
8.3.4	Phase fraction and phase (or grain) size in relation to mechanical properties of TRIP steel.....	97
8.3.5	Phase fraction and phase (or grain) size and other derived parameters in relation to mechanical properties for TRIP.....	98
8.3.6	Bainite laths widths in relation to heat treatment (Object Based Quantitative Analysis).....	100
8.3.7	Ferrite, martensite and bainite volume fractions in relation to mechanical properties (CP series) .....	102
8.3.8	Effective Grain Size in relation to Strength (M series) .....	105
8.4	Task 8.3 Selecting optimal procedures for microstructural quantification .....	106
8.4.1	Steelgrade or microstructure independ procedures:.....	107
8.4.2	Steelgrade or microstructure depend procedures:.....	107
	Conclusions .....	109
	Exploitation and impact of the research results.....	110
	List of figures and tables .....	111
	Abbreviations .....	117
	Publications .....	119
	References .....	120

## Final summary

Project title: Microstructural Quantification of Multi Phase Steels (MICRO-QUANT)  
Period of Reference: 01/07/06 – 31/12/09  
Contract Number: RFSR-CT-2006-00017

### Overall project objective

The overall objective of this project is the exploration of non-conventional and advanced methodologies for quantification of complex microstructures of steel grades with industrial relevance, including HSLA, DP, TRIP, LB, CP and M. Main techniques described in this report are: SEM/ (QIA), SEM/EBSD, nano-SIMS, EPMA and nanohardness.

### Work package 1 Collection of samples and initial characterization

The main objective of this work package is to obtain a range of industrial steel samples, with microstructures consisting of different combinations of phases and phase constituents. These samples were characterized by means of: (1) conventional light-optical microscopy, (2) chemical analysis of average composition, and (3) mechanical testing. The results of these analyses are summarized in the form of several tables and were used as basic input for all other work packages.

#### Task 1.1 Collection of samples

The chosen series of samples consists of the following industrial relevant grades: HSLA (Corus) HSLA (VAS), DP600 (Corus), TRIP700 (TRIP), LB (KIMAB), CP800 (TKS) CP1000 (TKS) and MS1200 (TKS). This sample series (RRT samples) covers a wide range of microstructures that are regarded as challenging for quantification with standard light-optical microscopy and were made available for all partners.

#### Task 1.2 Conventional light optical microscopy

Basic conventional light-optical microscopy was used to characterise the microstructures of the RRT series. For all samples it was concluded that microstructural quantification based on light-optical microscopy was inaccurate with respect to certain microstructural parameters, such as size distribution of the second phases in DP600 and TRIP700 or even impossible.

#### Task 1.3 Chemical analysis

The chemical composition of all RRT samples was accurately measured and summarized in a table.

#### Task 1.4 Mechanical testing

For all RRT samples their basic mechanical properties were determined and summarized in tables. The mechanical parameters included are:  $R_p$   $R_m$   $A_g$   $A_{80}$  (measured for all samples in both RD and TD direction, for TRIP700 and DP600 also the 45° RD/TD direction was determined). Micro-Vickers hardness was measured for all RRT samples.

### Work package 2 Definitions of phases and phase constituents, and properties

The first prerequisite for quantifying microstructures is to identify phases and phase-constituents that are present in steel microstructures. The main objective of this work package is to identify and characterise these phases and phase constituents. Subsequently, a unified set of definitions and consistent terminology for phases and microstructural constituents is presented. For relevant phases the mechanism of formation and the characteristic morphologies is described. Most important objective of this work package is the development of a scheme for classification of microstructures based on the definitions formulated for individual phases and microstructural constituents. The last objective is to identify and define relevant microstructural parameters, which can be measured in order to quantify properties of individual phases and microstructural constituents.

#### Task 2.1 Definitions of phases and phase constituents

An overview of the nomenclature used in this report of major matrix phase constituents and minor secondary phases is presented. For both the major matrix phase constituents and the minor secondary phases an overview is given of their most important morphological characteristics (LOM and SEM) and crystallographic properties (EBSD). For the most relevant phases, or phases where confusion might occur, more detailed descriptions are presented.

## Task 2.2 Development of a classification scheme

In the classification scheme that was developed, the description of matrix phases and secondary phases follows closely the pattern occurring in real micrographs. This approach offers the flexibility necessary for the description of any combination of main matrix phases with secondary minor phases. Moreover, by using this approach it can be used as a basis for an accurate quantification strategy. Although precipitations strengthening carbides are not the main focus of this project, these carbides are also included in the classification scheme. Since the classification scheme allows for adding new components or phases without the necessity to alter the terminology, it can be easily adapted to new insights. A series of typical examples of complex microstructures and phase constituents is presented to facilitate the use of the classification scheme. All RRT materials were classified according to the developed classification scheme.

## Task 2.3 Definition of microstructural parameters

An extensive inventory of parameters, which are relevant for a quantitative description of matrix and second phase constituents has been collected and is presented in the tabular form. For each parameter a short description is given and for some less well-known parameters (mean-free distance; continuity and contiguity) a more detailed description is presented to prevent any misinterpretation of these parameters.

# Work package 3 Development of electron optical microstructural imaging and quantitative image processing

The main objectives of work package 3 are the quantification of the morphology of individual phases and phase constituents in complex microstructures based on electron-optical imaging (i.e. SEM) in combination with Quantitative Image Analysis (QIA) processing or by SEM in combination with Electron Backscatter Diffraction methods. First step is to obtain robust and reliable sample preparation procedures for these SEM/QIA and SEM/EBSD methods. The final objective is to give an overview of useful methods or procedures for microstructural quantification based on SEM and SEM/EBSD.

## Task 3.1 Specimen preparation

Pristine specimen preparation is essential for any accurate microstructural investigation. For evaluation of multi-phase microstructures with SEM this is even more important. Therefore, several methods were tested and evaluated in this work package. These methods included besides standard LOM based sample preparation methods also two heavy metal based etchants that potentially could give an enhanced contrast in SEM-BS imaging. However, application of heavy metal based etchants was found not to be successful. For SEM sample preparation special attention has to be paid to micro scratches, which can heavily interfere with QIA feature detection. In general, SE and Inlens detection is more vulnerable for these (micro) scratches. It was shown that electropolishing in combination with OPS can be used for sample preparation for very detailed high resolution images. Deformation free preparation is for EBSD sample preparation the most important parameter. For general EBSD preparation it is concluded that electro-polishing or OPS give the best overall results. For TRIP EBSD samples, the meta-stable retained-austenite offers an additional challenge for sample preparation and is extensively discussed in this report. A combination of electro-polishing and OPS was found to be the best and most efficient way to prepare TRIP samples for EBSD analysis.

## Task 3.2 Development of procedures for SEM imaging

Effective microstructural imaging for quantification purposes depends on two main issues: (1) optimal trade-off between resolution and statistics, and (2) adequate visualisation of relevant microstructural features based on suitable (chemical) etchings or polishing and electron detection. With this in mind, an inventory of resolution and statistical considerations is presented, together with illustrative examples where LOM and SEM images of the same sample area are compared. As a rule of thumb: tint etching generally works well in combination with Back Scatter detection, mild Nital etching or electropolishing works best with SE or inlens detection. For advanced image analysis methods (i.e., context- /object-based), where relative high-resolution images are needed, scratch free surfaces are essential. Mild Nital etching or electro-polishing are the preferred methods to achieve this goal.

## Task 3.3 Development of procedures for EBSD imaging

Post processing of raw EBSD data, like standard data clean-up procedures in EBSD software can significantly influence results. It was found that standard grain dilation gives good allround results

on basic prepared samples. However, when grain size is essential, a full iterative grain dilation procedure is preferred.

The development of methods for accurate partitioning of phase constituents in multi-phase microstructures is the main focus of this task. Since efficient partitioning will be closely related to the intrinsic properties of phase constituents, an overview is presented showing which EBSD parameter (Image quality (IQ), Kernel Average Misorientation (KAM), Grain Size (GS) etc.) can be used to make adequate partitions to capture ferrite, martensite, retained austenite and bainite from an EBSD mapping. For all RRT the main EBSD partitioning strategies -and limitations- are presented.

The application of grain reference orientation deviation (GROD) for the partitioning of bainite fractions was also investigated but was found to be very susceptible to artefacts in the measurement that are difficult to remove. Therefore, this method is regarded as not suitable for robust partitioning. However, it can be used for phase identification purposes.

#### Task 3.4 Development of procedures for quantitative image analysis

This task focuses on the development of quantitative image processing of SEM images by means of software applications based on two essentially different approaches: pixel-based approach and the more advanced context- or object-based image analysis approach. These two different image analysis software approaches and methodologies are briefly discussed.

For SEM images of Nitral or electro-polished DP and TRIP samples a *pixel-based* image analysis method is described that results in a partitioned and subsequently quantified matrix and secondary phase. The basic procedures for ferrite and second phase detection in DP and TRIP are discussed. Additionally, a method is described to separate bainite from martensite in the partition of second phase constituents DP.

A *pixel-based* method for the detection and quantification of cementite is described. The combination of InLens and SE2 electron image formation was found to give a high contrast between carbides and ferrite matrix without disturbing edge effects.

A description of *context- and object-* based image analysis software packages (MicroGOP2000S and eCognition) is presented. It was found that the image classifier module used in the microGOP system could cope with all microstructures investigated in this project. The eCognition package had to take several hurdles before it was ‘operational’, but finally succeeded in realising a challenging quantification of lathlike bainitic constituents in a martensitic matrix.

A new methodology is presented how EBSD image quality and kernel average misorientation maps can be combined and used for phase identification and quantification. A comparison of the content of bainitic ferrite and martensite between different steel grades using this combination method yields a consistent sequence. The procedure yields good results for all steel grades except for the martensitic steel, which is not distinguishable from a bainitic microstructure.

### Work package 4 Morphological quantification of phases and phase constituents

WP 4 deals with the quantification of the morphology of individual phases and phase constituents in complex microstructures of multi-phase steels mainly based on electron-optical imaging methods in combination with quantitative image analysis (QIA).

#### Task 4.1 Volume fraction

Volume (area) fractions of on the RRT samples as determined by different partners are compared. The DP600 and TRIP700 are the most extensively analysed steel grades, followed by the HSLA and finally the CP grades. Several DP and TRIP series were analysed and compared with mechanical properties, see also §8.2. For HSLA there is a reasonable agreement between context- and pixel-based QIA. Only the context-based image analysis software packages were able to produce quantification results for CP800/CP1000 and were in good agreement.

#### Task 4.2 Grain size (distribution)

The mean grain size values for HSLA and CP obtained with context-based analysis procedures were in good agreement. It was found that analysis procedures that detect small heterogeneous structures as one feature can lead to inaccurate grain-size values.

#### Task 4.3 Ferrite-second phase boundary interface

The strengthening mechanism of multi-phase steels is partly based on the pinning of dislocations within the ferrite matrix by second-phase constituents. Therefore, quantification of boundary interface between ferrite and second-phase constituents is important in relation to an appreciation of mechanical performance.

#### Task 4.4 Shape factor

Results of shape factor analysis obtained with different software packages are presented. Included are: mean grain perimeter, total perimeter per area, aspect ratio and fullness ratio. Many measured values show good comparability. However, for perimeter and perimeter derived values, discrepancies were observed. These discrepancies are caused by the same underlying detection/magnification related problems as described for volume fraction and grain size. The mean values of a series additional shape factors (border index, shape index, compactness, roundness, elliptic fit and density) are reported for RRT samples. Trends between ferrite shape factors and different steel grades are presented.

#### Task 4.5 phase connectivity (mean free distance, continuity and contiguity)

A limited amount of measurements on phase connectivity were performed on selected Round Robin samples with SEM/QIA according to methods/definitions as described in task 2.3. Phase connectivity parameters are mainly of interest when volume fractions in a series of samples are similar while (mechanical) properties differ significantly. This was illustrated in §8.3.5 for a series of TRIP samples.

#### Task 4.6 Banding and clustering

This task has focussed on a quantitative assessment of banding and clustering of phases and phase constituents in microstructures of multi-phase steels due to macro-segregation. A number of methods to define and quantify the degree of banding and clustering have been investigated. It was found that the covariogram method is a very useful tool to quantify the degree of banding in DP microstructures.

### Work package 5 Orientation and crystallographic characterization

#### General objective

EBSD (Electron Back Scatter Diffraction) has been used for microstructural characterisation and analysis of complex microstructures in HSLA, LB, DP, TRIP and M steels. As part of WP 5 an extensive Round Robin Test (RRT) has been conducted focusing on a range of parameters specified in accordance with the task structure of the work package. The parameters measured from the test were processed and EBSD results from partners were analysed with regard to consistency and scatter. The results of this comparison are reported in task 5.5.

#### Task 5.1 Effective grain size

Based on the HSLA steel studies, the  $15^\circ$  has been accepted and used as the critical misorientation parameter for all steel types investigated.

#### Task 5.2 Distribution of boundary misorientation

It was thought that the Misorientation Angle Distribution (MAD) could be a tool to separate martensitic microstructures from bainitic ones, but so far the analysis within this project cannot give consistent rules for separating these two phases. MAD was however found to be very useful for verification of already partitioned phases.

#### Task 5.3 Lattice imperfection (defect density)

The Image Quality (IQ) of an EBSD measurement depends mainly on the lattice distortion due to local stress and was used as a rough estimate for local dislocation density. On the other hand, the lattice distortion which leads to local misorientations has been estimated using the Kernel Average Maps (KAM). In the KAM map, low values of KAM ( $<1^\circ$ ) were related to polygonal ferrite whereas higher values correspond with bainitic ferrite. Strong discrepancy between IQ-based and KAM-based analysis results was observed. It is concluded that additional investigations of bainitic ferrite using transmission electron microscopy are necessary.

#### Task 5.4 Volume fraction of phases

Practical EBSD strategies (partitioning rules) were developed for identification and partitioning of phase constituents in DP and TRIP microstructures including martensite, retained-austenite, and bainite. These partitioning rules were also used for the “EBSD guided” nano-indentation described in WP 7.

#### Task 5.5 Additional parameters

An extensive overview is presented of the EBSD round robin results. It was not the intention to compare processed EBSD datasets but comparison of raw data was the main issue. The analysis showed that EBSD measurements, when set-up in a similar way, with similar step size and comparable microscope resolution, give similar results. However, the results also showed that the output from EBSD measurements can vary a lot. What we can learn from this study is that it is

extremely important to plan the experiments accurately and to present the parameters used for the measurements together with the results, or else the results are quite meaningless. The analysis furthermore showed that an exercise like this needs to be highly constrained; for each material a number of parameters must be defined, or else the results will be difficult to compare. The most important parameters are to be defined beforehand and must be equal for all laboratories involved. These parameters are: phases needed to be included, step size and size of data set, and position and sheet plane.

#### Task 5.6 Texture

The main texture components were determined and described for all RRT samples. The texture in the TRIP700 steel has been found very homogeneous over the specimen thickness, while the DP600 texture was weaker near the surface, as would be expected when assuming additional shear deformation due to friction during rolling. The textures of the MS1200 and HSLA31415 steels were nearly random over the whole specimen thickness, which is typical for steels hot-rolled within the austenite regime. The HSLA grade 100 and CP1000 showed a strong, homogeneous  $\alpha$ -fibre normally associated with rolling deformation within the ferrite. This texture decreased towards the surface. The CP800 displayed a very strong partial  $\alpha$ -fibre which is mainly comprised of components near the  $45^\circ$  ND-rotated cube component, which also drops off towards the surface.

### Work package 6 Chemical characterization

#### General objective

Main objective of this work package is to formulate procedures to perform elemental mappings of banding due to macro-segregation of alloying elements and quantify the amount of band-like segregation patterns. Next objective is the optimisation of automated inclusions/precipitation measurements with respect to their chemistry and size. Develop methods for qualitative and quantitative analysis of the micro-chemistry of individual phases is the last objective.

#### Task 6.1 Chemical segregation

In this task chemical segregation was analysed in order to assess the potential of Electron probe micro-analyzer (EPMA). Two examples were chosen to verify the capacity of this technique: one for DP steel and another for the TRIP. As a global conclusion it can be stated that EPMA permits the characterization of macro-segregation, of all metallic elements. The elements like C are very difficult to quantify with this technique because of their large solubility and diffusivity. However, taking into account their interaction with other metallic elements (for example C will segregate mostly in the same zones than Mn) it's possible to get some qualitative information.

#### Task 6.2 Chemistry of inclusions/precipitates

The optimization of automated inclusion/precipitation measurements with respect to their micro-chemistry and size was performed for the RRT samples. This was performed in three steps. First the chemical composition of inclusions with a diameter  $> 1 \mu\text{m}$  were measured for the majority of the RRT samples (only "heavy" elements were included in this quantification: Mg, Al, Zr, Nb, S, Si, Ca, Ti, Mn). The obtained quantification results were compared with the results from the bulk chemistry and it was found that for most elements this bulk chemistry is reflected in the inclusion chemistry. The next step was to determine to which extent lighter elements (N, O) can be included in the quantification in order to differentiate between N/O based inclusions. It was found that to some extent this is possible, although overlapping signals can cause inaccuracies. Determination of the minimum inclusion size was the final step of this task. From this study it was concluded that inclusions/precipitates larger than 100 nm can be measured with sufficient accuracy to be properly classified.

#### Task 6.3 Chemistry of individual phases

This task focuses on analytical measurements of the micro-chemistry of individual phase constituents with Electron Probe Micro Analysis (EPMA) and Nano Secondary Ion Mass Spectrometry (Nano-SIMS). In particular carbon is of interest in this context. After a short introduction of nano-SIMS technology, this technique is used to study carbon re-partitioning during tempering of martensite in DP steel. The results obtained in this study are very useful to describe martensite evolution for different tempering conditions and will increase understanding and controlling of this phenomenon. One of the applications of Nano-SIMS is illustrated by the mappings of carbon repartitioning at a local scale. A second nano-SIMS application is illustrated by two carbon depth-profiles (500 nm depth). One depth-profile was obtained from a lath-bainite and another from a granular bainite zone. In zones with lath shaped bainite, carbon 3D-reconstruction

shows no strong connectivity of carbon containing areas. On the contrary, in zones with granular bainite, carbon 3D-reconstruction shows a strong connectivity over relative large distances. A third topic studied with nano SIMS was the boron state found in Nb or Mo alloyed steel grades. By combining the different ion maps ( $^{11}\text{B}$ ,  $^{11}\text{B}^{12}\text{C}$ ,  $^{11}\text{B}^{16}\text{O}$  and  $^{12}\text{C}$ ) the boron distribution in ferrite grains was determined as a function of alloying elements Nb and Mo.

EPMA was used to determine the chemistry of individual phases in DP and TRIP microstructures. It was found that there is relatively little segregation of Mn or Si in the DP samples. Contrary to the DP sample, Mn and Si mappings – as well as the Al mapping – for the TRIP700 reveal a high degree of micro-segregation. Investigations have shown that carbon measurements using EPMA are sensitive for surface topography after etching and carbon contamination during the EMPA measurement. However it was shown that the influence of a mild surface topography on the carbon quantification is very limited. With respect to carbon contamination, use of a cold finger and oxygen yet could not fully avoid carbon deposition and a large correction of 0.7-0.8 wt% carbon was still required.

## Work package 7 Nano scale mechanical testing

### General objective

The main objective of this work package is to investigate the merits and limitations of nano-indentation for the evaluation of nano-hardness of phase constituents in DP and TRIP microstructures.

#### Task 7.1 Development of a nano-indentation approach

Nano indentation was found a promising method to determine the hardness of phase constituents in a multi-phase microstructure and to observe its dynamic response to local deformation. However, to appreciate its merits and limitations, several issues have been considered, including: (1) conventional nano-indentation testing versus Continuous Stiffness Measurement (CSM), (2) type of indenter, (3) resolution and (4) sample preparation (5) interpretation of local perturbations or discontinuities of load-displacement curves. These aspects have been addressed and are summarized as part of this work package. An overview of typical nano-hardness values reported in literature for ferrite, bainite, (tempered)martensite and retained-austenite is presented and evaluated. An empirical correlation has been formulated (equation 7-11) to establish a link between nano-hardness as measured with a Berkovich indenter and micro-Vickers. This correlation has opened a gate to link nano-hardness to local chemical composition for ferrite and martensite (i.e., in particular carbon content).

#### Task 7.2 Correlation between nano hardness and phase properties

The nano-hardness of ferrite in DP600 and TRIP700 reported by partners in this project is around 3 GPa with relatively little spread. For tempered and fresh martensite, typical nano-hardness values of respectively 5-9 and 7-16 GPa have been measured. The nano-hardness of austenite is discussed in detail in task 7.3. The relationship between composition, crystallography and nano-hardness of ferrite and martensite is discussed. For ferrite it was found that when the micro-hardness/chemical composition relation derived by Brisson and Blondeau was used in combination with the empirical correlation between nano-hardness and micro-Vickers as formulated in WP1 a nano-hardness was predicted of 2.4 GPa. This is in agreement with experimentally determined values. The total spread in ferrite nano-hardness values of 1 GPa measured on the same sample area is attributed to variation in crystallographic orientation of ferrite grains. Using a similar approach as for ferrite, the nano-hardness/chemistry relation for martensite was determined and expressed in equation 7-16.

#### Task 7.3 Retained austenite stability

A methodology is described how to use phase information obtained from EBSD measurements, as a guide to place nano indent exactly in predetermined phase constituents. Based on this EBSD-guided nano-indentation, the impact of nano-indentation of retained-austenite in TRIP steel on the characteristics of load-displacement curves has been investigated and compared with literature. Experimental evidence is presented that indentation-induced phase transformation of retained-austenite to martensite provokes perturbations and/or discontinuities in the load-displacement curve at the unloading stage. Finally, the relative stability of lath- versus block-shaped retained-austenite is discussed. It was found that lath retained-austenite appears more stable than blocky retained-austenite.

## Work package 8 Validation of procedures

The main objective of this work package is the evaluation of procedures which have been developed in this project. Present an overview and selection and documentation of procedures for microstructural quantification with the long-term aim (outside the scope of this project) of European standardization of these procedures.

### Task 8.1 Testing the reproducibility of procedures

During the run of the project it was found that not all partners, for different reasons, could cope with the quantification of all RRT microstructures. This was related to **a**) sample preparation (EBSD sample preparation for TRIP700 was found to be very critical) **b**) limitations of available equipment (resolution of a LaB<sub>6</sub> SEM was not sufficient for several structures) and **c**) software (not all image analysis software packages were able to cope with the quantification of CP, LB or M structures). With this in mind, the reproducibility of procedures has been tested, and partly imbedded, in work package 8.2. The reproducibility of EBSD measurements of the RRT has been described extensively in section 5.6. The general conclusion is that EBSD measurements in itself are reproducible, but that the actual quantification of a measurement strongly depends on parameter settings. The identified critical parameters are field size, step size, grain tolerance angle (GTA) and minimum grain size. To obtain reproducible quantification results from SEM microstructures, it is important to realize the impact of inhomogeneity of the microstructure in relation to the magnification used, and the impact of submicron sized grains or second phase constituents. These aspects have also been discussed in WP3 (§3.3.1) and in WP4 in this report.

### Task 8.2 Testing the discriminative power of procedures in relation to mechanical properties

Quantification of microstructural parameters is only relevant if the obtained quantified parameters also correlate to mechanical properties of the samples or correlate to process parameters used during the production of the samples. In this task the most promising methods which were developed in this project were tested to see if the obtained quantitative results can be linked to mechanical or process parameters. The work package is structured in such a way that for every RRT grade a series of samples is produced with significantly variation in mechanical properties or production parameters.

•(DP) For a series of DP steels with different mechanical properties morphological parameters were quantified in all three planes and correlated to mechanical properties. After determination of the independent variables, reasonable correlations were found using 2 planes (RD/ND and TD/ND) but improved correlations were found when all 3 planes were used for the correlation with UTS, YS and El using three independent variables: 1) ferrite grain size; 2) second phase volume fraction; 3) martensitic island size. In a second, refined approach, the calculated bainite volume fraction was included. The bainite volume fraction was estimated using a thermo dynamic model, and was not determined from the microstructure. Good linear statistical correlation of elongation (range: from 11 to 31%) and microstructural parameters (bainite fraction, size of martensite islands and ferrite grains). Good linear statistical correlation of Ultimate Tensile Strength (UTS) (range: from 450 to 950 MPa) and microstructural parameters (size of ferrite grains, bainite and martensite fraction) that can be slightly improved using complex function correlation. Good linear statistical correlation of Yield Strength (YS) (range: from 300 to 750 MPa) and microstructural parameters (bainite fraction, size of martensite islands) were found, that might slightly be improved by using complex function correlation and adding ferrite grain size. No satisfactory results were obtained for statistical correlations (linear or complex) with  $R_{area}$  (range: from 33 to 80%) and other microstructural parameters. It was thought, that  $R_{area}$  might relate to the morphology of second phase constituents. Hence, the morphology was introduced in the correlation but did not result in significant improvement of the microstructure/mechanical property correlations.

For two series of DP grades (DP\_a and DP\_b) with different chemical compositions the bainitic and martensitic volume fractions were determined from SEM images according to procedures described in WP4. The samples were produced with different reduction percentages and different top temperatures. Correlations were found between bainite and martensite evolution as a function of top temperature. The reduction showed no influence on the amount of bainite and martensite.

The validation of the procedures developed in WP3 to WP5, and especially those for EBSD, was done on a series of DP steels produced at Arcelor with varying mechanical properties. Based on the microstructural parameters obtained by LOM (second phase fraction) and EBSD (ferrite grain size), a correlation was found with mechanical properties. A good correlation was found between ferrite-bainite fraction and tensile strength, while this was less for uniform elongation.

•(TRIP) Metallographic analysis, according to procedures described in §2.2.1.4.1 in combination with a thermo-kinetic model simulation to determine the bainite fraction, was made. Although the data base of TRIP steels was not very large the same statistical approach as for DP steels was applied. Contrary to the DP series, in case of TRIP the bainite fraction didn't correlate with any mechanical parameter. Arcelor has reached to the conclusion that the bainite fraction simulated by thermo-kinetic modeling is not correct and another method is necessary to define this fraction properly (outside the scope of this project). Despite these difficulties, a statistical analysis was made. The statistical parameters of individual best fitting correlations between UTS, YS, El and microstructural parameters are shown. Since the data set was relatively small and the calculated bainite fraction was regarded as unreliable, the obtained results are only indicative.

Two TRIP series, with the same chemical composition, produced with two different annealing cycles were used to investigate the discriminative power of procedures developed. Both series show a significantly different tensile strength evolution for the different annealing cycles. Based on the 2<sup>nd</sup> phase fraction determined by LOM or XRD there is no obvious correlation between 2<sup>nd</sup> phase fraction and tensile strength. The UTS does not show a clear dependency of average ferrite grain size for cycle 1. For cycle 2 a small dependence is observed with grain size. The UTS in two TRIP series with the same chemical composition but produced with different annealing cycles and top temperatures shows a clear correlation with ferrite/martensite + ferrite/retained austenite grain boundary length.

•(LB) The potential of the object-based analysis approach which has been described and discussed in section §3.5.3, was investigated. An object-based analysis procedure was created for extraction of morphological properties from 18 different samples consisting of a mixture of bainite and Martensite/Austenite constituents. The developed analysis routine was applied to FEG-SEM images. Despite large variations in morphologies of the 18 samples the analysis routine was able to cope with these variables without operator interventions. The discriminative power of the method was illustrated by the clear relationship between lath width distributions and heat treatments given to the samples.

•(CP)

To validate procedures developed in §3.5.4 and to test the discriminating power of these procedures, a series of CP specimens were produced with a pronounced spread in mechanical properties. Ferrite, bainitic ferrite and M/RA volume fractions were quantified based on EBSD IQ and KAM maps according to procedures described in section 3.5.4. The method was able to quantify ferrite, bainitic ferrite and M/RA phase constituents and relate observed changes to coiling temperature and tensile properties. In addition, using a simple rule-of-mixture employing volume fractions and Vickers hardness of single phases it was possible to fit the measured hardness quite well.

•(M) A series of martensitic samples were characterized using EBSD analysis. The effective grain size was determined for all samples using mean linear intercept method (GTA 15°). The sample preparation and EBSD procedure derived from procedures described in WP3 and WP5 have resulted in a discriminative method for determination of correlations between effective grain size and R<sub>p</sub> and R<sub>m</sub> for a series of martensitic steels.

#### Task 8.3 Selecting optimal procedures for microstructural quantification

Although in the original aim it was stated that a generic approach for all microstructures would be strived for, it was found during the run project that this is not realistic. Therefore, steel grade or microstructure *independent* procedures are presented first together with the reference to the paragraphs in which they are described. In the second part steel grade or microstructure *dependent* quantifiable parameters are linked to procedures and to paragraphs in which they are described.



# 1 WP 1 Collection of samples and initial characterization

Task	Deliverable	D#
1.1	Collection of a wide range of multi-phase microstructures	D1
1.2	Optical assessment of multi-phase microstructures	D2
1.3	Chemical analysis of targeted steels	D3
1.4	Mechanical testing of targeted steels	D4

## 1.1 General objective

The main objective of this work package was to obtain a range of steel samples, which are relevant for industrial use, with microstructures consisting of different combinations of phases and phase constituents. These aforementioned samples have been initially characterized by means of: (1) conventional light-optical microscopy, (2) chemical analysis of average composition, and (3) mechanical testing.

## 1.2 Task 1.1 Collection of samples

Several types of single-phase and multi-phase steels have been collected and distributed among all RFCS partners during the first two Semesters. Table 1.1 shows an overview of materials collected during this period. These materials form the basis of Round Robin Trials (RRT's) and the development of methods for quantitative microstructural analyses. All of these steels can be considered as typical industrial High-Strength Steels apart from fully lower-bainitic (LB) steel developed by KIMAB. This LB steel has been TMCP (Thermo Mechanically Controlled Processing) processed under laboratory conditions with isothermal transformation at 350°C.

**Table 1.1** *Inventory of materials selected for Round Robin trials.*

Steel grade	HR/CR*	Supplier
HSLA grade 100	HR	CORUS
HSLA31415 steel	HR	VAS
MoB LB steel (Lab.TMCP)	HR	KIMAB
Dual Phase (DP) grade 600	CR (Heat treated)	CORUS
TRIP grade 700	CR (Heat treated)	ARCELOR
Complex Phase (CP) grade 800	HR	TKS
Complex Phase (CP) grade 1000	HR	TKS
Martensitic steel (M) grade 1200	HR	TKS

\* Rolling condition: hot-rolled (HR) or cold-rolled (CR).

## 1.3 Task 1.2 Conventional light optical microscopy

Various partners (i.e., Arcelor, Corus, CRM, TKS, and VAS) have collected conventional light-optical micrographs of the RRT steels - listed in Table 1.1 - for qualitative microstructural assessment. Several conventional etching methods were used for all planes (RD/TD; ND/TD; ND/RD). Illustrative micrographs of RRT samples (ND/RD plane) are shown in Figure 1.1

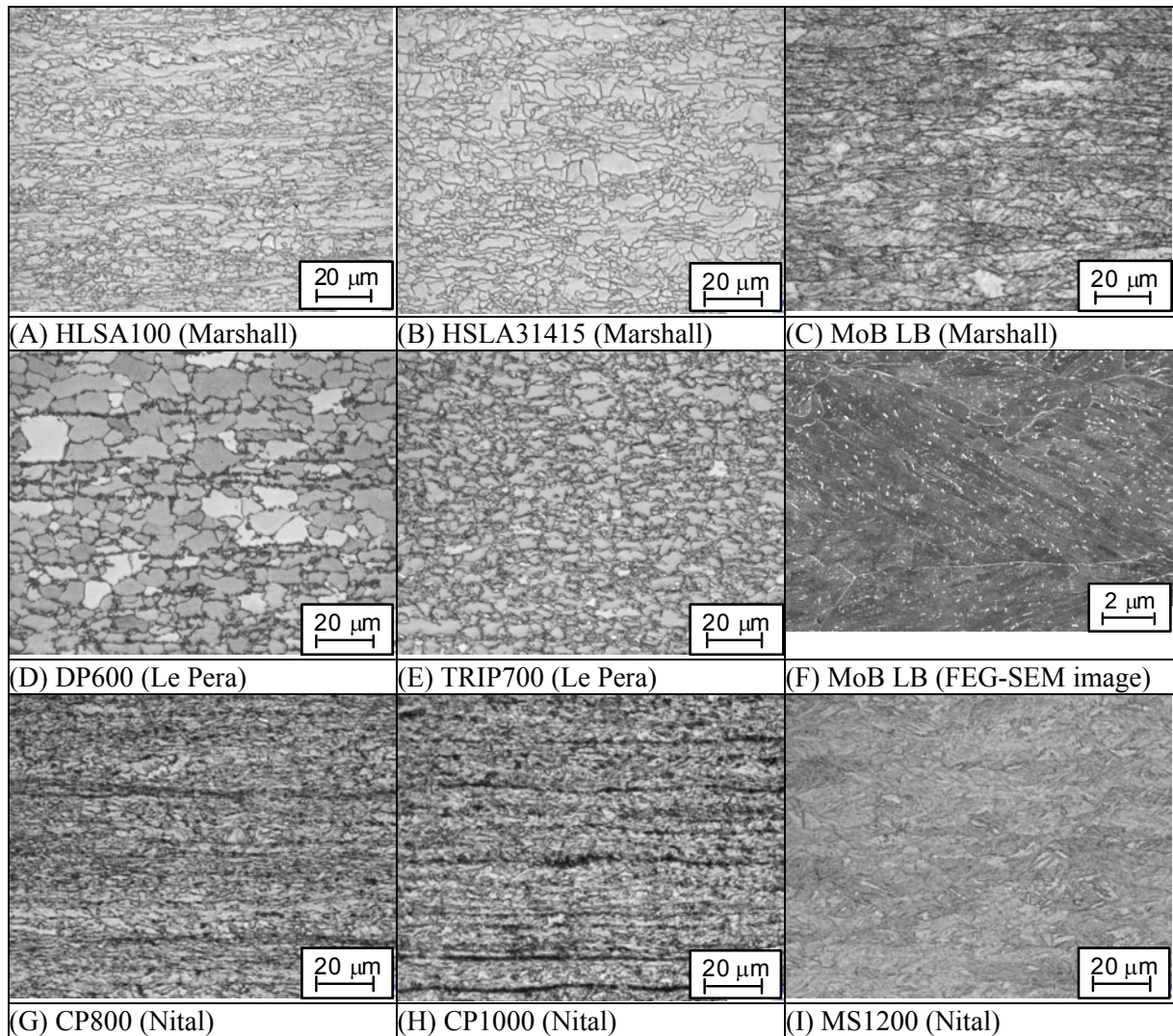


**Figure 1.1** Illustrative micrographs of RRT samples (ND/RD plane)

### 1.3.1 HSLA grade 100

CRM has employed a Marshall etching to reveal the ferrite grain boundaries. This etching reveals that grains are elongated in the rolling direction and have an irregular shape. A wide range of grain sizes can be seen, varying in dimensions from relatively quite large to an abundance of very small grains. CRM has reached the conclusion that conventional light-optical microscopy is not suitable to determine any parameter of the ferrite phase with accuracy. (see Figure 1.1(A))

### 1.3.2 HSLA31415 steel

Both Marshall and Le Pera etchings have been applied by CRM on the HSLA31415 steel. The ferrite grain boundaries are visualised by both etchants, although the Marshall etching gives a more clear view, see Figure 1.1(B). With the Le Pera etching (no image), darker zones can be distinguished. These zones correspond with quite small grains. Again, similar to the HSLA grade 100, CRM and Arcelor concluded that quantification based on light-optical microscopy was feasible

### 1.3.3 MoB LB steel

Qualitative characterisation of the lower-bainitic microstructure of the MoB LB grade has been performed using light-optical microscopy with Marshall etching (see Figure 1.1(C)) and FEG-SEM (Figure 1.1(F)). A comparison between both techniques shows that only FEG-SEM provides the required resolution in relation to the dimensions of characteristic bainitic features in LB steels. For this reason no efforts have been undertaken to quantify the MoB LB microstructure based on light-optical microscopy.

### **1.3.4 Dual Phase (DP) grade 600**

Nital etching (no image) has proven to be useful to reveal grain boundaries of ferrite in DP600, while martensite appeared as dark islands. Based on the RD-TD plane, CRM has determined an average ferrite grain size of  $\sim 10 \mu\text{m}$  with an average stretch factor of 1.12. According to CRM, the ferrite grains seen on the two other planes have a compressed and elongated appearance in rolling direction. CRM's micrographs show evidence of "squeezed" martensite bands in between the ferrite grains. CRM has employed a Le Pera etching to determine the amount of martensite, which appeared white or dark brown depending on its carbon content and degree of etching, see Figure 1.1(D). The martensite fraction varied between 8% measured on the RD-TD plane and 15% on the ND-TD plane. This latter value is similar to the value measured by Arcelor. However, based on magnetic saturation analysis, Arcelor conclude that roughly 2% of the second phase is retained-austenite. Based on a Le Pera etching, revealing also ferrite grain boundaries, CRM obtained an average ferrite grain size of  $5.4 \mu\text{m}$  based for both the ND-RD and ND-TD planes. The ferrite grains had a stretch factor of 1.31. With light-optical microscopy, grains smaller than  $1-2 \mu\text{m}$  cannot accurately be determined and measured correctly according to CRM. They conclude that this has to be taken into account because almost 15% of the grains are measured in this range. Arcelor reaches a similar conclusion for the quantification of the dimensions of the second phase islands.

### **1.3.5 TRIP grade 700**

CRM used a Le Pera etching to reveal different phase constituents. Both retained-austenite and martensite appeared as white islands, whereas ferrite grains appeared light or dark brown depending on their crystallographic orientation, see Figure 1.1(E). Bainitic phase constituents appear as dark brown regions. In literature several methods have been described to identify microstructural constituents in TRIP steel.<sup>[1][2]</sup> Arcelor has developed an approach to identify and quantify different types of microstructural constituents within a multi-phase microstructure (see developments as part of Task 2.1). This VMK approach is based on three consecutive etchings: (1) Villela, (2) Metabisulfide, and (3) Klemm. (See for more details §2.2.1.4.1).

Alternatively, the amount of retained-austenite in TRIP can be measured by means of magnetic saturation or XRD. The RA fraction determined with magnetic saturation was 11.6%. (CRM) Quantification of the RA fraction based on XRD analysis yields in this case  $12.8 \pm 0.9\%$ . These values are in agreement with the RA fraction obtained with the VMK approach – i.e.,  $10.1 \pm 2.0\%$ .

### **1.3.6 Complex Phase (CP) grade 800**

The CP800 grade has been supplied by TKS and comprises primarily ferrite and bainite. According to CRM, the Klemm and Nital etchings reveal ferrite grain boundaries. A Nital etching is more effective in showing ferrite grain boundaries, see Figure 1.1(G). The average grain size is quite small. Based on conventional light-optical micrographs, CRM reaches the conclusion that light-optical microscopy proves to be inadequate to quantify neither the properties of the ferritic matrix (e.g. grain size, stretch factor, etc.) nor the characteristics of secondary phase constituents. This is in agreement with findings from TKS that the average ferrite grain size is below  $2 \mu\text{m}$ .

### **1.3.7 Complex Phase (CP) grade 1000**

The CP1000 grade has been supplied by TKS and comprises primarily ferrite, bainite, and martensite. Both Nital and Klemm etchings have been applied on the CP1000 steel. According to CRM, ferrite grain boundaries proved to be visible with both etchants, although Nital etching gives a more pronounced outlining, see Figure 1.1(H). The CP1000 microstructure turns out to be too fine grained for CRM to allow any quantification based on light-optical microscopy. This is in agreement with findings from TKS, that the average grain size is  $< 2 \mu\text{m}$ .

### **1.3.8 Martensitic steel (M) grade 1200**

The MS1200 grade has been supplied by TKS and comprises mainly a martensitic microstructure with some bainite. Both a Nital and a Marshall etching have been applied by CRM to develop the microstructure of the MS1200 steel. The grain boundaries have been visualised by means of Nital etchant, see Figure 1.1(I). Marshall etching gave good results for the RD-TD plane but resulted in an over-etched picture for the two other planes. No parameters have been quantified by CRM based on

LOM. Based on a Béchet-Beaujard etching and intercept method, Arcelor has determined a packet size of roughly 19 µm in rolling direction and 6.7 µm in transverse direction.

## 1.4 Task 1.3 Chemical analysis

Table 1.2 shows the average chemical composition of the selected RRT steels listed in Table 1.1.

**Table 1.2** Average chemical composition (in weight-%) of the RRT materials.

Grade	Supplier	C	Mn	Si	Al	Cr	P	S	Ni	Mo	Cu	B	Sn	Ti	Nb	V
HSLA100	Corus	0.065	1.677	0.095	0.049	0.011	0.013	0.003	0.021	0.003	0.011	0.001	-	0.130	0.072	0.007
HSLA31415	VAS	0.075	1.88	0.093	0.05	0.04	0.009	0.002	0.27	0.009	0.013	0.0002	0.0003	0.13	0.045	0.28
LB MoB	KIMAB	0.086	1.92	0.098	0.021	0.013	0.01	0.002	0.013	0.57	0.02	0.0018	-	0.019	0.056	0.01
DP600	Corus	0.102	1.641	0.251	0.035	0.575	0.016	0.004	0.026	0.002	0.012	0.0005	0.002	0.003	0.002	0.004
TRIP700	Arcelor	0.160	1.670	0.360	1.090	0.02	0.08	0.00	0.02	0.0	0.02	-	0.00	0.01	0.00	0.00
CP800	TKS	0.07	1.77	0.46	0.025	0.32	0.014	0.003	0.034	0.014	0.066	0.0004	0.005	0.11	0.002	0.004
CP1000	TKS	0.14	1.91	0.64	0.039	0.31	0.014	0.002	0.049	0.017	0.048	0.0006	0.003	0.11	0.002	0.007
MS1200	TKS	0.12	1.51	0.12	0.028	0.22	0.019	0.002	0.027	0.01	0.029	0.0016	0.002	0.037	0.002	0.005

"-" = not determined

## 1.5 Task 1.4 Mechanical testing

Table 1.3 shows the mechanical properties of the RRT steels listed in Table 1.1.

**Table 1.3** Mechanical properties of the RRT materials..

Grade	Rolling direction (RD)					45° direction					Transverse direction (TD)				
	R <sub>p0.2</sub>	R <sub>m</sub>	A <sub>g</sub>	A <sub>80</sub>	R <sub>mxA80</sub>	R <sub>p0.2</sub>	R <sub>m</sub>	A <sub>g</sub>	A <sub>80</sub>	R <sub>mxA80</sub>	R <sub>p0.2</sub>	R <sub>m</sub>	A <sub>g</sub>	A <sub>80</sub>	R <sub>mxA80</sub>
	MPa	MPa	%	%	MPa	MPa	MPa	%	%	MPa	MPa	MPa	%	%	MPa
HSLA100	767	829	11.1	21.5	17824	-	-	-	-	-	784	846	9.6	21.2	-
HSLA31415	760	820	-	21	17220	-	-	-	-	-	-	-	-	-	-
LB MoB	958	1069	5.1	13.9	14859	-	-	-	-	-	958	1069	5.1	13.9	14859
DP600	400	619	14.8	22.3	13804	408	619	13.7	21.2	13123	393	623	14.3	23.6	14703
TRIP700	463	736	22.35	27.85	20498	465	732.5	22.65	29	21243	482.5	742.5	22	28.1	20864
CP800	702	805	7.3	15.2	12236	-	-	-	-	-	786	825	3.8	9.5	7838
CP1000	767	1032	7.8	13.9	14345	-	-	-	-	-	832	953	2.5	9	8577
MS1200	1044	1279	3.6	7.8	9976	-	-	-	-	-	1040	1271	2.6	6.3	8007

**Table 1.4** Vickers hardness (HV0.5) of the RRT materials..

Steel grade	HV0.5	St. dev.
HSLA100	280	2
HSLA31415	285	4
MoB LB	328	1
DP600	192	4
TRIP700	210	3
CP800	262	1
CP1000	319	2
MS1200	413	4

## 2 WP2 Definition of phases, phase constituents, and properties

Task	Deliverable	D#
2.1	Create unified definitions and terminology for constituents	D5
2.2	Development of a Classification Scheme (CS)	D6
2.3	Unified definitions/terminology for microstructural properties	D7

## 2.1 General objectives

The first prerequisite for quantifying microstructures is to identify phases and phase-constituents that are present in steel microstructures. The main objective of this work package is to create a unified set of definitions and consistent terminology for phases and microstructural constituents. For the most relevant phases, the mechanism of formation and the characteristic morphologies observed in micrographs is described. These descriptions served as input for the development of a practical scheme for classification of microstructures. Finally, microstructural parameters are identified and defined, which must be measured in order to characterise individual phases and microstructural constituents.

## 2.2 Task 2.1 - Definition of phases and phase constituents

The work was focused on establishing theoretically and experimentally based criteria for the identification of phases and phase constituents. Emphasis has been put towards some of the most common low-temperature transformation products in typical HSLA and AHS steel microstructures, i.e., martensite, retained-austenite, carbide-free bainite, and bainitic ferrite. The microstructure of commercial low and ultra-low carbon multi-phase steels has been qualitatively described as a mixture of major matrix-phase constituents with minor secondary phase components with particular emphasis on practicality for industrial use. Their definitions are based on both morphological and crystallographic appearance [3, 4, 5, 6, 7, 8, 9].

Table 2.1 presents various types of major matrix-phase constituents and minor secondary phase components. In the classification system the main matrix phases are divided into three groups depending on the mechanism of formation (Table 2.2). It was decided during co-ordination meetings to include pearlite as a main matrix phase constituent, but with the remark that pearlite does not appear as a matrix phase in AHS steels. Acicular ferrite (AF) was left as a type of bainitic ferrite with the remark that AF forms within austenite grains. Pearlite, acicular ferrite and martensite can be treated either as a matrix or a secondary phase depending on the phase content. Morphological and crystallographic features of matrix phase constituents are presented in Table 2.3.

**Table 2.1** Nomenclature proposed for the major matrix phase constituents and minor secondary phase components.

Major matrix-phase constituent	Minor secondary phase components
- Polygonal ferrite	- $\epsilon$ -Carbide
- Quasi-polygonal (recovered) ferrite	- Cementite
- Massive ferrite	- Pearlite lamellar/degenerate
- Pearlite *	- Retained-austenite
- Widmanst�tten ferrite	- Martensite /Austenite constituents
- Acicular ferrite *	- Mixture of incomplete transformation products
- Granular bainitic ferrite	- Carbide-free bainite
- Lath-like bainitic ferrite	- Upper bainite / degenerate upper bainite
- Martensite lath *	- Lower bainite / degenerate upper bainite
- Martensite plate *	- Martensite / tempered / autotempered martensite
- Deformed ferrite	

\* Classification into matrix or secondary phase depends on the phase content

**Table 2.2** *Morphological and crystallographic features of matrix phase constituents.*

Matrix phase constituents		Morphological [LOM/SEM]		Crystallographic* [EBSD]		Comments
<b>Reconstructive transformation regime</b>						
<b>Ferrite</b>	Polygonal ferrite	$\alpha_p$	Equiaxed, polyhedral shaped crossing over austenite grain boundaries.	No substructure, low dislocation density. IQ high, KAM low		
	Quasi-polygonal (recovered) ferrite	$\alpha_q$	Irregular, changeful shape, crossing over austenite grain boundaries.	Mostly recovered with substructure. IQ high, KAM medium high	Forms at lower temperatures below polygonal ferrite.	
	Massive ferrite	$\alpha_m$	Coarse ferrite in very-low-carbon steels with the same composition as the parent austenite.	May contain a high dislocation density and sub-boundaries.	No partitioning but may contain M/A constituents.	
<b>Pearlite</b>	Lamellar pearlite	$P_L$	Cooperative growth of ferrite and cementite.		(not a matrix phase in a multiphase steel)	
	Degenerate pearlite	$P_D$				
	Fine colony pearlite	$P_F$				
<b>Sidewise / displacive transformation regime</b>						
<b>Bainitic Ferrite</b>	Widmannstätten ferrite	$\alpha_w$	Coarse, elongated site-plates.	No evidence of substructure. IQ high, KAM low	Nucleate at austenite grain boundaries or from polygonal ferrite allotriomorphs.	
	Acicular ferrite	$\alpha_a$	Small shaped and pointed like a needle interlocking structure formed within austenite grains.	Several ferrite crystal variants.		
	Bainitic ferrite - granular	$\alpha_{BG}$	Moderately recovered "lath-less", conserving prior $\gamma$ grain boundaries	Highly dislocated. IQ low, KAM high	Connected with granular second phases.	
	Bainitic ferrite – lath-like	$\alpha_b$	Lath-like, shear-like, conserving prior austenite grain boundaries.	Highly dislocated. IQ low, KAM high		
<b>Martensite</b>	Lath martensite	$\alpha_l$	Dislocated lath martensite at low / medium C-contents.	IQ very low	Lath-like distinguishable from $\alpha'_l$ by TEM	
	Plate martensite	$\alpha'_t$	Twinned, plate at higher C-contents.	IQ very low	Plate-like distinguishable from $\alpha'_l$ by TEM	
<b>Deformation regime</b>	Deformed ferrite	$\alpha_d$	Elongated grains containing shear bands	Highly dislocated. IQ low, KAM high		

\*IQ – Image Quality and KAM – Kernel Average Misorientation [10,11]

**Table 2.3** *Morphological and crystallographic features of minor secondary phase components.*

Minor secondary phase	Sub-structure	Symbol	Morphological [LOM/SEM]	Crystallographic* [EBSD]	Comments
$\varepsilon$ -Carbide		$\varepsilon$	Semi-coherent particles with the ferrite matrix.		Identifiable only by TEM
Cementite		Cem $\text{Fe}_3\text{C}$	Non-coherent particles	3-variants crystallographic orientation with ferrite.	Can be contrasted by hot etching with basic sodium picrate
Retained-austenite		RA	Highly carbon enriched residual austenite; mainly polygonal Smooth with no inner structure based on LOM or FEG-SEM after etching.	FCC XRD: lattice constant changes with carbon content.	May show polishing marks from mechanical polishing after etching with Nitral or electro-polishing.
Martenite/Austenite constituents		M/A	Islands with M and A.	Crystallographic relationship between A and M.	
Mixture of incomplete transformation products		Mix	Debris of incomplete transformation products.		
Bainite	Carbide-free bainite	$\text{BC}_{\text{free}}$	$\text{M}/\text{A}$ islands instead of cementite.		
	Upper bainite	$\text{B}_{\text{U}}$	Intra-lath cementite.		Non-cooperative growth.
	Lower bainite	$\text{B}_{\text{L}}$	Inter-lath cementite.		Non-cooperative growth.
Pearlite	Lamellar pearlite	$\text{P}_{\text{L}}$	Eutectoidal transformation product		Cooperative growth.
	Degenerate pearlite	$\text{P}_{\text{D}}$	Incomplete eutectoidal transformation product		Cooperative growth.
Martensite	Featureless	$\text{M}_{\text{l}}$	Smooth with no inner structure based on LOM after etching. Mild structure only visible by FEG-SEM	IQ and CI very low KAM very high	high carbon content
	Structured	$\text{M}_{\text{2}}$	With inner structure based on LOM after etching.	IQ and CI very low KAM very high	low carbon content
	Tempered/auto-tempered	TM	With $\varepsilon$ -carbide or cementite.	IQ and CI low KAM high	distinguishable from $\text{M}_{1/2}$ by TEM

\* CI – Confidence Index [10.11]

## 2.2.1 Microstructural aspects AHSS

### 2.2.1.1 Bainitic ferrite and massive ferrite

Microstructures in commercial complex-phase steels with carbon contents of 0.1 wt% typically consist of nearly equiaxed ferrite grains and bainitic microstructures Figure 2.1(A). Cementite may also be present as dispersed particles in bainitic regions. In very-low-carbon steels with carbon contents of about 0.004 wt%, it is possible by rapid cooling to transform from a single-phase austenite microstructure to single-phase ferrite microstructure without a composition change. Boron promotes this type of transformation process. The obtained microstructure consists of relatively coarse ferrite grains with irregular grain boundaries and substructures within grains (Figure 2.1(B)). This microstructure is defined as massive ferrite (see Table 2.2 and Table 2.2).

By using conventional light-optical microscopy it is possible to identify bainitic regions in complex-phase steel based on the appearance of cementite particles and acicular type of ferrite. But it is very difficult to quantify the amount of bainite by image analysis. In the case of massive ferrite light-optical microscopy is only just suited to obtain a description of the microstructure.

Investigations of TKS show that in case of massive ferrite it is possible to register changes in the density of misorientations depending on coiling temperature of hot-rolled material. Some of the obtained massive ferrite structures are very similar to bainitic ferrite based on their EBSD (in particular with respect to misorientation angles) characteristics. For this reason, only TEM investigations in combination with EBSD can lead to a real understanding of microstructural differences between bainitic and massive ferrite.<sup>[25]</sup>

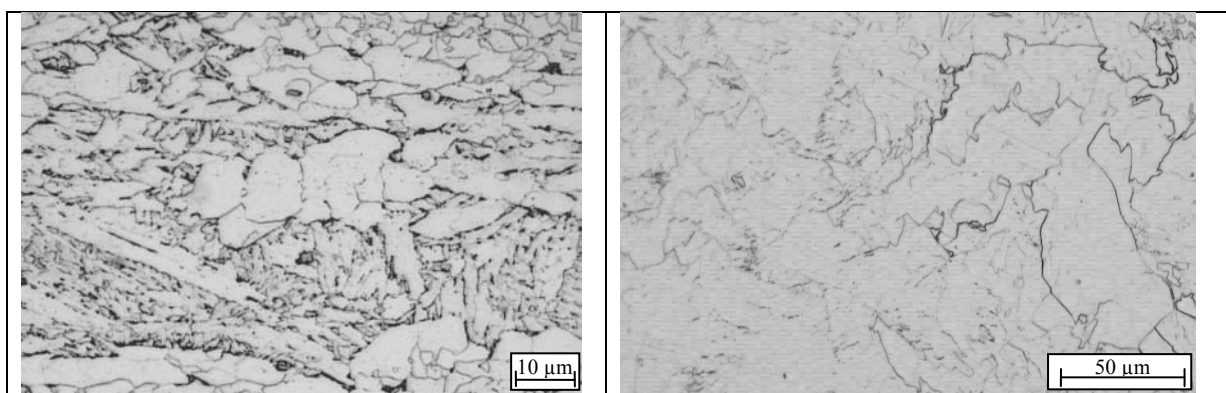


**Figure 2.1** Light-optical micrographs of (A) Complex-phase steel (0.1 wt% C) with equiaxed ferrite and bainitic areas (B) Very-low-carbon steel (0.004 wt% C) consisting of massive ferrite.

### 2.2.1.2 Granular bainite and lath bainite in bainitic ferrite

Bainitic ferrite is characterised by a relatively high dislocation density and is often difficult to distinguish from polygonal ferrite using LOM or SEM.

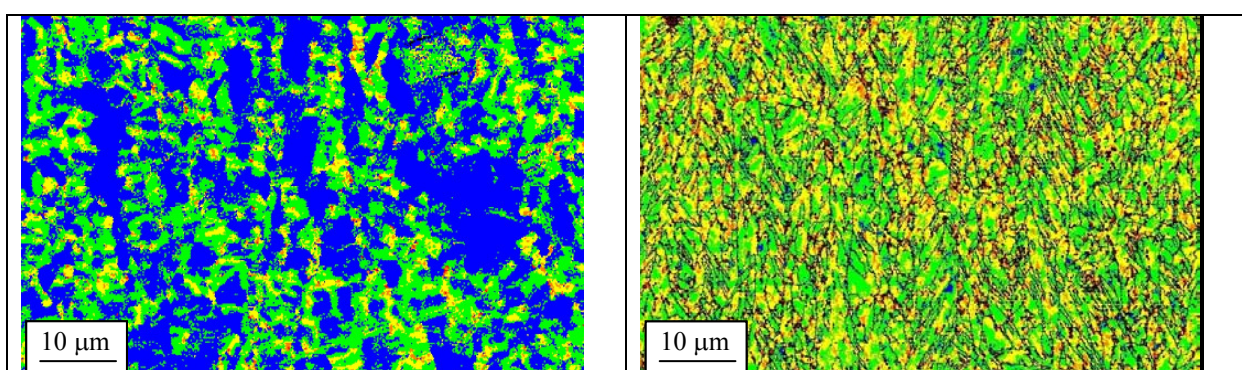


**Figure 2.2** Kernel Average Misorientation maps for two different bainitic microstructures: (low blue) (high red), (a) granular bainite and (b) lath bainite.

A possible way to characterise bainitic ferrite is local misorientation introduced in the microstructure by dislocations and sub-grain boundaries. TKS has investigated this approach. The misorientation density can be visualised and quantified based on Kernel Average Misorientation from EBSD mappings, see Figure 2.2.

### 2.2.1.3 Acicular ferrite, upper/lower bainite and martensite

Gourgues et al.<sup>[10]</sup> have done an extensive study EBSD based on microstructures corresponding to acicular ferrite, (upper/lower) bainite, and martensite steels. Figure 2.3 shows characteristic histograms of experimental misorientation angle distributions of these steels reported in their study. From this Figure, conclusions can be drawn with respect to the characteristic properties of misorientation angle distributions in these major phase constituents. As it turns out, lower bainite and martensite show a pronounced peak around 60°. This peak for these two phase constituents has a considerably higher relative intensity than for acicular ferrite and upper bainite. Misorientation angle distributions corresponding to these latter two constituents have a relatively high intensity between 50-55°. For lower bainite and martensite, the peak between 50-55° is much less pronounced. Typical misorientation distributions for RRT material HSLA100 MS1200 are shown in §5.6.2.1 and 5.6.2.7, respectively, (Figure 5.1 and Figure 5.6.)

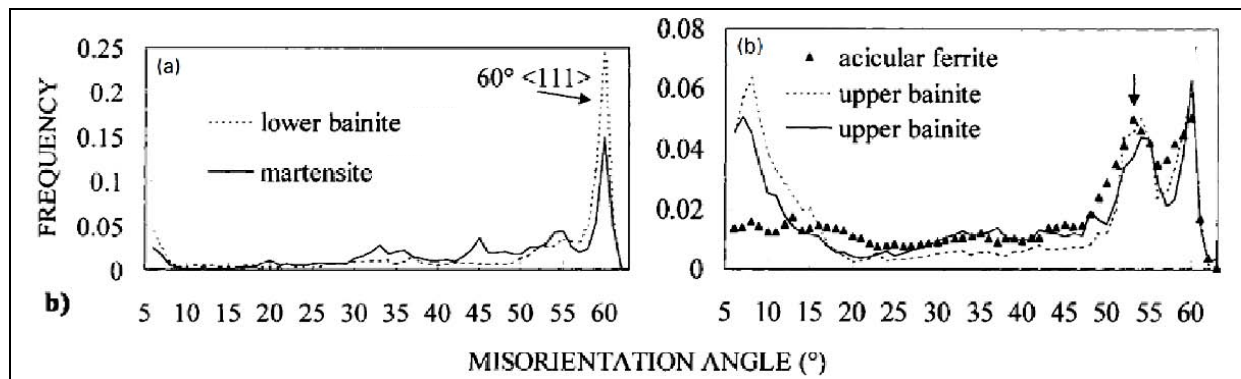


**Figure 2.3** Characteristic histograms of experimental misorientation angle distributions of steels comprising a predominantly single-phase matrix consisting of: acicular ferrite, upper bainite, lower bainite, and martensite. Images from a study by Gourgues et al<sup>[10]</sup>

### 2.2.1.4 Martensite and retained-austenite in DP/TRIP steel

Microstructures of DP and TRIP steel grades are characterised by martensite and retained-austenite islands dispersed within a ductile ferritic matrix. An accurate identification of these microstructural components is of crucial importance for any microstructural quantification. However, several practical aspects hinder an unambiguous identification of these constituents. One of these issues is related to specimen preparation of meta-stable RA (see §3.2.5). Another problem is introduced by high-carbon martensite which can have a similar etching response as retained-austenite. As a result, discrimination between martensite and retained-austenite based on conventional light-optical microscopy or even high-resolution SEM is not in all cases trivial. The next sections are aimed at exploring methods to identify martensite and retained-austenite using LOM (§2.2.1.4.1), SEM (§2.2.1.4.2) and EBSD (§2.2.1.4.3)

#### 2.2.1.4.1 Martensite and retained austenite in DP/TRIP steel imaged with LOM

Arcelor has developed a procedure comprising a sequence of etchants in order to outline and quantify secondary phase constituents in DP and TRIP microstructures. Based on this method, quantification of the area fraction of martensite, retained-austenite, and their sum has been carried out on a series of samples. In order to obtain good statistics, quantification of the second phase fractions has been performed on 10 images (2576 x 1932 pixels) for each tint etching, representing 14112 µm<sup>2</sup> per image and 141120 µm<sup>2</sup> for all 10 images. Results are shown in Figure 2.4

**Table 2.4** Overview of the VMK etching approach.

Etchant	Remark	Quantify
Villela*	Reveal the microstructure.	Dark beige area's associated with martensite (M)
Metabisulfite	Tint Fe <sub>3</sub> C-rich phase constituents, RA islands not affected	
Klemm	Tint ferrite by deposition of a thin film of ferrous sulphide	White area associated with retained-austenite (RA)
Le Pera	Quantify properties linked to the sum of (M/RA) islands	Light areas linked to the sum of (RA+M)

\* Normally (if the etching is sufficiently long), etch of perlite is delayed and only martensite and carbides is etched. In case of light etching (<1s), that was used in this case only carbides are revealed.

A typical result of the VMK etching approach is shown in Figure 2.4. The white islands in the Klemm etched optical micrograph correspond to RA islands. Subsequent thresholding and quantitative image analysis has been performed. Quantitative outcome for four different samples is presented in Table 2.5

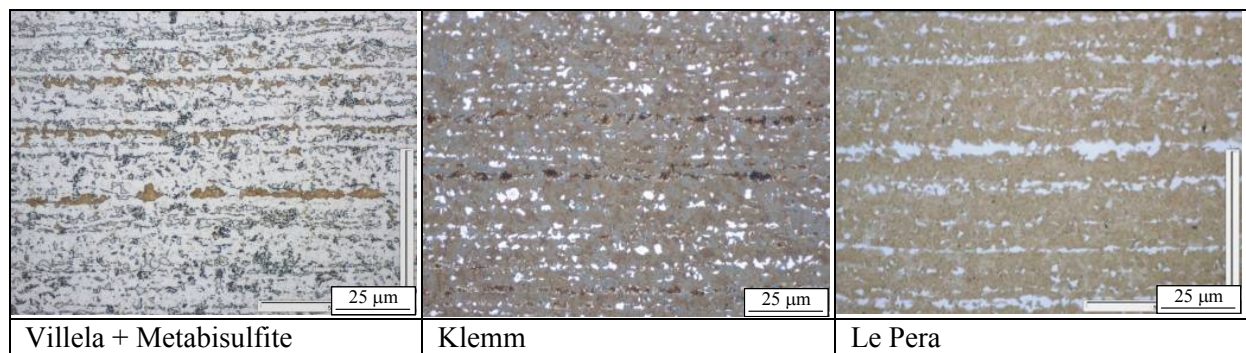


**Figure 2.4** Typical example of the VMK etching approach (sample B from Table 2.5)

**Table 2.5** Martensite and retained-austenite fractions for several samples containing M and RA as measured by LOM-QIA based on various (tint) etchings.

Sample	M (VM*)	RA (Klemm)	M+RA**	M+RA (Le Pera)
A	8.2	9.9	18.1	17.0
B	7.0	6.5	13.5	11.3
C	26.5	1.4	27.9	29.3
D	23.6	4.1	27.1	27.1

\* VM = Villela+MetaBisulfite, \*\* combined 2<sup>nd</sup> phase fractions of VMB and Klemm etching

Results shown in Table 2.5 support the idea that the proposed combination of etchants offers an adequate and efficient technique to distinguish M from RA in DP and TRIP microstructures and that it allows a basic quantification of M and RA fractions in AHSS microstructures by means of conventional light-optical microscopy when second-phase dimensions of are within resolution limits of LOM.

#### 2.2.1.4.2 Martensite and retained-austenite in DP/TRIP steel imaged by SEM

With respect to martensite as a second phase constituent, two major types can be distinguished: (1) structured martensite and (2) featureless martensite. The main physical difference between these two types is their carbon content, which is low in structured martensite and relatively high in featureless martensite. Featureless martensite has an appearance similar to retained-austenite when investigated by means of light-optical microscopy after chemical etching.

Figure 2.5(A and B) shows FEG-SEM images of a DP600 microstructure. Only with high-resolution FEG-SEM the mild structure – *not visible with light-optical microscopy* – in typical featureless martensite islands in a cold-rolled DP600 microstructure with circa 10% martensite and an average composition of 0.08 wt% carbon is visible. Figure 2.5(C) shows second phase islands in the TRIP700 microstructure, which – even with high-resolution FEG-SEM imaging – lack any structure.

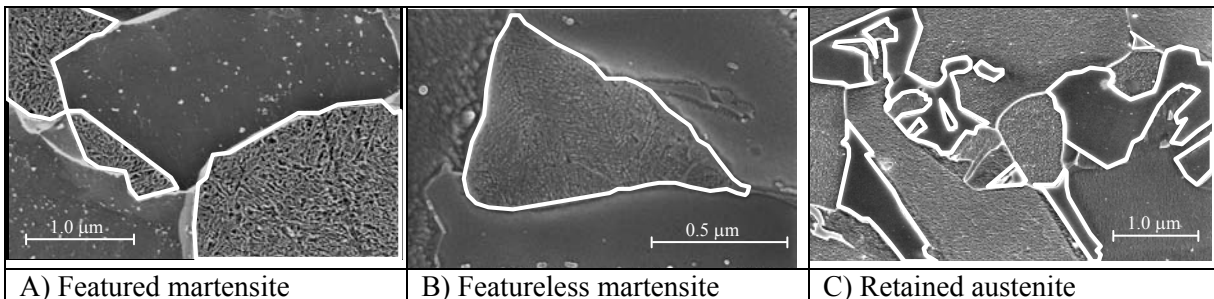


**Figure 2.5** FEG-SEM (5KV, inlens-SE) images of white outlined (A) featured martensite in a DP steel (B) featureless martensite in DP600 and (C) retained-austenite in TRIP700. Clearly, the martensite island in the DP600 microstructure (C) still shows a mild structure, corresponding to featureless martensite in LOM. The TRIP700 microstructure shows exclusively second-phase islands without hardly any visible inner structure based on FEG-SEM imaging. This is regarded as typical for retained-austenite islands, although exceptions can occur (see §3.2.4)

#### 2.2.1.4.3 Martensite and retained austenite in DP/TRIP steel imaged by EBSD

Martensite can be considered as a microstructural component, comprising an intricate structure of laths, blocks and packets<sup>[10]</sup>. A schematic representation of low-carbon martensite is shown in Figure 2.6.

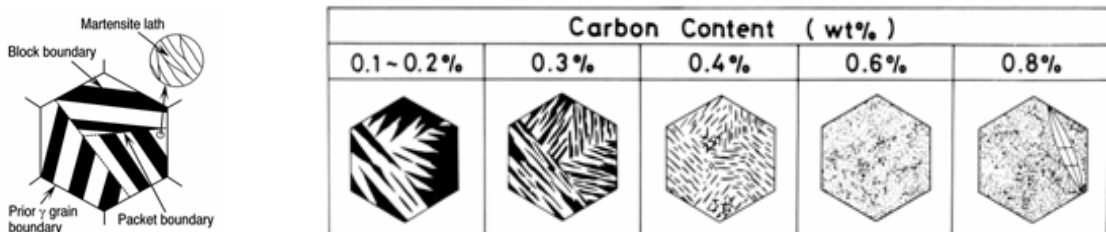


**Figure 2.6** (left) Schematic representations of low-carbon martensite with their typical intricate structure of crystallographic blocks and packets. Each individual component in this representation is defined as a block. Multiple blocks sharing a similar morphological and crystallographic orientation are defined as packets. The misorientation between neighbouring packets for low-carbon martensite is mainly 60° and occasionally 55°<sup>[10]</sup>. (right) Refinement of the martensite structure with increasing carbon content.

Figure 2.7 shows images of the RRT DP600. DP600 contains 0.102 wt% C and a martensite fraction of 15%. The average carbon content of M islands is therefore estimated to be roughly 0.68 wt%. Since size of crystallographic components of martensite is related to carbon content (Figure 2.6), this carbon content results in relative small crystallographic packets, see Figure 2.7).

Discriminating between ferrite and martensite using EBSD is not straightforward since both microstructural constituents have a BCC lattice structure. However, there are several characteristic property differences between ferrite and martensite, which potentially allow effective partitioning of martensite dispersed in a ferrite matrix. A summary of these properties is given below:

1. **GS** Typical DP microstructure will comprise a bimodal Grain Size (GS) distribution of the dimensions of ferrite/martensite grains.
2. **IQ** Martensite islands will have a lower Image Quality (IQ) than ferrite grains.
3. **CI** Martensite islands will have a lower Confidence Index (CI) than ferrite grains.
4. **KAM** Kernel Average Misorientation (KAM) of M islands will be higher than that of ferrite grains.

Figure 2.7(F) shows an example of martensite partitioning for the RRT DP600 microstructure based on IQ (see Figure 2.7(B)). Results show that IQ offers the most suitable method for martensite partitioning in DP or TRIP-assisted microstructures. Partitioning based on CI thresholding is not very effective and additionally gives interference from ferrite grain boundaries with equally low CI. It

should be noted that the effectiveness of IQ thresholding to partition martensite in an AHSS microstructure is related to carbon content: partitioning based on IQ will be most effective for higher carbon contents, i.e., > 0.4 wt%. Effective partitioning of martensite with carbon levels below this value will be difficult based on IQ thresholding. However, for most industrial hot-rolled and cold-rolled DP microstructures with roughly 10-25% martensite and an average carbon content of 0.1 wt%, IQ partitioning of martensite (carbon content between 0.4 – 1 wt%) will be quite effective and a suitable basis for advanced microstructural quantification based on EBSD.

The kernel average misorientation (KAM) and misorientation angle distribution (MAD) are more suitable means to facilitate identification of martensite and qualitative microstructural assessment. Figure 2.7(D) shows an example of KAM maps of martensite and surrounding ferrite. The KAM map of martensite corroborates the fact that this type of constituent comprises a high dislocation density and submicron sized crystallographic units, resulting in high KAM values<sup>[11]</sup>. Obviously for ferrite, this is much less the case. Only adjacent to martensite islands an increase in KAM values is observed, possibly due to transformation induced work hardening (Figure 2.7(C)). It is well-known from literature<sup>[3,10]</sup> that the MAD of martensite has a pronounced peak at 60°. Figure 2.7(G) illustrates this feature based on a martensite partition for a DP microstructure.

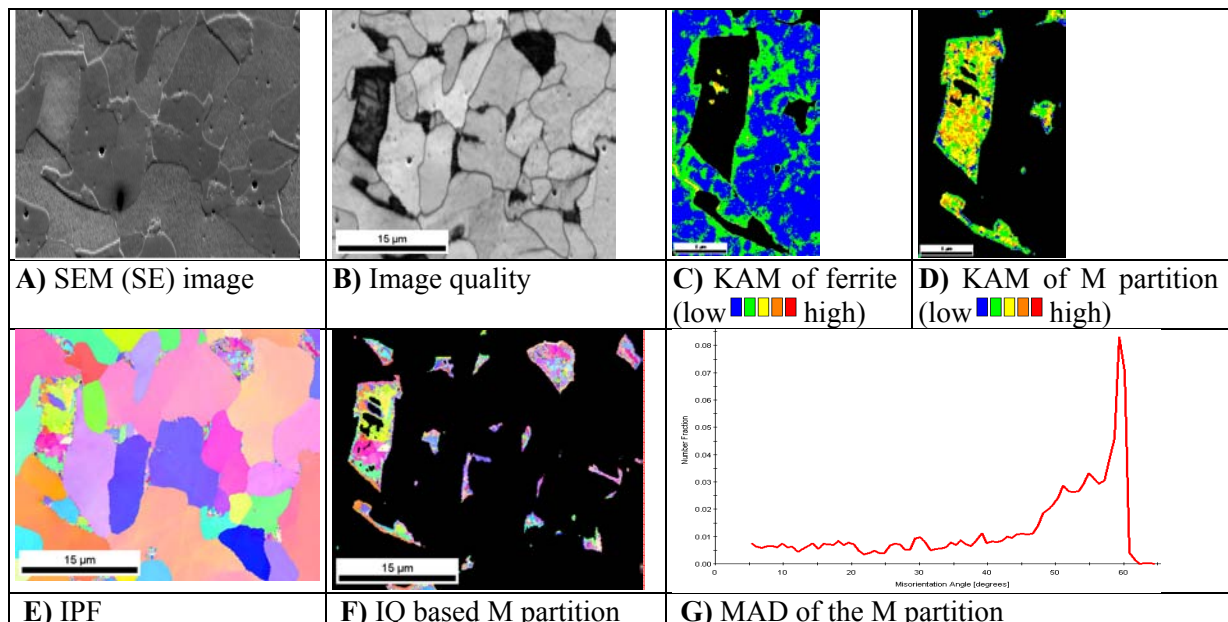


**Figure 2.7** SE image (A) and corresponding EBSD maps (B-G) of the DP600 microstructure. See text for details. KAM = kernel average misorientation, IPF = inverse pole figure, IQ = image quality and MAD = misorientation angle distribution.

### 2.2.1.5 Carbide-free bainite

Cold-rolled TRIP steels obtain their final functional properties after a specific two-stage annealing treatment consisting of an intercritical annealing stage between the  $A_1$  and  $A_3$  temperatures, followed by an isothermal treatment in the bainitic region (the overaging step). This overaging step contributes to the stabilisation of (retained)-austenite islands in the microstructure of the final product. This stabilisation is chemically achieved by efficient partitioning of carbon from newly formed pro-eutectoid ferrite upon quenching to parent austenite during bainitic phase transformation. The bainitic constituent creates a long interface between pro-eutectoid ferrite and the parent austenite, thus facilitating efficient carbon partitioning. Figure 2.8 shows a schematic model of bainite in TRIP microstructures as put forward by Zaeffler et al.<sup>[21]</sup>. According to their study, this type of bainite is different from classical bainite by the fact that it does not show any carbide precipitation and comprises ferritic laths consisting of one single orientation. In addition, this type of bainite (so-called carbide-free bainite, see Table 2.3) consists of alternating laths of ferrite and austenite, instead of ferrite and cementite in case of classical bainite.

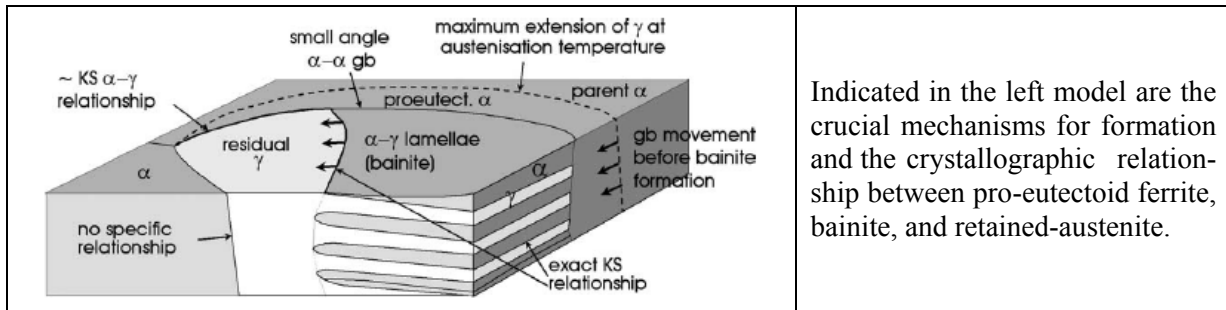


**Figure 2.8** Schematic model of the carbide-free bainite as put forward by Zaeffler et al.<sup>[21]</sup>

### 2.3 Task 2.2 - Development of a Classification Scheme

The approach for classification of multi-phase steels proposed by KIMAB has been accepted by partners. The description of matrix phases and secondary phases follows closely the pattern occurred on the real micrographs offering the full flexibility necessary for describing any combination of main matrix phases with secondary minor phases. In addition to matrix and secondary phases, precipitation strengthening carbides are also included in this classification. The system also allows for adding new components without the necessity to alter the terminology. Table 2.6 presents the classification scheme for multiphase steels. According to this classification RRT microstructures investigated within this project (RRT samples) are characterized in Table 2.7.

**Table 2.6** Classification Scheme for multi-phase steels.

Matrix phases	Secondary minor phases			Precipitation strengthening carbides	
	Distribution	Form	Type	Type	Density
<ul style="list-style-type: none"> <li>- Polygonal ferrite</li> <li>- Quasi-polygonal ferrite</li> <li>- Massive ferrite</li> <li>- Pearlite</li> <li>- Widmanstätten ferrite</li> <li>- Acicular ferrite</li> <li>- Granular bainitic ferrite</li> <li>- Lath-like bainitic ferrite</li> <li>- Martensite lath</li> <li>- Martensite plate</li> <li>- Deformed ferrite</li> </ul>	<ul style="list-style-type: none"> <li>(i) no second phases</li> <li>(ii) between grains, laths</li> <li>(iii) inside grains, laths</li> </ul>	<ul style="list-style-type: none"> <li>-round particles</li> <li>-elongated particles</li> <li>-films</li> <li>-discrete islands</li> <li>-grains</li> <li>-blocky regions</li> </ul>	<ul style="list-style-type: none"> <li>- <math>\epsilon</math>-carbide</li> <li>- Cementite</li> <li>- Pearlite</li> <li>- lamellar/degenerate</li> <li>- Retained-austenite</li> <li>- Martensite / Austenite constituents</li> <li>- Mixture of incomplete transformation products</li> <li>- Carbide-free bainite</li> <li>- Upper bainite / degenerate upper bainite</li> <li>- Lower bainite / degenerate lower bainite</li> <li>- Martensite featureless / structured / tempered (auto-tempered)</li> </ul>	No M(C,N) $\epsilon$ -Cu Mo <sub>2</sub> C	Low High Very high

Figure 2.9 illustrates typical examples of complex microstructures. All samples were fine mechanically polished with an oxide polishing suspension (OP-S) to remove any deformation layer from the surface and to minimize surface topography. SEM (JSM 7000F) images showing channelling- and atomic number contrasts were captured using back-scattered electron mode.

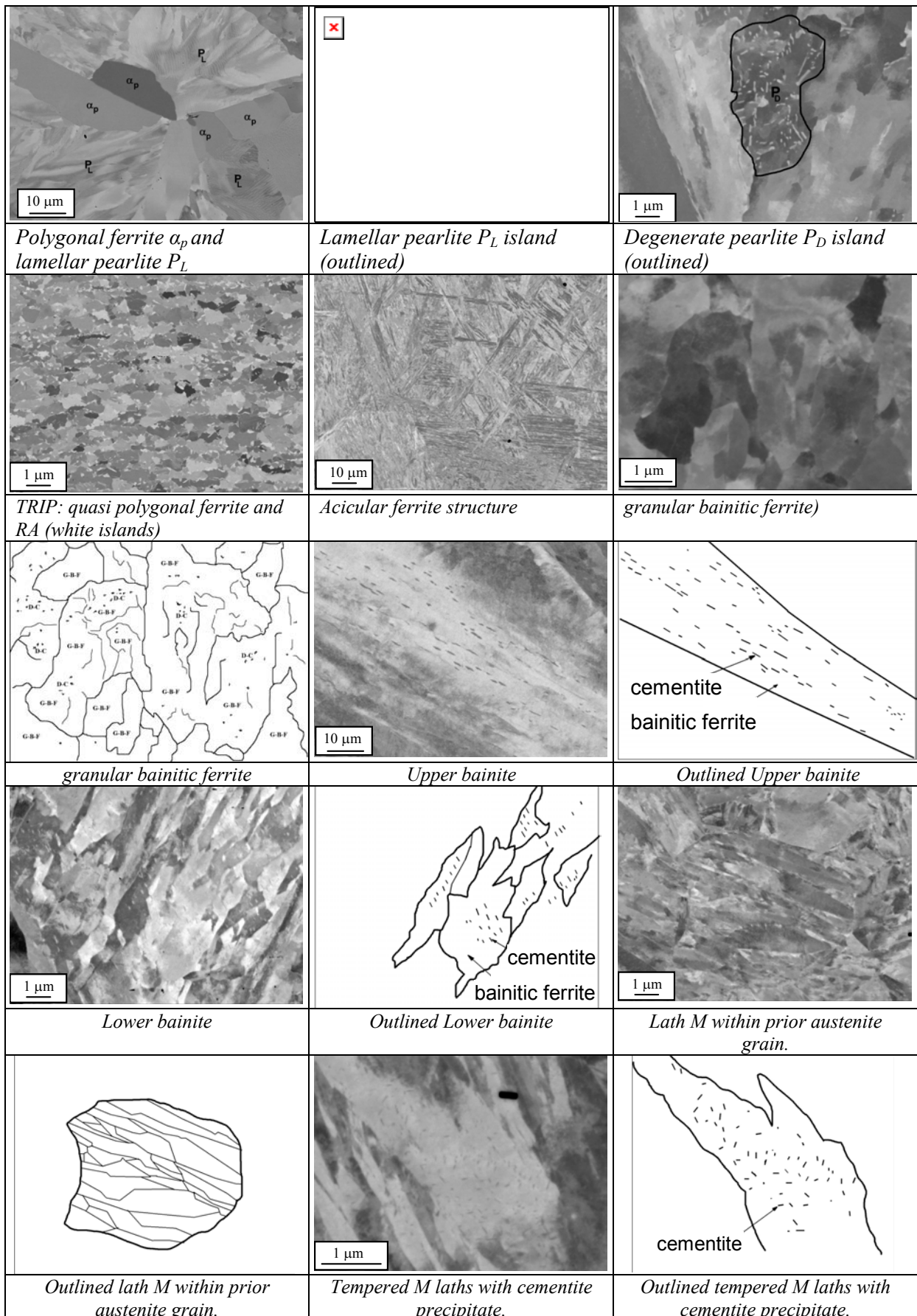


**Figure 2.9** Examples of complex microstructures. The samples were fine mechanical polished with OPS. SEM images show channelling- and atomic number contrasts in BS mode (10KV).

**Table 2.7** Classification of investigated RRT steels (carbide classification not included)

RRT Steel	Matrix phases	Secondary minor phases			Precipitation strengthening carbides	
		Distribution	Form	Type	Type	Density
HSLA100	Granular bainitic ferrite	between grains	blocky regions	degenerate pearlite	-	
		inside grains	round particles	cementite		
HSLA31415	Granular bainitic ferrite	inside grains	round particles	cementite	-	
MoB LB	Lath-like bainitic ferrite	inside laths	elongated particles	cementite	-	
DP600	Quasi-polygonal ferrite	between grains	blocky regions	martensite/austenite	-	
		between grains	discrete islands	retained austenite		
TRIP700	Quasi-polygonal ferrite	between grains	discrete islands	retained austenite		
			discrete islands	martensite/austenite		
CP800	Granular bainitic ferrite / lath-like bainitic ferrite	between grains / between laths	discrete islands	martensite/austenite	-	
			discrete islands	martensite		
			elongated particles	cementite		
CP1000	Granular bainitic ferrite / lath-like bainitic ferrite	between grains / between laths	discrete islands	degenerate pearlite	-	
			discrete islands	martensite/austenite		
			elongated particles	cementite		
MS1200	Lath martensite	inside laths	elongated particles	cementite	-	

## 2.4 Task 2.3 - Definition of microstructural parameters and properties

An inventory of parameters considered to be relevant to provide a quantitative description of matrix and second phase constituents has been made and is presented in Table 2.9 and Table 2.10. The parameters are to a large extent related to morphological and crystallographic properties of ferrite matrix and second phase constituents. Hence, these parameters offer a sound basis for the quantitative assessment of ferrite grain size strengthening and transformation strengthening due to low-temperature transformation products present in AHSS microstructures. The parameters directly related to solid-solution strengthening and precipitation strengthening (WP6) are not included in this inventory. However, strengthening due to these two mechanisms and also work hardening can to some extent be determined from nano-hardness measurements. Further developments in this direction were part of WP6/7. In the next paragraphs additional details are given for the mean-free distance, contiguity and continuity parameters.

### 2.4.1 Mean-free distance

The mean-free distance  $\lambda_i$  in direction  $i$  is defined in equation 2-1<sup>[12]</sup>:

$$\lambda_i = \frac{1-A}{N_L} \quad \text{equation 2-1}$$

where A is the area fraction of secondary phase constituents in a plane of polish parallel to direction  $i$ , and  $N_L$  is the number of secondary phase constituents intercepted by a line of unit length passing in direction  $i$  through the microstructure.

### 2.4.2 Contiguity and network probability of secondary phase constituents

The parameter of contiguity of a particular microstructural component has been defined in references [13,14,15]. Contiguity is considered to be a measure for the fraction of surface area of a phase (or phase constituent) shared with a phase (or phase constituent) of the same phase. In a three-dimensional setting, this parameter can be considered as a measure for connectivity of a particular phase. In a two-dimensional context, contiguity  $C_\alpha$  associated with phase  $\alpha$  can be determined from a plane of polish and can be defined according to equation 2-2, where  $B_{\alpha\alpha}$  is the total boundary of grains/islands of phase  $\alpha$  shared with grains/islands of the same phase per unit area and  $B_{\alpha\beta}$  the total boundary between grains/islands of phase  $\alpha$  and those associated with phase  $\beta$  per unit area, see also Figure 2.10.

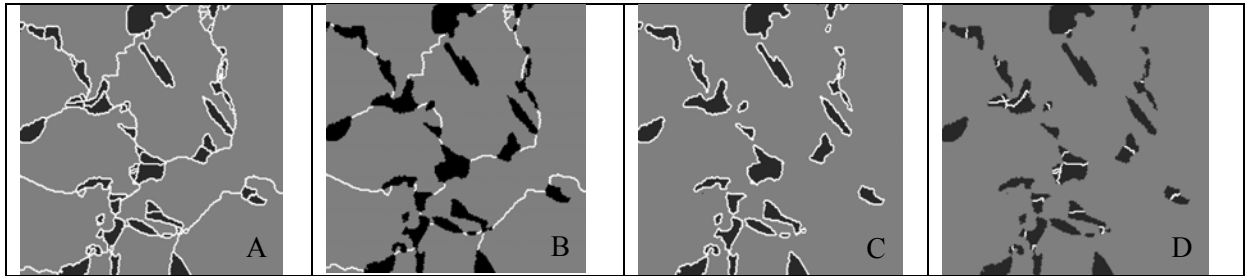


**Figure 2.10** Illustrative example of a two phase ( $\alpha$  and  $\beta$ ) microstructure with A) all grainboundaries, B)  $\alpha$ - $\alpha$  grainboundaries, C)  $\alpha$ - $\beta$  grainboundaries and D)  $\beta$ - $\beta$  grainboundaries.

$$C_\alpha = \frac{2B_{\alpha\alpha}}{2B_{\alpha\alpha} + B_{\alpha\beta}} \quad \text{equation 2-2}$$

Separation  $S_\alpha$  associated with phase  $\alpha$  can be formulated according to the same terminology see equation 2-3.

$$S_\alpha = \frac{B_{\alpha\beta}}{2B_{\alpha\alpha} + B_{\alpha\beta}} = 1 - C_\alpha \quad \text{equation 2-3}$$

In the derived equations (equation 2-4 to equation 2-7) the volume (or area) fractions of the phases are also taken into account.

equation 2-4	equation 2-5	equation 2-6	equation 2-7
Contiguity volume/area	Separation volume/area	Contiguity degree	Separation degree
$V_\alpha^c = V_\alpha \bullet C_\alpha$	$V_\alpha^s = V_\alpha \bullet S_\alpha$	$F^c = V_\alpha^c + V_\beta^c$	$F^s = V_\alpha^s + V_\beta^s$

$V_{\alpha(\text{or } \beta)}$  = volume/area fraction ferrite (or RA or M).

**Table 2.8** EBSD based Contiguity/separation and their derived parameters of TRIP700

	$C_\alpha$	$S_\alpha$	$V_\alpha^c$	$V_\alpha^s$	$F^c$	$F^s$
Ferrite	0.49	0.51	0.54	0.46		
austenite	0.09	0.91	0.008	0.08	0.55	0.54

### 2.4.3 Continuity

The parameter continuity has been defined in reference<sup>[16]</sup>. Skeleton-based continuity is the degree of interconnectivity or degree of skeleton formation of the phase where the total length of the skeleton lines is a measure of the length of continuous paths through the phase and is related to the sum of the lengths of the skeleton lines of all phases in the microstructure. Skeletonization of a binary image can be understood as thinning out the detected structure to the width of a line whilst the topology of the structure (i.e. the continuity and frequency of branching) remains unchanged. The total length of the skeleton lines is a measure of the length of continuous paths through that phase. Figure 2.11 schematically depicts a two-phase microstructure with skeleton lines superimposed.

$$M_\alpha = \frac{L_\alpha}{\sum L_i} \quad M_\beta = \frac{L_\beta}{\sum L_i} \quad \sum L_i = L_\alpha + L_\beta \quad \sum M_i = 1 \quad \text{equation 2-8}$$

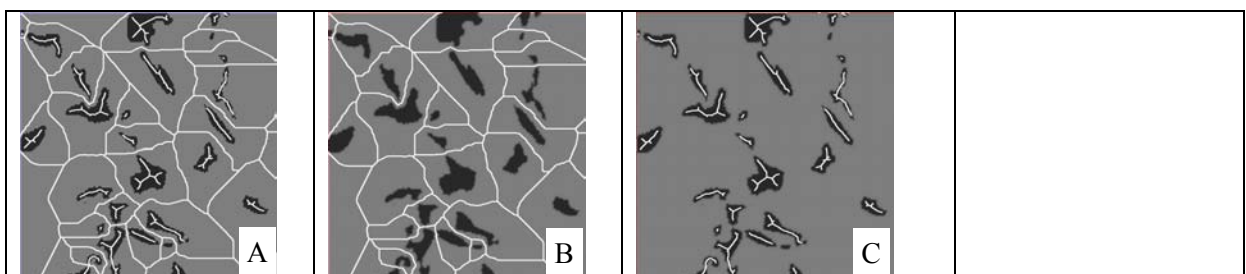


**Figure 2.11** Illustrative example of a two phase ( $\alpha$  and  $\beta$ ) microstructure with A) all phases skeletonised ( $L_i$ ), B)  $\alpha$  phase skeletonised ( $L_{\alpha i}$ ), C)  $\beta$  phase skeletonised ( $L_{\beta i}$ ).

**Table 2.9** List of parameters selected for description of phase properties.

Category	Parameter	Unit	Explanation
<b>Morphology</b>			
<b>Area fraction</b>	$A_A$	area fraction	[ - ] or [ % ] Area fraction of phase constituents
<b>Dimension</b>	$D_{eq}$	diameter	[ $\mu\text{m}$ ] Circle area equivalent diameter
	P	perimeter	[ $\mu\text{m}$ ] Perimeter
	$P_T$	total perimeter	[ $\mu\text{m}^{-1}$ ] Total sum of perimeter of phase constituent per unit area
<b>Shape</b>	$R_A$	aspect ratio	[ - ] $R_A = \text{length} / \text{width}$
	$R_F$	fullness ratio	[ - ] $R_F = (\text{area} / \text{convex area})^{1/2}$
<b>Spatial arrangement</b>	$\rho$	number density	[ $\mu\text{m}^{-2}$ ] Number of features per unit area
	$\lambda$	mean distance <sup>[12]</sup>	[ $\mu\text{m}$ ] Edge-to-edge uninterrupted distance: $\lambda = (1 - A_A)/N_L$
		free	
			$N_L$ is the number of intersections per unit length of test lines with phase constituents that occupy the area fraction of $A_A$ . The test lines oriented in 0, 45, 90, 135 degrees.
$\Delta c$	connectivity	[ $\mu\text{m}$ ]	Distance between neighbouring features
c	contiguity <sup>[13]</sup>	[ - ]	Area fraction of same phase regions (or the same phase constituent)
s	separation	[ - ]	Area fraction of 3D surface between different phase regions (or the different phase constituents)
$C_{sk}$	continuity <sup>[16]</sup>	[ - ]	Skeleton-based continuity: degree of interconnectivity or degree of skeleton formation of the phase where the total length of the skeleton lines is a measure of the length of continuous paths through the phase and is related to the sum length of the skeleton lines of all phases in the microstructure.
$\rho_B$	density of bands	[ $\mu\text{m}^{-1}$ ]	Number of bands per unit thickness of the plate
$\Delta_B$	band gap	[ $\mu\text{m}$ ]	Distance between adjacent bands
$B_{TF}$	full thickness bands	[ - ]	Number of bands over full thickness of the plate
D	clustering	[ - ]	Clustering of features with different dimensions e.g. in case of bimodal grain size distribution
Ph	clustering	[ - ]	Clustering of features belonging to different phases or phase constituents

**Table 2.9** *Continued*

EBSD			
<b>Dimensions</b>	$D_{\text{eff}}$ effective grain size	[ $\mu\text{m}$ ] or [ $\mu\text{m}^2$ ]	Size representing clusters of adjacent grains, closely aligned that can act as one effective grain, ( $D_{\text{eq}}$ or Area)
<b>Orientation</b>	Crystallographic orientation	[-]	shown as an orientation map
	BM boundary misorientation	[degrees]	shown as a histogram or orientation map
	J texture index	[-]	Texture index represents the strength of texture. The index is calculated using orientation distribution function (ODF) which can be achieved through evaluation of a set of pole figures or diffraction spectra. The bigger is value of index J the stronger is the texture.
<b>Distortion</b>	IQ image quality	[-]	Tool for partitioning of individual phases and/or phase constituents, shown as a histogram or map
	CI confidence Index	[-]	Tool for partitioning of individual phases and/or phase constituents, shown as a histogram or map
	KAM Kernel Average Misorientation	[degrees]	Tool for partitioning of individual phases and/or phase constituents, shown as a histogram or map
<b>Chemistry</b>	EPMA and Nano-SIMS		
	Measurements of the micro-chemistry of individual phase constituents with various analytical techniques, such as Electron Probe Micro Analysis (EPMA) and Nano Secondary Ion Mass Spectrometry (Nano-SIMS). In particular carbon is of interest in this context.		
<b>Hardness</b>	Hn	Nano-hardness	[GPa]
	HV	Micro-hardness	[-]
	E-modulus		[GPa]

**Table 2.10** Parameters selected for description of phase properties.

Major matrix-phase	Area frac.	Dimension		Shape		Phase connectivity		Banding		Cluster		EBSD		Chemical		Hardness		
		A <sub>A</sub>	D <sub>Eq</sub> Grain	R <sub>A</sub>	P <sub>T</sub>	P <sub>F</sub>	P <sub>A</sub>	$\alpha$	$\beta$	$\gamma$	$\delta$	$\Delta_B$	B <sub>FT</sub>	P <sub>B</sub>	D <sub>eff</sub>	EPMa	Nano SIMS	MH
Polygonal ferrite	x	x		x	x	x	x			x	x	x	x	x	x	x	x	x
Quasi-polygonal ferrite	x	x		x	x	x	x			x	x	x	x	x	x	x	x	x
Massive ferrite	x	x		x	x	x	x			x	x	x	x	x	x	x	x	x
Widmanst�tten ferrite	x	x		x	x	x	x			x	x	x	x	x	x	x	x	x
Acicular ferrite	x	x		x										x	x	x	x	x
Bainitic ferrite	granular	x		x										x	x	x	x	x
	lath-like	x		x										x	x	x	x	x
Martensite	lath	x		x										x	x	x	x	x
	twin	x		x										x	x	x	x	x
<b>Minor secondary phases</b>																		
$\varepsilon$ -Carbide	coherent	x		x										x	x	x	x	x
Carbide		x		x										x				
Cementite		x												x				
Retained-austenite	x	x		x	x	x	x			x	x	x	x		x	x	x	x
Marteniste/Austenite constituents	x	x		x	x	x	x			x	x	x	x		x	x	x	x
Mixture of incomplete transf. products	x	x		x	x	x	x			x	x	x	x		x	x	x	x
Martensite	x	x		x	x	x	x			x	x	x	x		x	x	x	x
Bainite	x	x		x	x	x	x			x	x	x	x		x	x	x	x
Pearlite	x	x		x	x	x	x			x	x	x	x		x	x	x	x

See Table 2.9 for a detailed description of the abbreviated parameters.



### **3 WP3 Development of electron optical microstructural imaging and quantitative image processing.**

Task	Deliverable	D#
3.1	Specimen preparation	D8
3.2	Development of procedures for SEM imaging	D9
3.3	Development of procedures for EBSD imaging	D10
3.4	Development of procedures for quantitative image analysis	D11

#### **3.1 General objective**

Main objectives for WP 3 are quantification of the morphology of individual phases and phase constituents in complex microstructures based on electron-optical imaging (i.e. SEM) in combination with Quantitative Image Analysis (QIA) processing or by SEM/Electron Backscatter Diffraction methods. First step is to obtain robust and reliable sample preparation procedures for these SEM/QIA and SEM/EBSD methods. The final objective is to give an overview of useful methods and procedures for microstructural quantification based on SEM and SEM/EBSD input.

#### **3.2 Task 3.1 Specimen preparation**

##### **3.2.1 Evaluation of standard specimen preparation methods for SEM imaging.**

Pristine specimen preparation is essential for accurate microstructural investigations. For evaluation of multi-phase microstructure using SEM, several methods were tested in this context. Special attention is required for micro scratches which can heavily interfere when using QIA. In general, SE and Inlens detection is more vulnerable for (micro) scratches. Deformation free preparation is the most important parameter for EBSD sample preparation. For TRIP EBSD samples, meta-stable retained-austenite offers additional challenges for sample preparation and is addressed in section 3.2.5.

The basic approach was to evaluate standard LOM etching methods with respect to their contrast observed with SEM imaging. Standard tint etchings, including Villela, Klemm and Beraha, have been tested for their ability to enhance contrast between matrix and second phase in DP and TRIP grades. Nital and Marshall etching as well as electro-polishing/etching have been tested for their ability to reveal grain boundaries in all relevant steel grades. Secondly these etchants have been tested for their ability to enhance contrast between matrix and second phase. Not only the etchant used, but also the type of SEM detector influences the final image contrast, see section 3.3. KIMAB has shown that electro-polishing in combination with OPS can be used for sample preparation for very detailed high-resolution images. Unfortunately QIA is difficult in this case. More details of the pros and cons of sample preparation methods in relation with SEM imaging will be address in section 3.3.

##### **3.2.2 Special tint etchants containing heavy elements**

TKS has investigated the possible merits of an etchant containing cadmium acetate and sodium thiosulfate. Solutions of sodium thiosulfate containing heavy metal (lead, cadmium) salts are suggested in literature<sup>[17]</sup> as alternative for tint etchants based on elements such as sodium or potassium. The general idea behind this concept is that the heavy elements could provide an enhanced BS contrast between ferrite and second phase in DP and TRIP steels. A cadmium-based etchant was applied to the DP and TRIP steel. Locally precipitated heavy atom (in this case Cd) shows sufficient contrast in the SEM BS image to achieve phase differentiation by QIA. However, because of moderate contrast enhancement results and toxicity of the etchant the procedure was not investigated further.

##### **3.2.3 Correlation between etching response and crystallographic orientation**

This section focuses on the study of Corus to establishing a correlation between crystallographic orientations and etching response<sup>[9]</sup>. In order to study in more detail the correlation between Klemm etching response of ferrite grains and their crystallographic orientation, a specific microstructural region was investigated by both SEM-EBSD and LOM based on Klemm. Visual comparison of the images

suggests, in agreement with earlier conclusions in literature<sup>[18]</sup> on the chemical etching response of steels, the following correlation:

**Klemm etching response (from intense to mild): [111] > [101] > [001]**

### 3.2.4 Etch response, SEM morphology, EBSD phase identification and crystallographic orientation of RA

In §2.2.1.4.2 it was stated that in SEM images, martensite islands can be distinguished from retained-austenite islands by their surface morphology after mild nital etching or electro-polishing. High resolution SEM SE-images show for retained-austenite a smooth surface and for martensite a featured surface structure. In general there morphological differences can indeed be used as a rule of thumb. However, based on this rule one could conclude that the central part of the retained-austenite island in Figure 3.1 is transformed to martensite. But the phase map and IPF, shown in Figure 3.1, show that the central part of the island has a twin relation with the top part. The difference in surface morphology of the second-phase island is apparently caused by the different etch response of the central part of the RA<sup>[19]</sup>.

The central dark area, which is identified as M based on low IQ, corresponds with the featured surface morphology shown in Figure 3.2(A/B). For comparison, the typical martensitic surface morphology observed in DP600 is shown in Figure 3.2 C. (Note: with LOM this type of martensite would be identified as featureless) 2.2.1.4.2. This example shows that phase identification based on only on surface morphology can easily lead to misinterpretation.

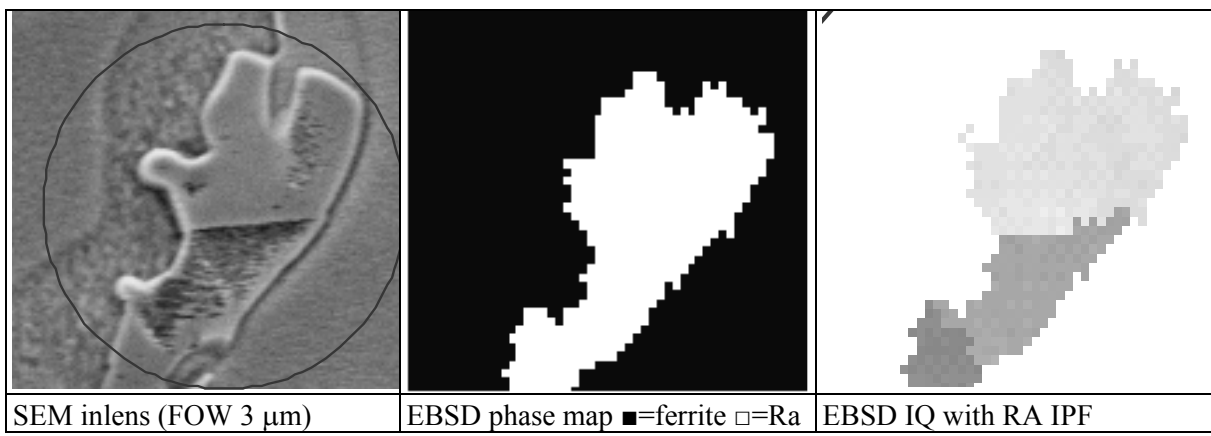


**Figure 3.1** Relation between SEM morphology, EBSD phase map and IPF of the same RA island.

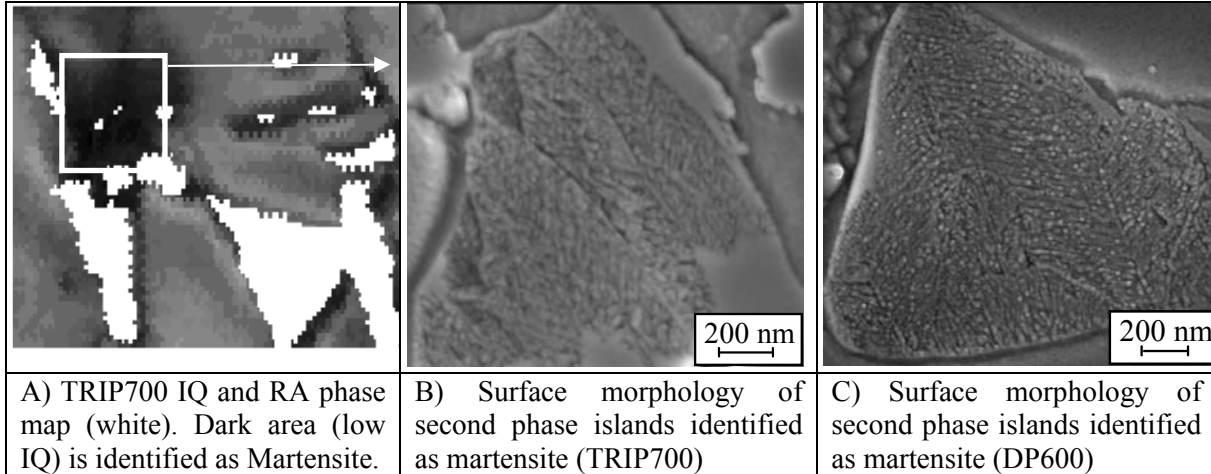


**Figure 3.2** Comparison between the morphology of M islands found in TRIP700 and DP600.

### 3.2.5 Evaluation of different specimen preparation methods for EBSD analysis

EBSD measurements demand a pristine polished surface free of any deformation left behind from grinding and polishing stages at the beginning of the specimen preparation process. Inadequate surface

preparation may have a dramatic effect on (electrolytic) etching response (relevant for light-optical or SEM imaging) or on EBSD patterns. Comparison of different preparation methods carried out at TKS shows a strong influence of preparation on the image Quality (IQ) confidence index (CI) and kernel average misorientation (KAM). All sample preparation methods tested are compared in Table 3.1.

**Table 3.1** Overview of different specimen preparation approaches employed for EBSD measurements.

	Method	Advantages	Disadvantages	
1	Mechanical polishing (alumina / diamond)	availability; fast; standard preparation method	surface deformation	-
2	Mechanical polishing (OPS)	availability	slow	+
3	Electropolishing*	(availability); fast	expertise necessary	+
4	Chemical polishing	(availability); very fast	highly corrosive etchant; difficult with RA steel	○
5	Ion-polishing	comparable to TEM preparation	expensive equipment; slow; complex; “curtaining”	-
6	Combination approach**	(availability)	none	++

\* Sample mounting for EBSD measurements is preferably done in conductive resin. Corus used both Struers PolyFast (Carbon-filler, thermosetting bakelite resin) and Struers Condufast (Fe-filler, acrylic resin). Best electro-polishing results were obtained with Polyfast. \*\* OPS + electropolish or chemical polish.

It was shown that deformation, induced during specimen preparation, can lead to RA→M phase transformation for TRIP steels. The best general approach for steel preparation for EBSD analysis was the following, used by KIMAB: a very gentle manual grinding and polishing is employed, starting with 400 and finishing on 1200. Subsequently, manual polishing is performed with 3µm, 1µm, and finally 0.25µm diamond. The final stage consists of electro-polishing for 5-10 seconds with a 5-10% perchloric acid solution. Corus has investigated the influence of specimen preparation on retained-austenite quantification for the TRIP700.<sup>[19,25]</sup> The best results were obtained using a procedure similar to that of KIMAB (2400 paper 10N 1min; 6 µm cloth 20N 3min; 3 µm Mol cloth 20N 3min; 3 µm Plus cloth 20N 3 min; 1 µm Nap cloth 20N 1.5min; OPS 15N 5 min; electro-polishing Struers AI+AII 2°C 5min)<sup>[19]</sup>. All results from reported TRIP700 RA fractions determined with LOM, SEM, XRD, MAG, EBSD, are combined in Figure 3.3. Based on volume fractions shown in this graph it is justified to conclude that RA volume fraction in TRIP700 is close to 12±2%.

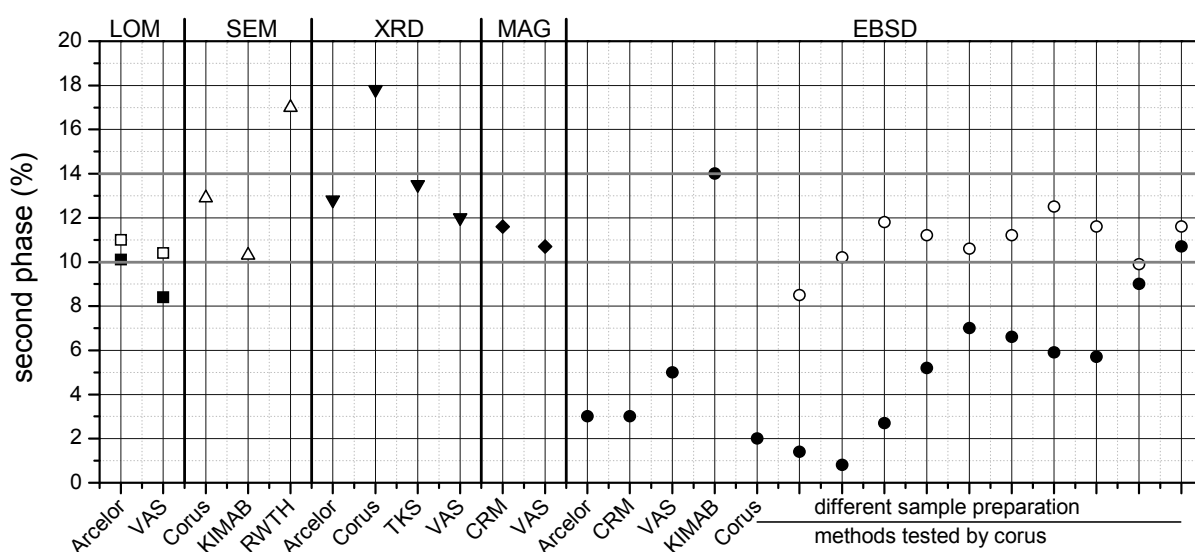


**Figure 3.3** Combined results for second-phase determination in TRIP700, measured by different partners with different (preparation) techniques. ■ (closed symbols) = retained-austenite; □ (open symbols) = retained-austenite + martensite.

### 3.3 Task 3.2 Development of procedures for SEM imaging

This Task is focused on SEM imaging of microstructures. This imaging is the basis for further development of quantitative image processing as part of Task 3.4 (see Section 3.5). Effective microstructural imaging for quantification purposes depends on two main issues: (1) optimal trade-off between resolution and statistics, and (2) adequate visualisation of relevant microstructural features based on suitable (chemical) etchings or polishing and electron detection (SE, QBSD, In-Lens ...). Section 3.3.1 will be aimed at resolution and statistical considerations. Different approaches for microstructural visualisation based on SEM will be dealt with in Section 3.3.2.

#### 3.3.1 Resolution and statistical considerations

For detection of spherical islands and assuming that the error in measurement of the dimensions of second phase islands is primarily controlled by the accuracy of boundary detection, the relative error can be formulated as follows<sup>[25]</sup>:

$$\text{Error} = \frac{\text{pixel size}}{D_{\text{equiv}}} \times 100 \quad \text{equation 3-1}$$

Detection based on SEM at high magnification will thus lead to a more accurate quantitative measurement of – in particular – submicron sized second-phase islands in, e.g., the microstructures of higher grades DP, TRIP, and CP steels. Thus, using an approach employed by Corus, collecting 25 images at a magnification of 5000:1 with a field of view of 55 x 41 µm in SEM the relative error compared to equivalent LOM at 350:1 can be reduced from circa 40% to 5%. Apart from an error related to resolution in relation to the dimensions of second-phase islands, the degree of homogeneity of a microstructure and the size of the total field of analysis plays an important role.

Evaluation of data from Round Robin DP600 and TRIP700 microstructures done at Corus indicates that the error introduced by the degree of microstructural homogeneity is considerably lower than the intrinsic measurement error (equation 3-1). This value is roughly around 5% for the measurement of dimensions of features based on image processing at a magnification of circa 5000:1. This illustrates the necessity to employ a sound trade-off between resolution (high magnification) and statistics (large field of analysis) in an approach for adequate microstructural quantification.

#### 3.3.2 Microstructural imaging based on SEM

Primary focus for a SEM-QIA approach is to quantify the microstructural properties related to the ferrite matrix and second-phase islands possibly dispersed in this matrix. This allows an assessment of grain-size strengthening (or in case of a partially or fully martensitic microstructure, strengthening due to the size of effective crystallographic units in martensite) and transformation strengthening due to low-temperature transformation products. Adequate electron detection should thus provide solid ground for identification and subsequent quantification of grain boundaries and/or second-phase islands.

Work by Corus shows the advantages of backscatter electron (BSE) detection over conventional light-optical microscopy (LOM) for the DP600 microstructure based on etching with Klemm to visualise the microstructure (Figure 3.4). SEM imaging may thus offer enhanced resolution and contrast as compared to LOM.

Images obtained by TKS with a FEG-SEM via In-Lens detection (at low accelerating voltages) and with BSE (at high accelerating voltages) for HSLA, DP600, TRIP700, and MS1200 after mild Nital etching and deep-etching using Nital or sodium-metabisulfite show that identification and quantification of second-phase islands via SEM SE or BSE is well possible due to good contrast between phase constituents. However, accurate grain boundary detection of ferrite grains in HSLA is considered to be impossible due to lack of contrast. The same can be said for the detection of high-angle boundaries in the MS1200 microstructure. Work done by VAS shows that ferrite grain boundaries in HSLA grades or

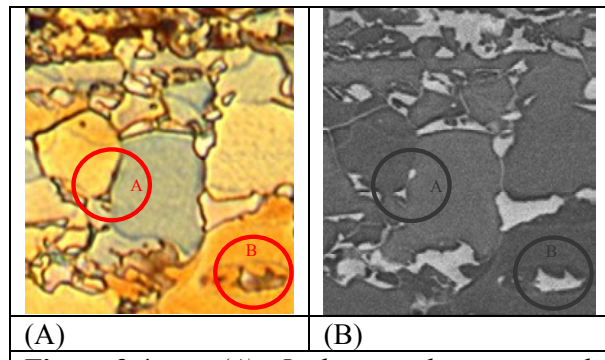


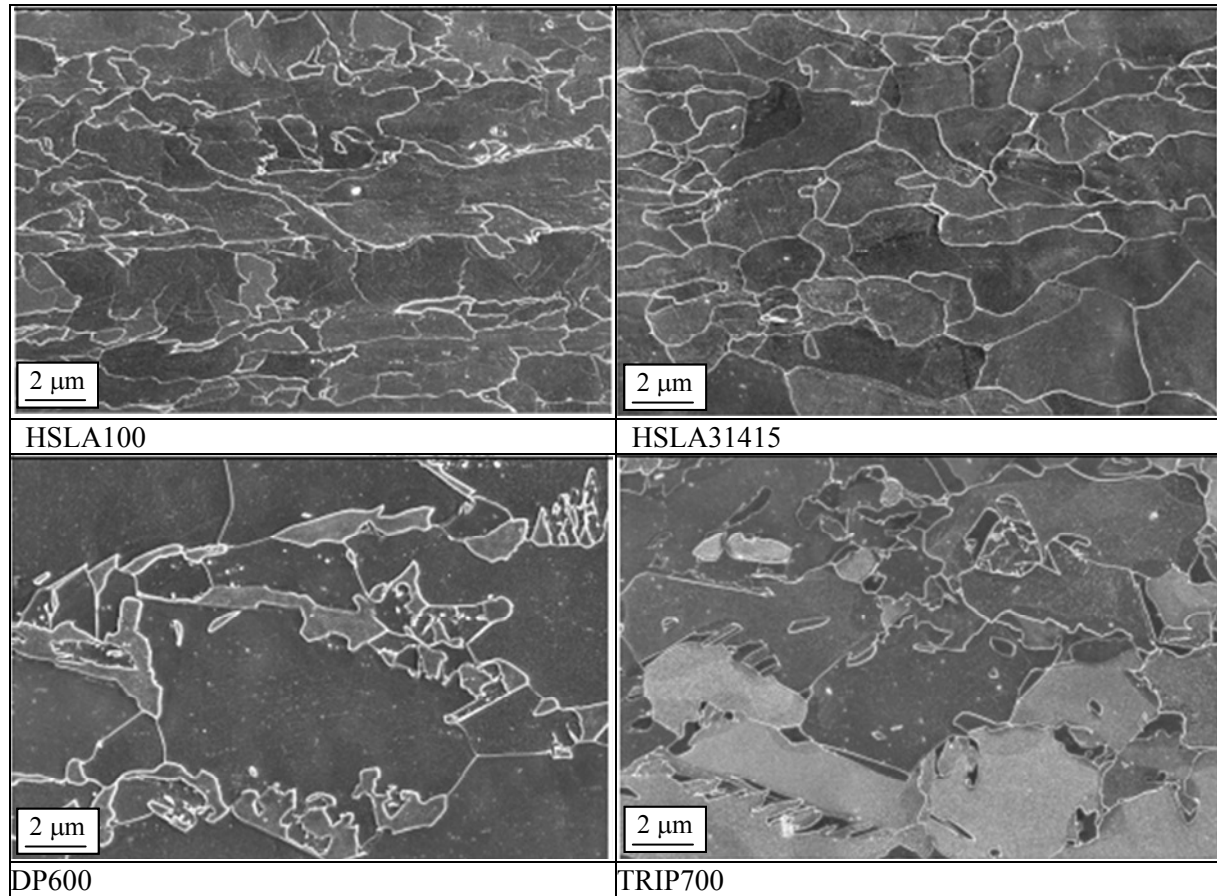
**Figure 3.4** (A) Light-optical micrograph and (B) QBSD (15KV) SEM image of DP600 based on Klemm etching of identical region. Circles indicate specific features.

high-angle boundaries of martensite packets in MS1200 can be effectively outlined by FEG-SEM In-Lens imaging based on Marshall etching.

Work carried out by Corus on SEM imaging with the purpose of subsequent image processing and microstructural quantification has shown that good results can be obtained with a rather simple but highly reproducible etching procedure: mild Nital etching for 5 seconds based on a 1% solution. Imaging providing good contrast between ferrite matrix and second-phase islands without significant interference from grain boundaries can be achieved either via BSE or SE detection.

Extensive work carried out by CRM investigating the merits of Nital, Villela, Klemm, and Beraha etchants for the complete range of RRT targeted steel grades confirms that a mild Nital etching (2% solution) and Beraha etchant yield a good contrast between ferrite matrix and second-phase islands in DP and TRIP microstructures. However, a similar approach for the CP800 and CP1000 microstructures turns out to be ineffective.

Various partners have investigated the strength of electro-polishing for microstructural quantification based on SEM-QIA. Among these are KIMAB, RWTH, and VAS. Both KIMAB as well as RWTH employ a sophisticated approach for quantitative image processing, i.e., context-based recognition of phase constituents. This requires highly resolved FEG-SEM images with microstructural details at different levels of magnifications and hence a pristine contrasting method, which offers a very mild etching response to develop even the most finest microstructural features (such as inner structure in high-carbon martensite in DP/TRIP, or  $\epsilon$ -carbides) without the chance of losing features due to over-etching. In this context, electro-polishing is considered to be most efficient and highly suitable for context-based image processing. Representative images are shown in Figure 3.5. In conclusion: tint etching works well in combination with QBSD, whereas Nital or electro-polishing works best with SE or inlens detection.



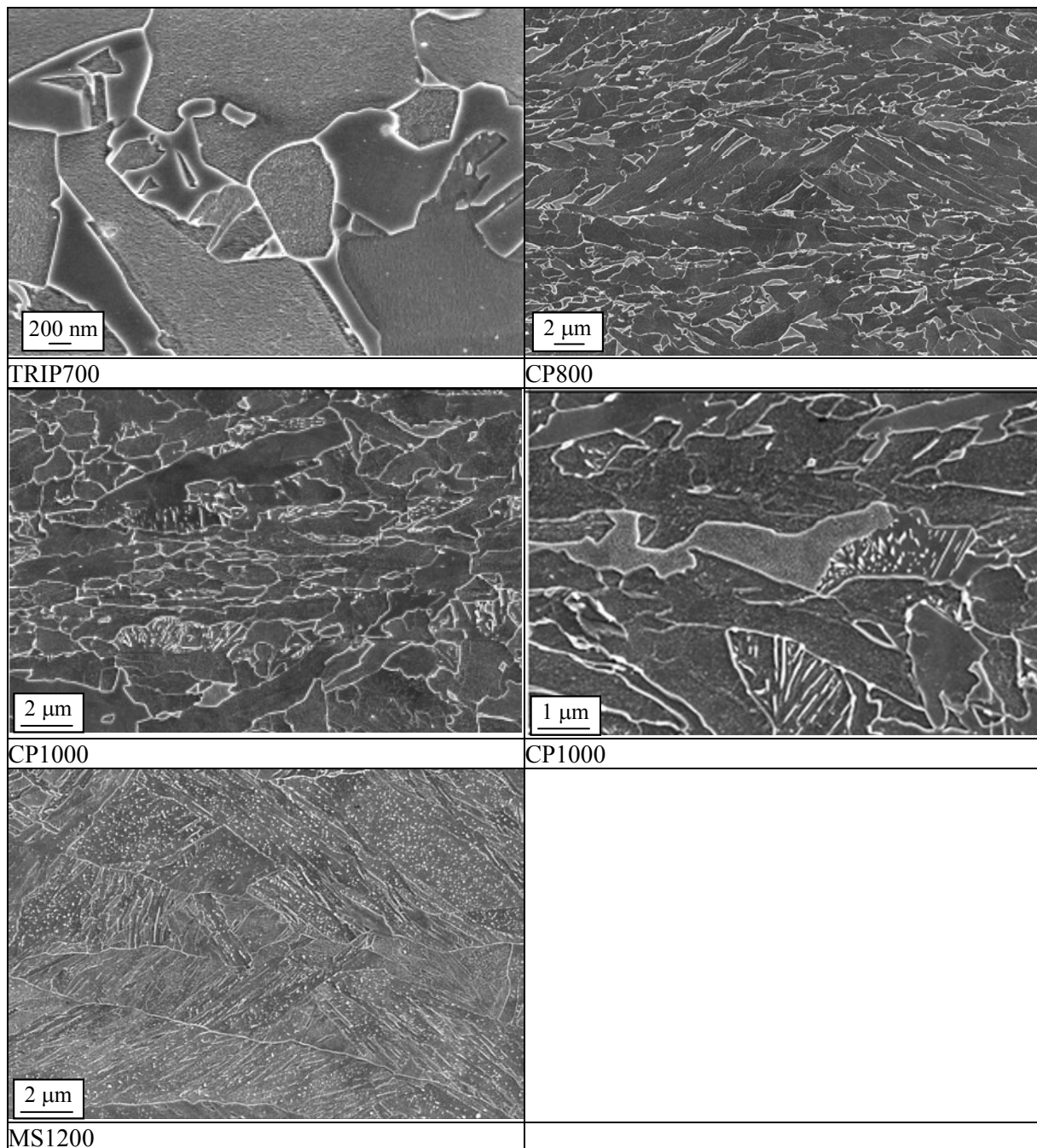


**Figure 3.5** Representative SEM images (InLens, 5KV) of the electropolished RRT materials of ND/RD.

### 3.3.3 Comparison of LOM / SEM and EBSD results of an identical sample area.

Studies by Corus regarding the microstructural comparison of SEM (or LOM) measurements after EBSD or EPMA measurements were performed using ion-beam cleaning (GATAN PECS). It was shown, that the same position in a specimen could be investigated by LOM and FEG-SEM with no deterioration of microstructure. With this method etch response and LOM visibility of microstructural components can be easily cross-checked with EBSD and EPMA results. This gives a more firm basis for phase identification.

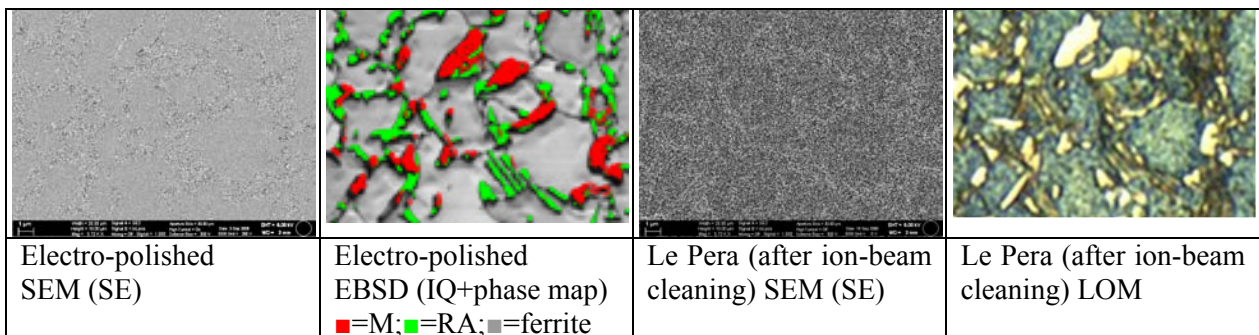


**Figure 3.6** Comparison of identical surface areas of TRIP700 sample, (all images FOW= 20 $\mu$ m).

### 3.4 Task 3.3 Development of procedures for EBSD imaging

Task 3.3 is aimed at developing methods for accurate partitioning of different phase constituents in multi-phase microstructures. Since efficient partitioning will be closely related to the intrinsic properties of phase constituents, the activities in this Task are closely related to those already discussed in Section 2.2 on definitions for phases and phase constituents. Section 3.4.1 will provide a concise overview of various methods developed within the project to partition specific phase constituents in HSLA and AHSS microstructures based on their definition as formulated in Section 2.2. Section 3.4.2 will give a concept flow chart for parameters considered to be relevant for specific EBSD analyses. Section 3.4.3 will focus on the effect of measurement parameters (i.e. lateral resolution and data clean-up) on EBSD data. Finally Section 3.4.4 will target the use of grain reference orientation deviation (GROD) for the identification of bainite.

#### 3.4.1 EBSD partitioning of phase constituents

Table 3.2 provides an overview of criteria to partition specific phase constituents in the investigated steel types. Although the project aims for a generic approach, Table 3.2 considers partitioning of phase constituents in relation to the overall type of microstructure in terms of steel products. This is justified by the fact that identification of microstructural constituents based on suitable partitions will require differentiation of these constituents in relation to its surrounding constituents. In this context, an effective partition will be, to a certain degree, dependent on the properties of all type of constituents present in a microstructure in order to obtain a unique property or threshold for partitioning.

**Table 3.2** Microstructural components in investigated microstructures and possible methods to identify and partition these constituents. Partition method is derived from work carried out by several partners. Abbreviations: F = ferrite, M = martensite, RA = retained-austenite, B = bainite, KAM = kernel average misorientation, IQ = image quality, GS = grain size, GAM = grain average misorientation, GROD = grain reference orientation deviation, HAB = high-angle boundary, FCC = face-centred cubic.

Steel	Microstructural constituents				Partitioning of constituents			
	F	M	RA	B*	F	M	RA	B
HSLA	•	-	-	•	IQ+KAM	-	-	IQ+KAM
DP	•	•	-	•	IQ / GS	IQ/GS or IQ+GS	-	none**
TRIP	•	•	•	•	IQ / GS	IQ/GS or IQ+GS	FCC	GROD/GAM/HAB
CP	•	•	•	•	IQ+KAM	IQ+KAM	FCC	IQ+KAM
PM/M	-	•	-	•	-	IQ+KAM	-	IQ+KAM

\* Type of bainite depends on microstructure: for HSLA this is described as bainitic ferrite for DP and TRIP this is either carbide-rich bainite (lamellae of ferrite and cementite) or carbide-free bainite (lamellae of ferrite and retained-austenite). For CP steels all three types are found; \*\* see text below (DP)

**HSLA** Microstructure may comprise polygonal and quasi-polygonal ferrite as well as bainitic ferrite. The latter ferritic structure will have a considerably higher dislocation density than the other two ferrite structures. Kernel average misorientation (KAM) has proven to be an effective tool to identify bainitic ferrite in HSLA type of microstructures.

**DP** A DP microstructure will comprise ideally of quasi-polygonal ferrite together with martensite. However, these microstructures may also contain a certain amount of bainite. This bainite can

be described as carbide-rich bainite; no effective method for partitioning of these constituents in DP has yet been developed. EBSD studies by several partners have shown convincingly that image quality (IQ) may be used as an adequate method to discriminate between  $\alpha$ -ferrite and  $\alpha'$ -martensite. Partitioning of ferrite/M in DP grades with a bimodal ferrite/M distribution can be significantly improved using IQ based partitioning in combination with grain size based partitioning. The IQ/KAM combination approach, as was used for CP grades, was not extensively investigated for DP grades.

- TRIP** A TRIP microstructure will ideally comprise small retained-austenite islands dispersed in a quasi-polygonal ferrite matrix. In practice, also martensite islands may be present. Similar for DP microstructures,  $\alpha$ -ferrite and  $\alpha'$ -martensite can be differentiated based on IQ and/or grain size. Retained-austenite can be easily identified based on its face-centred cubic (FCC) lattice structure. In order to stabilise retained-austenite, TRIP microstructures are developed by a deliberate overaging stage. This process introduces bainitic structures, which will predominantly consist out of carbide-free bainite. This type of bainite comprises lamellae of alternating plates of ferrite and retained-austenite, which can be identified by KS high-angle boundary misorientation maps in combination with steep gradients in grain average misorientation maps.<sup>[21]</sup>
- CP** Partitioning of microstructural constituents in hot-rolled CP steels has proven to be highly complicated until now due to the complex nature of its mixture of phase constituents as well as the (sub)micron dimensions of both the ferrite matrix and second-phase islands. The most effective method employed was combining IQ and KAM data into a single false-colour image in which phase separation can be achieved (see Section 3.5.4).
- PM/M** (Partial) martensitic steel will comprise predominantly martensite with a minor bainite component, depending on alloying and thermal-mechanical processing. Only if this bainite is transformed at elevated temperatures in the bainitic regime, upper bainite components may be differentiated from martensite.

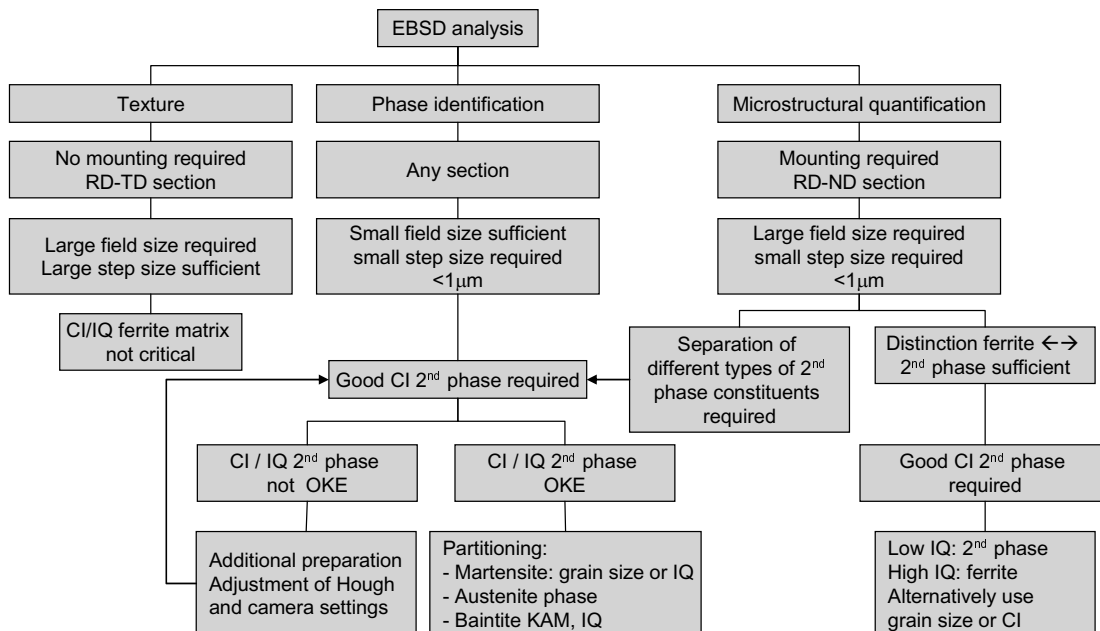


**Figure 3.7** Flow chart for a number of relevant parameters concerning EBSD analysis.

### 3.4.2 Flow chart for EBSD analysis

Research activities as part of Work Package 3 and 5 on EBSD analysis of complex microstructures of HSLA and AHSS steel grades has convincingly shown that this type of analysis may provide highly detailed microstructural information. However, issues such as specimen preparation, effective partitioning, resolution, statistics, and data clean-up will play an essential role in this type of measurement. Figure 3.7 provides a concept decision tree based on desired microstructural information from EBSD measurements and some critical crossroads, which will need careful consideration when designing the experiment and processing of the data. Not included in this flow chart is data clean-up.

### 3.4.3 Influence of measurement parameters

Arcelor and TKS have investigated the influence of EBSD data processing and the level of data clean-up on the quantitative outcome of EBSD analyses of microstructures of HSLA and AHSS steel grades. EBSD is particularly adapted to the study of bainitic microstructures for which microstructural boundaries as observed by optical microscopy do not always correspond to a similar crystallographic orientation differences<sup>[20]</sup>. For these microstructures, contrast band images (i.e., contrast band (HKL) is similar to image quality (TSL)) show a significant part of non-indexed pixels positioned on ferrite grain boundaries, which would suggest that they correspond to carbides. Investigations by Arcelor show, that correction improves the grain size distribution by removing a significant part of small sized grains due to indexation defects.

Comparison of different cleaning techniques on RRT steel types at TKS showed that the grain dilation algorithm gives the best all round results. If grain size determination is essential, the iterations should be performed until the very end, otherwise a single step yields good results (especially for spike removal) within the shortest calculation time of all algorithms tested.

Work done on RRT samples by Corus and CRM has led to an evaluation of the most obvious differences between EBSD analysis based on W-SEM or LaB<sub>6</sub> on one hand and FEG-SEM on the other. The resolution of the FEG-SEM is much better, although the W/LaB<sub>6</sub>-SEM still shows changes between two subsequent EBSD patterns at a step size of 0.1 µm. The image quality in FEG-SEM is higher and shows more details, e.g., small variations in image quality within ferrite grains. The general conclusion is that for CP, LB and M microstructures only a FEG-SEM gives satisfactory/usefull results.

### 3.4.4 Applicability of grain reference orientation deviation (GROD)

Corus has investigated the value of using grain reference orientation deviation (GROD), which is described in literature for bainite detection.<sup>[21]</sup> The method was applied to TRIP assisted microstructures with an expected difference in bainite content.

The expected difference was, however, not revealed. The main reasons were a high amount of artefacts, similarities in GROD between strained and bainitic areas, and difficulties in ascertaining the Kurdjumov-Sachs orientation relationship associated with bainite. In conclusion, the method was deemed not suitable for a straight forward and robust partitioning of bainite in multi-phase steels, but can be used for phase identification.<sup>[22]</sup>

## 3.5 Task 3.4 Development of procedures for quantitative image analysis

SEM-QIA offers a good trade-off between resolution (accuracy) and the ability to scan statistical representative areas in a reasonable short time frame. Therefore this task focuses on the development of quantitative image processing of SEM images (or light-optical micrographs) by means of software applications based on two essentially different approaches: pixelbased approach and context/object based approach. The different image analysis software packages and methods applied by the partners will shortly be presented in the following.

### 3.5.1 Pixel-Based Analysis: QWin and AnalySIS

The software packages QWin from Leica (employed by Corus) and AnalySIS (employed by RWTH) are pixel-based image analysis systems and mainly based on the detection and thresholding of gray tone or colour levels. SEM images are usually displayed as 8-bit gray-scale images with 256 gray levels ranging from black to white. The core-step of pixel-based analysis is "thresholding", i.e. the definition of a certain array of gray levels associated with a target phase and thus selecting according pixels within the image (Figure 3.8). The optimal threshold settings depend on many influencing factors like the applied preparation and etching procedures or the parameter settings during the imaging procedure. They may differ significantly for each sample and have to be newly defined each time by an operator. For an effective and unambiguous detection, a suitable contrast between the targeted microstructural features and constituents is essential. This is usually achievable for differentiation between matrix and secondary phase in commercial DP and TRIP.

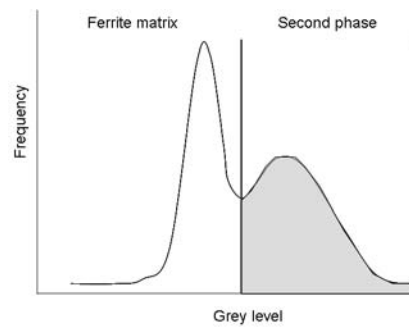


Figure 3.8 Thresholding

More complex microstructures comprising several individual phases, such as carbide-rich bainite or coarse lath-martensite, are more difficult to capture, since these constituents do not display homogeneous gray levels. Therefore, these more complex constituents can only be identified by taking into account neighbouring microstructural features. In pixel-based analysis, it is necessary to decide how to treat such phases if they occur. It is often reasonable to treat them as one feature belonging to the "2<sup>nd</sup> phase" or to the matrix phase, which can be achieved by supporting image operations like "erode", "closing" or "fill holes". In DP-grades for instance, the bainite fraction is usually very small and the influence of treating bainitic areas as 2<sup>nd</sup>-phase-constituents on results is neglectable.

The limited capability of common pixel-based SEM-QIA to distinguish between various secondary phase constituents is the main drawback of this method. It is therefore especially suitable for the quantitative analysis of martensite and retained austenite in commercial DP and TRIP steel grades, whereas it provides no means to differentiate between these two phases based on SEM imaging. Besides the means for volume fraction analysis, the software package provides routines for automatic grain separation for grain size analysis. However, depending on the contrast of grain boundaries within the image, manual interference results is often indispensable.

### 3.5.1.1 M/RA detection in DP and TRIP microstructures

The primary activities to develop accurate and efficient routines for QIA of multi-phase microstructures at Corus are focused on the detection of secondary phase constituents in dual-phase type steels. The most essential step is to filter out pixels associated with secondary phase constituents by accurate grey-level thresholding. The optimal setting of thresholds may differ significantly from sample to sample as well as from image to image in one series. The routine contains a loop, which allows re-defining thresholds if it turns out that an image is not well processed. Prior to detection of targeted features, the original image is inverted. The binary derived from this detection comprises not only secondary phase constituents, but also to some extent ferrite grain boundaries, which may have been mildly etched by the Nital solution. In order to suppress the contribution of ferrite grain boundaries, an "erode" operation is performed. Since bainite secondary phase constituents have a lamellar type of structure composed out of ferrite and either cementite or retained-austenite, the detection routine is aimed to identify such combined structures as one single feature. This is to a large extent achieved by a "fill holes" operation followed by a 6-fold "close" operation. A final "erode" operation has been incorporated in order to separate features that originally were isolated from each other but due to the 6-fold "close" operation became attached. An important drawback of the present SEM-QIA approach is the fact that the image analysis routine is not able to make a distinction between various secondary phase constituents such carbide-rich bainite, martensite, retained-austenite and/or carbide-free bainite. An alternative pixel based method which partly overcomes this problem is described in §3.5.1.2. The binary describing all secondary phase constituents is used as input for quantitative analysis. For evaluation of field-related properties, such as area fraction second phase, all features are taken into account. For quantification of feature-related properties, such as dimensions, all features, which are not completely confined within the image frame, are discarded from analysis.

### 3.5.1.2 Pixel-based detection of bainitic constituents in DP steels

Due to complex structures consisting of secondary phase constituents with a lamellar type of structure, the detection of classical bainite and carbide-free bainite in SEM images using pixel-based analysis is considered to be difficult or even impossible. However, a routine has been developed for the separation of homogenous second phase regions (martensite) and heterogeneous second-phase regions (bainite) using pixel-based image analysis. The routine is designed for SEM images of samples which have been mildly etched with Nital ( $\rightarrow$ "image A"). The routine differentiates between homogeneous 2<sup>nd</sup>-phase constituents (martensite) appearing as blocky bright areas, and heterogeneous 2<sup>nd</sup>-phase constituents (bainite) appearing as a conglomerate of small bright areas. Following image processing steps are performed:

- 1) Grey-level thresholding of original image A  $\rightarrow$  total second phase detection ( $\rightarrow$ image B)
- 2) Application of close operator to original image A, homogenizing the heterogeneous (bainitic) areas ( $\rightarrow$  image C)
- 3) Subtraction of image C from original image A ( $\rightarrow$  image D = A - C)
- 4) Thresholding of image D followed by a close operator  $\rightarrow$  bainite detection ( $\rightarrow$  image E)
- 5) Subtraction of binary result image E from binary result image B  $\rightarrow$  martensite detection ( $\rightarrow$  image F)

See for an application of this approach §8.3.2.

### 3.5.1.3 Cementite detection in HSLA microstructures

VAS has aimed its research on QIA towards cementite detection and quantification. For the quantification of carbides the obtained SEM images are preconditioned in order to reduce the noise level. In order to get representative information of the amount of carbides in HSLA material it is necessary to scan the sample at a relative low magnification level. A combination of InLens and SE2 electron image formation yields a high contrast

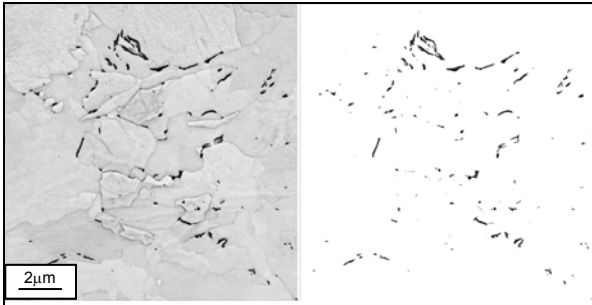


**Figure 3.9** *InLens+SE2 - SEM image at 25kX (left) and mean shift segmentation (right).*

minutes. The meanshift segmentation<sup>[25]</sup> shown in Figure 3.9 (right) reproduces the carbide structure well and lays the basis for useful quantification. The calculated fraction of precipitates is equal to 1.1% within the shown area. Without additional chemical information, it was not always possible to distinguish between cementite and other types of carbides (TiNb(CN)).

### 3.5.2 Context-Based Analysis: MicroGOP

KIMAB has employed the software MicroGOP2000/S for context-based SEM-QIA. The software also supports pixel-based analysis routines as described in the previous Chapter. The software also provides sophisticated grain boundary reconstruction routines by using line-detection, Euclidean distance maps and watershed algorithms. For the analysis of complex microstructures contextual methods take into account the data of each pixel as well as the data of its cross-neighbourhood, meaning the pixels in direct horizontal and vertical alignment to each analysed pixel (Figure 3.10).

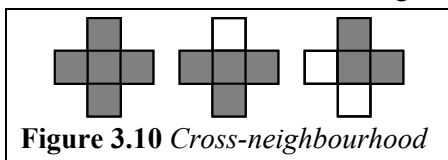


**Figure 3.10** *Cross-neighbourhood*

Three different discrimination rules are implemented in MicroGOP, resulting in nine situations that can be discriminated within the cross-neighbourhood. Up to sixteen classes can be defined. For training, a human operator has to correctly recognise and mark regions representing different classes first.

These marked regions are then statistically analysed by the system to obtain classification criteria for each class. During the following contextual analysis, a local dominant orientation or frequency or line (edge) component is calculated for every pixel and every neighbourhood. By this approach, an additional, contextual data is added to the image information. Both the resolution and the image magnification are very important parameters which influence the image classification. The results of phase recognition are usually further processed using binary image operations to refine results. Once the system is trained for a given sample, the entire analysis is done automatically. The degree of training and preparation work depends of course heavily on the complexity of the microstructure. KIMAB was able to analyse all Round Robin samples distributed in this project. Image Classifier (IC) integrated with the MicroGOP2000/S (image analysis system) is used at KIMAB as a main tool for processing images of complex microstructures. The IC was developed and successfully applied for bainitic microstructures within the previous ECSC project ECSC-7210/PR/247<sup>[24]</sup>. The following main steps of the quantitative characterisation are common to all types of microstructures: ①Identification and documentation of phase constituents using both light-optical and scanning-electron microscope. ②Collection of images for digital processing with Image Classifier module; the magnification of the microscope image and the image resolution shall be chosen depending on the type and scale of the microstructure, collection of scanning electron images at high magnification for the quantitative measurements of dispersed second phases. ③If necessary, application of the Image Classifier module to train the system and to identify phases followed by image processing and measurements. Detailed results on the development of procedures (comprising programming of Image Classifier-module, example images with their microstructural details, training procedure and measurements) for simple and

complex microstructures as well as examples of complex examinations of the selected microstructures are described in the mid-term report of the current project<sup>[25]</sup>.

The investigation indicated that only one, main IC module is necessary for the range of structures investigated here. Depending on phase constituents and their morphologies there were only small modifications necessary, but the major part of the IC module stayed the same. It works satisfactory for all investigated types of complex structures. IC allows for preliminary recognition and detection of microstructural features, converting them into a set of binary images. The binary image processing that follows IC-based detection is called here the post-classification processing and it has to be adjusted individually for every microstructure. It was shown that all microstructures investigated in this project can be described using the developed IC. The degree of training and preparation work depends, of course, on the complexity and homogeneity of the microstructure.

### 3.5.3 Object-Based Analysis: eCognition

The software eCognition produced by Definiens was applied for context-based SEM-QIA by RWTH. The software provides highly advanced image processing and analysis routines, including image segmentation, graphical filters, texture analysis, contextual relations, fuzzy logic, simultaneous processing of multiple scale levels, etc. The analysis is based on two main standard routines - segmentation and classification. In a first basic segmentation, the image is divided into so-called "image objects", which represent groups of related pixels. The segmentation process is controlled by parameters concerning the spectral values of the pixels and the shape of the resulting image objects (Figure 3.11). Because the resulting image objects represent an area within the image, features concerning size, shape, contextual relations, graphical texture, etc. can be directly processed during the following classification of the segmented image. Usually, additional segmentation and classification steps follow in order to refine results. The set-up of analysis routines and classification rules is a complex and very time consuming task, because it has to cover all the expertise necessary for microstructural identification. However, afterwards the analysis is performed automatically and in a non-subjective way. This effort is inefficient for small numbers of images or simple analysis tasks like volume fraction measurement in a well differentiable 2-phase microstructure. But once programmed, a routine is well suited to analyse many images of the same or similar microstructures.

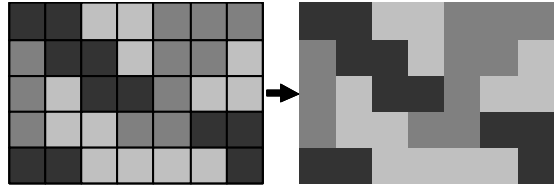


**Figure 3.11** Pixel and image objects.

#### 3.5.3.1 Structure cognition routines

The Round Robin samples distributed in this project have been analysed with eCognition according to the standard procedure described above. Two major drawbacks became apparent. First, the transferability decreased if large variations in the type of microstructure occurred or if the image taking settings or image quality changed above certain limit. Second, following the standard approach information on shape and context only become available after several segmentation, classification and refinement steps, which is a major obstacle for the analysis of complex microstructures with context and shape dependent classification systems. In order to enhance transferability and to provide shape and context data already at the start of the analysis, several structure detection and segmentation routines have been programmed by combining edge detection routines and graphical filters with image segmentation routines. These routines are able to detect structural elements within an image before the first classification step independently of the kind of microstructure and the image parameters. They provide immediate access to data on shape and context.

The most efficient structure cognition routine was tested as a basis for analysis of several series of steel grades with lath-like bainitic microstructures in a martensitic matrix. The routine was designed to extract the widths of the bainitic laths assuming this parameter to be most relevant for the dislocation movement restriction. The analysis routine was successfully applied to SEM image series of 18 different steel grades all showing different types of lath-like bainitic microstructures with appearances varying from small thin needles to long, broad laths with differently shaped boarders. Also the image quality and the brightness and contrast settings varied over a wide range. The analysis was successful. Being able to cope with the given variety of microstructures and image settings without operator interaction shows the potential of the approach to separate the analysis process into a structure cognition part and a classification part.

### 3.5.3.2 Line-Intercept-Analysis

For line intercept analysis a number of horizontal and vertical lines are drawn in the image for investigation. The number of lines depends on the size of structural elements and magnification and varied between 10 and 20 lines per image for the measurements on the Round Robin samples. On these lines interceptions with borders of the microstructural constituents (grain boundaries or phase interfaces) are marked. The resulting line segments are assigned to their respective phase. The sum of the length of all segments of a phase divided by the total length of all lines provides the phase fraction. A frequency distribution over the length of the segments of a phase gives information on size distribution for that phase. Attention must be paid that, for volume fraction measurements, partly visible grains at image borders must be taken into account while they are skipped for grain size analysis. The main advantage of this method is the simplicity of the approach, resulting in its extremely high applicability.

### 3.5.4 Combined IQ + KAM image analysis

For the identification of phases in CP steels using EBSD data, image quality (IQ) and kernel average misorientation (KAM) maps were combined using image analysis methods. First, a thresholding operation was performed translating the map data into grey scale images containing three saturation values (white, grey, black). For the KAM data white was assigned to misorientations between  $0^\circ$  and  $1^\circ$ , grey to  $1^\circ$  to  $2^\circ$  and black  $>2^\circ$ . For IQ the thresholds were determined manually from the image quality histogram. These two images were combined as different channels in a colour image. This combination yielded a colour scale that could be assigned to different phases, making it possible to identify ferrite, bainitic ferrite and martensite as well as grain-boundary regions, see Figure 3.12.<sup>[22]</sup>

The procedure was applied to steel grades investigated within this project and phase content was determined using image analysis. The procedure yields good results for all steel grades except for the martensitic steel, which is not distinguishable from a bainitic microstructure. A comparison of the content of bainitic ferrite and martensite between the different steel grades yields a sequence which is consistent with mechanical properties (Figure 3.13).

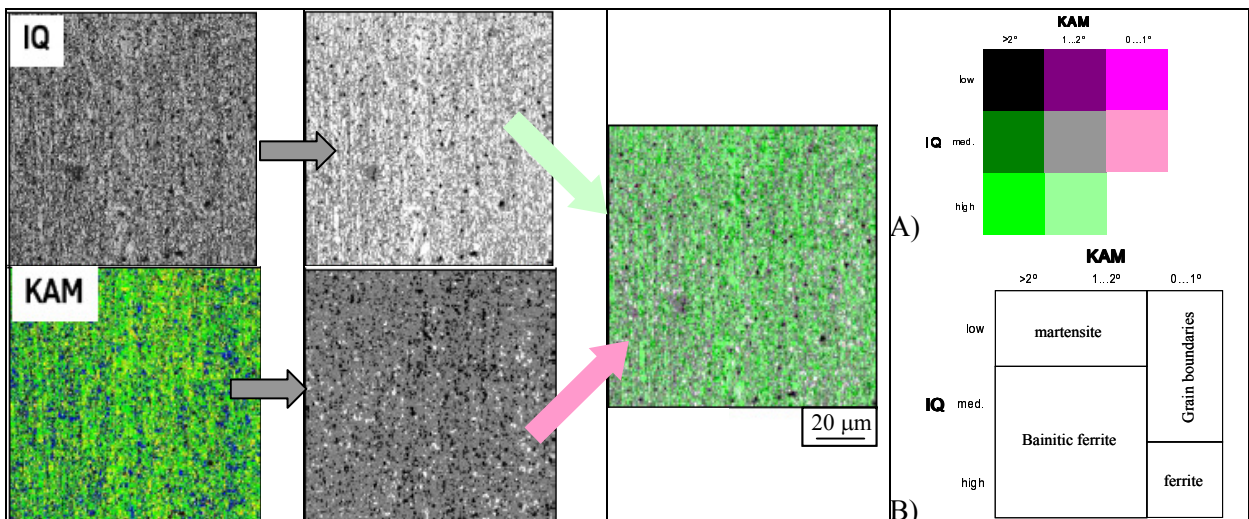


**Figure 3.12** Method used for combined representation of image quality and kernel average misorientation (IQ+KAM), see text for a detailed method description. Colour chart (a) and phase allocation (b) for combined [IQ+KAM] maps.

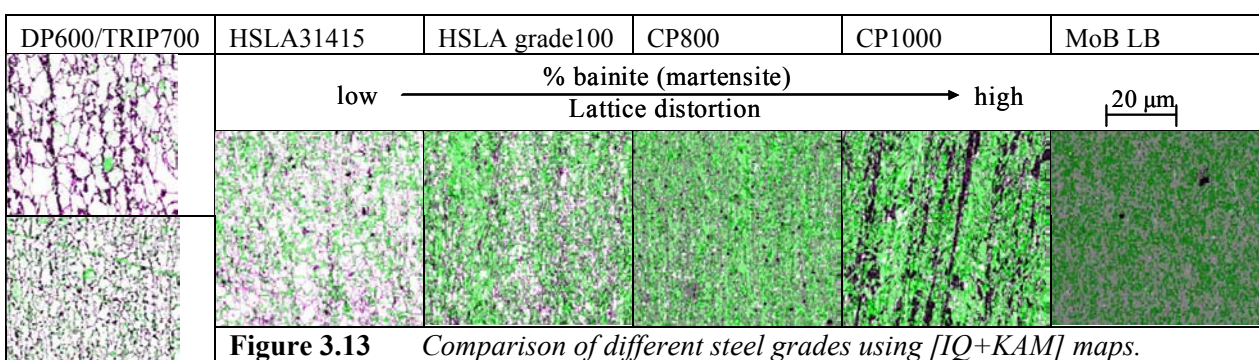


**Figure 3.13** Comparison of different steel grades using [IQ+KAM] maps.



## 4 WP 4 Morphological quantification of phases and phase constituents

Task	Deliverable	D#
4.1	Volume fraction	D12
4.2	Grain size (distribution)	D13
4.3	Ferrite-second phase boundary interface	D14
4.4	Shape factor	D15
4.5	phase connectivity (continuity and separation)	D16
4.6	Banding and clustering	D17

### 4.1 General objective

WP 4 deals with the quantification of the morphology of individual phases and phase constituents in complex microstructures of multi-phase steels based on electron-optical imaging methods and quantitative image analysis (QIA) processing. The Tasks in this WP correspond to the various morphological parameters that have been identified as key parameters for phase quantification, i.e. volume fraction, grain size, boundary interface, shape factor, phase connectivity, banding and clustering. The project partners worked on a range of steel types each using their own commercial QIA software package for processing SEM SE and BSE images. Most of these packages employ grey level detection of pixels (pixel-based), but also packages employing the principles of pixel structure and context processing (context-based) were utilised, see WP3.

### 4.2 Task 4.1 Volume fraction

Table 4.1 displays the results of volume fraction measurements of the Round Robin samples analysed by partners with different SEM-QIA approaches. The results with eCognition ("eCog") and line intercept analysis ("line cut") for the DP600 and TRIP700 grades contain two numbers, because they represent two different SEM image series - the first taken at RWTH, the second provided by Corus.

**Table 4.1** Results of the measurement of volume fraction for individual phases and phase constituents for all the type of microstructures specified in WP1.

Volume fraction in %	DP600		TRIP700		HSLA100		HSLA31415		CP800		CP1000	
	ferrite	2nd ph.	Ferrite	2nd ph.	Ferrite	2nd ph.	Ferrite	2nd ph.	Ferrite	2nd ph.	Ferrite	2nd ph.
RWTH (eCog)	83/83	17/17	82/85	18/15	86	14	90	10	90	10	81	19
RWTH (line cut)	83/85	17/15	76/84	24/16					91	9	85	15
RWTH (analysis)	85	15	81	19	94	6	96	4				
CORUS (Qwin)	89.9	10.1	87.1	12.9			99.6	0.4				
CRM (Kontron)	81.5	18.5										
KIMAB (microGOP)	87	13	89.7	10.3	97.2	2.5	99.6	0.4	92.8	7.2	85	15
TKS (analysis)	79.7	20.3										

The DP600 and TRIP700 are the most analysed steel grades, followed by the HSLA and finally the CP grades. This reflects the difficulties encountered during the analysis. Well contrasted DP and TRIP microstructures are easier to handle by image analysis than the other ones.

The analysis results vary for nearly each grade. The results of the DP steel grade have a maximum discrepancy of about 10 %, for the TRIP steel it is even higher with nearly 14%. The HSLA results match well with the exception of the values measured with eCognition. For the two CP steel grades, there is good consistency between results obtained by RWTH and by Swerea KIMAB. Comparison of M/RA volume fraction values in TRIP700 obtained with different techniques is addressed in section 3.2.5.

#### 4.2.1 General influences on analysis results

Several factors influence the results and cause discrepancies. Besides possible differences due to local variations in distribution of the microstructural constituents within different Round Robin samples, the magnification of analysed images has a considerable effect on the results. At higher magnifications,

more details of the microstructure can be differentiated. In DP steel for instance, clusters of 2<sup>nd</sup>-phase constituents, which are detected as full 2<sup>nd</sup>-phase areas at lower magnifications can show areas of ferrite at higher magnifications, which alters the results significantly. A good trade off between magnification and analysis procedure is essential. The first eCognition routine for the analysis of DP steels has been insensitive to small structures like 2<sup>nd</sup>-phase clusters. A later, improved version provided more detailed analysis and decreased the area fraction value for the 2<sup>nd</sup> phase by 2%. This also had a significant impact on grain size as will be discussed in the next chapter.

Another source of failure is "overdetection" of phases or grain boundaries. The first analysis of the RWTH image series of the TRIP700 steel grade showed a ferrite volume fraction of 78 %. However a close inspection of the results revealed a rather "generous" detection of the 2<sup>nd</sup> phase. Many detected borders slightly extended the boundaries of the real structures by about 1 pixel, which is barely visible. Additionally, some grain boundaries have been detected as 2<sup>nd</sup> phase constituents. The correction of these misclassifications raised the ferrite content by 4 % to a value of 82 %. This source of failure can also concern pixel-based analysis, if there is no sharp contrast but gradients at the grain or phase boundaries. In case of such gradients, small differences in thresholding will have a large effect on the quantification result.

#### 4.2.2 Correlation to mechanical properties

In order to correlate tensile data and properties of second-phase islands and ferrite matrix Corus produced several series of DP steels with varying microstructures. The microstructures were investigated based on RD-ND planes with SEM-QIA. The area fraction of the 2<sup>nd</sup> phase ( $A_A$ ) and the boundary interface per area ( $L_A$ ) have been plotted versus  $R_m$  and  $R_p$  for all steels with  $A_A < 30\%$ . The resulting graphs displayed in Figure 4.1 provide information on how  $R_m$  and  $R_p$  are influenced by changes in second phase fraction and its distribution. It is observed that  $R_m$  and  $R_p$  increase with increasing  $A_A$  and  $L_A$ . Analysis of raw data on size and shape suggested that variations in  $R_m$  for AHSS grades are predominantly controlled by second-phase fraction, whereas gradients in  $R_p$  for these materials are to a large extent also governed by variations in dimensions of second-phase islands and ferrite grains.

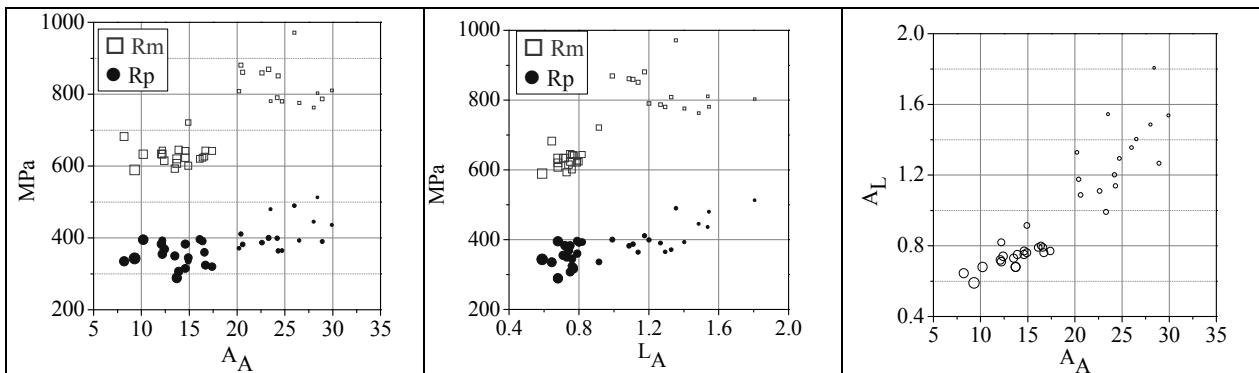


**Figure 4.1** Plots of  $R_m$  and  $R_p$  versus Area fraction ( $A_A$ ) and boundary length ( $L_A$ ). Symbols sizes represent the mean free distance ( $\lambda$ ).

#### 4.2.3 Comparison SE images / QBSD images

Closely related to the requirements of resolution and contrast of constituents is the choice of SEM imaging method. In this WP, SE and QBSD images have been analysed. The maximum attainable contrast proved to be higher in QBSD-images than in SE images. For pixel-based image analysis this is usually an advantage. On the downside, QBSD images were more sensitive to displaying undesired artefacts with the same brightness as 2<sup>nd</sup>-phase constituent. This interference can be reduced by careful preparation. Highly resolved FEG-SEM SE-images provide better display of details. As discussed, this is important the detection of small phase constituents.

### 4.3 Task 4.2 Grain size (distribution)

Table 4.2 displays the average grain size of microstructures of RRT samples analysed with different SEM-QIA approaches. Results from eCognition ("eCog") and line intercept analysis ("line cut") for the DP600 and TRIP700 grades are from two different SEM image series - the first series taken at RWTH, the second series provided by Corus. The results for the distinct steel grades always have the same

length scale, but there are large deviations, the reasons for which will be discussed. Some partner encountered problems during the analysis of the HSLA steel grades due to lack of grain-boundary contrast. Investigations showed that beside normal Nital-etching, high-angle misorientations can be revealed with Marshall etching and appropriate SEM imaging parameters. Further problems occurred for the CP grades due to the high complexity and small dimensions of their microstructure. The problems, encountered during microstructural quantification by partners for specific steels, are also reflected in the number of accomplished analyses for the distinct steel grades. Overviews of grain size distributions are reported in progress reports.<sup>[22]</sup>

**Table 4.2** *Measurement of the average size of individual phases and phase constituents for all type of microstructures as specified in WPI (values reported are the equivalent diameter ( $D_{eq}$ ) values except for the line cut method)*

Mean grain size in $\mu\text{m}$	DP600		TRIP700		HSLA100		HSLA31415		CP800		CP1000		M
	ferrite	2 <sup>nd</sup> ph.	ferrite	2 <sup>nd</sup> ph.	ferrite	2 <sup>nd</sup> ph.	ferrite	2 <sup>nd</sup> ph.	ferrite	2 <sup>nd</sup> ph.	Ferrite	2 <sup>nd</sup> ph.	packets
RWTH (eCog)	3.9 / 2.0	1/0.7	1.6/2.6	0.7/0.7	1.67		2.31		1.1	0.8	1.3	1	
RWTH (line cut)	3.8/3.4	1/0.9	1.4/2.3	0.5/0.7	1.65		1.07		0.81	0.31	0.68	0.35	4.67
RWTH (analysis)					0.33		0.45						
Corus (Qwin)	7.12	0.86	4.04	0.68									
KIMAB (microGOP)	5.4	1.2	4.2	0.83	1.7	0.7	2.2	0.3	1.55	0.54	1.57	2.2	8.5
TKS (analysis)	4.43	0.72											

### 4.3.1 General influences on analysis results

Analysis procedures that detect small heterogeneous structures as a one feature can have a large impact on grain size values. An example of this is the detection of clusters of small ferritic and 2<sup>nd</sup>-phase constituents or bainitic areas in DP steels discussed in §3.5.1.2. When using pixel based analysis, such regions are often regarded as one entity. This approach is assumed to be justified since ferrite grains are confined between martensite islands and will not be as free with respect to deformation as non-confined ferrite grains. In this regard, magnification is also very important, because higher magnifications reveal more internal structures of 2<sup>nd</sup>-phase clusters and more enclosed ferritic areas become detectable. These effects can alter the results heavily. The first eCognition routine for the analysis of the Round Robin DP microstructure was insensitive to small structures like 2<sup>nd</sup>-phase clusters. For the RWTH-images series this routine yielded mean equivalent diameters of 4.9  $\mu\text{m}$  for the ferrite grains and 2.5  $\mu\text{m}$  for 2<sup>nd</sup>-phase constituents. With the application of an improved analysis routine with more detailed analysis, these values decreased considerably by 20 % and 60 % down to 3.9  $\mu\text{m}$  and 1,0  $\mu\text{m}$  respectively.

### 4.3.2 Line intercept analysis

The line intercept analysis requires special care, since it follows a different approach, which means the results are only to a certain degree comparable. Equivalent diameter measured by other analysis software packages represents the grain area as visible within the image. The line intercept method provides segments of lines which cut grains randomly. For regular (polygonal) shaped grains, average intercept length is comparable with equivalent diameter. The results for the DP and TRIP steels confirm this. However, for more complexly shaped microstructural constituents like the ferrite grains in the HSLA and especially CP grades, the line segment lengths deviate heavily from the equivalent diameters.

### 4.3.3 Lower bainitic steel grade

In addition to the Round Robin materials listed in the Table 4.2, a lower-bainite (LB) microstructure has been analyzed with MicroGOP. Lower bainite of high-strength low carbon steels displays a lath-like ferritic morphology. This differs from plate-like appearance of LB in steels with higher carbon contents. The characteristic difference in comparison with upper bainite is the occurrence of cementite precipitation within ferrite laths, which are mostly aligned to the lath boundaries with their longest axis inclined at about 60° to the growth direction of the laths. A major problem in developing structure-property relationships for bainite is the definition of effective grain size. The lath width was considered to be of major influence and has been measured via context-based analysis by KIMAB. A mean value of 0.59  $\mu\text{m}$  was measured. The size of the intra-lath cementite particles was also analyzed and was in the range of  $8 \times 10^{-3}$  to  $3 \times 10^{-1} \mu\text{m}$ , with the majority below  $1 \times 10^{-1} \mu\text{m}$ .

### 4.3.4 Correlation to mechanical properties

In §8.2 several series of RRT related steel grades have been produced, mechanically tested and analyzed with SEM-QIA, with the aim to correlate phase-fractions and dimensions of retained-austenite, martensite and ferrite with mechanical properties.

## 4.4 Task 4.3 Ferrite-second phase boundary interface

The strengthening mechanism of multi-phase steels is partly based on the pinning of dislocations within the ferrite matrix by second-phase constituents within this matrix. Therefore, quantification of boundary interface between ferrite and second-phase constituents will be important in relation to appreciation of mechanical performance. This task was focused on the quantification of ferrite/2<sup>nd</sup>-phase boundary interface length, i.e., the total perimeter of the second phase divided by the corresponding detection area. Table 4.3 displays the results of the boundary interface measurements for the Round Robin DP, TRIP and both CP steel grades. RWTH analyzed two distinct SEM image series - the first series taken at RWTH, the second series provided by Corus.

**Table 4.3** *Ferrite/Second-phase boundary interface lengths ( $\mu\text{m}^{-1}$ )*

Boundary interface lengths	DP600		TRIP700		CP800	CP1000
	RWTH images	Corus images	RWTH images	Corus images		
RWTH (eCog)	3.6	20.0	13.0	13.0	3.4	4.9
Corus (Qwin)		0.48		0.8		
KIMAB (microGOP)		0.17		0.22	0.89	1.35

### 4.4.1 General influences on analysis results

There is a striking discrepancy between the results achieved shown in Table 4.3, especially between the results obtained for the DP steel. For the Corus image series, values differ by a factor of 40 between the results obtained by Corus and RWTH. Between Swerea KIMAB and RWTH, the difference even exceeds a factor 100. The differences between methods for the other steel grades are also high, but not in this magnitude. These discrepancies can be understood by comparison with results from the first analysis attempt by RWTH. In this attempt, for the DP a boundary interface length of  $0.85\mu\text{m}^{-1}$  was measured based on the RWTH-image series, which is much closer to the results of other partners. With the new refined analysis routine, which features improved detailed analysis of 2<sup>nd</sup>-phase clusters, more small ferritic areas are identified within these clusters, increasing dramatically the value of the interface length. This is equivalent to the discussed differences between the grain size values. Again, the magnification of the images is also an important factor as more microstructural details are distinguishable at higher magnifications. This is a possible explanation for the observed differences between values measured by RWTH for the two different DP-steel image series. Due to a 5 times higher magnification of the SEM images provided by Corus, more details of the microstructure are distinguishable, allowing the detection of smaller constituents and hence an increase of interface length.

## 4.5 Task 4.4 Shape factor

Table 4.4 shows results of shape factor analyses of the Round Robin samples. Listed are the mean grain perimeter, the total perimeter per area, the aspect ratio and the fullness ratio. Many measured values show good comparability. Quite striking is the similarity of the values measured for the two CP steels. On the other hand, many discrepancies are seen. Discrepancies between perimeter values are cause by the same underlying detection/magnification related problems as described for volume fraction and grain size. Aspect ratio values show little variation between the steel grades and no significant trend is visible. Fullness ratio results show a significant difference between the CP and the HSLA steel grades. Additional six shape parameters have been extracted with eCognition (see Table 4.5 and Table 4.6)<sup>[26]</sup>. Analysis targets have been ferritic grains of Round Robin materials and a fully polygonal ferritic microstructure as reference.

**Table 4.4** Results for the shape factor analysis. Distribution of the shape of individual phases and phase constituents for all type of microstructures as specified in WP1 are given.

Shape factor	DP600		TRIP700		HSLA100	HSLA31415		CP800	CP1000
	ferrite	2 <sup>nd</sup> ph	ferrite	2 <sup>nd</sup> ph	ferrite	ferrite	2 <sup>nd</sup> ph	ferrite	ferrite
<b>Ø-perimeter (µm)</b>									
eCOG	28.6	21.7			13.09	15.6		12.1	12.7
analySIS					1.46	1.87			
Qwin	25.3	4.1	14.3	2.95					
MicroGOP	29.5	6.4				10.1	1.1		
<b>Perimeter (µm)</b>									
eCOG	1.15	0.85			3.77	3.17		4.91	4.85
analySIS					15.7	11.5			
Qwin		0.5		0.8					
<b>Aspect ratio</b>									
eCOG	1.7	2			1.8	1.8		1.8	1.8
analySIS					1.8	1.9			
Qwin	1.2	2	1.13	1.93					
MicroGOP	1.7	2				1.8	1.8		
<b>Fullness ratio</b>									
eCOG	0.43	0.24			0.34	0.36		0.29	0.27
analySIS					0.54	0.57			
Qwin		0.88		0.91					

**Table 4.5** Short description of shape parameters that have been used.

Border index	Shape index	Compactness	Roundness	Elliptic fit	Density
Ratio between object boundary length and the boundary length of the smallest enclosing rectangle	Boundary length divided by four times the square root of the constituent's area	Product of length and width of the smallest enclosing rectangle divided by area	Radius of smallest enclosing ellipse minus radius of largest enclosed ellipse	Degree of fitting to ellipse with same area and length-width-proportions	Object area divided by ellipse radius
$\frac{2(l_v + w_v)}{4\sqrt{\#P_v}}$	$\frac{b_v}{4\sqrt{\#P_v}}$	$\frac{l_v w_v}{\#P_v}$	$\varepsilon_{\max} - \varepsilon_{\min}$	$2 \cdot \frac{\#\{(x, y) \in p_v : \varepsilon_v(x, y) \leq 1\}}{\#P_v} - 1$	$\frac{\sqrt{\#P_v}}{1 + \sqrt{VarX + VarY}}$
[1,∞], 1=ideal	[1,∞], 1=ideal	[0,∞], 1=ideal	[0,∞], 0=ideal	[0,1], 1=ideal	[0, *]

\* depends on shape of image object

Table 4.6 lists the mean values for the investigated microstructures. Similar values of a feature are given the same greyscale, envisioning several trends. The ferritic constituents of the TRIP700 and the DP600 steel grades are nearly identical in all six shape features. The same applies for the two HSLA steel grades, whose feature values are also very similar to those of the polygonal ferrite. The only larger deviation occurs within the feature "density". All other ferritic components from different microstructures clearly differ in two or more features.

It has to be noticed, that all listed values are mean values, representing a large number of individual grain features. This has a leveling effect on results, i.e. it will probably be possible to obtain more distinct differences by addressing individual grains. By this it will be possible to quantitatively classify ferritic grains according to their shape by the use of parameters like the selected ones.

**Table 4.6** Shape factors determined for ferrite grains of RRT materials. Shape factors with similar values have the same greyscale.

	Border index	Shape index	Compactness	Roundness	Elliptic fit	Density
Polygonal ferrite	1.34	1.43	1.47	0.55	0.78	1.82
HSLA100	1.38	1.51	1.65	0.64	0.72	1.63
HSLA31415	1.34	1.46	1.56	0.59	0.75	1.65
Mob LB	1.50	1.72	1.78	0.72	0.65	1.58
DP600	1.84	1.96	1.82	0.95	0.64	1.92
TRIP700	1.82	1.98	1.84	1.02	0.62	1.82
CP1000	1.61	1.73	1.85	0.92	0.63	1.86

## 4.6 Task 4.5 phase connectivity (mean free distance/continuity/contiguity)

Table 4.7 lists the results of the phase connectivity measurements performed on selected Round Robin samples with SEM-QIA. Phase connectivity parameters are mainly of interest when volume fractions in a series of samples are similar while (mechanical) properties differ significantly. This is addressed section 8.3.5. Three parameters have been selected for the measurements: mean free distance, continuity, contiguity. For detailed definitions see §2.4.1 to §2.4.3. In the access of the mean free distance of 2<sup>nd</sup> phase constituents in DP600 and TRIP700 steels, certain facilitating assumptions can be made. Due to the fact that in these steel types the second phase constituents are located at the ferrite grain boundaries, the mean free distance is approximately equal to the mean ferrite grain size.

**Table 4.7** *Results of the quantitative assessment of phase connectivity (continuity/contiguity/separation) for relevant microstructures as specified in WPI*

Phase connectivity	DP600		TRIP700		HSLA31415	
	ferrite	2 <sup>nd</sup> ph	ferrite	2 <sup>nd</sup> ph	ferrite	2 <sup>nd</sup> ph
<b>Mean free distance</b>						
Qwin (   / ⊥)	6.8 / 5.7 µm		3.8 / 3.4 µm			
MicroGOP (   / ⊥)	8.0 / 5.8 µm	1.8 / 1.4 µm			18.9 / 12.5 µm	1.2 / 1.4 µm
<b>Contiguity</b>						
Qwin	0.65		0.59			
OIM-EBSD			0.49			
<b>Continuity</b>						
MicroGOP	0.76	0.24			0.96	0.04

## 4.7 Task 4.6 Banding and clustering

This task has focussed on a quantitative assessment of banding and clustering of phases and phase constituents in microstructures of multi-phase steels due to macro segregation. A number of methods to define and quantify the degree of banding and clustering have been investigated and are outlined in the following sections.

### 4.7.1 ASTM Standard Practice (Designation: E 1268-99)<sup>[27]</sup>

A banded microstructure is a separation of one or more phases or constituents in a two-phase or multi-phase microstructure, into distinct layers parallel to the deformation axis due to elongation or micro-segregation, as defined by the ASTM committee. The practice proposes a characterization by an anisotropy index (AI) or a degree of orientation, which relies on simple stereological methods: the counting of feature interceptions (N) or feature boundary intersections (P) by lines of a test grid perpendicular to and parallel with the deformation direction. For testing, the method has been adapted to automatic image analysis, to enable statistically significant measurements. The analysis results were not satisfactorily discriminating, even when comparing strongly banded and weakly banded structures. The method also proved to be very sensitive to grains linking and to failures like concavities. The benefits of this method are its easy adaptability, as it is based on counting methods and its good comparability to manual methods. If the method is used, low magnifications (50x to 200x) and the use of binary images (created by thresholding) are recommended.

### 4.7.2 Method based on progressive erosion<sup>[22]</sup>

CRM has tested a method that is based on the measurement of the evolution of the volume fraction of ferrite when it is progressively eroded in 2 directions by a linear element. The percentage is decaying much more rapidly when eroding perpendicular to the rolling direction than parallel to it, see Figure 4.2. An “erosion-based” anisotropy index is defined, representing the ratio of the decay distances in both directions. By defining a characteristic decay distance  $d_e$  as the one at which the measured fraction of ferrite is equal to 1/e of its initial value ( $F(d_e) = F(0)/e$ ), it is possible to define an “erosion-based” anisotropy index:  $AI_{eros} = d_e^h/d_e^v$ , which in this case leads to a value of 2.26 (32.5/14.4), see Figure 4.2(right graph). This method is relatively fast and able to discriminate between differently banded structures. Results are close to the human feeling of the banding degree. On the downside the choice of the “decay” distance is rather arbitrary.

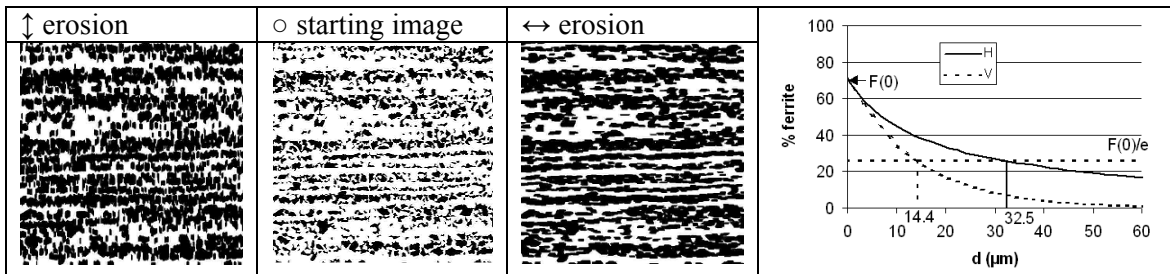


**Figure 4.2** Progressive erosion based method and anisotropy index parameter description.

#### 4.7.3 Method based on meangreying<sup>[22]</sup>

To obtain the graph related to a horizontal vicinity analysis, for every position from top to bottom of the image, the maximum length of a segment in rolling direction for which the 2<sup>nd</sup>-phase fraction remains under a threshold related to the global area fraction is measured. The same set is measured in vertical direction. A global index can be obtained by summing the lengths in both directions, and taking the ratio of those sums as an anisotropy index. During the measurements performed in the project, the method provided fairly good discrimination of differently banded structures. A deeper amplitude analysis could be used for assessing more completely the degree of banding. Also, the periodicity of bands and the interband spacing could be approached with a Fourier analysis. The downsides of the methods are that it is rather time consuming and can't be performed manually due to the complex length measurements. Also the choice of the vicinity thresholds is arbitrary.

#### 4.7.4 Covariogram

The covariogram approach, put forward by Arcelor, is a new method to evaluate banded microstructures<sup>28</sup>. Since it was found to be a powerful tool in quantifying banded microstructures the method is described in more detail. The covariogram in a binary image represents the probability that two points X and X+h separated by a distance h belong to the same phase Y:  $C(X, h) = P(x \in Y, x+h \in Y)$ . In practical application, the covariogram can be obtained by plotting the evolution of volume fraction of Y as a function of a displacement h, obtained by the intersection of the initial microstructure and the same microstructure shifted by distance h. The method has been tested both on simulated (Voronoi Tessellation method) and real microstructural images, see Figure 4.3 and Figure 4.5.

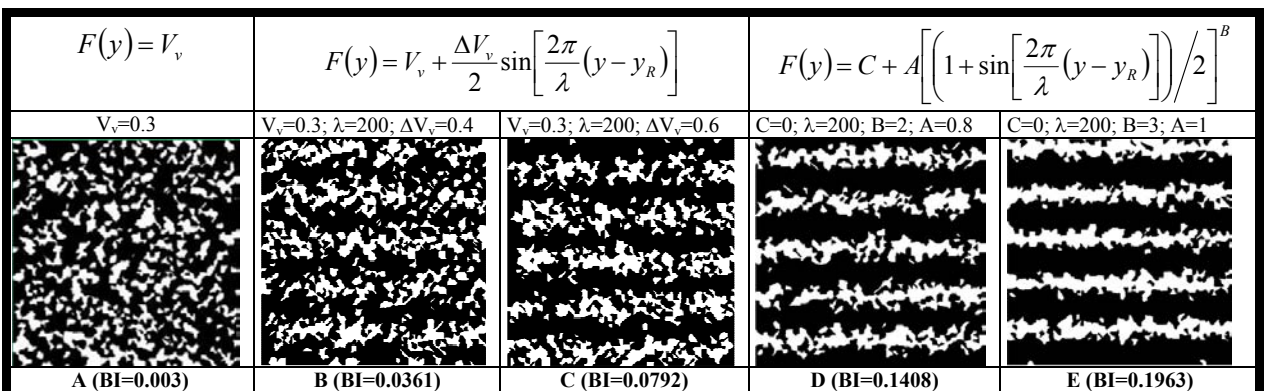


**Figure 4.3** Simulated (banded) microstructures for evaluating the covariogram method.

It provided satisfactory results and was able to clearly differentiate between microstructures with different amounts of banding from homogeneous to strongly banded structures. The intensity of the banded structure (or BI index) is defined as the difference between covariance value at the first minimum and the first maximum as illustrated in Figure 4.4(left). The position of first maximum (HM) corresponds to the period of banding (see Figure 4.4). By applying the covariogram method to the inverse microstructure one can get information about the thickness of bands. This parameter was not investigated in this study. The covariograms and BI indexes shown in Figure 4.4 are obtained from the simulated microstructures shown in Figure 4.3.

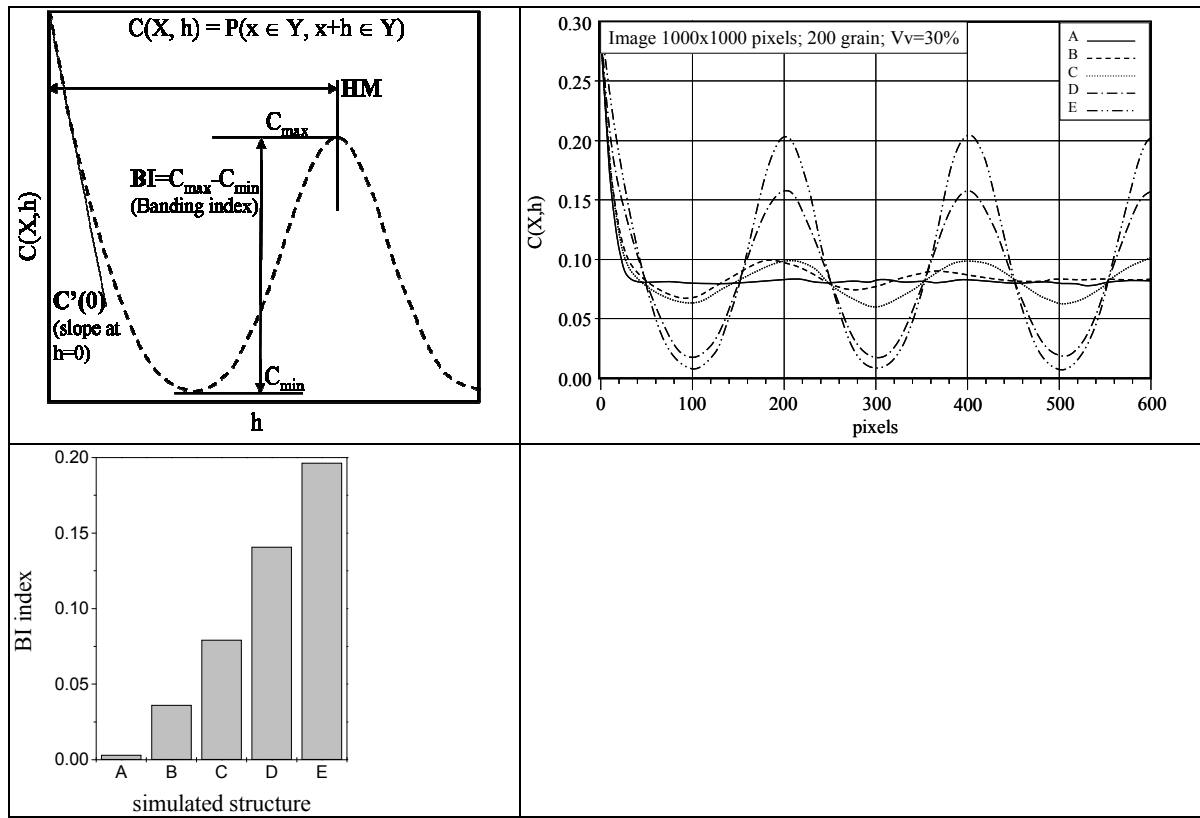


**Figure 4.4** (left top) typical covariogram obtained for a banded structure. The intensity of the banded structure (or BI index) is defined as the difference between covariance value at the first minimum and the first maximum (right top) covariograms obtained for the simulated microstructures of Figure 4.3. (left bottom) BI indexes of simulated structures.

To study the effect of holding temperature, holding time and cooling rate on banding in DP steel, a DP grade was subjected to different heat treatments as presented in Figure 4.6. The time at 650°C is chosen in such a way that all samples obtained a similar volume fraction of second phase at the end of the treatment. The LOM images of the samples were analyzed with the covariogram method. The results of the analysis are presented in Figure 4.6 (right). It is concluded that the BI index gives a good quantitative representation of the observed banded structures.

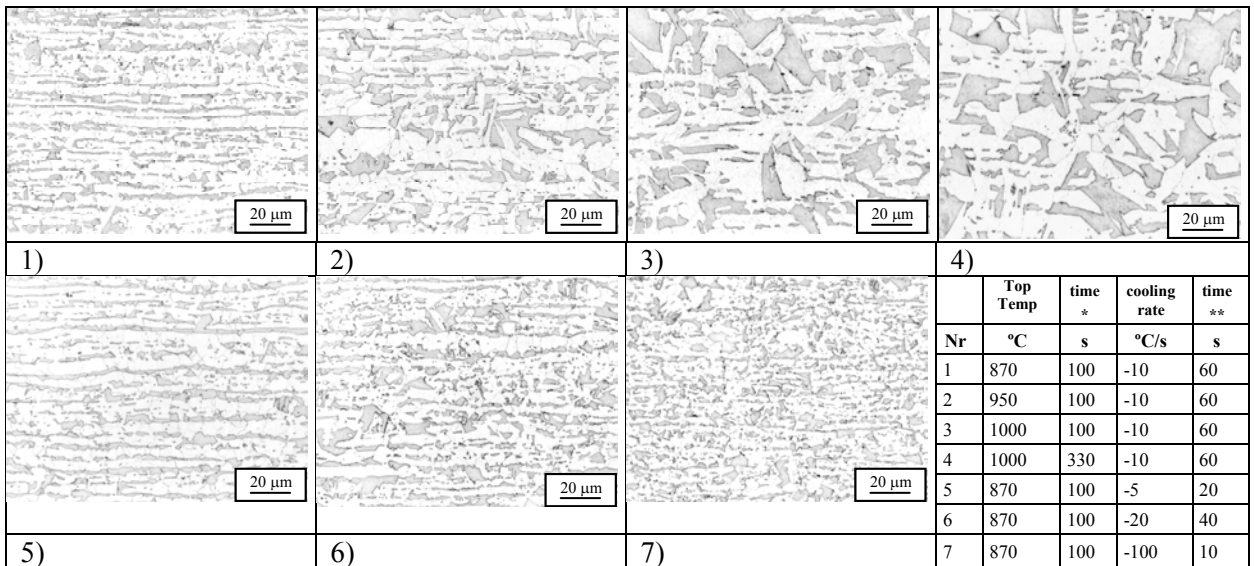


**Figure 4.5** Overview of real microstructures used to evaluate the covariogram method. For all samples heating rate is 10°C/s to reach the top temperature. (time\* at top temperature; time\*\* at 650°C).

Based on results shown in Figure 4.6 (right) it is concluded that:

- Increasing the holding temperature significantly decreases the BI index
- The BI index is hardly influenced by the increased holding time at 1000°C
- Increasing the cooling rate decreases the banding index (BI).

The slope ( $C'0$ ) of the covariogram curve at  $h=0$  is a parameter that can be used to get an idea of global size of the microstructure: the finer the microstructure the higher is the slope, see Figure 4.4(left). This parameter was first tested on simulated microstructures as shown in Figure 4.7. These results confirm that ( $C'0$ ) is quite sensitive to size evolution. However, more studies are necessary to confirm these results and improve the understanding of the evolution of this parameter.

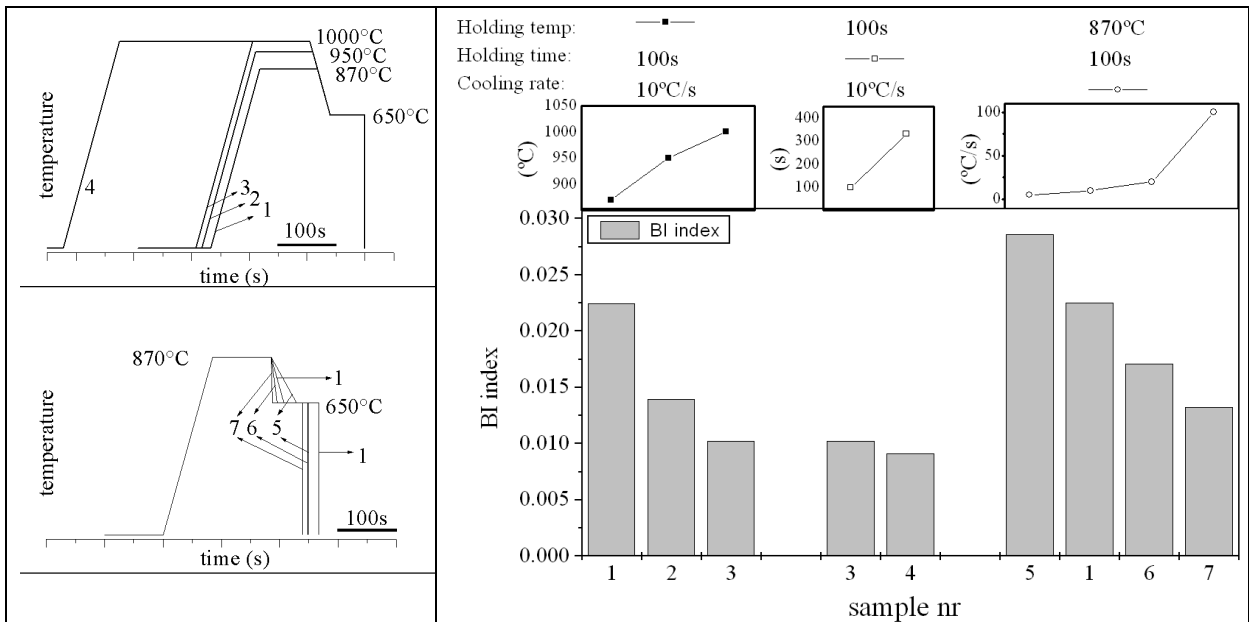


**Figure 4.6** (Left) Heat cycles used to obtain microstructures shown in Figure 4.5 (numbers in graph refer to numbers in Figure 4.5). (Right) BI index determined for the microstructures of Figure 4.5 combined with process parameters.

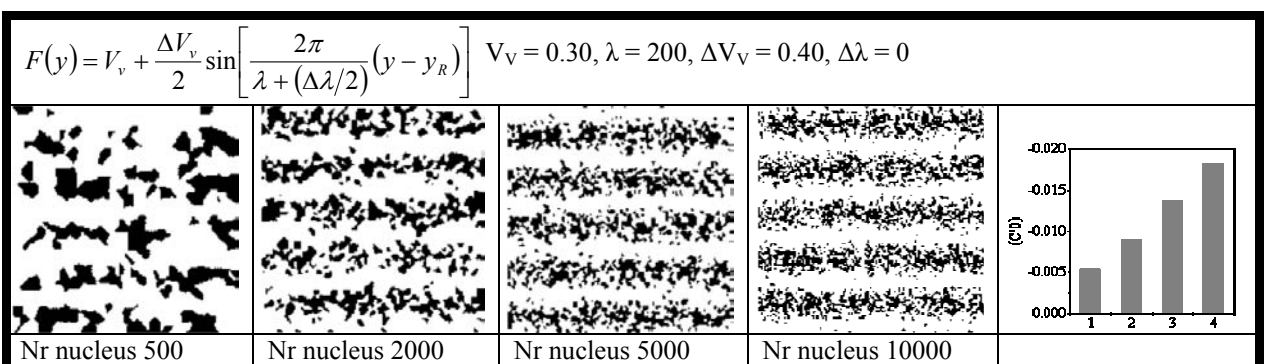


**Figure 4.7** Simulated microstructures with, from left to right, decreasing feature sizes. The response of the  $C'0$  parameter on the change of feature size is shown in the left graph.

#### 4.7.5 Other basic methods

Additionally, three more basic methods have been tested on homogeneous, clustered and banded model microstructures. First, frequency histograms of 2<sup>nd</sup>-phase constituents in the direction of two main coordinates have been created, but showed no promising results. They provided only useful information for very regular banding, which is unlikely to occur in real microstructures. Second, polar coordinates have been utilized. The vectors connecting each pair of simulated 2<sup>nd</sup>-phase constituents were calculated and pictured in polar coordinates. Although some effects were visible, the results provided no additional information which could be used as basis for a description of banded and clustered structures. In the third tested method, the polar coordinates method was modified to take into account only the nearest neighbours. The vectors between each 2<sup>nd</sup>-phase constituent and its 10 nearest neighbours were

calculated. Afterwards, histograms of the lengths and angles of the calculated vectors were created. For the simulated model microstructures, the resulting histograms showed distinct maxima according to the type of phase distribution. For the homogeneous structure, no maxima occurred in the histograms, while more than one maximum occurred in the vector lengths histogram for clustered or banded structures. For a banded structure the angles histogram additionally showed maxima according to the inclination of the bands within the image. However, when the method was transferred to the (real) DP600 and the TRIP700 microstructures, no significant differences could be measured.

## 5 WP 5 Orientation and crystallographic characterization

Task	Deliverable	D#
5.1	Effective grain size	D18
5.2	Distribution of boundary misorientation	D19
5.3	Lattice imperfection (defect density)	D20
5.4	Volume fraction of phases	D21
5.5	Additional parameters	D22
5.6	Texture	D23

### 5.1 General objective

EBSD (Electron Back Scatter Diffraction) technique has been used for microstructural characterisation and analysis of complex microstructures in HSLA, LB, DP, TRIP and M steels. As part of WP 5 the Round Robin Test (RRT) has been conducted focusing on a range of parameters specified in accordance with the Task structure of the Work Package. The parameters measured from the test were processed and EBSD results from partners were analysed by KIMAB regarding consistency and scatter.

### 5.2 Task 5.1 Effective grain size

One of the main parameters for the definition of effective grain size is grain boundary misorientation. To determine the influence of misorientation on effective grain size, statistical parameters describing grain diameters have been calculated from EBSD/OIM measurements. Based on the HSLA steel examination by VAS, the 15° has been accepted and used as the critical misorientation parameter for all steel types investigated.

### 5.3 Task 5.2 Distribution of boundary misorientation

Distributions of misorientation angles for Round Robin steel grades have been investigated in parallel with images of band contrast, orientation maps, Euler angle maps with grain boundaries of a range of misorientation angles, etc. A lot of information on material condition and thermo-mechanical history can be found from MAD analysis. A recrystallised material with random texture shows a typical MAD, and any form of plastic deformation or texture changes the MAD. Bainite and martensite show very typical MAD with high frequencies of misorientations at low angles (below 15°) and at high angles (over 50°). It has been thought that MAD could be a tool to separate martensitic microstructures from bainitic ones, but so far the analysis within this project cannot give consistent rules for separating these two phases. MAD has only been used to verify misorientation relations between already partitioned phases in TRIP, see §8.3.5.

### 5.4 Task 5.3 Lattice imperfection (defect density)

X-ray diffraction measurements by TKS of retained-austenite and lattice constants within ferrite and austenite showed high percentage of austenite within the TRIP steel. The relatively high lattice constant of this austenite can be attributed to a higher than normal carbon content within this phase. However,

Table 5.1 Amount of RA and lattice constants based on XRD analysis for RRT steels			
		Lattice constance (nm)	
grade	RA %	RA	Ferrite
LB	0.0	-	0.2869
DP600	1.5	0.3605	0.2871
TRIP700	13.5	0.3619	0.2872
CP800	1.5	0.3603	0.2868
CP1000	3.5	0.3602	0.2871
MS1200	<1	-	0.2871

small amounts of austenite were also found in the CP and DP steels. The lattice constants of austenite in these steels were close to the theoretical value of 0.3600 nm and thus significantly lower than in the TRIP steel. The lattice constant of ferrite within the measured data showed only very little variance and was slightly higher than the literature reported value of 0.286 nm. Two different approaches for the distinction between polygonal and bainitic ferrite in EBSD/OIM measurements have been investigated.

The Image Quality (IQ) of an EBSD measurement depends mainly on lattice distortion due to local stress and was used as a rough estimate for local dislocation density. On the other hand, lattice distortion which leads to local misorientations, has been estimated using Kernel Average Misorientation (KAM) which was obtained by calculating the average of misorientations between a point and all its neighbouring points. The grey level distributions of pixels corresponding to the IQ values in the map were measured using an automated image analysis system. Three phases were distinguished in the histogram using three visible distribution peaks. Very low IQ values were assumed to belong to martensite and cementite, low IQ values were associated with bainitic ferrite and higher IQ values with polygonal ferrite. In the KAM map, low values of KAM ( $<1^\circ$ ) were related to polygonal ferrite, whereas higher values corresponded with bainitic ferrite. Strong discrepancy between IQ-based and KAM-based analysis results was observed. Hence additional investigations of bainitic ferrite using transmission electron microscopy are necessary.

## 5.5 Task 5.4 Volume fraction of phases

Partitioning of phases in TRIP700 has been investigated by means of a Gaussian fitting procedure of band contrast distributions. This was based on the assumption that each microstructure constituent is characterized by different defect densities, represented on the band contrast (BC) distribution by a Gaussian curve. A method was developed to clean the data set from grain boundary contributions. Quantification was not yet possible.

Practical EBSD strategies (partitioning rules) were developed for identification and partitioning of phase constituents in DP and TRIP microstructures including martensite, retained-austenite, and bainite. The results obtained by partitioning were used for “EBSD guided” nano-indentation. In the case of the DP600 microstructure, martensite was partitioned by setting the following three criteria: phase alpha AND grain size  $< 0.8$  micron AND average IQ of grains  $< 750$ . Partitioning of retained-austenite in the TRIP steel was based on its distinctive FCC lattice structure. The EBSD + image analysis based strategy for the volume fraction determined with combined IQ /KAM for the CP grades was described in detail in §3.5.4

## 5.6 Task 5.5 Additional parameters

The purpose of the Round-Robin (RR) excursion was to see how quantitative data obtained from EBSD measurements varied between laboratories. It is inevitable that EBSD measurements executed in different laboratories, in different companies with different equipment and procedures etc. will show a spread in results. It was the actual measurement that was the issue. The analysis and extraction of parameters were planned to be done by one laboratory, KIMAB.

The analysis showed that EBSD measurements, when set-up in a similar way, with similar step size and comparable microscope resolution, give similar results. The results however also showed that the output from EBSD measurements can vary a lot. What we can learn from this study is that it is extremely important to plan the experiments accurately and to present the parameters used for the measurements together with the results, or else the results are quite meaningless. The analysis furthermore showed that an exercise like this needs to be highly constrained; for each material a number of parameters must be defined, or else the results will be difficult to compare.

The most important parameters to be defined beforehand and thus equal for every laboratory involved are; phases to be included, step size and size of data set, also the position and sheet plane on which the measurements should be done. Choosing the RD-TD plane, RD-ND cross-section, or TD-ND cross-section will all give different results. Perhaps the most important parameter when setting up the experiment in the microscope is the step size, which determines what microstructure feature size still can be measured. The maximum resolution of EBSD is very high: measured as the area (or volume) that produces the diffracted pattern, around 10 nm in steels using a FEG-SEM. But, what decides the smallest features possible to analyse in an EBSD experiment is the length between each analysed spot. The smallest feature that can be trusted is difficult to judge, it is different for different applications, but for automated EBSD scans a rule of thumb is that a reliable object (e.g., a grain or sub grain) needs at least 4 pixels to be accounted for, or else it must be thought of as possible mis-indexed pixels. Therefore a material with an average grain size of 5  $\mu\text{m}$  (diameter) would need a step size of 0.25  $\mu\text{m}$  if the smallest grains included in the analysis are 0.5  $\mu\text{m}$ . If smaller grains should be included in the analysis, then a smaller step size must be used. It is equally erroneous to use a too small step length as a

too big one, e.g. to use a step length of 0.020 µm to characterize the texture or grain size of a material with an average grain size of 50 µm. Then each grain will contain several millions of measurements and no meaningful results will be obtained even after days of scanning. Finally, if a material contains features of different size classes, it is probably necessary to set up different experiments for the different features.

In this exercise several of the above parameters were not addressed and the results from the measured EBSD data were therefore very different in some cases. Also, the different suppliers of EBSD equipment treat data differently using different acquisition and data analysis algorithms, and also different coordinate systems. In the end it was not possible for KIMAB to import and subsequently analyse data that was acquired using TSL equipment.

### 5.6.1 Experimental

Seven different materials were distributed among the six participating laboratories (Table 5.2) and a selection of a limited set of parameters was agreed upon. The mission was to do measurements as good as possible with the routines commonly used at each laboratory. Three laboratories used TSL equipment and three used equipment from HKL (Oxford Instr.). Four laboratories used FEG-SEMs, one used LaB<sub>6</sub>-filament and one W-filament SEM.

**Table 5.2** *Participating laboratories and their EBSD equipment (at the time of measurement)*

Laboratory	SEM	Camera	Software
<b>KIMAB</b>	LEO Gemini 1530 FEG-SEM	HKL Nordlys II, digital	Channel 5 (HKL)
<b>Corus</b>	ZEISS ULTRA55 FEG-SEM	TSL Hikari, digital	OIM 5.2 (TSL)
<b>Arcelor</b>	JEOL 6400 W-fil	HKL Nordlys II, digital	Channel 5 (HKL)
<b>CRM</b>	Philips XL30 ESEM LaB <sub>6</sub>	TSL Digiview, digital	OIM 4.6 (TSL)
<b>TKS</b>	FEI Quanta FEG-SEM	TSL Digiview, digital	OIM 4.6 (TSL)
<b>VAS</b>	ZEISS SUPRA35 FEG-SEM	HKL Nordlys II, digital	Channel 5 (HKL)

### 5.6.2 Results

The materials and participating laboratories are presented in Table 5.3 where it is indicated which laboratory analyzed which materials. Several things made a comparison between the laboratories difficult, or putting it differently, made the results very different. Most important, the different laboratories have used different stepsizes and different field sizes for of the analyses. Below, the results for each material are presented. Another disturbing thing was that data from TSL software could not always be read by HKL Channel 5 software, the data was then not analyzed by KIMAB and is therefore some data is missing.

**Table 5.3** *Materials and participating laboratories.*

Lab	HSLA100	HSLA31415	DP600	TRIP700	CP800	CP1000	MS1200
Corus*	x	x	x	x	x	x	x
KIMAB	x	x	x	x	x	x	x
Arcelor	x		x	x	x		
CRM*	-	x	x	x			
TKS*	x		x	x	x	x	x
VAS	x		x	x	x	x	x

\* Some or all data sets were not possible for analysis at KIMAB

#### 5.6.2.1 HSLA100

HSLA100 was classified as a granular bainitic ferritic phase steel. All laboratories chose to identify only ferrite. The laboratories also used the same step size and similar size of the scan, except for Arcelor. Overall the results from the different laboratories gave similar results for this material. The grain sizes were similar both for 2° and 15° limit on misorientations. Looking deeper into the results there is a large difference in indexing, Corus using TSL software had 0.5 % non indexed point, KIMAB (HKL) had 8.8 % non indexed points, Arcelor (HKL) 11.5 % and VAS (HKL) 17.6 %, Table 5.4. Looking at the BC maps the results look (about) equally sharp for three of the laboratories (Figure 5.1) and the difference in hit rate (fraction indexed points) between them is due to the criteria for accepting the patterns. VAS used a criteria based on 8 detected bands, KIMAB used 6 bands and

Corus used “medium level” in the TSL software. The different levels of discrimination gave differences in the raw data quality. A study of misorientation distributions showed that both the Corus and KIMAB data contain systematic mis-indexing (rotation at 30°), see Figure 5.1. This problem is easily handled afterwards and in this case it was better (quicker, higher hit rate) to collect data in such a way that the hit rate was high and then correcting the data in the software (it is a problem though if the incorrect data is accepted as correct!). The VAS data looks different also in other respects though, which indicates that there are differences between the measurements. The VAS data could have been collected from another position in the plate than the other two data sets for example. This could be one reason for the observed discrepancies. The data from Arcelor suffered from poor focus, drift and also the choice of 5 bands for detection gave severe problems with misindexing. These data were too poor to get any valuable information from.

**Table 5.4** EBSD parameters for HSLA steel.

Material	Matrix size and step size (pixels, $\mu\text{m}$ )	Phase	Effective grain size D ( $\mu\text{m}$ )		Volume fraction* (%)		Zero solutions (%)	Mean BC	Mean MAD**
			misorient.		Raw	NR			
			2°	15°					
KIMAB	1000x1000, 0.15	Ferrite	0.9	2.0	91.2	99	8.8	98	0.54
Corus	868x934, 0.15	Ferrite	1.0	1.8	99.5	100	0.5	156	0.70
Arcelor	613x463, 0.20	Ferrite	Poor data	Poor data	88.5	99	11.5	110	0.45
VAS	900x900, 0.15	Ferrite	0.95	1.9	82.4	97	17.6	108	0.60

\* Zero solutions included as separate “phase”; \*\*CI for TSL

### 5.6.2.2 HSLA31415

This is steel with a mixture of polygonal ferrite and fine bainitic ferrite in the microstructure. All laboratories chose to identify only ferrite. The different laboratories also used the same step size and similar size of the scan, except for CRM. Again, as for the HSLA steel, the results from the different laboratories using the same step size gave similar results. The grain sizes were similar both for 2° and 15° limit on misorientations. A more thorough analysis of the data showed that there were differences though, in indexing, Corus using TSL software had 0.9 % non indexed point, KIMAB (HKL) had 3.8 % non-indexed points, CRM (TSL) 4.4 % and VAS (HKL) 13.9 %, see Table 5.5. Looking at the BC maps the results again look equally sharp for three of the laboratories and the difference in hit rate was due to the criteria for accepting the patterns. The different levels of discrimination gave differences in the raw data quality, in the same way as above, Corus and KIMAB data contained systematic misindexing. The data from CRM suffered from poor focus and drift.

**Table 5.5** EBSD parameters for HSLA31415.

Material	Matrix size and step size (pixels, $\mu\text{m}$ )	Phase	Effective grain size D ( $\mu\text{m}$ )		Volume fraction* (%)		Zero solutions (%)	Mean BC	Mean MAD**
			misorient.		Raw	NR			
			2°	15°					
KIMAB	900x900, 0.15	Ferrite	1.7	2.5	96.2	99.7	3.8	112	0.41
Corus	902x901, 0.15	Ferrite	1.6	2.5	99.1	100	0.85	162	0.69
CRM	286x867, 0.15	Ferrite	0.79	2.2	95.6	99.5	4.4	96	0.63
VAS	1000x1000, 0.15	Ferrite	1.5	2.6	86.1	98	13.9	97	0.52

\* Zero solutions included as separate “phase”; \*\*CI for TSL.

### 5.6.2.3 DP600

DP600 is a dual phase steel with a ferritic matrix and martensite as second phase. There are small amounts of residual austenite in the material, but most laboratories chose to identify only ferrite. The material is difficult to analyze in the way that the ferrite grains are large, about 5  $\mu\text{m}$  to 30  $\mu\text{m}$  in diameter, and the martensite much finer. The choice of 50 nm step size (Corus) therefore characterized the martensite and residual austenite well, but failed in characterizing the ferrite since only a few grains were included. The choice of 0.5  $\mu\text{m}$  step size (CRM) on the other hand characterized the ferrite well but failed in characterizing the second phase and residual austenite. Examples of the results of the measurements presented in Figure 5.2 and the analyzed data is given in Table 5.6. It is also obvious that the data was measured on different planes. The interpretation of the data is of highest importance; this is evident for the results from Corus that gave 0.36  $\mu\text{m}$  as the “overall” average ferrite grain size, and 1.4 for recrystallized ferrite grains. To get a good estimate of the polygonal ferrite grain size, texture,

misorientation distribution, etc. it is necessary to distinguish between the ferrite and martensite phases. These two phases are both identified as BCC ferritic, the small crystallographic difference cannot be handled during indexing. In this case it can be done by discriminating the grain size or by discriminating the band contrast component (BC). Discrimination on size gave an average ferrite grain size of 7.5  $\mu\text{m}$  with the average “aspect ratio” equal to 2 for the CRM data. A similar way of treating data but for the purpose to characterize the martensite gave an island size of 0.32  $\mu\text{m}$  for the martensite phase using the Corus data. In this example the laboratories have chosen to use completely different step sizes resulting in completely different results.

**Table 5.6** EBSD parameters for DP600.

Material	Matrix size and step size (pixels, $\mu\text{m}$ )	Phase	Effective grain size D ( $\mu\text{m}$ )		Volume fraction* (%)		Zero solutions (%)	Mean BC	Mean MAD**
			2°	15°	Raw	NR			
Corus***	801x1001, 0.05	Ferrite	1.4 (0.36)	-	-	98.5	3.5	-	0.72
		Austenite	-	-	-	1.5	-	-	-
Arcelor	613x463, 0.2	Ferrite	3.2	4.4	83.6	98	16.4	92	0.40
CRM	362x761, 0.5	Ferrite	3.0	6.3	99.1	100	0.9	174	0.66
VAS	600x600, 0.15	Ferrite	1.8	3.0	85.2	98.7	14.5	77	0.43
		Austenite	0.41	0.42	0.37	0.3	-	63	0.64

\* Zero solutions included as separate “phase”; \*\*CI for TSL.; \*\*\* not analyzed at KIMAB

#### 5.6.2.4 TRIP700 steel

TRIP700 is a ferritic phase steel with about 10-15 % residual austenite in the microstructure. The amount of austenite was measured to 14 % by X-ray methods but with EBSD the results were varying between 1.8 and 7.4 % in the raw data and between 3.9 and 10.8 % in the processed data. The very large influence of step size on EBSD results is obvious from the very different results in two data sets of data from KIMAB, one of them using a fine step size of 0.05  $\mu\text{m}$ , the other a larger step size of 0.25  $\mu\text{m}$ . In the EBSD map with the smaller step size the austenite fraction was found to be 10.8% and the average austenite island size 0.31  $\mu\text{m}$ . In the other analysis the fraction austenite was found to be 5.7% and the average austenite grain size 0.71  $\mu\text{m}$ . The problem with EBSD for analyzing residual austenite in TRIP steels is that austenite is meta-stable and therefore can easily transform to martensite. The BC EBSD maps from KIMAB and VAS are shown in Figure 5.3 and there is more martensite visible on the right map (dark phase). The laboratories used different step sizes and also total areas of the scans which gave different results. There were again differences in indexing, and fractions of ferrite/austenite varied substantially, see Table 5.7. It is also very probable that the data was obtained from different geometrical planes and positions in the sheet: the grains in Figure 5.3a are elongated along the x axes, whereas this is not the case in Figure 5.3b.

**Table 5.7** EBSD parameters for TRIP700 steel.

Material	Matrix size and step size (pixels, $\mu\text{m}$ )	Phase	Effective grain size D ( $\mu\text{m}$ )		Volume fraction* (%)		Zero solutions (%)	Mean BC	Mean MAD**
			2°	15°	Raw	NR			
KIMAB	650x650, 0.05	Ferrite	1.0	0.89	85.8	89.0	6.8/0.15	126	0.47
		Austenite	0.31	0.31	7.4	10.8		119	0.54
KIMAB	600x600, 0.25	Ferrite	2.5	3.1	85.0	93.6	9.4/0.7	126	0.47
		Austenite	0.70	0.71	5.6	5.7		119	0.54
Corus***	801x1001, 0.05	Ferrite	0.38	-	-	90.8	5.3/-	-	0.75
		Austenite	0.29	-	-	9.2		-	0.42
Arcelor	613x463, 0.1	Ferrite	1.6	2.5	78.1	91.1	20.1/5.0	70	0.35
		Austenite	0.67	0.69	1.8	3.9		61	0.36
VAS	1000x1000, 0.075	Ferrite	-	-	81.5	92.0	15.3/1.0	146	0.44
		Austenite	-	-	3.0	6.9		121	0.54

\* Zero solutions included as separate “phase”; \*\*CI for TSL.; \*\*\* not analyzed at KIMAB

#### 5.6.2.5 CP800 steel

This is a complex-phase steel with a mixture of polygonal ferrite, fine bainitic ferrite, martensite and retained-austenite. Two laboratories chose to identify only ferrite, and two included also austenite. Comparing ferrite grain size, the results from the different laboratories gave similar results for this material. Corus, using a smaller step size (0.05  $\mu\text{m}$ ) evaluated a smaller grain size than the other laboratories which used 0.15  $\mu\text{m}$  step size. The different stepsizes and fieldsizes offer an explanation for

the difference in detecting austenite (present only in small volumes). There were again differences in indexing as previously reported with differences in quality, see Table 5.8. Several EBSD maps showed drift problems and the stability of the microscope stages is one of the greatest problem for very detailed EBSD. Furthermore these issues are difficult to handle since they are not a linear phenomena that can be easily corrected for. The high quality EBSD map in Figure 5.4 (Corus) also show drift problems, if studying it closely. The amount of data was large, matrix size 800\*1000, and the analysis took over 8 hours to complete. The microstructure looks as it has shifted to the left during the first part of the analysis and also focus has deteriorated with time.

**Table 5.8** EBSD parameters for CP800.

Material	Matrix size and step size (pixels, $\mu\text{m}$ )	Phase	Effective grain size D ( $\mu\text{m}$ )		Volume fraction* (%)		Zero solutions (%)	Mean BC	Mean MAD**
			2°	15°	Raw	NR			
KIMAB	800x800, 0.15	Ferrite	0.91	1.54	87.4	99	12.6	100	0.53
Corus***	801x1039, 0.05	Ferrite	0.83	-	99.3	99.7	-	-	0.73
		Austenite	0.13	-	0.7	0.3			0.29
Arcelor	613x463, 0.1****	Ferrite	0.79*	0.81*			29.5	82	0.49
VAS	900x900, 0.15	Ferrite	0.92	1.7	81.5	100	18.5	103	0.49
		Austenite	-	-	0.03	0.0	-	-	0.54

\* Zero solutions included as separate "phase"; \*\*CI for TSL.; \*\*\* not analyzed at KIMAB, \*\*\*\* too small area for accurate measurement.

#### 5.6.2.6 CP1000 steel

A complex-phase steel as the CP800 steel above with a mixture of coarse and fine bainitic ferrite, martensite and retained-austenite. Only three laboratories supplied data or information that was possible to compare. Two laboratories chose to identify both ferrite and austenite, and one included only ferrite. Corus also differentiated between ferrite and martensite (subsequent to EBSD data collection). In this case the approaches from the laboratories were too different to produce comparable results, with a little more constrained description prior to the EBSD analysis the situation could have been different. The amount of austenite was 0.04 % in one case and 0.1 % in the other. The laboratories used different step sizes and sizes of the scans. There were again differences in indexing as previously reported. The difference in hit rate between laboratories were mainly due to criteria for accepting patterns (as described above for HSLA), but in this case with a very fine microstructure the choice of a smaller step size probably gave higher hit rate. This microstructure needed a step length of 0.05  $\mu\text{m}$  or even finer (martensite) to be characterized in detail. Table 5.9 gives statistical information from the different measurements.

**Table 5.9** EBSD parameters for CP1000.

Material	Matrix size and step size (pixels, $\mu\text{m}$ )	Phase	Effective grain size D ( $\mu\text{m}$ )		Volume fraction* (%)		Zero solutions (%)	Mean BC	Mean MAD**
			2°	15°	Raw	NR			
KIMAB	700x700, 0.15	Ferrite	0.90	1.5	87.6	99	12.4	95	0.54
Corus***	801x1001, 0.05	Ferrite	2.15	-	-	91.2	1	-	0.72
		Martensite	0.59	-	-	8.7			0.55
		Austenite	0.10	-	-	0.1			0.09
		Ferrite	0.81		79.9	-	20.0	75	0.45
VAS	500x500, 0.10	Austenite	-	-	0.04	-	-	-	-

\* Zero solutions included as separate "phase"; \*\*CI for TSL.; \*\*\* not analyzed at KIMAB

#### 5.6.2.7 MS1200 steel

This is a martensitic steel with a mixture of fine martensite and probably some bainite, and retained austenite. Only four laboratories supplied data or information that was possible to compare. Two laboratories chose to identify both ferrite and austenite, and two included only ferrite. With this type of fine microstructure it is important to choose the step size fine enough to resolve the fine microstructural features. The approaches for EBSD for the laboratories were too different to produce comparable results. The analyzed ferrite grain size was similar between KIMAB and VAS, with VAS showing a little smaller diameter. VAS used a smaller step size, which can explain the difference in results. The amount of retained-austenite was 1.2 % in one case and 0.01 % in the other. The laboratories used different stepsizes and fieldsizes, which can explain the difference. There were again differences in

indexing as previously reported. For this material the VAS laboratory showed higher indexing with 8 bands indexed than the other laboratories using HKL software and excellent data with no signs of misindexing. The KIMAB and Arcelor laboratories were less successful and the data showed significant amounts of misindexing. Corus, using TSL software showed very high hit rate (97%) but the data was not possible to analyze at KIMAB so the accuracy cannot be judged, see Table 5.10. This very fine microstructure needed a step length of 0.05  $\mu\text{m}$  or even finer to be characterized in detail. The different levels of discrimination gave differences in raw data quality, in the same way as described previously; see Figure 5.5 and Figure 5.6 below.

**Table 5.10** EBSD parameters for MS1200.

Material	Matrix size and step size (pixels, $\mu\text{m}$ )	Phase	Effective grain size D ( $\mu\text{m}$ )		Volume fraction* (%)		Zero solutions (%) Raw/NR	Mean BC	Mean MAD**
			2°	15°	Raw	NR			
KIMAB	710x710, 0.15	Ferrite	0.64	1.3	63.4	94.5	36.6/5.5	79	0.69
Corus***	801x1001, 0.05	Ferrite	0.35	-	-	98.8	-/3	-	0.59
		Austenite	0.08	-	-	1.2			
Arcelor	613x463, 0.2	Ferrite	0.65	1.2	62.3	89	37.3	11.0	0.63
VAS	700x700, 0.1	Ferrite	0.60	1.0	72.5	97.9	27.5/2.1	70	0.50
		Austenite	-	-	0.01	0.00	-/-	50	0.44

\* Zero solutions included as separate "phase"; \*\*CI for TSL.; \*\*\* not analyzed at KIMAB

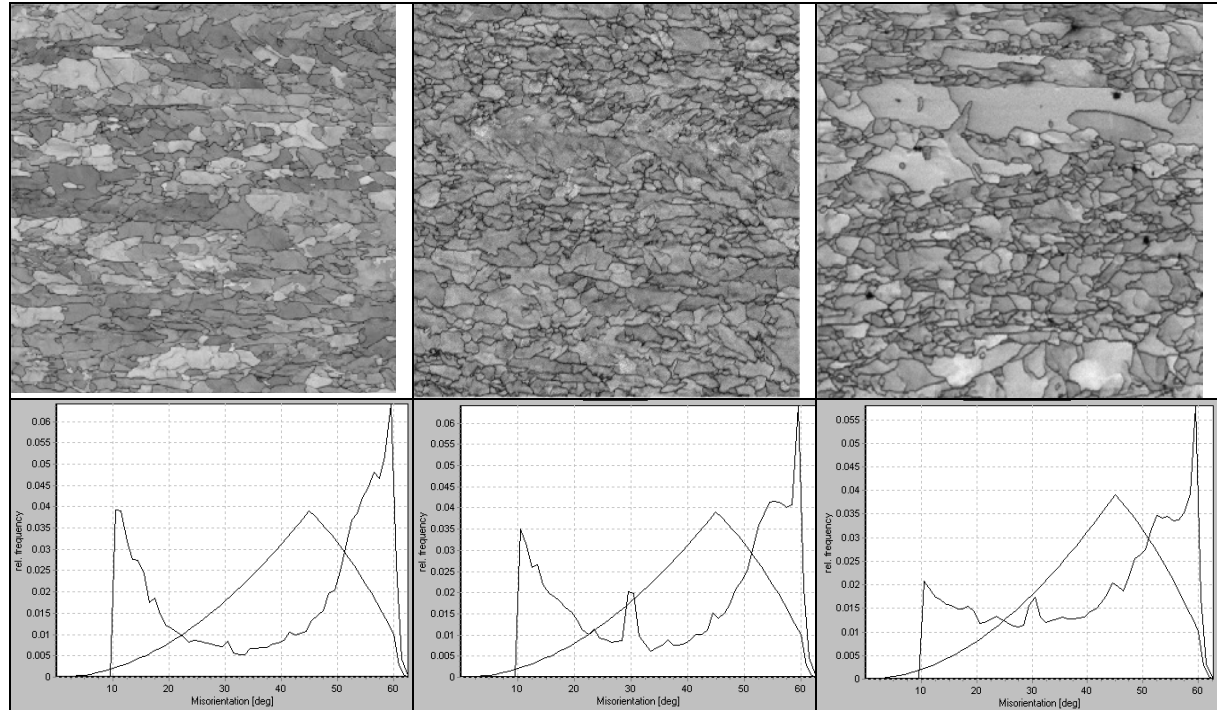


**Figure 5.1** HSLA steel. EBSD BC maps (FOW of 60  $\mu\text{m}$ ) and misorientation distributions measured by VAS (left), KIMAB (middle) and Corus (right). VAS made the analysis on the RD-TD plane in this investigation compared to RD-ND which KIMAB and Corus used.

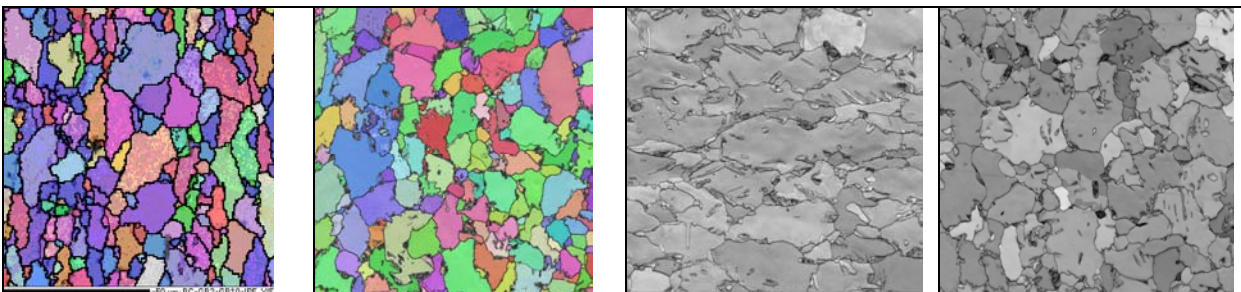


**Figure 5.2** EBSD IPF map measured by CRM, using 0.5  $\mu\text{m}$  step size (left) and the same microstructure measured by VAS using a step size of 0.15  $\mu\text{m}$  (right) (FOW = 90  $\mu\text{m}$ ).

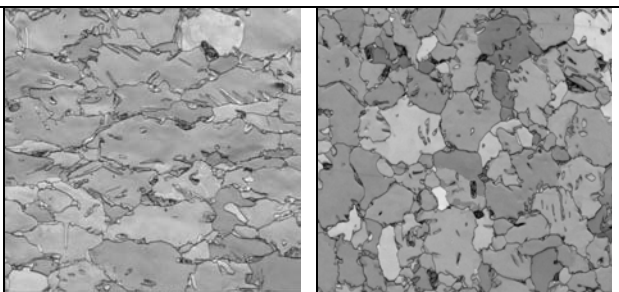


**Figure 5.3** TRIP700: EBSD BC map, measured by KIMAB using 0.05  $\mu\text{m}$  step size, (left) and VAS (right). Martensite (dark). (FOW = 35  $\mu\text{m}$ )

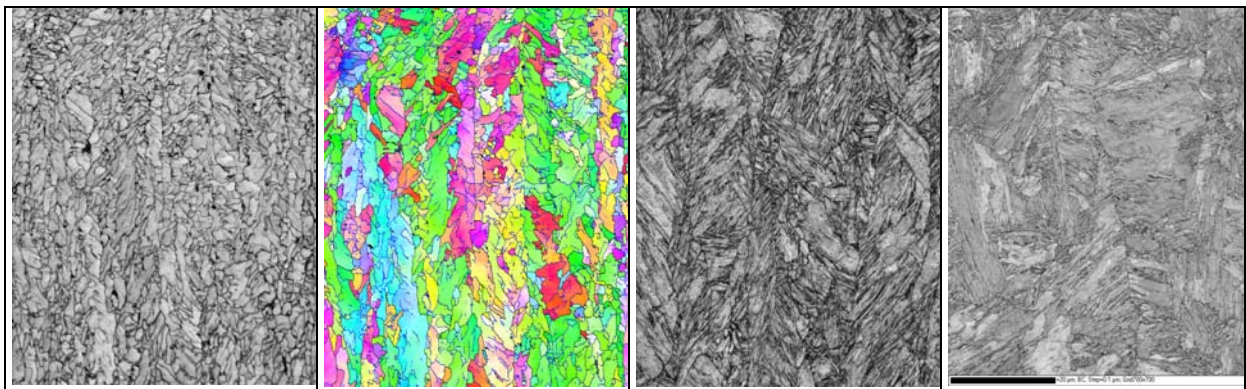


**Figure 5.4** CP800 EBSD map measured by Corus using  $0.05 \mu\text{m}$  step size. (left) BC and (right) IPF colour map (crystal orientation). Grain boundaries larger than  $2^\circ$  (blue) and  $15^\circ$  (black) are also included in IPF map) (FOW  $60 \mu\text{m}$ ).

**Figure 5.5** MS1200 EBSD map measured by Corus using  $0.05 \mu\text{m}$  step size (left) and VAS using  $0.10 \mu\text{m}$  step size (right). (FOW  $60 \mu\text{m}$ )

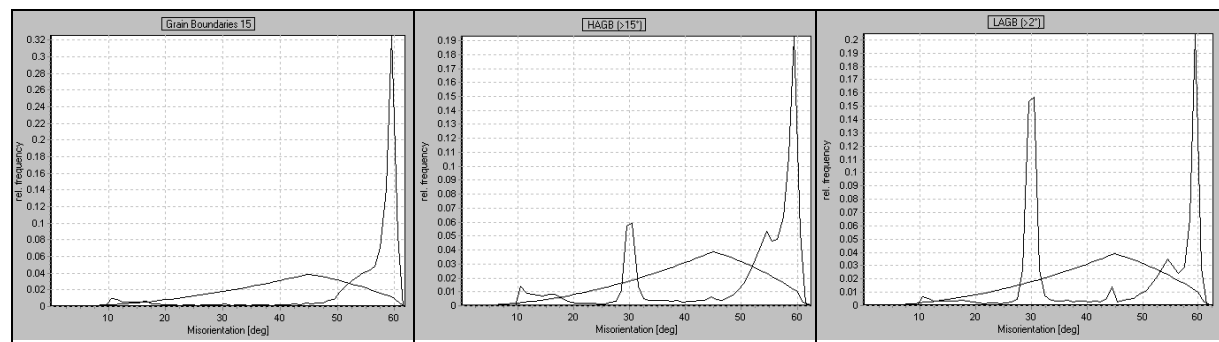


**Figure 5.6** MS1200: Misorientation distribution (cut-off at  $10^\circ$ ) derived from EBSD data measured by: VAS (left), KIMAB (middle) and Arcelor (right).

## 5.7 Task 5.6 Texture

Macro textures have been measured by TKS using X-ray diffraction for each steel type (except the lower bainite [LB] sample, where not enough material was available) at four depths through the thickness of the specimen. Both cold-rolled steels (DP600 and TRIP700) show similar textures with a relatively strong gamma ( $\gamma$ )-fibre and a weak but pronounced alfa ( $\alpha$ ) -fibre in the centre of the material. The texture in the TRIP700 steel has been found very homogeneous over the specimen thickness, while the DP600 texture was weaker near the surface, as would be expected when assuming additional shear deformation due to friction during rolling. The textures of the MS1200 and HSLA31415 steels were nearly random over the whole specimen thickness, which is typical for steels hot-rolled within the austenite regime. The HSLA grade 100 and CP1000 showed a strong, homogeneous  $\alpha$ -fibre normally associated with rolling deformation within the ferrite. This texture decreased towards the surface. The CP800 displayed a very strong partial  $\alpha$ -fibre which is mainly comprised of components near the  $45^\circ$  ND-rotated cube component, which also drops off towards the surface. The main components associated with shear were found in the zeta ( $\xi$ )-fibre ( $<110> \parallel \text{ND}$ ). Except for the DP600 steel, which shows a weak Goss component, all investigated grades show a random  $\xi$ -fibre from the centre up to near-surface region. At the very surface the CP1000 and HSLA grade 100 show texture components associated with shear deformation. All other steel show no change in the  $\xi$ -fibre.

## 6 WP 6 Chemical characterization

Task	Deliverable	D#
6.1	Chemical segregation	D24
6.2	Chemistry of inclusions/precipitates	D25
6.3	Chemistry of individual phases	D26

### 6.1 General objectives

Main objective of this work package is to formulate procedures to perform elemental mappings of banding due to macro segregation of alloying elements and to quantify the amount of band like segregation patterns. Next objective is the optimization of automated inclusions/precipitation measurements with respect to their microchemistry and size. Develop methods for qualitative and quantitative analysis of the microchemistry of individual phases is the last objective.

### 6.2 Task 6.1 Chemical segregation

In this task chemical segregation was analysed in order to assess the potential of EPMA (Electron probe micro-analyzer) technique. Two examples were chosen to verify the capacity of this technique: a DP steel and a TRIP steel.

#### 6.2.1 Chemical segregation in DP steel

In order to determine the evolution of segregation from the central line to  $\frac{1}{4}$  thickness of the sheet, EPMA analysis of C and Mn in DP steels was done. The results of electron probe microanalysis for Mn are shown in Figure 6.1. The images correspond to the Mn-distribution maps for the central zone of the specimen.

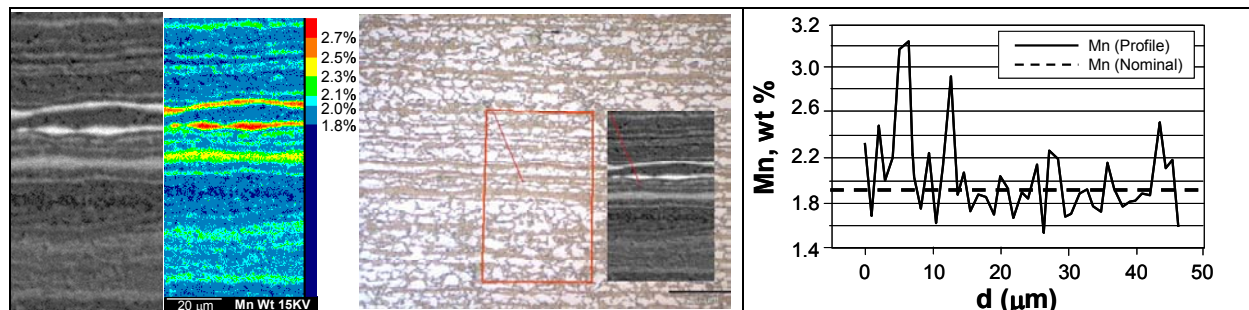


**Figure 6.1** Mn-distribution maps, Superposition of Mn map on microstructure and Mn profile in central segregation of DP steel.

It can be seen that martensite bands are located in regions with higher Mn content. In steels with low C contents, most of the pearlite is located in the high-Mn regions. Since the austenite forms from this pearlite, the martensite must also lie in regions with higher Mn content. Thus the formation of ferrite is promoted in the Mn depleted zones. Figure 6.2 shows the C and Mn distribution maps for the central zone and  $\frac{1}{4}$  thickness of the sample.

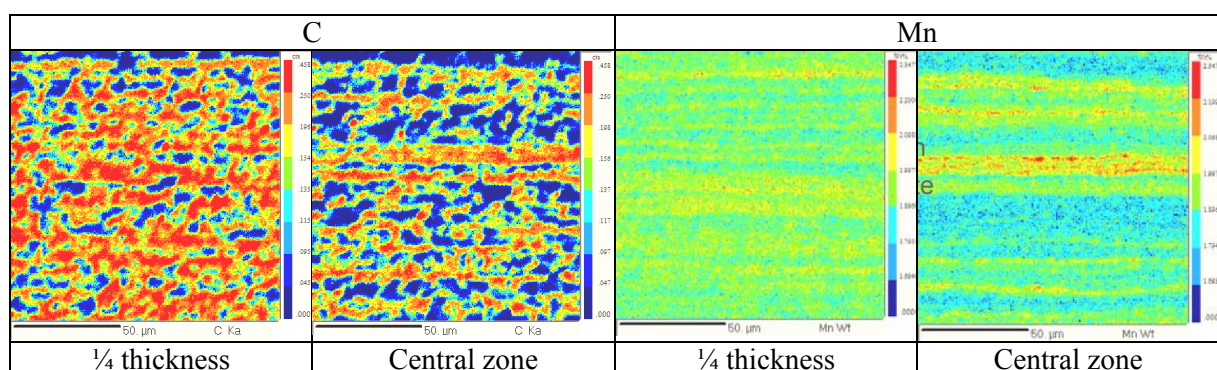


**Figure 6.2** C and Mn distribution maps of DP steel.

The comparison of C and Mn maps for central segregation and for  $\frac{1}{4}$  thickness yield to the following conclusions:

1. There is no significant difference between these two zones in terms of C content, but as the probability of C contamination is very high it's not possible to have a clear idea about C distribution, see also section 6.4.5.
2. Mn segregation is more pronounced in the central zone and these Mn-rich regions correspond to areas of martensite formation that finally result in a banded microstructure.

### 6.2.2 Chemical segregation in TRIP steel.

The objective of this study was to determine the evolution of segregation bands with the increase of soaking temperature. Studied microstructures observed in LOM are presented in Figure 6.3

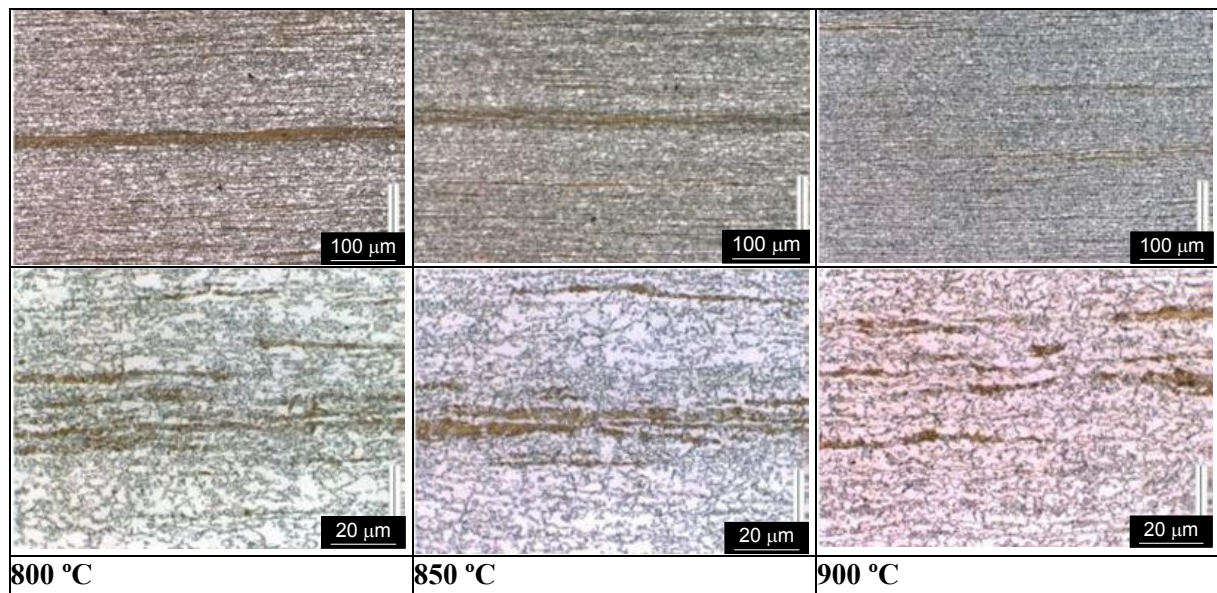


**Figure 6.3** LOM microstructures of TRIP samples with different holding temperatures.

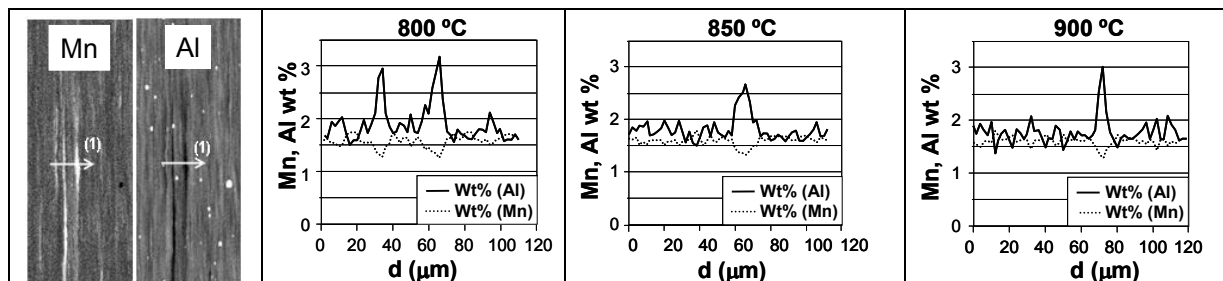


**Figure 6.4** Microprobe analysis of Al-Mn TRIP steel after soaking at different temperatures.

The microprobe analyses were done in order to observe segregation of carbon, manganese and aluminium. Figure 6.4 shows the EPMA results for samples with different holding temperature (800°C, 850°C and 900°C). On the SE images shown in Figure 6.4 white arrows indicate where the quantitative measurements were done. Table 6.1 shows the degree of segregation comparison (average/nominal content; max or min/nominal content) of C, Mn, Al for 3 different holding temperatures (HT) measured on central segregation.

**Table 6.1** Degree of segregation of C, Mn, Al for the three analyzed TRIP samples (HT 800, 850 and 890°C).

Sample	C (wt%)			Mn (wt%)			Al (wt%)		
	°C	average	min	max	average	min	max	average	min
800	1.82	0.4	3.2	1.86	0.9	2.8	0.97	0.8	1.2
850	1.59	0.7	2.5	1.34	0.8	1.7	1.03	0.9	1.1
900	1.64	0.6	3.0	1.28	0.9	1.7	1.00	0.9	1.1

By analyzing these results the following conclusions are drawn:

1. The scatter and contamination of C analysis is an obstacle for interpretation;
2. For Mn and Al the influence of temperature on central segregation was found not to be significant. However, it appears that segregation degree decreases slightly with increasing temperature. As a global conclusion it can be stated that EPMA technique permits the characterization of macro segregation of all metallic elements. The elements like C are very difficult to quantify with this technique because of their high solubility and diffusivity and of course the occurrence of carbon contamination during experiments. However, taking into account their interaction with other metallic elements (for example C will segregate mostly in the same zones than Mn) it's possible to get some qualitative information.

### 6.3 Task 6.2 Chemistry of inclusions / precipitates

The measurements performed in this project are not intended to develop a general classification scheme for all types of inclusions present in different steel grades. Instead the purpose of these measurements is to check if the general approach used to determine the chemical composition of inclusions is applicable for the different steel grades under investigation.

**Method:** EDX measurements with "Genesis" software were performed on SEM BS images at 15 KV. Elements used in quantification are C, O, Mg, Al, Zr, Nb, S, Si, Ca, Ti, Mn, Fe. Carbon, oxygen and iron are only used for identifying "dust" and iron(oxide) particles. After identification of these artifacts, a re-quantification of all the spectra is done using the following elements Mg, Al, Zr, Nb, S, Si, Ca, Ti, Mn. No light elements (<F) were used in the final quantification. The re-quantification was performed using a standard ZAF %wt correction.

**Results:** In Figure 6.5 an overview is shown of the area's which have been measured for a series of RRT materials. In this figure the size of particles is reflected by the circle diameter. The particles indicated by red circles are rejected particles based on the restriction  $C+O+Fe>85\%$ , (e.g. dust, holes or iron-oxide particles.)

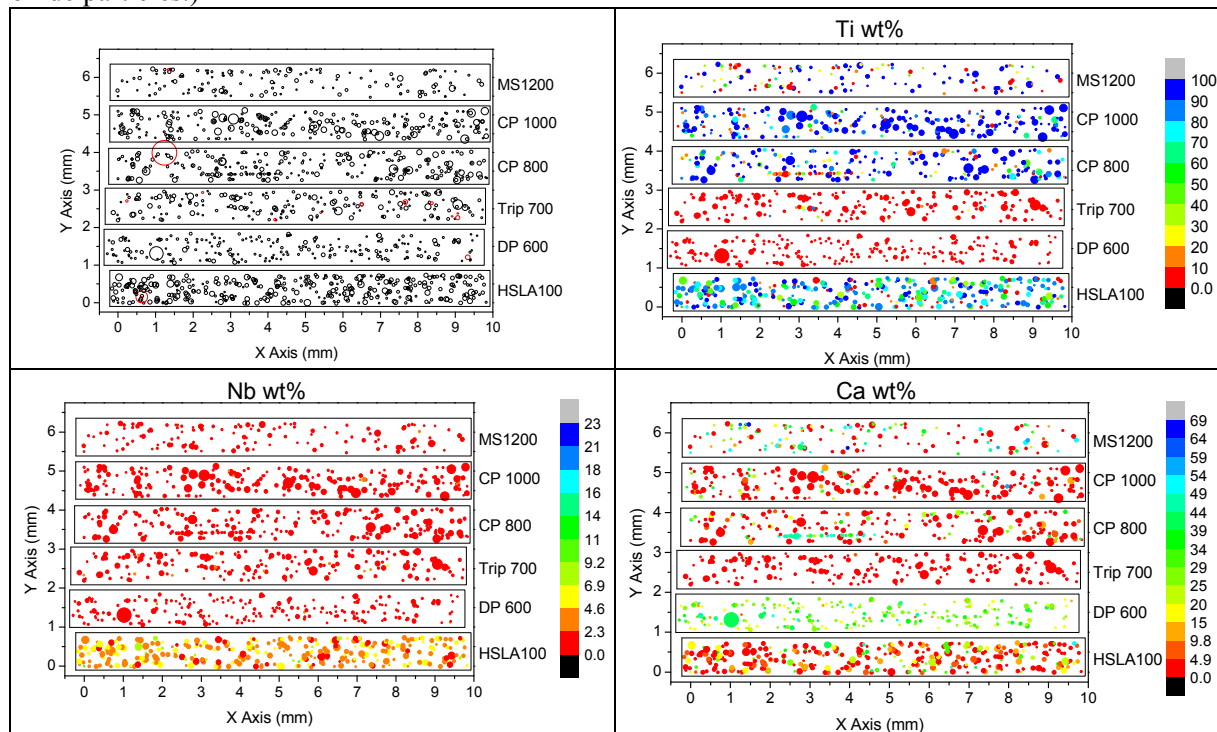


**Figure 6.5** Overview of measured particles on the RRT samples left top. When, after quantification (ZAF %wt),  $C+O+Fe>85\%$  the particle is rejected (marked with the red circles). The Ti, Nb and Ca maps represent typical elemental distributions in the samples. (note that N and O were not included in the quantification). The size of the circles is linearly related to the average diameter of the particles.

#### 6.3.1 Influence of the cut-off size of 1 or 2 $\mu\text{m}$ on some basic quantification parameters

The graphs shown in Figure 6.6 present quantified results of steel inclusions for the RRT materials. As can be seen from Figure 6.6 the influence of the cut-off size is relatively limited for the area fractions and average particle size. This influence is rather similar for all RRT samples. The biggest influence of

the cut-off size is, obviously, found in the total number of particles/area. Moreover, the influence of the cut-off size varies distinctively for the number of particles between the different RRT samples, -26% for HSLA100 ( $460_{(1\mu\text{m})} \rightarrow 340_{(2\mu\text{m})}$ ) and -56% for DP600 ( $400_{(1\mu\text{m})} \rightarrow 175_{(2\mu\text{m})}$ ).

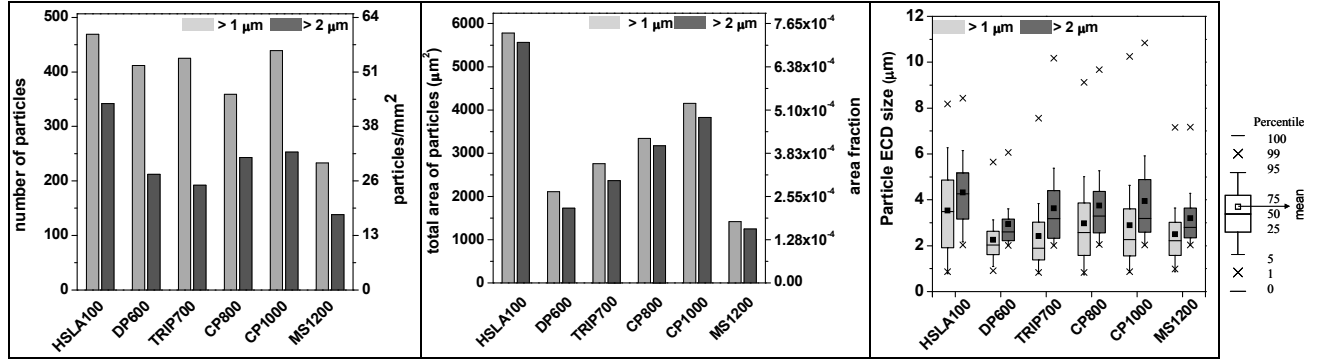


**Figure 6.6** Basic quantification results of the steel inclusions/precipitates found in the RRT materials as determined with EDX (■ particles  $> 1\mu\text{m}$ ; ■ particles  $> 2\mu\text{m}$ ).

### 6.3.2 Identification of: AlN or $\text{Al}_2\text{O}_3$ ; TiN<sub>2</sub> or TiN and $\text{Ca}_{(n)}\text{MnS}_{(1-n)}$ .

It was found that Al containing inclusions in CP1000 and TRIP700 have different chemical compositions. In the TRIP700 Al was mainly found in combination with N, whereas in the CP1000 the more common combination with O was found (see Figure 6.7). N and O are usually not included in the quantification since they can be very susceptible to interference with Ti, Mn and Fe L X-ray lines. Fortunately, for the current samples the interference with Ti, Mn and Fe L-lines was found to be relatively small and therefore N and O could be included in the quantification. The left top graph of Figure 6.7 shows a ternary graph of Al, N and O. Here it's clearly seen that the AlN inclusions are only found in the TRIP700 whereas the  $\text{Al}_2\text{O}_3$  inclusions are found in most other materials. A similar ternary graph is made for Ti, N and O. This is a more challenging graph since the Ti-L line partly overlaps with the N K-line. Nevertheless it seems justified to conclude that the Ti/N ratio is quite different for the CP1000 and can be found in the range of  $\text{Ti}_2\text{N}$  rather than in that of TiN. In the left bottom graph, where the Mn, Ca and S ternary graph is shown, it can be seen that for the DP600 there is a continuous range present for the stoichiometric ratio between Ca and Mn. ( $\text{Ca}_n\text{Mn}_{(1-n)}\text{S}$ ). This phenomenon can be explained by the coagulation of CaS and MnS inclusions.

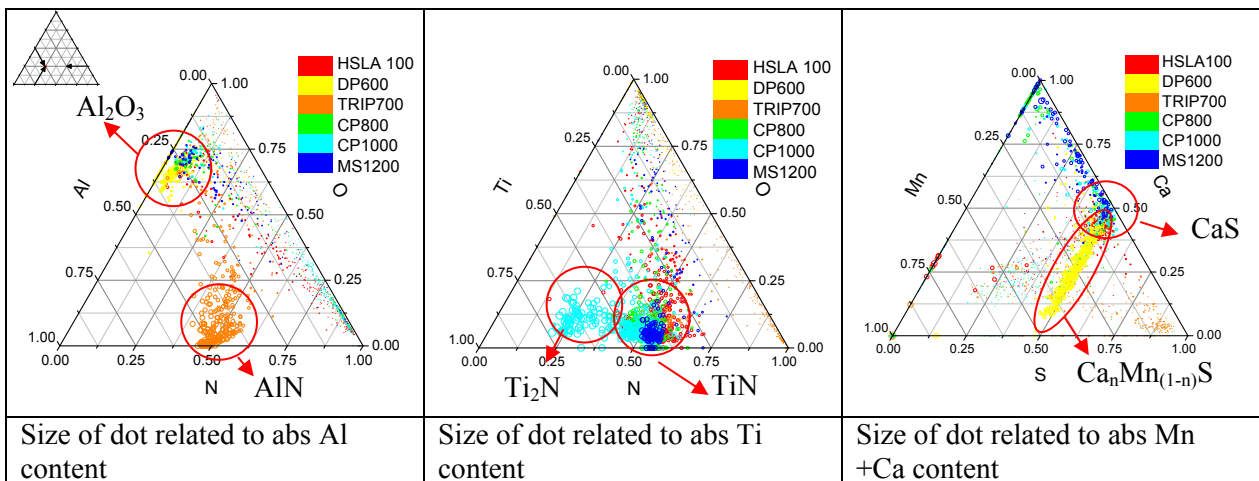


**Figure 6.7** Ternary graphs of Al, O, N; Ti, N, O and Mn, Ca and S.

### 6.3.3 Quantification and classification of inhomogeneous inclusions

A potential problem with the quantification and classification of inclusions is the fact that inclusions are often quite inhomogeneous, and consist in fact of different types of smaller inclusions, which conglomerates. A clear example of such an inclusion is shown in Figure 6.8. Since the inhomogeneity occurs in general on a small scale, there is not yet a practical solution for this problem. Therefore in this study all inclusions were treated as homogenous. Despite this problem, EDX measurement is found

effective to assess chemical composition of inclusions, and, as shown in Figure 6.8, to determine the chemical composition of heterogeneous individual inclusion.

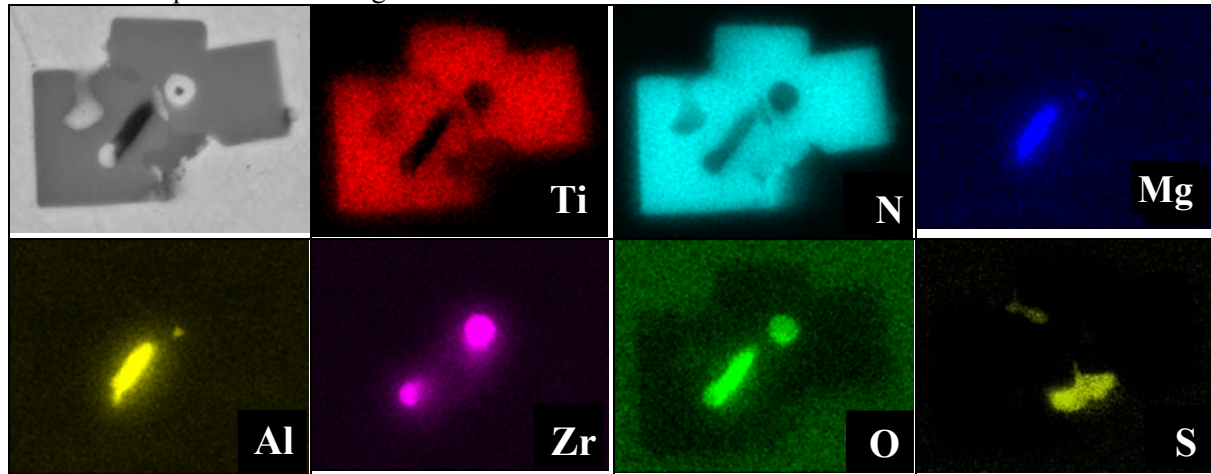


**Figure 6.8** EDX mapping of an inhomogeneous inclusion, size of the inclusion  $\approx 4\mu\text{m}$ .

### 6.3.4 Inclusion/precipitates analysis in an industrial 1200M steel (Contribution KIMAB)

INCA Feature is an automated detection and analysis system which uses a scanning-electron microscope for feature detection and measurement, and EDX microanalysis for determining the chemistry of each feature. The INCA system (Oxford Instruments) was introduced in 2003. The system includes both hardware and software with SEM-controlling functions. It is a module-based system within which the INCA Energy part for EDX analyses includes INCA Feature. Inclusion Classifier is an add-on to INCA Feature and these are jointly referred to as INCA Steel.

According to the pre-programmed schedule by the human operator, INCA Feature automatically detects the objects (e.g. inclusions, precipitates) in a mechanically polished section surface, using backscattered electrons to capture the atomic number contrast differences between object and the matrix. Image analysis is then applied to evaluate geometrical parameters such as size, shape and arrangement, whereas EDX analysis is used to resolve the chemical composition of each object. The analysis data are collected in a database which is, after the automatic run is finished, processed to classify objects according to their chemical composition and geometric parameters. Basic statistics and parameter distributions are obtained for varying chemical types identified according to their EDX spectra.

The polished surface section is divided into fields of view. Their physical size is determined by the utilized magnification. The system automation allows for, within limits, real time auto focusing and periodic compensation for possible changes in SEM-conditions.

Several parameters are to be used to control INCA Feature. On the microscope level accelerating voltage, working distance and probe current are important for the EDX analysis.

INCA Feature parameters for optimizing the efficiency and resolution of the EDX analysis are:

- Type of quantification result (i.e. normalized weight-% and un-normalized apparent concentrations),
- Acquisition speed, [counts/s], and dead time [%],
- Energy resolution range (process time),
- Time to collect EDX spectrum per object, [s/object],
- Lateral resolution limit for the spot analysis, related to the acceleration voltage and probe current levels.

Parameters related to image capturing and processing are:

- Image resolution [pixels],
- Time to scan for an approximate positioning of features, [ $\mu\text{s} / \text{pixel}$ ],
- Time to scan for a detailed positioning of features, [ $\mu\text{s} / \text{pixel}$ ].

The magnification determines the corresponding physical size of each pixel as related to the image resolution. The size of an object is calculated from the number of pixels within the object. The higher the magnification and the higher the image resolution, the smaller the physical size of each pixel and the more accurate the size of the object. The combination of magnification and image resolution also

sets a limit regarding smallest detectable object. The lateral resolution limits for the spot analysis with EDX sets a size limit for chemical type identification of the smallest object.

#### 6.3.4.1 Experimental settings

The analysis has been performed on Field Emission Gun SEM JSM 7000F (Jeol) using the EDX detector PentaFETx3 controlled by INCA Feature system (Oxford Instruments). Parameter settings used during analysis: Accelerating voltage 10 kV; Working distance 10 mm; Probe current 9 nA; Image magnification 2500x; Pixel size (ECD) 0.024  $\mu\text{m}$ ; Minimum object size 9 pixels (= 80 nanometres); Image size (single image) 2048 x 1408 px; Number of images 568; Total scanned area 0.97  $\text{mm}^2$ .

#### 6.3.4.2 Results

In Table 6.2 the summarized classification results are presented together with basic morphologic results. From this study it was concluded that inclusions/precipitates larger than  $\sim 0.1 \mu\text{m}$  can be measured with high enough accuracy to be properly classified.

**Table 6.2 Basic statistics results for sample 1200M RD/ND section.**

rank	Area fract.	numb. (%)	numb density	ECD*		length		Sum length	Aspect ratio		Maximum ECD* size in % of population					
				mean	max	mean	max		mean	max	10 %	25 %	50 %	75 %	90 %	100 %
All inclusions	0.102	1982	2049.3	0.3	17.3	0.5	25.1	1087.3	2.4	20.7	-	-	-	-	-	-
a. oxides	0.0414	50	51.7	1.0	17.3	1.7	25.1	87.9	1.7	5.2	0.08	0.15	0.3	0.4	0.5	17.3
b. sulfides	0.0051	540	558.3	0.3	2.5	0.5	14.4	279.2	2.5	20.2	0.08	0.15	0.3	0.4	0.5	2.5
c. Complex ox-sulph	0.0396	43	44.5	2.7	9.1	4.9	19.0	218.7	2.4	4.8	0.7	1.25	2.45	3.9	4.9	9.1
d. nitrides	0.0074	469	484.9	0.2	5.5	0.3	7.1	164.9	2.4	20.4	0.1	0.15	0.3	0.4	0.5	5.5
e. carbo nitrides	0.0082	880	909.9	0.2	3.0	0.4	5.9	336.7	2.3	20.7	0.1	0.15	0.3	0.4	0.5	3.0
a+b+c	0.0861	633	654.5	0.5	17.3	0.9	25.1	585.8	2.4	5.2	0.08	0.15	0.3	0.45	0.8	17.3
d+e	0.0155	1349	1394.8	0.2	5.5	0.4	5.9	501.5	2.4	20.7	0.08	0.15	0.3	0.4	0.5	5.5

\*ECD = equivalent circle diameter; (minimum ECD for all inclusions 0.080  $\mu\text{m}$ )

## 6.4 TASK 6.3 Chemistry of individual phases

This task focuses on analytical measurements of the micro-chemistry of individual phase constituents with various analytical techniques, such as Electron Probe Micro Analysis (EPMA) and Nano Secondary Ion Mass Spectrometry (Nano-SIMS). In particular carbon is of interest in this context, since it is of crucial importance in relation to issues such as austenite  $\rightarrow$  martensite phase transformation, retained-austenite stability in TRIP steels, and the morphological and mechanical properties of martensite islands in DP/TRIP steels. Arcelor has focused primarily on Nano-SIMS analyses in order to investigate re-partitioning of carbon in martensite islands in DP steel as a result of tempering and boron state with different alloying additions. The work reported by Arcelor has been carried out in collaboration with the Gabriel Lippmann Center (Department Science Analysis of Materials) at Luxembourg. Efforts of Corus have been aimed at EPMA analyses of the micro-chemistry of martensite islands in the RRT DP600 and TRIP700 microstructure.

#### 6.4.1 Principles of Nano-SIMS<sup>29</sup>

SIMS is based upon the sputtering of a few atomic layers from the surface of a sample, induced by a primary ion bombardment composed of  $\text{Cs}^+$  and  $\text{O}^-$  ions. The primary ion impact triggers a cascade of atomic collisions. Atoms and atomic clusters are ejected. During the ejection process, some of them are spontaneously ionized. These secondary ions are separated according to their mass, and an image containing quantitative information is formed for a selected mass. The Nano-SIMS 50 provides the capability of recording simultaneously five mass images together with a high mass separation ( $\text{Mass}/\text{dMass} > 5000$ ) at high transmission (70%) and a high spatial resolution (50 nm). In addition, the short working distance of the probe forming lens/extraction (see Figure 6.9) ensures a smaller spot size for a given beam current and higher collection efficiency compared to conventional SIMS. Finally the co-axial geometry also minimizes shadowing and topography effects.

From reference samples containing martensite and ferrite with a known carbon content, it is possible to establish a calibration curve that gives a linear relationship between secondary ionic intensities of  $^{12}\text{C}_2$  and carbon content.<sup>[25]</sup>

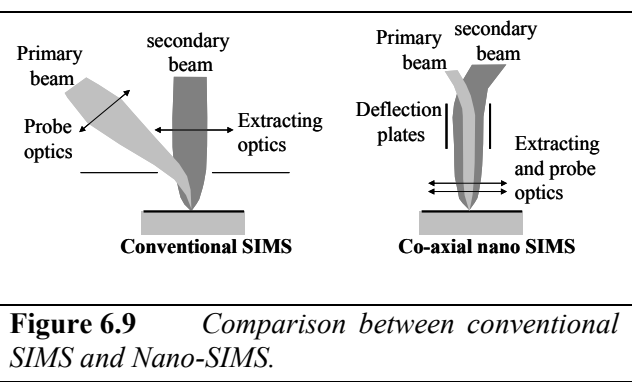


**Figure 6.9** Comparison between conventional SIMS and Nano-SIMS.

#### 6.4.2 3D-analysis of bainitic structures in TRIP steel

The principle of 3D-reconstruction of microstructure is based on acquisition with Nano-SIMS (depth resolution of a few nm and a lateral resolution of a few hundred nm) by tomography technique. This technique consists in recording series of 2D-SIMS scans during the sample sputtering induced by  $\text{Cs}^+$  bombardment. Due to the strong difference in carbon content between the ferritic matrix and M/RA islands, it is possible to image the microstructure of multi-phase steels by acquiring ion maps of the carbon distribution. The final depth of analysis (500 nm) was determined using an Atomic Force Microscope. One thousand images were recorded through 500 nm depth.

On a sample containing evidence for the presence of both lath- and granular-bainite nano-SIMS depth profiles were recorded, see Figure 6.10.

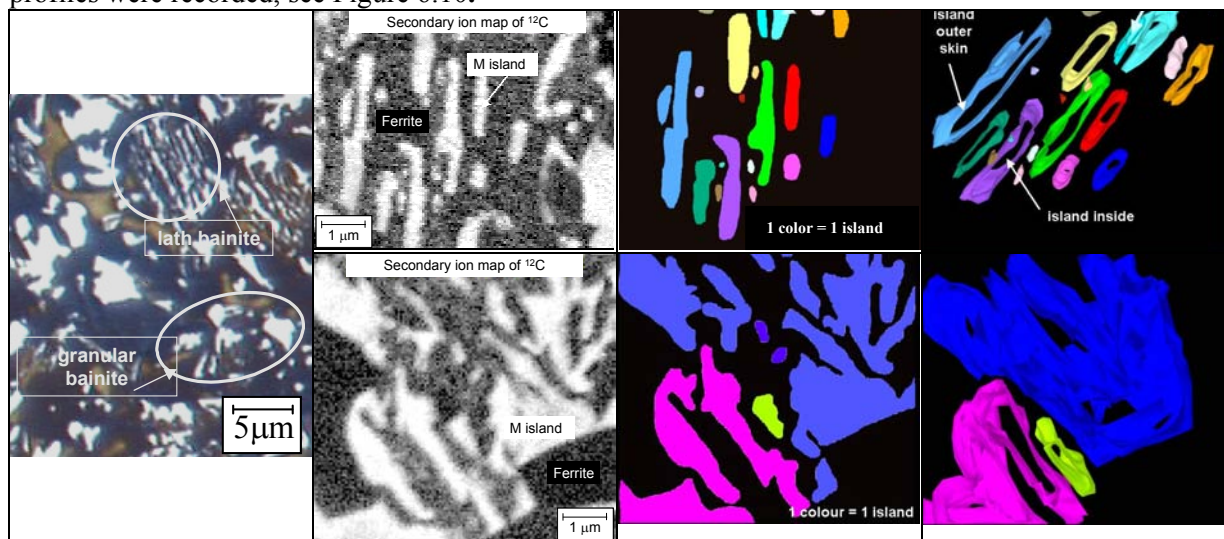


**Figure 6.10** (Left) LOM image of a sample containing both lath- and granular bainite. Nano-SIMS  $^{12}\text{C}$  map based 3D-reconstructions of lath-shaped bainite (top-series) and granular bainite (bottom-series). The 3D reconstruction shows only the perimeter “skin” of identified islands.

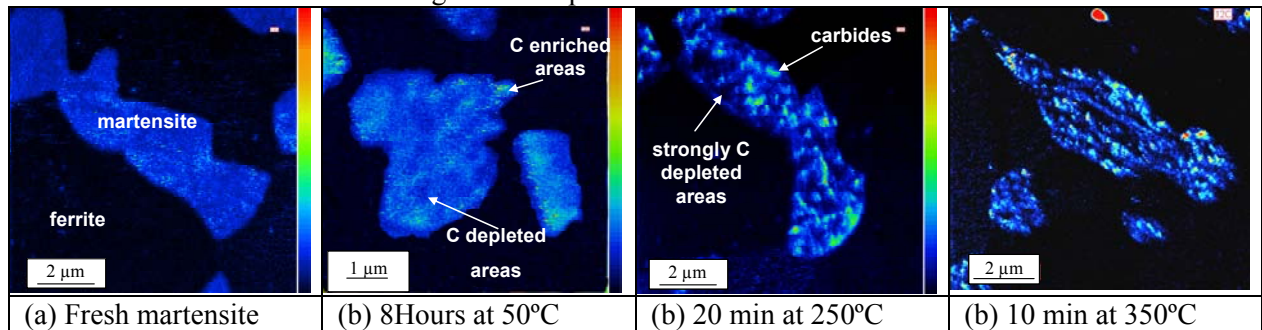
Through 500 nm depth, in zones with lath shaped bainite, 3D-reconstruction (see Figure 6.7) shows no strong evolution of microstructure, plate shaped M/RA islands and connections exists only between close islands. On the contrary, in zones with granular bainite, 3D-reconstruction (see Figure 6.8) shows

a strong evolution of microstructure, complex shape of M/RA islands and connections that are established over long distances.

#### 6.4.3 SIMS study of carbon re-partitioning during tempering of martensite in DP steel

In Figure 6.11 an example of Nano-SIMS is presented, where the evolution of carbon repartition in martensite is depicted during different steps of tempering treatment in DP steel:

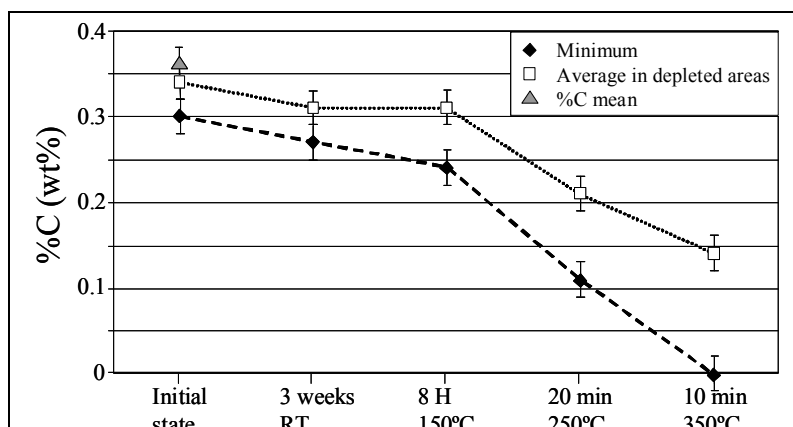
- In the fresh state carbon distribution is found to be homogeneous. (samples were produced in such a way no self tempering in martensite occurred)
- Tempering at 150°C for 8 hours: small changes in the carbon distribution in the martensite are detected. Carbon probably moves toward twin and/or lath boundaries,
- Tempering at 250°C for 20 min.: strong variations of free carbon content in martensite are measured, due to carbide precipitation and growth associated with C depletion of the martensite matrix.
- Tempering at 350°C for 10 minutes: leads to intense carbon concentration on lath boundaries and/or twin boundaries and shows strong carbon depletion inside martensite laths.



**Figure 6.11** Carbon re-partitioning in martensite islands for different tempering steps.

The results obtained in this study are very useful to describe martensite evolution for different tempering conditions and may allow understanding and controlling of this phenomenon. One of the benefits of Nano-SIMS is that it produces a map of carbon repartitioning at a very high resolution. It is a prime necessity to validate Nano-SIMS results from EELS (Electron Energy Loss Spectroscopy) measurements.

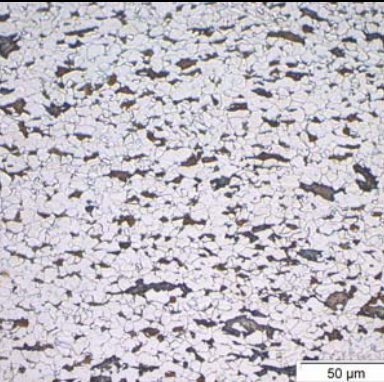
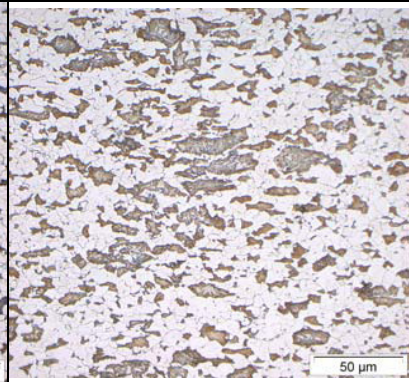
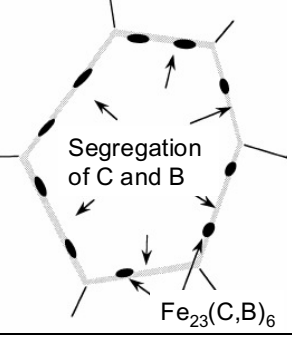
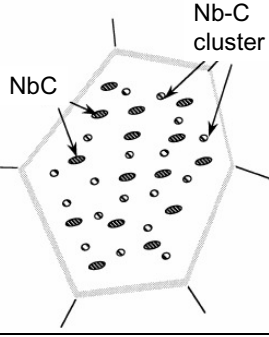
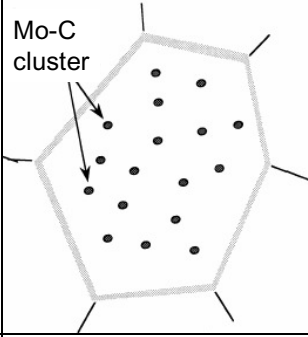
Figure 6.12 depicts the evolution of carbon content, from the initial state (0.35% in average). The average carbon content in depleted areas decreases with increasing tempering temperature down to 0.15% at 350°C. In some areas, carbon content decreases down to 0 (below detection limit) as in the surrounding ferritic matrix. This decrease in C content provides evidence of martensite softening, which explains part of the improvement in damage resistance.



**Figure 6.12** Quantitative carbon evolution in martensite islands for different tempering steps as measured by means of EELS.

#### 6.4.4 Investigations on boron state

Boron (B) is added to carbon steels to improve the robustness of thermo-mechanical processes and to improve its mechanical properties like hardenability, resistance to intergranular fracture, weldability, etc. Efficiency of B addition also depends on its actual state in the microstructure. For example, to be efficient during annealing, the B state has to be controlled during hot-rolling process, particularly to avoid the formation of  $\text{Fe}_{23}(\text{B},\text{C})_6$  precipitates. One way, mentioned in literature<sup>[30]</sup>, consists in addition of micro-alloying elements, like Nb or Mo (Figure 6.13), which limit diffusion of carbon towards austenite grain boundaries.

B	B + Nb	B + Mo
		
		
Formation of $\text{Fe}_{23}(\text{C},\text{B})_6$ + segregation of B	Segregation of B Suppression of C to GB	Segregation of B Suppression of C to GB

**Figure 6.13** Schematic diagram showing mechanism for suppression of  $\text{Fe}_{23}(\text{B},\text{C})_6$  formation due to combined addition of Nb and B or Mo and B, according to T. Hara et.al.<sup>[30]</sup> For all three grades a typical microstructure obtained after annealing and quenching at 600°C is shown.

Investigations were made on hot-rolled 0.08wt% C, wt2% Mn, 1.5 wt % Si steel grade with  $2.10^{-3}$  wt% B without and with addition of Nb or Mo. After an adapted thermo-mechanical treatment (with quenching at 600°C), obtained microstructures (see Figure 6.13) consisted of ferrite + martensite for grade with B alone or with B + Nb, and only of martensite for grade with B + Mo. Investigations with NanoSIMS were made to understand the effect of B addition combined or not with micro-alloying elements. They consisted of using:

- A combination of  $^{11}\text{B}$  and  $^{11}\text{B}^{12}\text{C}$  ion maps to spot  $\text{Fe}_{23}(\text{B},\text{C})_6$  precipitates,
- $^{12}\text{C}$  ion maps for the martensite islands location,
- $^{11}\text{B}^{16}\text{O}$  ion map to draw austenitic and ferritic grain boundaries.

The combination of the obtained maps gives the opportunity to understand the migration behaviour of boron (B), see Figure 6.14. For the addition of exclusively B (see also Figure 6.13 left image), the form in which B is present in microstructure is mainly in  $\text{Fe}_{23}(\text{B},\text{C})_6$  precipitates located at the ferrite grain boundaries.

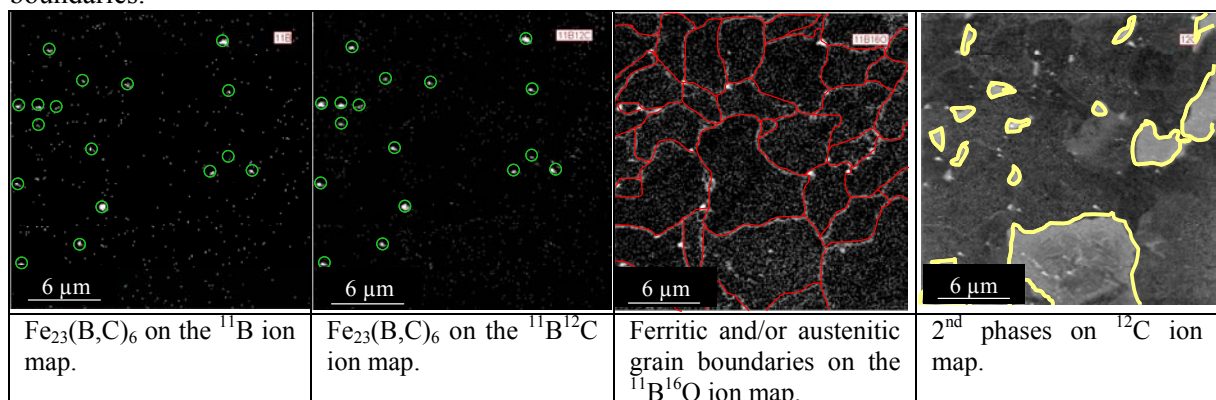


**Figure 6.14** Location of  $\text{Fe}_{23}(\text{B},\text{C})_6$  precipitates (green circles) in relation to the ferrite and/or austenite grains (red lines) and 2<sup>nd</sup> phase areas (yellow line) by combination of  $^{11}\text{B}$ ,  $^{11}\text{B}^{12}\text{C}$ ,  $^{11}\text{B}^{16}\text{O}$  and  $^{12}\text{C}$  ion maps for the “alone” boron grade.

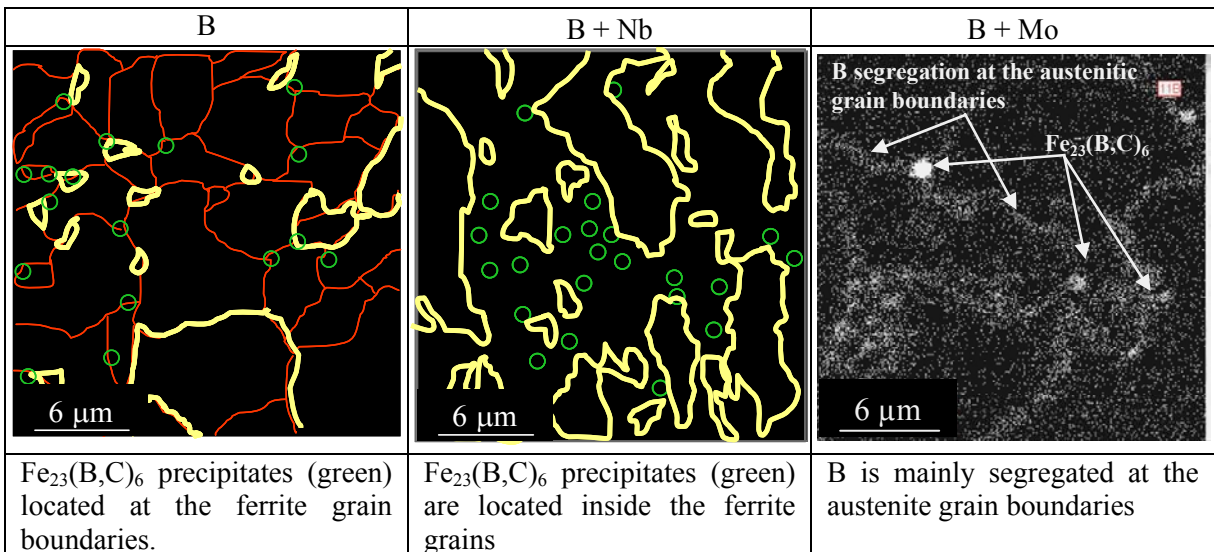


**Figure 6.15** Location of  $\text{Fe}_{23}(\text{B},\text{C})_6$  precipitates with left: no addition, middle: Nb addition and right: Mo addition. Yellow (M area) red ferrite/austenite grainboundary, green  $\text{Fe}_{23}(\text{B},\text{C})_6$  precipitates.

Nb micro-alloying is efficient to control C diffusion and to avoid precipitation in austenite, but not enough to avoid it in ferrite (Figure 6.15 A). Mo addition allows a good control of  $\text{Fe}_{23}(\text{B},\text{C})_6$  in austenite despite the strong boron segregation at austenite grain boundaries, as shown (Figure 6.15 B) by <sup>11</sup>B ion map (stored at high analytical resolution to the detriment of the lateral resolution).

#### 6.4.5 Quantification of the micro-chemistry of martensite and ferrite in DP and TRIP

Electron Probe Micro Analysis (EPMA) in combination with Wavelength Dispersive X-ray (WDX) detection was exploited as a tool to map chemical segregation and to quantify the micro-chemistry of individual phase constituents in a multi-phase microstructures. Corus has focused on the RRT DP600 and TRIP700 microstructure. Comparison between the DP600 and TRIP700 microstructures (Figure 6.16) shows that topography clearly visible in the TRIP700 microstructure surrounding M/RA islands is not observed for the investigated DP600 microstructure. This difference can be explained in terms of a difference in the degree of segregation of alloying elements between both grades as a result of intercritical annealing.<sup>[31]</sup>

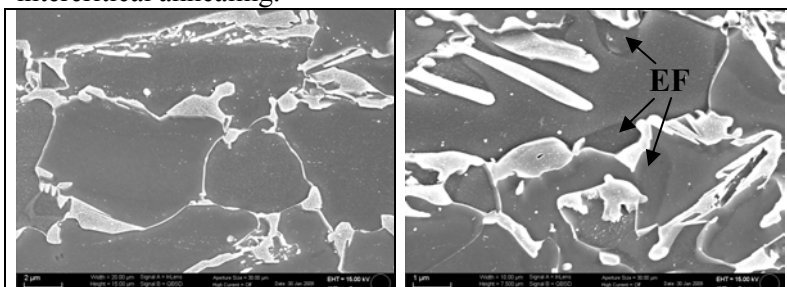


**Figure 6.16** SEM inlens images of DP600 (FOW 20  $\mu\text{m}$ ) (left) and TRIP700 (FOW 10  $\mu\text{m}$ ) (right) (electropolished).

Figure 6.17 and Figure 6.18 show EPMA mappings of the DP600 and TRIP700 alloying elements. In both cases, carbon (C) distribution provides a fingerprint of second phase constituents. Manganese (Mn) and silicon (Si) mappings for the DP600 grade reveal relatively little segregation. However, Mn and Si mappings – as well as the

aluminium (Al) mapping – for the TRIP700 reveal evidence of a high degree of micro segregation. The Mn mapping shows a continuous network of rich regions, corresponding with the ferrite grain boundary skeleton. Si and Al mappings show a complementary distribution, with enhanced levels confined to intercritical (old) ferrite. These segregation profiles reflect a correlation between intercritical transformation kinetics and diffusion.<sup>[31]</sup> Regions high in Mn correspond with austenite in the intercritical regime. A subsequent high quenching rate from the two-phase field will leave no opportunity for diffusion of elements apart from carbon and will maintain Mn-rich zones, which partially will transform to epitaxial ferrite (EF) during a relative slow cooling process in case of the TRIP700 grade. This explains the difference in composition with respect to Mn, Si, and Al between

epitaxial (new) and intercritical (old) ferrite in the TRIP700 microstructure. It is known that alloying elements may have a strong impact on etching response, which in turn indicates that the reflection of topography in ferrite surrounding M/RA visible in SE and EBSD images provides a fingerprint of epitaxial ferrite.<sup>[32]</sup>

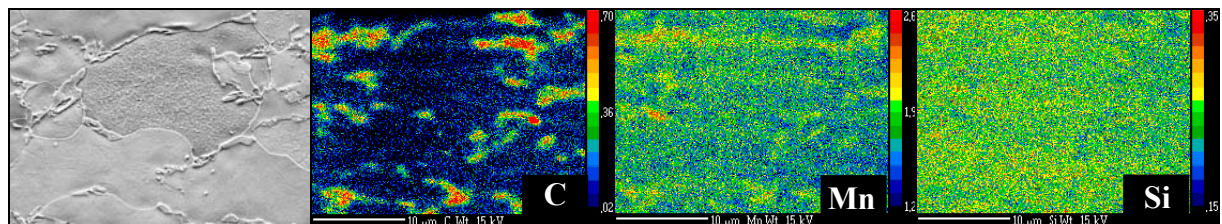


**Figure 6.17** DP600: quantitative EPMA mappings of C, Mn, Si together with the SE image (SE image was taken after the EPMA mapping (15KV, FOW 30  $\mu\text{m}$ ), ionbeam cleaning and mild electropolishing.

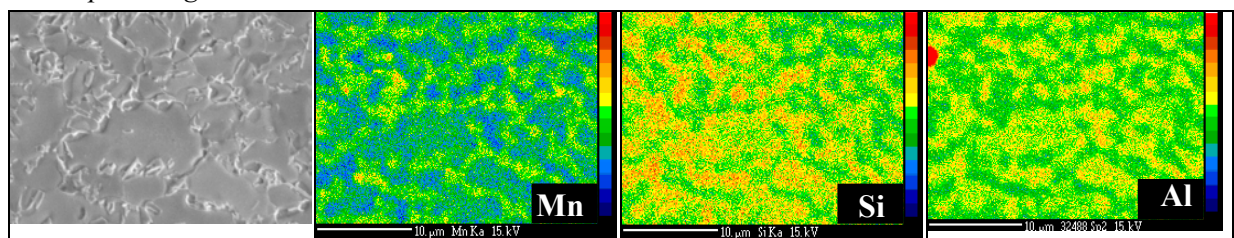


**Figure 6.18** TRIP700: quantitative EPMA mappings (15KV, FOW 30  $\mu\text{m}$ ) of Mn, Si, and Al.

#### Influence of surface topography on C quantification

It is known that slight topography, induced by mild electrolytic polishing, may have a profound impact on the quantification of light elements. Moreover, even though a cold-finger and oxygen-jet were used, carbon deposition on the sample surface during measurements could not be avoided. C-maps were corrected for beam-induced carbon deposit by subtracting the value of C-wt% measured on ferrite grains (which have nominally less than 0.008 wt% carbon)<sup>[25]</sup>. A correction of 0.7-0.8 wt% carbon was found to be necessary, which makes this carbon quantification method vulnerable for errors, see also section 6.2.1. From previous studies it was found that for electropolished samples, with pronounced topography, carbon *background* maps reveal the second-phase microstructure, indicating that topography contributes significantly to the carbon signal. For carbon background maps of standard polished samples this effect was absent. Main drawback on the measurement on no-topography samples is they are “in the blind” since there are hardly any microstructural features observed. Corus has investigated therefore the impact of *mild* topography in DP and TRIP microstructures on carbon quantification in the second phase areas. Mappings were made of standard prepared samples (no topography). After ion-beam cleaning -to remove the carbon deposits- and electro-polishing (mild topography), the samples were remeasured Figure 6.19. As can be seen from the carbon background maps, this mild topography has a minor influence on the carbon signal. By making the aforementioned corrections, similar quantitative results for carbon can be obtained (see Table 6.3). Similar results were obtained for carbon measurements on TRIP samples.

It is concluded that for EPMA measurement on specific microstructural areas, which can be only visualized by mild etching, a mild topography has a minor influence on the carbon quantification. The topography impact on quantification results can be checked with carbon background maps. In all other case measurements on samples with no topography is preferred.

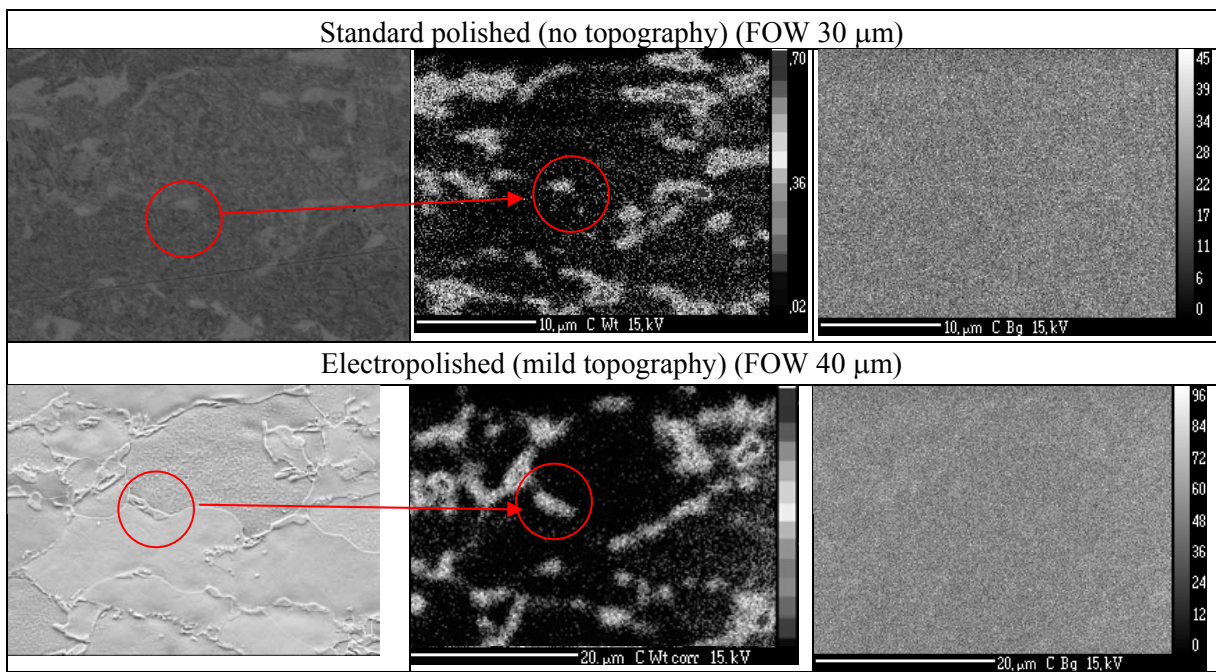


**Figure 6.19** DP600 SEM image (BS, 15KV) of standard polished and after mild electropolished (SE, 5 KV) together with EPMA carbon mappings and carbon background mappings.

Table 6.3 Quantified EPMA results, averaged over the total analyzed field.			
		EPMA	
element	Bulk	Standard polishing	Electro polishing*
C	0.102	0.14	0.12
Mn	1.641	1.72	1.68
Si	0.251	0.25	0.27
Al	0.035	0.04	0.04
Cr	0.575	0.61	0.60

\*mild topography

## 7 WP7 Nano scale mechanical testing

Task	Deliverable	D#
7.1	Development of a nano-indentation approach	D27
7.2	Correlation between nano hardness and phase (constituent) properties	D28
7.3	Retained austenite stability	D29

### 7.1 General objective

The main objective of this work package is to investigate the merits and limitations of nano-indentation for the evaluation of nano-hardness of phase constituents in DP and TRIP microstructures. This investigation has lead to recommendations for a best practice for nano-indentation of AHSS microstructures. Additionally, nano-indentation has been used to evaluate the nano-hardness range of phase constituents in DP and TRIP microstructures. An empirical correlation has been formulated to establish a link between nano-hardness as measured with a Berkovich indenter and micro-hardness measurement with a Vickers indenter. This has opened a gate to link nano-hardness to local chemical composition for ferrite and martensite. With the aid of EBSD-guided nano-indentation, the characteristics of load-displacement curves of retained-austenite in TRIP steel has been investigated and compared with literature. Experimental evidence is presented that indentation-induced phase transformation of retained-austenite to martensite provokes perturbations and/or discontinuities in the load-displacement curve during the unloading stage. Finally, the relative stability of lath- versus block-shaped retained-austenite is discussed.

### 7.2 Task 7.1 Development of a nano-indentation approach

#### 7.2.1 Conventional nano-indentation versus Continuous Stiffness Method

A promising method to determine the hardness of phase constituents in a multi-phase microstructure and to observe its dynamic response to local deformation is nano-indentation testing. However, to appreciate its merits and limitations in more detail, several issues have been considered, including: (1)

conventional nano-indentation testing versus Continuous Stiffness Measurement, (2) type of indenter, (3) resolution and (4) sample preparation. These aspects have been addressed as part of this project and are briefly described here. Parts of this work combined with aspects of the chemical analysis described §6.4.5 have been published in reference.<sup>[33]</sup>

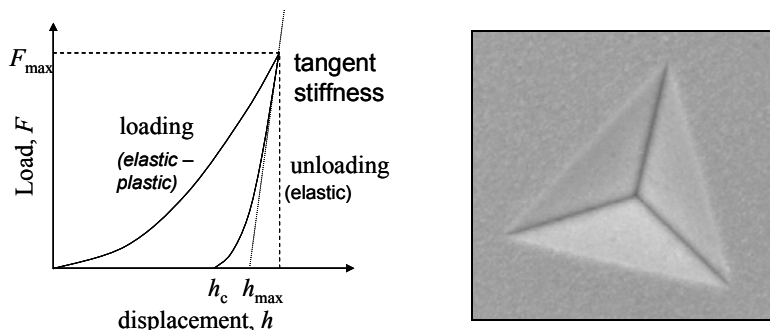


**Figure 7.1** (left) Load-displacement curve and (right) residual impression of a Berkovitch indenter.

#### 7.2.1.1 Conventional nano-indentation versus Continuous Stiffness Measurement (CSM)

Figure 7.1 (left) shows schematically a typical load-displacement curve. As the indenter is driven into the material, both elastic and plastic deformations cause the formation of a hardness impression (Figure 7.1 (right)) conforming to the shape of the indenter to some contact depth,  $h_c$ . As the indenter is withdrawn, only the elastic portion of the displacement is recovered. Some important quantities are the maximum peak load  $F_{max}$  and displacement  $h_{max}$ , the residual depth after unloading  $h_c$  and the slope of the initial portion of the unloading curve,  $S = dF/dh$ , which is known as the elastic stiffness of the contact.

The hardness of the test surface ( $H$ ) is determined using the equation

$$H = \frac{F_{\max}}{A(h_c)} \quad \text{equation 7-1}$$

where  $F_{\max}$  is the maximum load applied to the test surface and  $A(h_c)$  is the projected contact area. This projected contact area  $A$  depends on  $h_c$ , which can be estimated using

$$h_c = h_{\max} - \varepsilon \frac{F_{\max}}{S} \quad \text{equation 7-2}$$

where  $h_{\max}$  is the maximum displacement,  $F_{\max}$  is the maximum load applied to the test surface,  $S$  is the stiffness during unloading and  $\varepsilon$  is a constant which depends on indenter geometry (0.75 for Berkovich and Vickers indenters).

The most widely used method for calculating the contact area  $A$  was developed by Oliver and Pharr<sup>[34]</sup>. The Oliver-Pharr data analysis procedure begins by fitting load-displacement data acquired during unloading to the power-law relation

$$F = B(h - h_c)^m \quad \text{equation 7-3}$$

where  $F$  is the load applied to the test surface,  $h$  is the displacement,  $B$  and  $m$  are empirically determined fitting parameters, and  $h_c$  is the residual displacement after complete unloading. The unloading stiffness,  $S$ , is then established by analytically differentiating this equation and evaluation at the maximum depth of penetration,  $h = h_{\max}$ , or

$$S = \frac{dF}{dh}(h_{\max}) = Bm(h - h_c)^{m-1} \Big|_{h_{\max}} \quad \text{equation 7-4}$$

Finally, the projected contact area  $A$  is calculated by evaluating an empirically determined area function at contact depth,  $h_c$ :

$$A = f(h_c) \quad \text{equation 7-5}$$

This area function, also known as the shape function or tip function, relates the cross-sectional area of the indenter to the distance from its tip.

In order to calculate the hardness ( $H$ ), one must know the elastic stiffness of the contact,  $S$ . Traditionally,  $S$  is determined from the slope of the load-displacement curve acquired at the beginning of the unloading stage. However, such a calculation allows one to determine  $S$  (and thus  $H$ ) at the maximum penetration depth only. An alternative method is the *Continuous Stiffness Measurement* (CSM) option. This method allows a continuous measurement of  $S$  during loading and not just at the point of initial unloading. This is accomplished by superimposing a small oscillation on the primary loading signal (typically 2nm at 45Hz) and analysing the resulting response of the system by means of a frequency-specific amplifier. *With a continuous measure of  $S$ , one obtains hardness as a continuous function of surface penetration.* This has a major advantage over conventional nano-indentation testing: it enables an evaluation of the steady-state region for the hardness as a function of displacement and avoids any impairing interference from indentation size effect<sup>[35]</sup>. At the same time the CSM method enables an evaluation of the influence of surrounding constituents on the nano-hardness of a region of interest. This interaction may become more significant as the interaction volume beneath the indenter increases (i.e., decrease in resolution) with increasing load.

The systematic error for nano-hardness measurements has been determined based on nano-indentation on fused silica. This study yielded an average nano-hardness of 9.4 GPa for fused silica with a standard deviation of 0.05, i.e., a 99%-error margin of 0.15 GPa. A study by Kopernik et al.<sup>[36]</sup> reported a standard error of 0.157 GPa for nano-hardness measurements on a CMn steel with a nano-hardness of 2.01 GPa for ferrite.

### 7.2.1.2 Indenter type and resolution

Indenter shape has a strong influence on indentation behaviour<sup>[37]</sup>. In general, two classes of indenters can be distinguished: (1) conical/pyramidal indenters and (2) spherical indenters. Pyramidal indenters, such as Cube-corner, Berkovich, Vickers and Knoop indenters are sharp and offer a relative high lateral resolution, whereas spherical indenters are blunt and have a limited lateral resolution. The most frequently used indenter for nano-indentation measurements is the Berkovich indenter. This indenter

has the advantage that it has the same geometry as a Vickers indenter and that it has a specific relation with micro-Vickers, which in principle facilitates a comparison between both types of measurements. Regarding resolution, this is dependent on applied load or indentation displacement. A rule of thumb is that the resolution is equal to 10–15 times the indentation depth. This implies a resolution of circa 0.3–0.6 µm for relative shallow indentations with a typical displacement of 30–40 nm or circa 1.0–1.8 µm for indents corresponding with a 100–180 nm displacement. In general this means that for typical DP/TRIP microstructures with ferrite grains with dimensions of several microns an accurate measurement of the nano-hardness of individual ferrite grains can be achieved without major influence of neighbouring phase constituents. However, for M/RA islands in a DP/TRIP microstructure with partly submicron dimensions this is less obvious.

A typical analysis of the nano-hardness of individual ferrite grains and second-phase islands in a multi-phase steel microstructure will show variations in nano-hardness between ferrite grains which exceed the typical relative error margin. These variations in nano-hardness between ferrite grains (differences close to 0.5 GPa have been measured) can be attributed to differences in crystallographic orientation. Within individual ferrite grains small variations are measured in nano-hardness. However, these differences are all within or close to the experimental error introduced by the measurement. For M/RA islands, considerable variations are measured within individual M/RA islands. These differences exceed by far the experimental error and should thus be attributed to:

- (1) Limited resolution of nano-indentation in comparison to dimensions of M/RA islands
- (2) Locally different physical conditions (e.g., chemical composition, Fe<sub>3</sub>C-particles, block/packet structure) within individual M/RA islands.

### 7.2.1.3 Sample preparation

Furnémont et al.<sup>[38]</sup> have investigated the influence of specimen preparation on nano-hardness measurements. They used three final specimen preparation techniques: (1) mechanical polishing, (2) electro-polishing and (3) thermal etching. Figure 7.2 shows load-displacement curves of indentations carried out in ferrite in TRIP steel after these three different preparation methods. The data in Figure 7.2 shows that hardness varies according to preparation method. The hardness after electro-polishing or thermal etching is the same and is considerably lower than that measured after mechanical polishing. Furnémont et al.<sup>[38]</sup> conclude that this difference can be attributed to the influence of a strain-hardened layer in case of mechanical polishing, which perturbs the hardness measurement. Apparently, electro-polishing or thermal etching is effective in removing this strain-hardened layer. At the same time, electro-polishing provides surfaces with low surface topography, which is also a requirement for accurate nano-indentation analysis. Therefore, electro-polishing is recommended as the best suited specimen preparation method for nano-indentation.

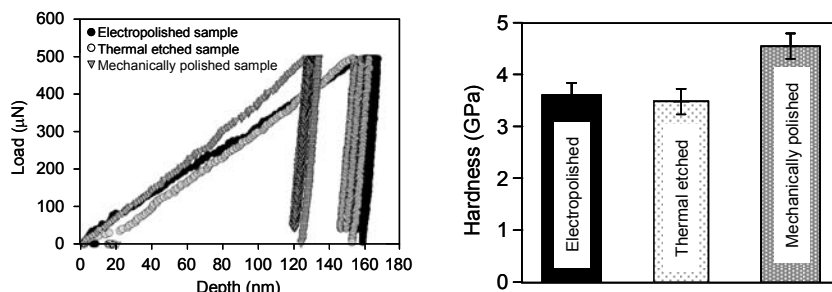


**Figure 7.2** (left) Load-displacement curves of indentations carried out in ferrite and (right) the average ferrite hardness after three different preparation modes of the surface of the same specimen (images taken from a publication by Furnémont et al.<sup>[38]</sup>).

Apart from removal of a strain-hardened surface, particular attention should be paid to reducing the degree of transformation of retained-austenite to martensite as a result of preparation. Variations in polishing conditions as part of EBSD work on TRIP steels has yielded significant variations in retained-austenite fraction measured with EBSD. This confirms that preparation may activate deformation-induced transformation of retained-austenite. In particular large retained-austenite grains would seem to be prone to transformation as a result of their lower carbon concentration and larger exposed surface area as a result of sectioning. In this context, relatively large blocky shaped retained-austenite islands are expected to be considerably more prone to deformation-induced transformation than relatively small lath-shaped retained-austenite. Apart from evidence of transformation, twinning in retained-austenite grains in TRIP steel (see section 7.4, Figure 7.6), possibly induced by preparation, is also observed.

Deformation-induced transformation of retained-austenite to martensite will affect its response and properties as measured by nano-indentation.

### 7.2.2 Empirical correlation between micro-Vickers and nano-hardness

All nano-indentation measurements as part of this project have been carried out with a Berkovich indenter. One of the advantages of this type of indenter is that it has a similar geometry as a micro-Vickers tip. This implies that – in principle – nano-hardness values obtained with a Berkovich indenter can easily be converted to micro-Vickers values. Common practice is that nano-hardness ( $H_N$ ) is expressed in GPa units, whereas micro-Vickers is expressed in HV units. The following expression correlates GPa units to HV<sup>[39]</sup>:

$$H_{\text{in GPa units}} = H_{\text{in HV units}} / 92.65 \quad \text{equation 7-6}$$

A study of Rice and Stoller<sup>[39]</sup> has shown that any change in hardness measured with a nano-indenter (applied loads of 500 µN, 1 mN and 10 mN) is nearly identical to the bulk property change measured in a Vickers hardness test (200g-HV):

$$\Delta H_N \text{ [in GPa units]} = 1.067 \Delta H_V \text{ [in GPa units]} \quad \text{equation 7-7}$$

Furthermore, their study indicated that there is a “zero-offset” for  $H_N(HV)$ . This “zero-offset” ( $H_{N,0}$ ) is a function of displacement. The physical origin of this offset is not understood.<sup>[39]</sup> A fit of the data (fixed displacements of 50, 100 and 400 nm with applied loads in the range of 200 to 3400 µN) from Rice and Stoller yields the following correlation between displacement  $h_{\max}$  (in nm) and nano-hardness offset ( $H_{N,0}$ ) (in GPa):

$$H_{N,0} = 10.685 h_{\max}^{-0.527} \quad \text{equation 7-8}$$

This implies that the following correlation can be formulated which correlates  $H_N$  to  $H_V$  (both expressed in GPa units) based on the displacement during nano-hardness testing:

$$H_N = 1.067 H_V + 10.685 h_{\max}^{-0.527} \quad \text{equation 7-9}$$

Load-displacement curves recorded during typical nano-hardness measurements carried out by Corus allow a quantitative assessment of  $h_{\max}$ . Figure 7.3 shows a plot of displacement  $h_{\max}$  versus calculated nano-hardness  $H_N$  based on an extensive nano-indentation study on DP microstructures.

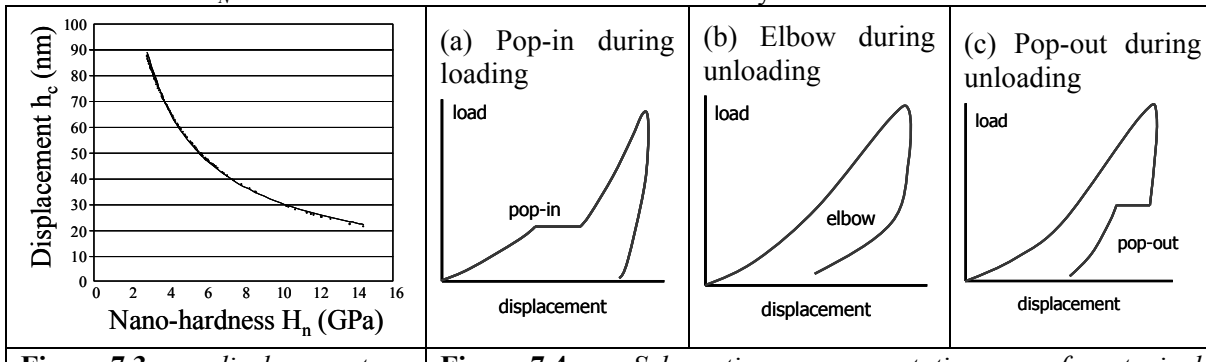


**Figure 7.3** displacement  $h_{\max}$  versus nano-hardness  $H_N$  based on nano-indentation mappings (7x7 indents covering 20x20 µm) with a maximum load of 500 µN.

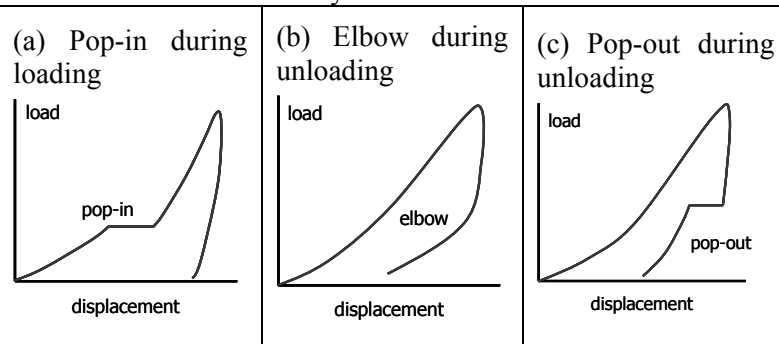


**Figure 7.4** Schematic representations of typical discontinuities or gradients that may occur in a load-displacement curve during loading (a) and unloading (b and c).

For this study several DP microstructures have been analysed by means of a grid of 7x7 indents with a step size of 2 µm. Maximum load for this investigation was 500 µN. A fit of the data shown in Figure 7.3 yields the following correlation between  $h_{\max}$  (nm) and  $H_N$  (GPa):

$$h_{\max} = 213.89 H_N^{-0.845} \quad \text{equation 7-10}$$

This implies that nano-hardness  $H_N$  as determined by a Berkovich indenter correlates with the micro-hardness in HV as measured by micro-Vickers according to:

$$H_N = 12.8 \times 10^{-3} HV + 0.863 \text{ or vice versa } HV = 78 H_N - 67.3$$

**equation 7-11**

### 7.2.3 Indentation-induced phase transformation

Apart from nano-hardness, load-displacement curves may exhibit interesting local perturbations or discontinuities, which are characteristic of energy-absorbing or energy-releasing events occurring beneath the indenter tip<sup>[40]</sup>. Figure 7.4 shows schematically illustrated three of these examples, which correspond to three different physical phenomena: (1) pop-in during loading, (2) elbow behaviour during unloading and (3) pop-out during unloading. In general, the first phenomenon is ascribed to dislocation activity and the onset of plastic deformation, whereas the second two are attributed to evidence of indentation-induced phase transformation accompanied by a certain degree of volume expansion beneath the indenter tip during unloading.

Several studies<sup>[37,38,41,42,43,44]</sup> have paid attention to evidence of transformation in load-displacement curves. Much of this work has been focused on transformation of Silicon<sup>[37,42,43]</sup>. In this work, elbow and pop-out behaviour (see Figure 7.4) are attributed to transformation of Silicon accompanied by a certain degree of volume expansion during the unloading stage. Indenter type<sup>[37]</sup>, loading rate<sup>[37,42,43]</sup> as well as maximum load<sup>[42,43]</sup> will dictate the degree of volume expansion below the indenter and hence force either elbow (relatively small volume change) or pop-out (relatively large volume change) behaviour during unloading. Relatively high maximum loads and high loading rates will promote pop-out behaviour, whereas relatively low maximum loads and low loading rates will lead to elbow behaviour.

Pop-in behaviour during loading is generally attributed to dislocation activity and the onset of plastic deformation<sup>[40,43,45]</sup>. Again, loading rate has an influence on the number and size of pop-in discontinuities: an increase in loading rate will reduce the number and size of pop-in discontinuities. At relatively high loading rates pop-in behaviour during loading may be even completely suppressed.

The number of nano-indentation studies in literature on multi-phase steels, such as DP and TRIP, is quite limited to date. Several studies<sup>[38,44,46,47]</sup> have reported nano-hardness values for ferrite, bainite, (tempered) martensite and retained-austenite in DP and TRIP steels. Table 7.1 gives an overview of reported values by various experimental studies. Most studies<sup>[44,46,47]</sup> report a nano-hardness of ferrite in the range of 2.9 to 3.7 GPa. Exception to this is the relatively high value reported by Furnémont et al.<sup>[38]</sup> of 4.8 GPa. Nano-hardness of bainite in TRIP steels has been reported to be around 7.0 to 7.5 GPa. These values are quite similar to that reported for tempered martensite. Table 7.1 illustrates that for untempered martensite quite different values have been reported for DP steels in literature. Reported values range from 8.5 - 11.5 GPa in a study by Angeli et al.<sup>[46]</sup> and 5.5 - 7.0 GPa reported in a study by Delince et al.<sup>[47]</sup>. A study on TRIP steel by Furnémont et al.<sup>[38]</sup> reports a much higher value of around 16.7 GPa for martensite. Also for retained-austenite there are inconsistencies in literature. According to Angeli et al.<sup>[46]</sup> the nano-hardness of retained-austenite islands can not be measured due to indentation-induced phase transformation of retained-austenite into martensite. This is in contrast to studies by Furnémont et al.<sup>[38]</sup> and Ahn et al.<sup>[44]</sup> that do report nano-hardness values for retained-austenite. However, both studies report completely different values: the former study reports a typical nano-hardness of 10 GPa, whereas the latter study reports 4.65 GPa.

**Table 7.1** Reported nano-hardness values in literature for phase constituents in DP and TRIP steels (all measurements have been done with a Berkovich indenter).

Constituent	DP steel (GPa)		TRIP steel (GPa)		
	Angeli <sup>[46]</sup>	Delince <sup>[47]</sup>	Angeli <sup>[46]</sup>	Furnémont <sup>[38]</sup>	Ahn <sup>[44]</sup>
Ferrite	3.0	2.86 - 3.11	3.7	4.8	3.37
Bainite			7.5	7.0	
Martensite	8.5 - 11.5	5.46 - 6.99		16.7	
Tempered martensite	6.5				
Retained-austenite				10.0	4.65

Angeli et al.<sup>[46]</sup>: maximum load of 200-250  $\mu\text{N}$ ; Delince et al.<sup>[47]</sup>: maximum load of 250  $\mu\text{N}$ ; Furnémont et al.<sup>[38]</sup>: maximum load of 200  $\mu\text{N}$ ; Ahn et al.<sup>[44]</sup>: maximum load of 800  $\mu\text{N}$ .

Only two studies listed in Table 7.1 report to have observed indentation-induced phase transformation of retained-austenite to martensite in TRIP steel<sup>[38,44]</sup>. According to both studies, pop-in behaviour during loading and subsequent increase in gradient of the load-displacement curve provides evidence of

indentation-induced phase transformation of retained-austenite. However, in other nano-indentation studies on materials that have received considerably more attention - such as work on transformation of Silicon -, such discontinuities in load-displacement curves are typically ascribed to dislocation activity and not to phase transformations.

### 7.3 Task 7.2 Correlation between nano-hardness and phase properties

#### 7.3.1 Nano-hardness of phase constituents in DP and TRIP steels

Table 7.2 gives an overview of measured nano-hardness values and ranges for various phase constituents in the DP600 and TRIP700 Round Robin Test material (see WP1). In general, the nano-hardness of ferrite reported by partners in this project is around 3 GPa. For tempered and fresh martensite, typical nano-hardness values of respectively 5-9 and 7-16 GPa have been measured. EBSD-guided nano-indentation analysis of retained-austenite islands in a TRIP700 microstructure indicates that its hardness is comparable to that of ferrite, i.e., around 3 GPa. This value is somewhat lower than the value reported by Ahn et al.<sup>[44]</sup> and considerably lower than the value reported by Furnémont et al.<sup>[38]</sup>. Section 7.4 will pay more attention to EBSD-guided nano-indentation analysis of phase constituents in a TRIP700 microstructure and will focus on evidence of indentation-induced phase transformation of retained-austenite to martensite in load-displacement curves.

**Table 7.2** Reported nano-hardness values for phase constituents in DP600 and TRIP700 steels (all measurements have been done with a Berkovich indenter).

Partner	DP600 STEEL				TRIP700 STEEL		
	F	TM	M		F	M	RA
<b>Corus</b>	2.0-3.3	-	8-16		2.0-3.3	8-16	2.5-3.3
<b>KIMAB</b>	2.7-3.4	5-9	13.6		-	-	-
<b>VAS</b>	3.0	6.6	7-10		-	-	-

#### 7.3.2 Relationship between composition and nano-hardness for ferrite

The empirical formulation below derived by Brisson and Blondeau relates micro-hardness of ferrite to its chemical composition and cooling rate during its transformation from austenite.

$$HV_F = 42 + 223\%C + 53\%Si + 30\%Mn + 13\%Ni + 7\%Cr + 19\%Mo + 10 \log(v_R(10 - 19\%Si + 4\%Ni + 8\%Cr + 130\%V)) \quad \text{equation 7-12}$$

with  $v_R$  as cooling rate in Kelvin/hour. The validity of this formula is restricted to the following conditions:  $\leq 0.50\%C$ ,  $\leq 0.50\%Si$ ,  $\leq 1.75\%Mn$ ,  $\leq 2.25\%Cr$ ,  $\leq 1.00\%Mo$ ,  $\leq 3.00\%Ni$ ,  $\leq 0.10\%V$ ,  $\%Mn+\%Ni+\%Cr+\%Mo < 5\%$  and  $v_R = 10 \dots 1000 \text{ K/h}$ . Although not all conditions are met in the present case, equation 7-12 yields a ferrite micro-hardness of circa 120 HV for both the DP600 and TRIP700 based on their average chemical composition listed in Section 1.4. This hardness value is dominated by the average intrinsic hardness of ferrite grains. Based on equation 7-11 this corresponds with an average intrinsic nano-hardness of ferrite grains of circa 2.4 GPa.

Nano-indentation hardness measurements of ferrite grains in microstructures of the investigated DP600 and TRIP700 steels yield values for ferrite grains which range from 2.0 to 3.4 GPa. The relative large variation in nano-hardness of the ferrite matrix can be attributed to differences in crystallographic orientation between ferrite grains, inhomogeneous strain distribution as well as to nearby microstructural components such as grain boundaries, other phase constituents.

The experimental nano-hardness values of 2.0 to 3.4 GPa for the ferrite matrix correspond well with the calculated hardness based on equation 7-12 and converting micro-Vickers in HV units to hardness values in GPa units based on equation 7-11. If only the geometry aspect would have been taken into account based on equation 7-6, the calculated nano-hardness values in GPa units would have been only 1.28 GPa, which is far too low in comparison with the measured nano-hardness values of 2.0–3.4 GPa. This supports the notion that conversion from HV to GPa involves more than only equation 7-6 and that the empirical relationship equation 7-11 between micro-Vickers in HV and nano-hardness in GPa provides a good empirical correlation.

### 7.3.3 Relationship between composition and nano-hardness for martensite

A study by Ohmura *et al.*<sup>[48]</sup> on the correlation between nano-indentation and micro-hardness of fully martensitic steels as a function of carbon content (average wt% carbon of 0.1 to 0.8 wt%) has shown that nano-hardness of martensite increases with increasing carbon content especially when it is lower than 0.6 wt%. From their study the following dependency between nano-hardness and carbon content up to 0.6 wt% can be extracted:

$$\frac{\Delta H_N}{\Delta \%C} = 9.5 \quad \text{equation 7-13}$$

Beyond a carbon content of 0.6 wt%, nano-hardness of martensite is much less dependent on carbon content and would seem to reach a plateau. Ohmura *et al.*<sup>[48]</sup> report for a 0.8 wt% fully martensitic steel a nano-hardness value of 10.7 GPa (or 767 HV).

Brisson and Blondeau established the following dependency between micro-hardness and chemical composition and cooling rate:

$$HV_M = 127 + 949\%C + 27\%Si + 11\%Mn + 8\%Ni + 16\%Cr + 21^{10} \log[v_R] \quad \text{equation 7-14}$$

with  $v_R$  as cooling rate in Kelvin/Hour. The validity of the formula is restricted to the following conditions:  $0.075 \leq \%C \leq 0.45$ ,  $\leq 1.50\%Si$ ,  $\leq 1.6\%Mn$ ,  $\leq 3.00\%Cr$ ,  $\leq 5.00\%Ni$ , and  $v_R > 100,000$  K/h. The relationship shown in equation 7-14 is according to Brisson and Blondeau only valid for an estimate of the hardness in HV of martensite with a carbon content between 0.075% and 0.45%. An estimate of the hardness of martensite with carbon content  $\geq 0.45\%$  should thus be considered with care.

Given the average chemistry of the DP600 RRT steel supplied by Corus (see Section 1.3) and a cooling rate of circa 30 K/s, equation 7-14 for the micro-hardness in Vickers based on Brisson and Blondeau can be re-written into:

$$HV_M = 949\%C + 268 \quad \text{equation 7-15}$$

or in terms of nano-hardness expressed in GPa units into:

$$H_N = 12.2\%C + 4.3 \quad \text{equation 7-16}$$

Expressing the carbon content of martensite in terms of its nano-hardness yields:

$$\%C = 0.082H_N - 0.35 \quad \text{equation 7-17}$$

Several studies on nano-indentation have focused exclusively on single-phase microstructures, i.e., either fully ferritic steels<sup>[39,49]</sup> or partial martensitic steels<sup>[39,48]</sup>. Other studies<sup>[38,44,46,47]</sup> have shifted this focus of nano-indentation on single-phase steels to nano-indentation of individual phases and phase constituents in multi-phase microstructures of DP and TRIP steels. Angeli *et al.*<sup>[46]</sup> have measured the nano-hardness of ferrite grains and martensitic phase constituents in DP steels (average composition of 0.10 %C, 0.15%Si, 1.2 – 1.6%Mn, and 0.8%Cr+Mo). Based on their study a correlation between the nano-hardness of martensite and carbon content is stated according to: 11.5 GPa for 0.6 wt%C, 8.5 GPa for 0.4 wt%C, and 6.5 GPa for 0.2 wt%C. A linear fit of this data<sup>[46]</sup> results into:

$$H_N = 12.5\%C + 3.83 \quad \text{equation 7-18}$$

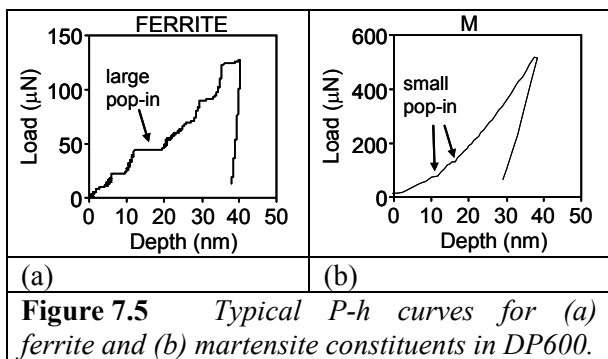
The co-efficient of 12.5 is considerably higher than that determined by Ohmura et al for martensite with a carbon-content in the range of 0.2% to 0.6%. On the otherhand this value is in good agreement with the co-efficient shown in equation 7-16, and confirms the correlation between  $H_N$  and carbon content of martensite.

## 7.4 Task 7.3 Retained austenite stability

### 7.4.1 Indentation-induced transformation of austenite and micro-crack formation in TRIP

Figure 7.5 shows representative P-h curves for DP600 ferrite and martensite. Both curves show a dramatic difference in appearance, with that of ferrite being dominated by pronounced discontinuities – so-called pop-ins –, which correspond with plastic deformation. These intense pop-ins are absent in the P-h curve of martensite, reflecting an essential difference in crystallographic structure of both constituents.

Nano-hardness ( $H_N$ ) values for ferrite and martensite (M) derived from P-h curves shown in Figure 7.5 are 2.3 and 11.4 GPa, respectively. Since  $H_N$  of ferrite grains is dependent on their crystallographic orientation,  $H_N$  values for ferrite range between 2.0-3.3 GPa.  $H_N$  values for martensite show large scatter due to limited spatial resolution of the indenter and range between 8-12 GPa. These values are in good agreement with values reported in literature for ferrite and martensite in DP steels<sup>[46]</sup>.



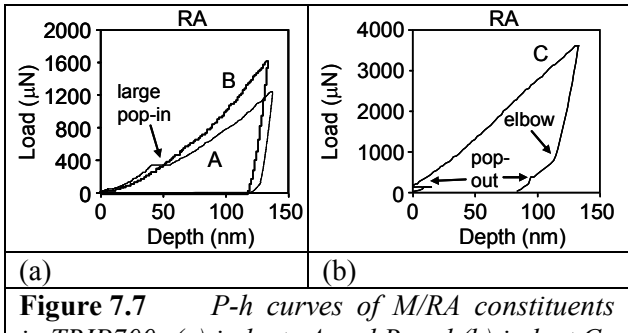
**Figure 7.5** Typical P-h curves for (a) ferrite and (b) martensite constituents in DP600.

Figure 7.6 shows a SEM image of three indents positioned in the TRIP700 microstructure together with corresponding EBSD data collected prior to indentation. Based on EBSD analysis, it can be concluded with confidence that indents A and B are located in retained-austenite (RA). Corresponding P-h curves are shown in Figure 7.7(a), from which  $H_N$  values have been derived of 2.5 and 3.3 GPa for indent A and B, respectively. These values are similar to those measured for ferrite. This observation is in line with studies on duplex steels which have shown that the micro-hardness of ferrite and austenite is similar<sup>[50]</sup>. The P-h curve of indent C (Figure 7.7 (b)) has been obtained with a considerably higher maximum load and is positioned in ferrite, exactly in between two retained-austenite grains with similar orientation. The  $H_N$  value obtained for this indent is 12.2 GPa. This value is much higher than that of ferrite and coincides with a value typical for martensite. In turn, this strongly suggests that surrounding retained-austenite – and possibly retained-austenite located below the surface – has been subject to indentation-induced RA→M transformation. The elbow and small pop-out event in the unloading part of the P-h curve, which are commonly attributed in literature to an increase in volume resulting from (partial) transformation<sup>[37,43]</sup>, provide important support for this conclusion.



**Figure 7.6** TRIP700 (a) SEM image (FOW 3.5 μm), (b) inverse pole figure and (c) image quality maps in combination with a phase map (— twin (60°) boundaries). EBSD data has been collected prior to nano-indentation. Indents A, B and C are discussed in the text.

Figure 7.8 provides a SEM image showing an additional series of indents positioned in ferrite and M/RA constituents together with corresponding Image Quality (IQ) maps acquired before and after indentation. A comparison between both IQ maps reveals that deformation induced by the indenter significantly lowers the IQ value. This can be clearly observed for indent D positioned in the middle of a ferrite grain. However, the effect on IQ is exclusively limited to the contact surface of the indenter tip and hardly extends outwards. Indent E has been positioned on the edge of a second phase constituent, which – based on EBSD – is identified with high confidence as austenite. The IQ maps reveal that the indentation process lowers significantly the average IQ value of the retained-austenite grain.



**Figure 7.7** *P-h curves of M/RA constituents in TRIP700: (a) indents A and B and (b) indent C.*

limited to the contact surface of the indenter. These observations together provide strong support for the argument that the significant change in IQ of the retained-austenite grain probed by indent E is a result of indentation-induced RA $\rightarrow$ M transformation. Additional evidence to support this conclusion can also be derived from the P-h curve of indent E as discussed below.

The  $H_N$  value for intercritical ferrite derived from the P-h curve (Figure 7.9 (left)) corresponding to indent D is 2.3 GPa, which is similar to values measured for ferrite in DP600. As discussed, indent E has been positioned in a retained-austenite grain (Figure 7.9). Similar to indent C, its P-h curve (Figure 7.10 (right)) provides evidence of elbow behaviour.

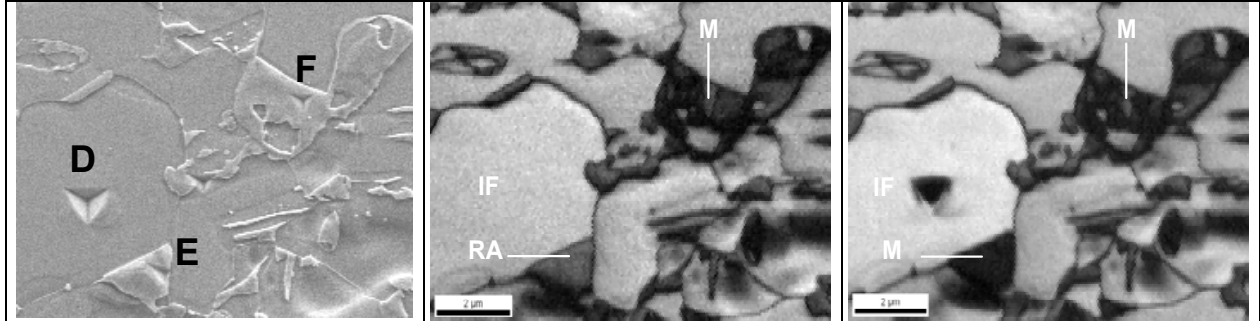


**Figure 7.8** *TRIP700 (left) SEM image and image quality maps prior (middle) and post nano-indentation (right). (FOW 12  $\mu$ m) Indents D, E and F are discussed in the text.*

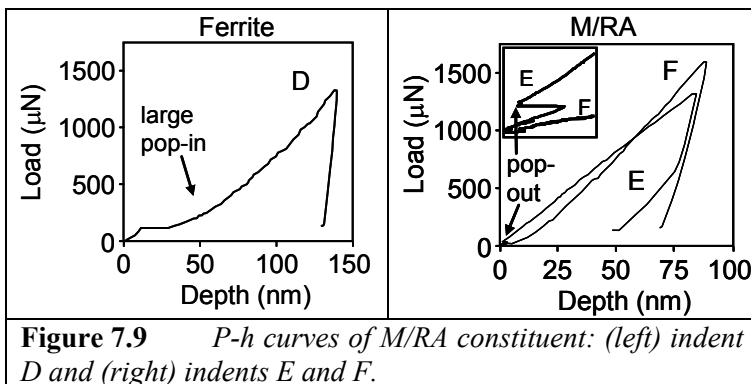


**Figure 7.9** *P-h curves of M/RA constituent: (left) indent D and (right) indents E and F.*

value of 8.3 GPa – shows no elbow or pop-out behaviour during unloading is in line with the observation based on EBSD that this indent has been positioned in a martensite islands (Figure 7.8). This finding corroborates the conclusion that meta-stable retained-austenite is prone to transformation due to specimen preparation, which in turn might offer an explanation for the much higher  $H_N$  value for retained-austenite (10 GPa) reported in a previous nano-indentation study on phase constituents in TRIP steels<sup>[38]</sup>.

The P-h curve for indent C (Figure 7.7(b)) shows a pronounced pop-out during early stages of loading, reflecting an intense oscillation of the indenter tip. This feature is related to formation of a distinct micro-crack (Figure 7.6) running along the interface between ferrite and indentation-induced martensite. The P-h curve for indent E (Figure 7.9(right)) shows a similar feature, albeit less pronounced. Visual inspection reveals that here also a micro-crack is present at the interface between

However, the spatial extent of the indentation effect on IQ is considerably larger than that for indent D and covers practically the complete surface of the exposed retained-austenite grain, resulting in an average IQ value which is similar to that of martensite. Although indent E has been positioned on the edge of the retained-austenite grain, no impact of the indentation on IQ values of the neighbouring ferrite grain is observed. At the same time, the impact on IQ for indent F positioned in martensite is again limited to the contact surface of the indenter. These observations together provide strong support for the argument that the significant change in IQ of the retained-austenite grain probed by indent E is a result of indentation-induced RA $\rightarrow$ M transformation. Additional evidence to support this conclusion can also be derived from the P-h curve of indent E as discussed below.

Again, this observation suggests transformation<sup>[37,43]</sup>, which in turn explains the relatively high  $H_N$  value of 7.3 GPa. This value is in line with the assumption that an indent positioned near the edge of a retained-austenite grain subject to transformation, will partially probe surrounding ferrite and hence yield a  $H_N$  value somewhat below that of martensite. The fact that the unloading part of the P-h curve of indent F –  $H_N$

epitaxial ferrite and indentation-induced martensite. These micro-cracks are absent for indents positioned in retained-austenite grains that did not undergo transformation – i.e., indents A and B (Figure 7.6). The observation in this study that evidence of transformation in P-h curves of retained-austenite constituents and micro-crack initiation would seem to be closely related phenomena is in line with previous investigations on strain-induced damage initiation in TRIP steels<sup>[51,52,53]</sup>. These studies have shown that transformation of retained-austenite facilitates void nucleation and that crack initiation occurs at the interface between ferrite and martensite that has been mechanically transformed.

#### 7.4.2 Lath-shaped and block-shaped retained-austenite in TRIP steel

It is generally accepted that the size of retained-austenite islands is related to their carbon concentration and hence to their resistance to deformation-induced phase transformation to martensite. Given a certain average carbon content for the bulk, an increase in size of retained-austenite islands will yield a lower carbon concentration in these islands. Reason for this is the fact that less carbon is partitioned across the moving  $\alpha$ - $\gamma$  interface as a result of the formation of epitaxial ferrite during the cooling stages of the thermal annealing cycle of DP and TRIP steels. Therefore, retained-austenite islands characterised by a small residual volume after the complete annealing cycle and preferably accompanied with a large  $\alpha$ - $\gamma$  interface, i.e., lath-shaped retained-austenite, are anticipated to have the highest carbon concentration. This line of reasoning implies that lath-shaped retained-austenite will generally be more stable than block-shaped retained-austenite, especially when these block-shaped retained-austenite islands have relatively large dimensions. This is in line with experimental observations based on EBSD measurements that large block-shaped retained-austenite islands may be prone to transformation induced by specimen preparation, whereas this effect is not observed for lath-shaped retained-austenite.

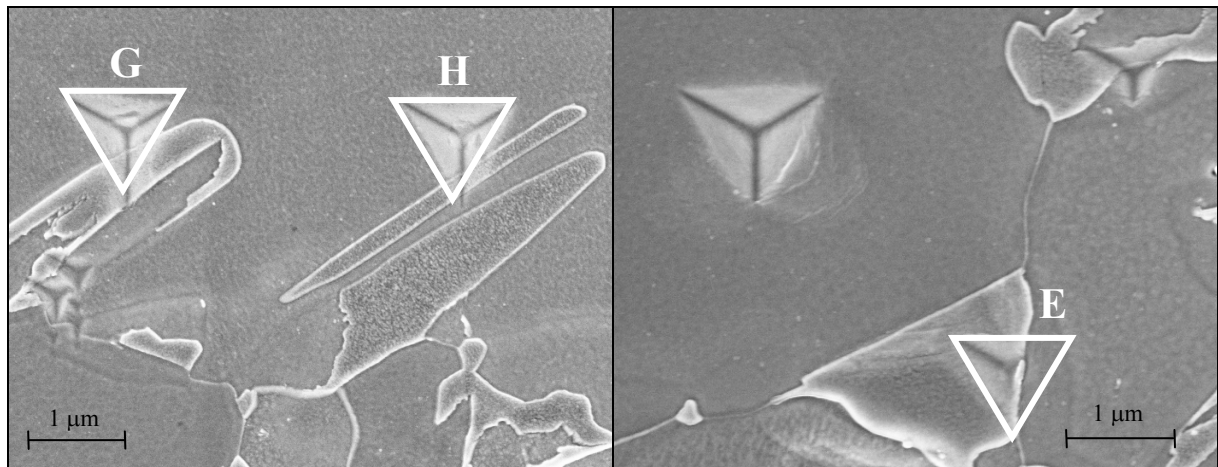
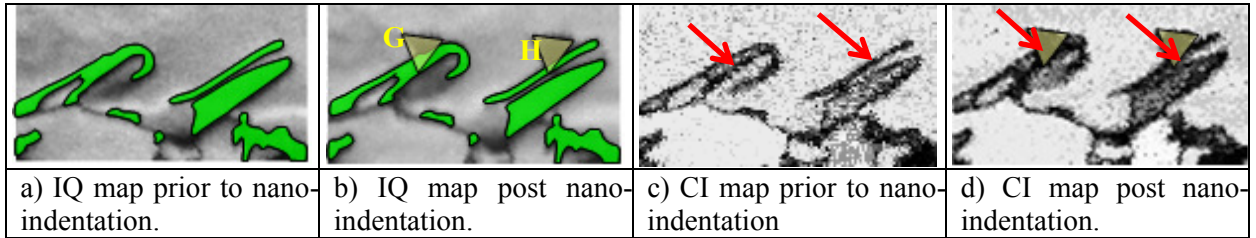


**Figure 7.10** SEM images of (left) lath-shaped RA islands and (right) block-shaped RA islands. Triangular features correspond to the residual impression of nano-indentations labelled E, G and H.

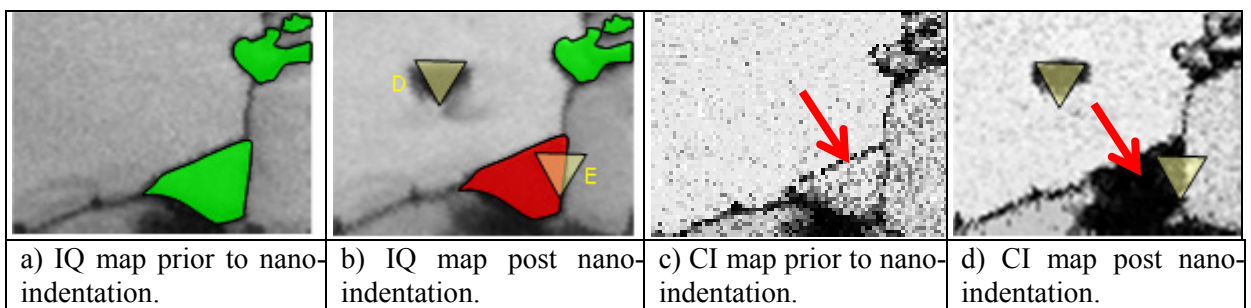
Figure 7.10 shows examples of SEM images of lath-shaped and block-shaped retained-austenite islands. Also visible in the images shown in Figure 7.10 are residual impressions of nano-indents that have been positioned in lath-shaped (indents G and H) and block-shaped (indent E) retained-austenite islands. In this Section, a comparison is made based on EBSD-guided nano-indentation analysis between lath-shaped and block-shaped retained-austenite. EBSD data prior and post nano-indentation corresponding to indents G and H for lath-shaped retained-austenite and indent E for block-shaped retained-austenite will be discussed.

Figure 7.11 shows EBSD data corresponding with the lath-shaped retained-austenite islands shown in Figure 7.10(a). Figure 7.11(a) and (b) correspond with the Image Quality (IQ) maps prior to and post nano-indentation. The corresponding confidence index (CI) maps prior to and post nano-indentation are shown in Figure 7.11(c) and (d). Indicated in green in the IQ maps are regions that have been identified with high confidence as retained-austenite. Indents G and H have been positioned partially in lath-shaped retained-austenite islands. The corresponding nano-hardness values for indents G and H are 3.94 and 3.00 GPa, respectively. Figure 7.12 shows similar EBSD data but now for block-shaped retained-austenite. Indicated in Figure 7.12(b) and (d) are the positions of indents D and E that have already been discussed in the previous Section. Indent E has been positioned partially in a second phase constituents

that prior to nano-indentation was identified with high confidence as retained-austenite based on EBSD analysis. This retained-austenite island is block-shaped. The corresponding nano-hardness value is 7.3 GPa. As discussed in detail in the previous Section, EBSD and nano-indentation data indicate that indent E has induced transformation of the complete surface area of the block-shaped retained-austenite island to martensite.



**Figure 7.11** EBSD data prior (a and c) to and post (b and d) nano-indentation analysis of lath-shaped retained-austenite islands (indents G and H). (Detail of Figure 7.10 left) Green regions correspond with retained-austenite. Triangles correspond with the position of the nano-indentations. The red arrows in the CI maps emphasize the change in confidence index due to nano-indentation.



**Figure 7.12** EBSD data prior (a and c) to and post (b and d) nano-indentation analysis of a block-shaped retained-austenite island (indent E). (Detail of Figure 7.10 right) Green regions correspond with retained-austenite. Red region corresponds with mechanically transformed martensite. Triangles correspond with the position of the nano-indentations. The red arrows in the CI maps emphasize the change in confidence index due to nano-indentation.

The complete surface area of the block-shaped retained-austenite island prior to nano-indentation has a high confidence index according the CI map (Figure 7.12 (c)). Its average confidence index is comparable to that of adjacent ferrite grains. This is considered typical for a phase constituent that has been formed via reconstructive growth and is characterised by a low dislocation density. Although indent E has only partially been positioned on the block-shaped retained-austenite island (Figure 7.12(b)), a comparison between the CI map prior (Figure 7.12(a)) to and post (Figure 7.12 (b)) nano-indentation clearly shows that the confidence index of the complete island has been lowered dramatically as a result of the indent. Apparently not only the immediate region of the residual impression of the indent has a poor confidence index due to surface deformation, but also the remainder of the retained-austenite island (indicated by a red arrow in Figure 7.12(c) and (d)). This latter is considered to be due to mechanically induced transformation of austenite to martensite. Such a dramatic change in confidence index is not observed when lath-shaped retained-austenite islands are probed via nano-indentation. In particular for indent G it can be seen that only the immediate region of the residual impression of the indent suffers from a low confidence index, whereas just below this region (indicated by a red arrow in Figure 7.11(c) and (d)), the lath-shaped retained-austenite constituents has kept its relatively high confidence index. This is considered to be typical for retained-austenite that has not been subject to transformation. These observations support the notion that lath-shaped retained-austenite islands are highly resistant to mechanically induced phase transformation, whereas block-shaped retained-austenite islands – in particular when their dimensions are relatively large – are considerably less stable.

Unfortunately, nano-indentation with its sub-micron spatial resolution in combination with EBSD offers only limited possibilities to investigate the stability of lath- or block-shape retained-austenite with sub-micron dimensions. For very fine lath-shaped retained-austenite as for instance present in microstructures of Quench and Partition steels the spatial resolution of nano-indentation will be

insufficient for analysis. Nevertheless, nano-indentation whether or not in combination with EBSD does offer possibilities to investigate the stability of relatively large block-shaped retained-austenite in TRIP steels.

## 8 WP 8 Validation of procedures

Task	Deliverable	D#
8.1	Reproducibility of procedures	D30
8.2	Discriminative power of procedures in relation to mechanical properties	D31
8.3	Selecting optimal procedures for microstructural quantification	D32

### 8.1 General objective

The main objective of this WP is the evaluation and application of procedures, which have been developed in this project. Next objective is to present an overview, selection and documentation of procedures for microstructural quantification with the long-term aim (outside the scope of this project) of, providing relevant information for European standardization of these procedures.

### 8.2 Task 8.1 Testing the reproducibility of procedures

Important for the design and selection of optimised procedures for microstructural quantification is that these procedures are non-subjective with regard to interpretation, robust with regard to small operational deviations in practice. Moreover, procedures must and function accurately independently of the type of multi-phase steel product under investigation. During the run of the project it was found that not all partners, for different reasons, could cope with the quantification of all RRT microstructures. This was related to **a**) sample preparation (EBSD sample preparation for TRIP700 was found to be very critical) **b**) limitations of available equipment (resolution of a LaB<sub>6</sub> SEM was not sufficient for several structures) and **c**) software (not all image analysis software packages were able to cope with the quantification of CP, LB or M structures). With this in mind, the reproducibility of procedures has been tested, and partly imbedded, in work package 8.2: when a procedure is not reproducible within certain limits its very unlikely a link with a mechanical or process parameter will be found.

The reproducibility of EBSD measurements of the RRT has been described extensively in section 5.6. The general conclusion is that EBSD measurements in itself are reproducible, but that the actual quantification of a measurement strongly depends on parameter settings. The identified critical parameters are field size, step size, grain tolerance angle (GTA) and minimum grain size. In a few occasions misindexing was found to result in less accurate results (see also 5.6.2.7). Although sample preparation in general is extremely important for EBSD measurements, only for TRIP samples, sample preparation was found of crucial importance and large discrepancies were observed between quantitative results from different partners (section 3.2.5). Differences in post treatment (data set partitioning) of the data sets can even lead (obvious) to much larger differences in quantitative results. Different clean-up procedures performed on (basically good quality) data sets were found to have only limited influence on quantified results.<sup>[19]</sup>

To obtain reproducible quantification results from SEM microstructures, it important to realize the impact of inhomogeneity of the microstructure in relation to the magnification used, and the impact of submicron sized grains or second phase constituents. These aspects have also been discussed in WP3 (§3.3.1) and in WP4 in this report.<sup>[19,28]</sup>

### 8.3 Task 8.2 Testing the discriminative power of procedures in relation to mechanical properties

Microstructural characterization is often used to understand the mechanical properties of steel products and as a tool for subsequent optimization of mechanical properties. Conventional methods to this purpose usually rely on light-optical microscopy. However, these methods do not always offer the resolution to adequately assess the differences in complex multi-phase microstructures of steels with different mechanical properties. In this task a range of samples, with complex multi phase microstructures and with significantly different mechanical properties have been investigated. For this reason, it is important to assess how procedures developed in this project are able to enhance the ability to quantify the difference between these microstructures. For RRT analogue microstructures (i.e. DP, TRIP CP, LB and M) this discriminative power is determined by relating quantified parameters to specific mechanical properties.

### 8.3.1 Phase fraction and phase (or grain) size in relation to mechanical properties for a DP series.

This section focuses on morphological quantification of phase constituents with the aim to establish an experimental correlation between tensile data and microstructural features based on LOM, SEM for different DP steels (performed by Arcelor). Characterization and quantification of DP microstructures was performed according to procedures described in §2.2.1.4.1 (in 3 planes). The objective of this task was to correlate tensile properties with quantified microstructural features. Good correlations were found for UTS, YS and El using mean microstructural parameters in all 3 planes. The only correlation that can be ameliorated is for  $R_{\text{area}}$  i.e. the percentage decrease in the cross-sectional area of a tensile test piece caused by wasting or necking of the specimen. It is a measure of ductility. Results of all metallographic characterizations in 3 planes are combined in Table 8.1. Also the mean values between pairs of different planes and also mean values between the three planes together were calculated.

**Table 8.1** Combined, mechanical and microstructural data for DP.

No	YS MPa	UTS MPa	Total El %	Ra, %			Martensite, %			average Area M+RA, $\mu\text{m}^2$			FGS, $\mu\text{m}$		
				RD-ND	TD-ND	RD-TD	RD-ND	TD-ND	RD-TD	RD-ND	TD-ND	RD-TD	RD-ND	TD-ND	RD-TD
1	307	453	32.2	1.29	0.90	0.61	1.23	1.10	1.39	0.57	0.49	0.75	6.83	6.22	6.16
2	310	476	31.4	1.66	2.98	0.48	10.61	8.25	2.02	0.88	0.68	0.46	6.21	6.37	6.33
3	324	492	29.4	4.62	3.99	1.14	8.71	6.82	4.56	0.93	0.87	0.71	4.41	4.36	6.94
4	326	528	30.1	2.20	1.63	1.22	15.95	13.26	4.38	1.25	1.27	0.73	4.28	4.38	6.00
5	363	605	27.7	3.03	2.46	1.46	1.31	2.99	15.87	0.36	0.50	1.44	5.40	5.68	6.27
6	379	629	23.7	2.56	2.32	1.89	20.64	20.03	16.20	1.42	1.43	1.15	3.41	3.27	6.65
7	394	638	24.6	1.63	1.81	2.49	17.50	14.07	9.51	1.17	1.12	1.07	4.74	4.63	6.02
8	422	680	22.6	2.49	2.56	1.15	8.38	11.39	13.64	0.90	1.12	1.19	4.25	3.53	5.15
9	450	682	19.8	2.59	2.19	3.69	15.43	14.32	7.51	1.06	0.99	1.57	4.67	3.57	4.54
10	417	688	23.3	2.82	3.18	3.23	19.70	16.98	10.11	1.42	1.28	1.03	2.65	4.38	5.56
11	460	706	23.5	1.18	2.16	4.03	15.74	5.49	5.97	1.08	0.55	0.39	3.08	2.93	5.76
12	389	733	19.7	2.33	2.44	2.50	4.49	5.26	9.85	0.70	0.66	1.93	3.27	2.96	5.57
13	517	817	19.2	1.35	1.69	0.56	24.09	19.71	14.74	2.80	2.14	2.03	3.60	3.47	3.37
14	474	829	17.6	2.13	1.76	0.78	7.63	12.09	11.72	0.81	1.06	1.01	4.06	3.07	6.21
15	530	860	14.6	1.30	3.92	3.15	20.85	13.50	15.55	1.48	1.37	1.72	2.61	2.72	2.73
16	757	939	10.7	4.63	2.15	1.18	23.19	21.48	13.22	5.00	2.17	1.63	5.60	5.25	4.39

(RA = retained austenite, M = martensite, FGS = ferrite grain size) UTS= ultimate tensile strength, YS = yields strength, El = elongation  $A_{80}$

**Table 8.2** Mean values of microstructural parameters (fractions of austenite and martensite, area of martensite + retained austenite and mean ferrite grain size) calculated using different combinations of individual measurements in various planes.

No	Mean TD-ND/RD-TD				Mean RD-ND/RD-TD				Mean RD-ND/TD-ND				Mean RD-ND/TD-ND/RD-TD				
	Ra	M	Area M+Ra	FGS	Ra	M	Area M+Ra	FGS	Ra	M	Area M+Ra	FGS	Ra	M	Area M+Ra	FGS	
%	%	$\mu\text{m}^2$	$\mu\text{m}$	%	%	$\mu\text{m}^2$	$\mu\text{m}$	%	%	$\mu\text{m}^2$	$\mu\text{m}$	%	%	$\mu\text{m}^2$	$\mu\text{m}$		
1	0.8	1.3	0.6	6.2	1.0	1.3	0.7	6.5	1.1	1.2	0.5	6.5	0.9	1.2	0.6	6.4	1.1
2	1.7	5.1	0.6	6.4	1.1	6.3	0.7	6.3	2.3	9.4	0.8	6.3	1.7	7.0	0.7	6.3	3.5
3	2.6	5.7	0.8	5.6	2.9	6.6	0.8	5.7	4.3	7.8	0.9	4.4	3.3	6.7	0.8	5.2	3.7
4	1.4	8.8	1.0	5.2	1.7	10.2	1.0	5.1	1.9	14.6	1.3	4.3	1.7	11.2	1.1	4.9	2.1
5	2.0	10.3	1.0	6.0	2.2	9.5	0.9	5.8	2.7	2.1	0.4	5.5	2.3	7.3	0.8	5.8	8.2
6	2.1	18.4	1.3	5.0	2.2	18.7	1.3	5.0	2.4	20.3	1.4	3.3	2.3	19.2	1.3	4.4	8.4
7	2.2	11.8	1.1	5.3	2.1	13.5	1.1	5.4	1.7	15.8	1.1	4.7	2.0	13.7	1.1	5.1	9.5
8	1.9	12.7	1.2	4.3	1.8	11.2	1.0	4.7	2.5	9.9	1.0	3.9	2.1	11.2	1.1	4.3	9.5
9	2.9	10.9	1.3	4.1	3.1	11.5	1.3	4.6	2.4	14.9	1.0	4.1	2.8	12.4	1.2	4.3	8.6
10	3.2	12.9	1.2	5.0	3.0	14.2	1.2	4.1	3.0	18.3	1.4	3.5	3.1	15.2	1.2	4.2	9.7
11	3.1	5.7	0.5	4.3	2.6	10.9	0.7	4.4	1.7	10.6	0.8	3.0	2.5	9.1	0.7	3.9	10.6
12	2.5	6.9	1.3	4.3	2.4	6.5	1.3	4.4	2.4	4.9	0.7	3.1	2.4	6.1	1.1	3.9	19.8
13	1.1	17.2	2.1	3.4	1.0	19.4	2.4	3.5	1.5	21.9	2.5	3.5	1.2	19.5	2.3	3.5	22.3
14	1.3	11.9	1.0	4.6	1.5	9.7	0.9	5.1	1.9	9.9	0.9	3.6	1.6	10.5	1.0	4.4	28.1
15	3.5	14.5	1.5	2.7	2.2	18.2	1.6	2.7	2.6	17.2	1.4	2.7	2.8	16.6	1.5	2.7	19.7
16	1.7	17.4	1.9	4.8	2.9	18.2	3.3	5.0	3.4	22.3	3.6	5.4	2.7	19.3	2.9	5.1	32.3

\* Bainite fraction calculated by thermo-kinetic model, for details, see refined approximation.

### First approach

Looking for correlations between microstructure and mechanical properties a statistical analysis was performed on this database. In the first approach a simplified dual phase microstructure was used. This means that retained-austenite was assimilated to martensite (it's mostly true because it will transform at low deformation rates into martensite) and bainite was integrated in ferrite fraction (because of the difficulty to quantify bainite fraction by standard methods). As a consequence there remain three independent microstructural parameters: 1) ferrite grain size (FGS), 2) M+Ra area fraction (D) and 3) M+Ra island size (C). However, it was found that also a rather good correlation exists between M+Ra area fraction (D) and M+Ra island size (C). This correlation was observed for individual and coupled planes. As a result, there remain only two independent parameters: FGS and (M+Ra area fraction or M+Ra island size). Different couples of parameters were used to reveal if there is a preference between area fraction (D) and islands size (C) to correlate with mechanical properties. Empirical correlations for 2D (RD-ND / TD-ND) mean values (equation 8-1 to equation 8-4), and correlations for 3D (RD-ND / TD-ND / RD-TD) mean values (equation 8-5 to equation 8-8) are shown below.

$$UTS = -87.99 + 1427.91/\sqrt{FGS} + 21.68 \times C \quad 2D \quad R^2 = 74.3 \% \quad \text{equation 8-1}$$

$$UTS = -132.08 + 1551.03/\sqrt{FGS} + 210.2 \times D \quad 2D \quad R^2 = 73.6 \% \quad \text{equation 8-2}$$

$$YS = -246.06 + 1839.33/\sqrt{FGS} + 27.42 \times C \quad 2D \quad R^2 = 80.6 \% \quad \text{equation 8-3}$$

$$YS = -289.44 + 1958.53/\sqrt{FGS} + 1.4 \times D \quad 2D \quad R^2 = 79.1 \% \quad \text{equation 8-4}$$

$$UTS = 49.43 + 622.73/\sqrt{FGS} + 38.21 \times C \quad 3D \quad R^2 = 85.6 \% \quad \text{equation 8-5}$$

$$UTS = -3.86 + 759.58/\sqrt{FGS} + 1.88 \times D \quad 3D \quad R^2 = 84.1 \% \quad \text{equation 8-6}$$

$$YS = -116.76 + 913.75/\sqrt{FGS} + 85.05 \times C \quad 3D \quad R^2 = 87.2 \% \quad \text{equation 8-7}$$

$$YS = -290.05 + 1429.14/\sqrt{FGS} + 2.07 \times D \quad 3D \quad R^2 = 85.1 \% \quad \text{equation 8-8}$$

C = Ra+M island size; D = Ra+M area fraction; FGS= ferrite grain size

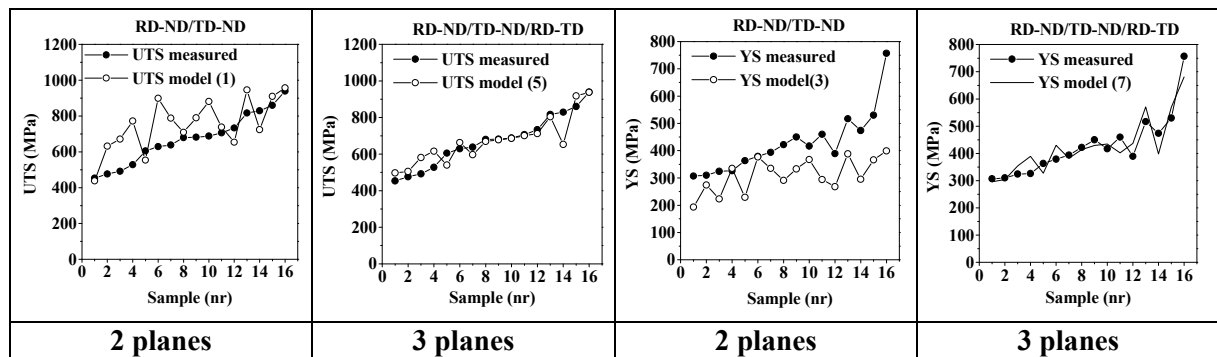


**Figure 8.1** Graphical representation of the performance of the 2D and 3D derived equations for UTS and YS (respectively equation 8-1, equation 8-3, equation 8-5 and equation 8-7).

The empirical equations for UTS and YS reveal the evolution of these parameters as a function of fraction and the reciprocal grain size. This statistical modelling shows that the mean values from 3 planes (RD-ND / TD-ND / RD-TD) give a far better description of mechanical properties than the statistical modelling depending on 2 planes. This means that they contain more information about the microstructure than 2 or 1 dimensional mean values. Moreover, the martensite island size (C) gives a better description of mechanical properties than the fraction of martensite (D).

### Refined approach

As mentioned before, it is known that in DP steel there is some amount of bainite and for some grades this quantity is not negligible. Hence, as a next step, it was decided to evaluate bainite fraction using thermo-kinetic models. The thermo kinetic model used for prediction of bainite fraction for DP steel

was based on the Avrami law. Data from Table 8.2 was used in this analysis: %Bainite\*; %RA+M; Size RA+M; Ferrite Grain Size (FGS)  $\mu\text{m}$ .

As previously, first the correlations inside the family of microstructural parameters were verified. The same correlation between martensite fraction and size was found. Other logic coupled parameters can be found for ferrite, bainite and martensite fraction.

Almost all identified microstructural parameters have more or less a strong correlation with all mechanical properties. Therefore, the necessary parameters to describe each mechanical parameter, preserving statically correct results, were determined. The results are presented in Figure 8.2. It can be seen in Figure 8.2 that bainite has an important role in the prediction of mechanical properties as it correlates with all mechanical parameters. Analyzing this diagram, it is necessary to take into account that fraction and size of RA/M islands are correlated.

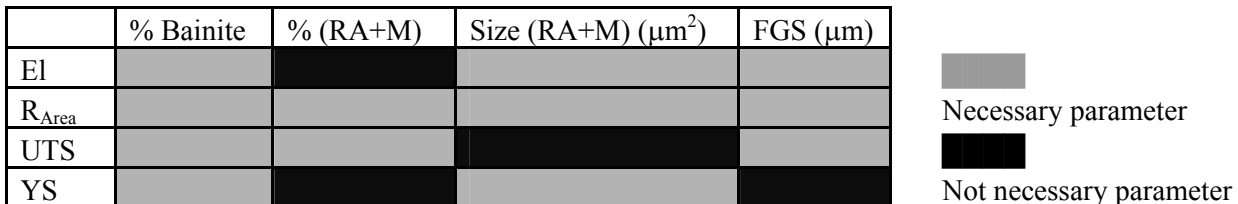


**Figure 8.2** Diagram showing necessary parameters to describe mechanical properties for DP steel-grades.

Using the necessary parameters, linear correlations were established (see Figure 8.3). Analyzing these results, it is possible to state that using more complex functions gives a slightly better description of UTS and YS, but that this not leads to improvement on El and  $R_{\text{Area}}$ . In conclusion, the following results can be highlighted:

- 1) Good linear statistical correlation of elongation (range: from 11 to 31%) and microstructural parameters (bainite fraction, size of martensite islands and ferrite grains).
- 2) Good linear statistical correlation of UTS (range: from 450 to 950 MPa) and microstructural parameters (size of ferrite grains, bainite and martensite fraction) that can be slightly improved using complex function correlation.
- 3) Good linear statistical correlation of YS (range: from 300 to 750 MPa) and microstructural parameters (bainite fraction, size of martensite islands) were found, that might slightly be improved using complex function correlation and adding ferrite grain size.
- 4) No satisfactory results for statistical correlations (linear or complex) of  $R_{\text{area}}$  (range: from 33 to 80%) and microstructural parameters. It was thought, that  $R_{\text{area}}$  might relate to morphology of the second phase. Hence, the integration of morphology in the correlation is introduced in the next paragraph.

$UTS = 672.3 + 11.5 \times \%B + 2.73 \times \%(\text{RA\_M}) - 37.3 \times FGS$	<b>equation 8-9</b>
$YS = 247.4 + 6.57 \times \%B + 85.3 \times \text{size}(\text{RA\_M})$	<b>equation 8-10</b>
$El = 24.4 - 0.42 \times \%B - 1.34 \times \text{size}(\text{RA\_M}) + 1.18 \times FGS$	<b>equation 8-11</b>
$R_{\text{area}} = 39.7 - 1.21 \times \%B - 0.91 \times \%(\text{RA\_M}) + 14.1 \times \text{size}(\text{RA\_M}) + 5.7 \times FGS$	<b>equation 8-12</b>

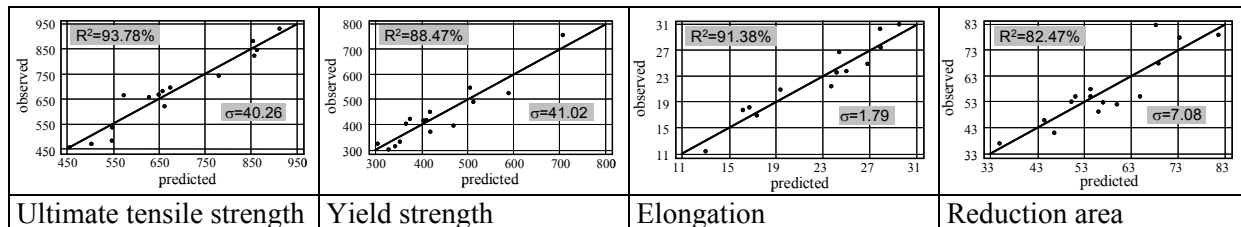


**Figure 8.3** Equations and statistical parameters ( $R^2$ ,  $\sigma$ ) of linear correlations between mechanical and microstructural parameters.  $R^2$  = coefficient of determination;  $\sigma$  = standard deviation.

#### Correlation between morphology of secondary phase and mechanical properties

To refine the statistical analysis between microstructural features and mechanical properties of the DP series a shape factor was included in the analysis. The used shape factor is the elongation of martensite + retained-austenite islands. The elongation is calculated as a ratio between maximal and minimal ferrets of islands. This parameter was measured only for islands inside analyzed images: edge-features

were eliminated. An effort was made to correlate this parameter with previously obtained mechanical properties. No significant correlation between UTS, YS, total El, R-area and shape factor (elongation) was found. The very high dispersion of elongation data is probably due to the incertitude introduced by the elimination of edge particles (for example, a long martensite band that touches the edge of the image will be eliminated). Nevertheless, taking into account this high dispersion of measurements, some tendency can be observed: the higher particle elongation corresponds with lower R<sub>area</sub> values.

### 8.3.2 Bainite and martensite volume fractions in relation to production properties (DP series)

Corus investigated two series of DP grades (DP\_a and DP\_b) with different chemical compositions. Both DP series consisted of nine samples corresponding with varying reductions and top-temperatures during processing. The image analysis procedure for determining M and bainite constituents, which was developed in WP4, was used for microstructural quantification. For both DP grades correlations were found between M/bainite area fraction and top temperature, (see Figure 8.4). No correlation was found between M/bainite area fraction and reduction. The relations found between top temperature and M/bainite area fraction are for both DP grades quite different. For DP\_a this could be explained by prolonged residing time in the bainitic phase field due to the higher top temperatures whereas DP\_b never crosses reaches the bainitic phase field<sup>[19]</sup>.

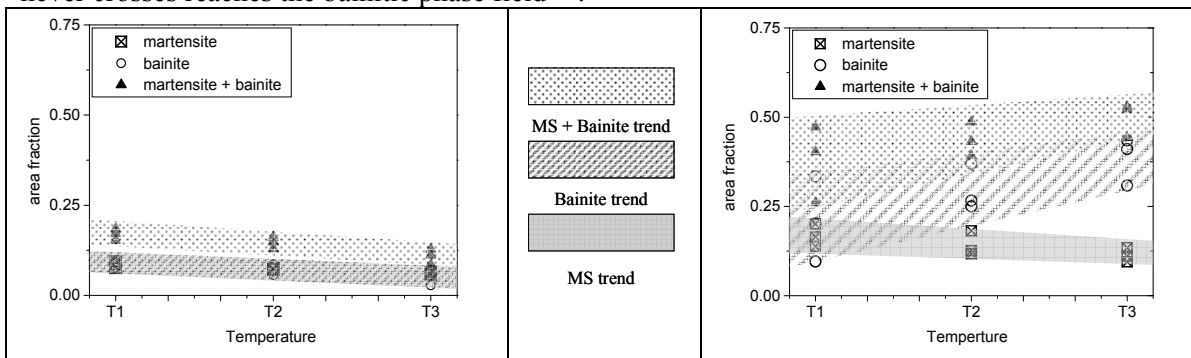


**Figure 8.4** Martensite, bainite and martensite+bainite area fractions vs. top temperatures (T1, T2 and T3) for DP-a (left) and DP-b (right).

### 8.3.3 Phase fraction and phase (or grain) size in relation to mechanical properties (DP series)

The validation of procedures developed in WP3 to WP5, especially those for EBSD, was done by CRM on a series of DP steels produced at Arcelor with varying mechanical properties. The samples were first analyzed by means of LOM regarding martensite and bainite fraction and ferrite grain size (diameter) if possible, see Figure 8.5 and Table 8.3 for details. All samples were investigated by means of EBSD to complete missing parameters. All specimens were prepared following a strict procedure. The specimens were ground on paper with grit 80, 220, 600, 1200 and polished with diamond paste of 3 and 1 µm followed by alumina paste of 0.3 µm. Finally, the specimens were polished with OPS suspension. No etching was applied. Measurements were performed on RD-ND planes. The acceleration voltage was 25 kV, the spot size 4.5 and the working distance (WD) 20 mm. The specimen was tilted at an angle of 75°. An area of 100µm \*130µm was measured with a step size of 0.2 µm.

From Figure 8.5 it is clear that the microstructure of sample 36 has a very low fraction of martensite and that martensite islands are 1 micron or less in size and located on ferrite grain boundaries. Due to the small amount and small size, no accurate distinction can be made between grain boundaries and martensite based on IQ, KAM or CI. Since no better alternative was available, a CI based partition was made of the raw data, where a CI lower than 0.05 includes ferrite grain boundaries as well as martensite islands. Also some points in the middle of larger ferrite grains are included, which for sure corresponds with ferrite. From this partitioning, 82% ferrite was found with a grain size of around 6.8 µm. This ferrite phase fraction is clearly an underestimation. The ferrite grain size of sample 36 determined with EBSD is in good agreement with the value obtained by LOM.

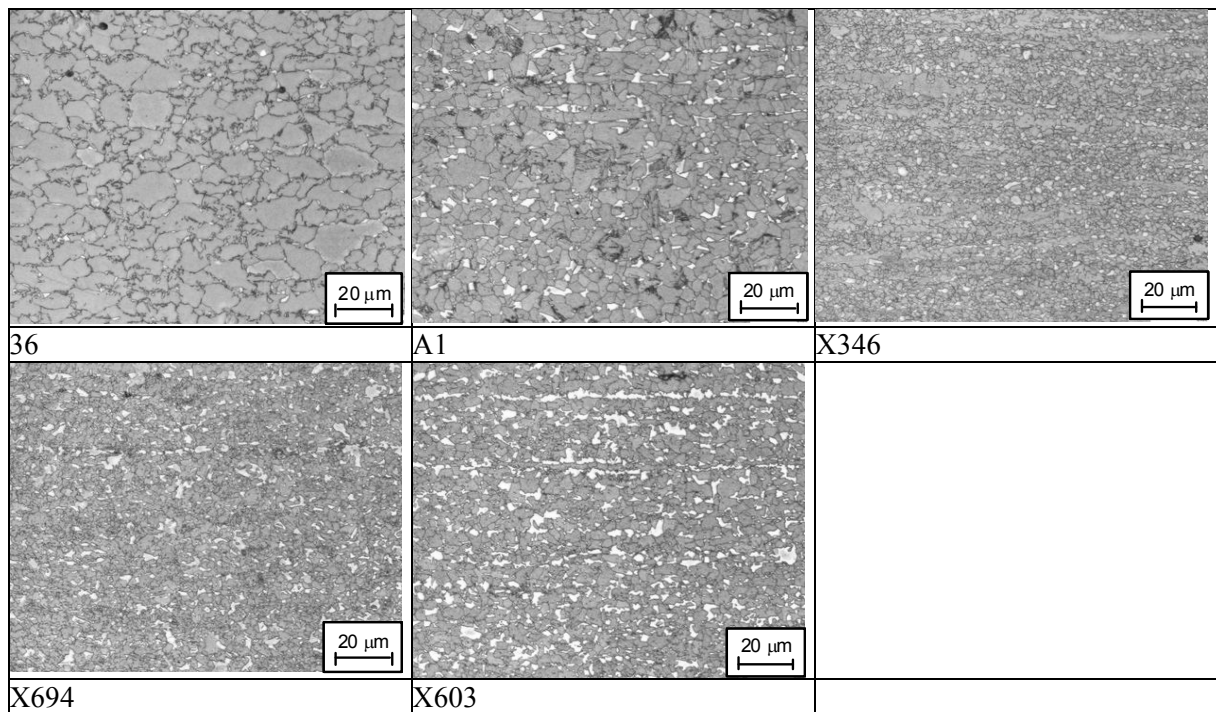


**Figure 8.5** Overview of DP steels for validation (etchant LePera).

**Table 8.3** Mechanical properties of a series of DP steels and microstructural parameters determined by LOM and EBSD.

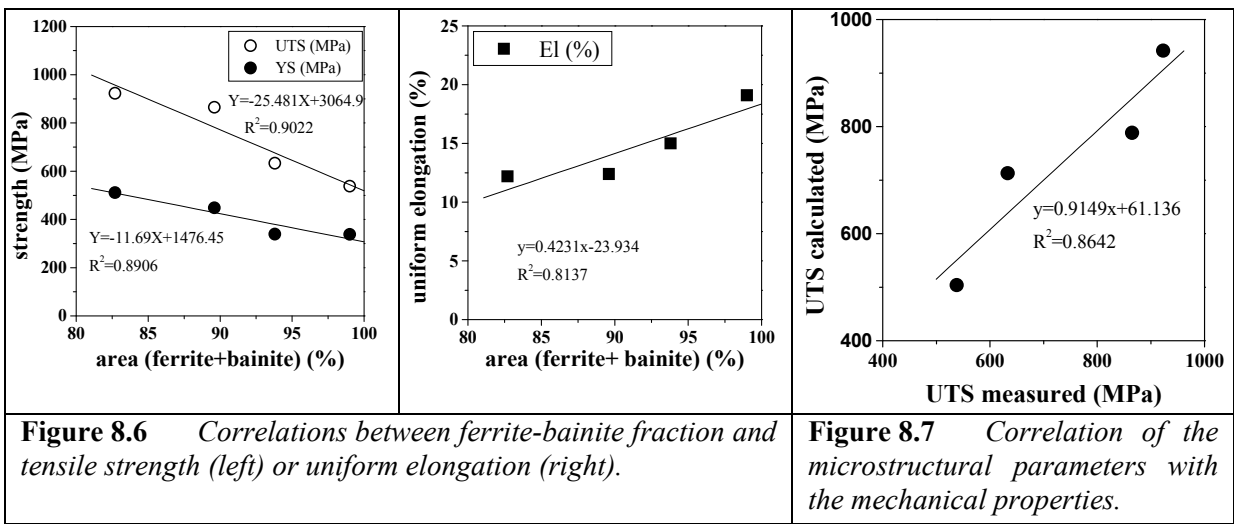
Sample code	Mechanical properties				LOM				EBSD*	
	YS (MPa)	UTS (MPa)	Uniform El (%)	Total El (%)	M (%)	B (%)	Ferrite+B (%)	FGS (μm)	Ferrite (%)	FGS (μm)
36	338	538	19.1	30.2	1	6.2	99	6.4	82	6.8
A1	339	633	15.0	23.0	6.2	6.8	93.8	**	74	4.3
X346	414	745	14.2	22.2	11.1	**	**	**	**	**
X694	448	865	12.4	17.0	10.4	5.2	89.6	**	78.6	4.2
X603	511	923	12.2	18.5	17.3	2.8	82.7	**	80	3.6

\* See text for details; \*\* Not possible to measure or determine.

The ferritic matrix of microstructure A1 is finer than that of 36 but the martensite islands are much larger. There are also bainite regions visible. When a partitioning is made based on CI, the ferrite area represents 74% which is also too low compared with light-optical microscopy. The average ferrite grain size is 4.3 μm. The ferritic matrix of microstructure X694 is again finer as that of A1. More martensite can be seen in smaller islands. There are also bainite regions visible albeit less clear. When a partitioning is made based on CI, the ferrite area represents 78.6% which again is too low compared with the optical microstructure. The average ferrite grain size is 4.2 μm. When this value is compared with LOM and with material A1, it is clear that in this specific case determination of the ferrite grain size by EBSD, is not accurate.

Sample X346 showed a lot of unrecrystallized ferrite areas which made it impossible to get an accurate result with the SEM-EBSD equipment at CRM. As was already concluded during the Round Robin Test, a SEM equipped with a LaB<sub>6</sub> filament is not suitable to investigate in detail fine advanced microstructures of modern high-strength steels. Material X346 is not taken into account to determine the correlation in following paragraphs.

Based on microstructural parameters quantified by LOM (second phase fraction) and EBSD (ferrite grain size), a correlation was found with mechanical properties presented in Figure 8.6. A good correlation was found between ferrite-bainite fraction and tensile strength (Figure 8.6 left), while this was less for the correlation with uniform elongation (Figure 8.6 right).



When the contribution of martensite and ferrite grain size, based on the Hall-Petch relation, to the tensile strength is taken into account, the correlation could not be significantly improved ( $R^2=0.86$ ) equation 8-13 was determined for the quantified microstructure properties related to UTS.

$$UTS = 12.68 f_{\alpha} \frac{1}{\sqrt{GS_{\alpha}}} + 22.49 f_M \quad \text{equation 8-13}$$

In equation 8-13: UTS = ultimate tensile strength (MPa);  $\alpha$ =ferrite+bainite; M=martensite; f=area (%); GS=grain size ( $\mu\text{m}$ ).

### 8.3.4 Phase fraction and phase (or grain) size in relation to mechanical properties of TRIP steel

Metallographic analysis, according to procedures described in §2.2.1.4.1 in combination with a thermo-kinetic model simulation to determine the bainite fraction, was performed by Arcelor. The results are shown in Table 8.4. In this study no distinction was made between RA and M fraction. The Martensite fraction was estimated to be maximal ~1-2%.

**Table 8.4** Results of mechanical tests, metallographic analysis and thermo-kinetic model simulation.

nr	UTS (MPa)	YS (MPa)	El (%)	M/RA fraction (%)	Average area M/RA islands ( $\mu\text{m}^2$ )	Bainite (%)
1	633	369	29.3	5.1	1.0	23
2	692	349	28.4	11.6	1.3	26
3	710	333	26.2	9.9	0.9	23
4	772	343	24.6	19.0	0.8	25
5	813	344	19	12.0	0.7	27
6	915	386	16.7	20.8	2.1	23

Although the database of TRIP steels is not very large, the same statistical approach as for DP steels was applied. The correlation matrix between different microstructural parameters didn't reveal any dependence. Having concluded this, the correlation matrix between microstructural and mechanical parameters was built. This matrix shows that each mechanical parameter correlates with only one microstructural parameter (El and UTS with % M/RA, YS with Area M/RA). This is illustrated with the diagram of Figure 8.8. In contrast to the DP series, in case of TRIP the bainite fraction doesn't correlate with any mechanical parameter. Arcelor comes to the conclusion that the bainite fraction simulated by thermo-kinetic model is not correct and that another method is necessary to define this fraction properly,(outside the scope of this project).

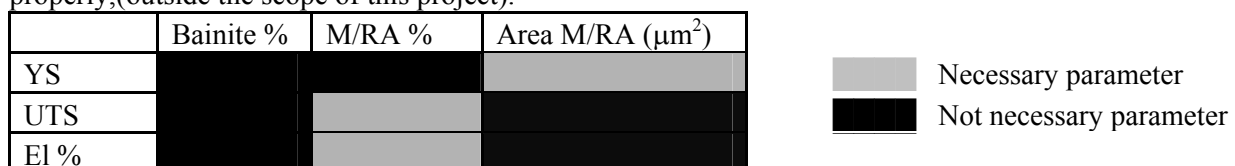


**Figure 8.8** Diagram showing necessary parameters to describe mechanical properties of TRIP steel-grades.

Despite these difficulties, a statistical analysis was made and the results are shown in Figure 8.9 and in equation 8-17 to equation 8-19 were the statistical parameters (coefficient of determination ( $R^2$ ) and correlation coefficient (CC)) of individual best fitting correlations between UTS, YS, El and different microstructural parameters are shown. Since the dataset are relatively small and the calculated bainite fraction is regarded as unreliable the obtained results are only indicative.

$UTS = 353.5 + 7.72 \times \%B + 12.25 \times \%M / RA + 47.02 \times areaM / RA$	equation 8-14
$YS = 345 + 0.85 \times \%B + 0.56 \times \%M / RA + 32.7 \times areaM / RA$	equation 8-15
$El = 46.3 - 0.54 \times \%B - 0.5 \times \%M / RA - 2.16 \times areaM / RA$	equation 8-16

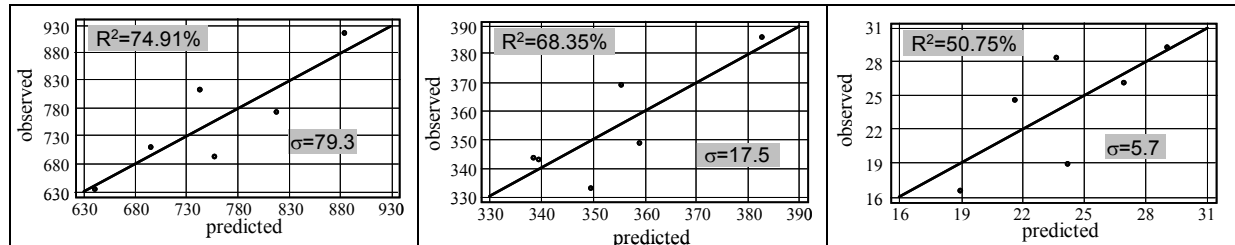


**Figure 8.9** Curves, equations and statistical parameters ( $R^2$ ,  $\sigma$ ) of linear correlations between mechanical and microstructural parameters.

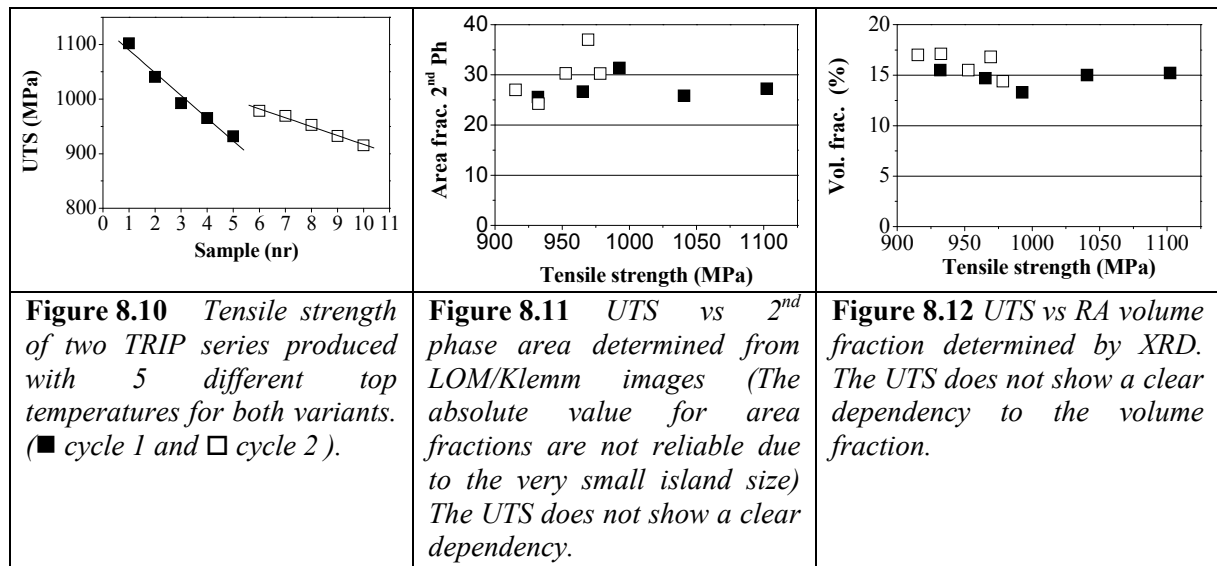
$$UTS = 1/(0.00167 - 0.0000253 \times f(M / RA)) \quad R^2 = 73.9 \quad CC = 0.86 \quad \text{equation 8-17}$$

$$YS = \sqrt{113793 + 7862 \times area(M / RA)^2} \quad R^2 = 67.55 \quad CC = 0.82 \quad \text{equation 8-18}$$

$$EL = \sqrt{-3.85 + 2020 \times \sqrt{1/f(M / RA)}} \quad R^2 = 49.38 \quad CC = 0.7 \quad \text{equation 8-19}$$

### 8.3.5 Phase fraction and phase (or grain) size and other derived parameters in relation to mechanical properties for TRIP.

Corus used TRIP grades to investigate the discriminative power of procedures developed in §2.2.1.4.3, §3.2.5 and §3.4.1. Two TRIP series, having the same chemical composition, were produced with different annealing cycles, cycle 1 and 2. Within these two main annealing cycles the top temperature was varied, see Figure 8.10. Challenging aspects of these series are the preparation of the meta-stable RA and the small size of the second phase features. Since both series show a significantly different tensile strength evolution for the two different annealing cycles it was decided to use tensile strength as the main parameter to study the discriminative power of developed procedures.



The second phase area fraction of all samples was first estimated by LOM (Klemm etching, Figure 8.13). The RA and body centred tetragonal (BCT) martensite fraction was also determined by XRD.

Second phase area fraction determined with LOM/Klemm was unreliable due to the very small microstructural features. This is both reflected by the large spread in 2<sup>nd</sup> phase area fraction compared to the spread in the XRD measurements and the difference in absolute value compared to the 2<sup>nd</sup> phase volume fraction determined with XRD, see Figure 8.11 and Figure 8.12. Based on the 2<sup>nd</sup> phase fraction determined by LOM or XRD there is no obvious correlation between 2<sup>nd</sup> phase fraction and tensile strength. The tensile strength varies from 900-1100 MPa whereas the 2<sup>nd</sup> phase volume fraction determined by XRD is for all samples within 15±2%. Phase, IQ and GS were used for EBSD data-set partitioning. After partitioning, MAD's were determined between specific phase interactions in order to check the obtained MAD's corresponds to the expected MAD's for specific phase interactions, see Figure 8.14.

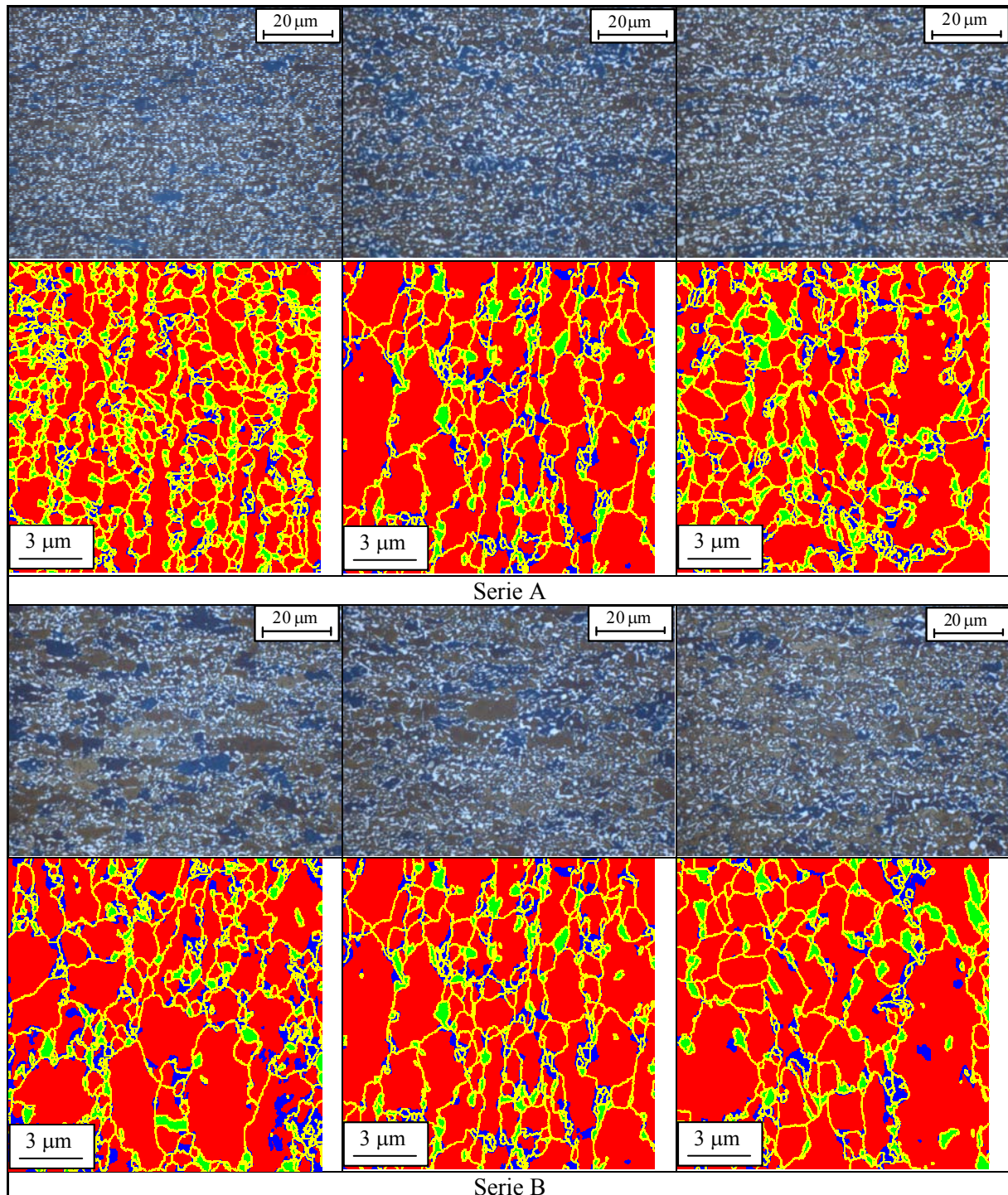


**Figure 8.13** Upper images LOM (Klemm, RD/TD; RD = horizontal; Lower images EBSD based phase map ■ = Ferrite ■ = retained austenite ■ = martensite ■ = grain boundaries (Scansize 15x15  $\mu\text{m}$ , step size 50 nm, RD/TD RD = vertical).

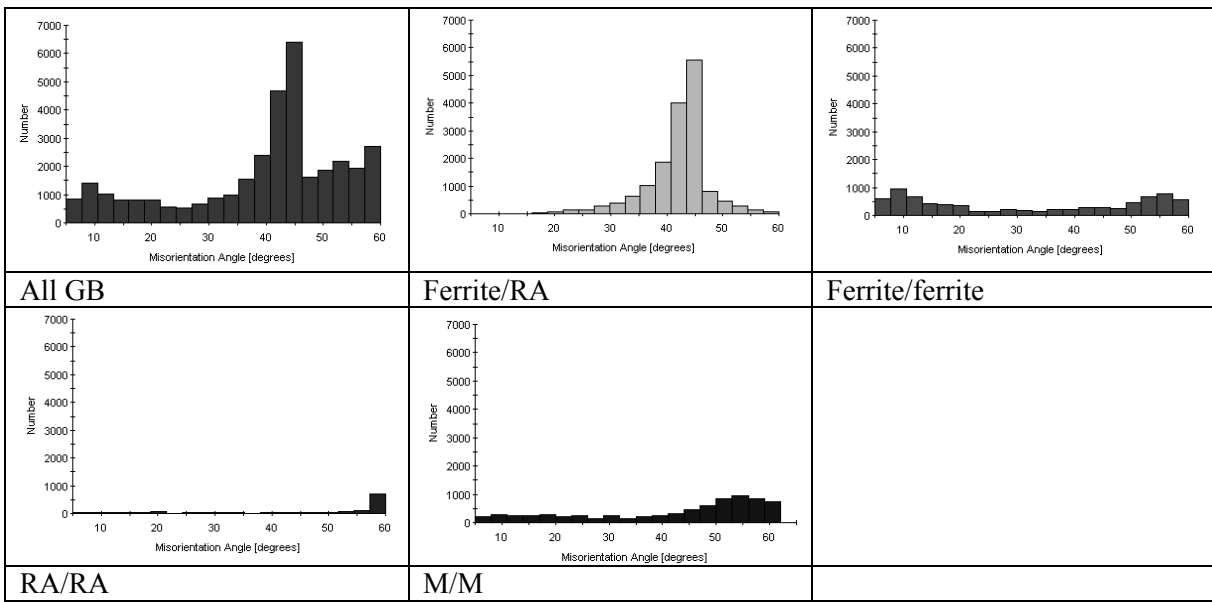
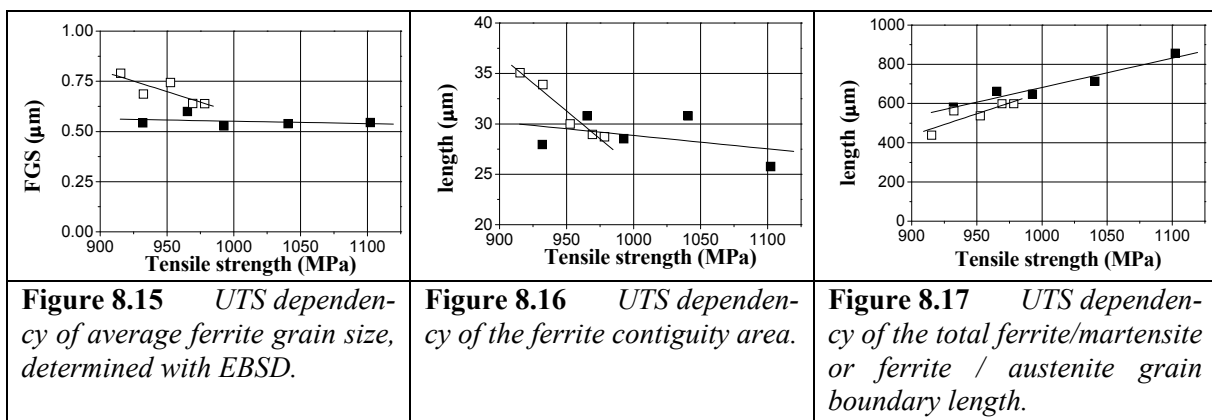


**Figure 8.14** Characteristic misorientation angle distributions for specific phase interactions for TRIP series.

The average ferrite grain size from both series was determined using EBSD. Scansize  $15 \times 15 \mu\text{m}$ , step size 50nm. For cycle 1 the average grain size was for the 5 different top temperatures quite similar ( $0.55 \mu\text{m}$ ). The UTS does not show a clear dependence on average grain size for cycle 1. For cycle 2 a small dependence is observed with grain size. As expected, a larger average grain size leads to a lower UTS ( $0.6 \rightarrow 0.8 \mu\text{m}$ ). See Figure 8.15. Interesting is the reason why there is no grain size dependency for cycle 1 which has a wide spread in UTS values. Therefore also other parameter dependencies were tested. The influence of the contiguity area (see §2.4.2) of the ferrite fraction is for both series different. The cycle 1 series shows no clear dependency of UTS on ferrite contiguity. However cycle 2 series does show a dependency with ferrite contiguity area.

In Figure 8.17 the UTS dependency of the total ferrite/martensite or ferrite / austenite grain boundary length is plotted. This quantified parameter shows a clear correlation with UTS.



### Conclusion

The UTS in two TRIP series with the same chemical composition but produced with different annealing cycles and top temperatures shows a clear dependency with the ferrite/martensite + ferrite/retained austenite grain boundary length.

#### 8.3.6 Bainite laths widths in relation to heat treatment (Object Based Quantitative Analysis)

RWTH investigated the potential of the object based analysis approach which has been described and discussed in section §3.5.3. A single object based analysis procedure was created for extraction of morphological properties from 18 different samples consisting of a mixture of bainite and M/RA constituents.<sup>[19,25]</sup> The 18 samples were produced out of four medium carbon steel grades. Samples were

grinded, polished, electrolytically polished and mildly etched with  $\text{HNO}_3$ . The developed analysis routine was applied to the FEG-SEM images. Due to the different compositions of the basic materials and heat treatments given, the resulting morphologies of the 18 samples show large variations, i.e. the lath-like bainite vary between small thin needles to long, broad laths with differently shaped boarders. Additionally, the image quality, brightness and contrast varied considerably, see Figure 8.18. The created analysis routine was able to cope with all these variables. Nearly no commonly used microstructural analysis method is able to cope with these described variations at the same time, without (subjective) operator interventions.

The microstructural analysis routine has been designed to detect and extract only the widths of bainite laths. This parameter is considered to be related to the possible distance for dislocations to freely move and hence relevant for mechanical properties. The detection of phase fractions and other parameters was neglected in order to simplify the analysis task and focus on the robustness of the approach with respect to the variety of bainite morphologies and image settings for the images. The strategy was to reliably extract a good portion of the identified laths and to neglect structures which are more difficult to classify.

In Figure 8.18 representative SEM-images from each investigated steel grade are shown. Below each image, the corresponding classification result is displayed, in which the identified bainite laths are coloured in orange. The image structures being identified as bainite had to meet also geometric criteria in order to be classified as “bainitic laths”. Their aspect ratio had to exceed 6.5, while the morphological compactness had to be lower than 3.1, (see for definition of compactness Table 4.5). In the following paragraphs four experimental series are discussed.

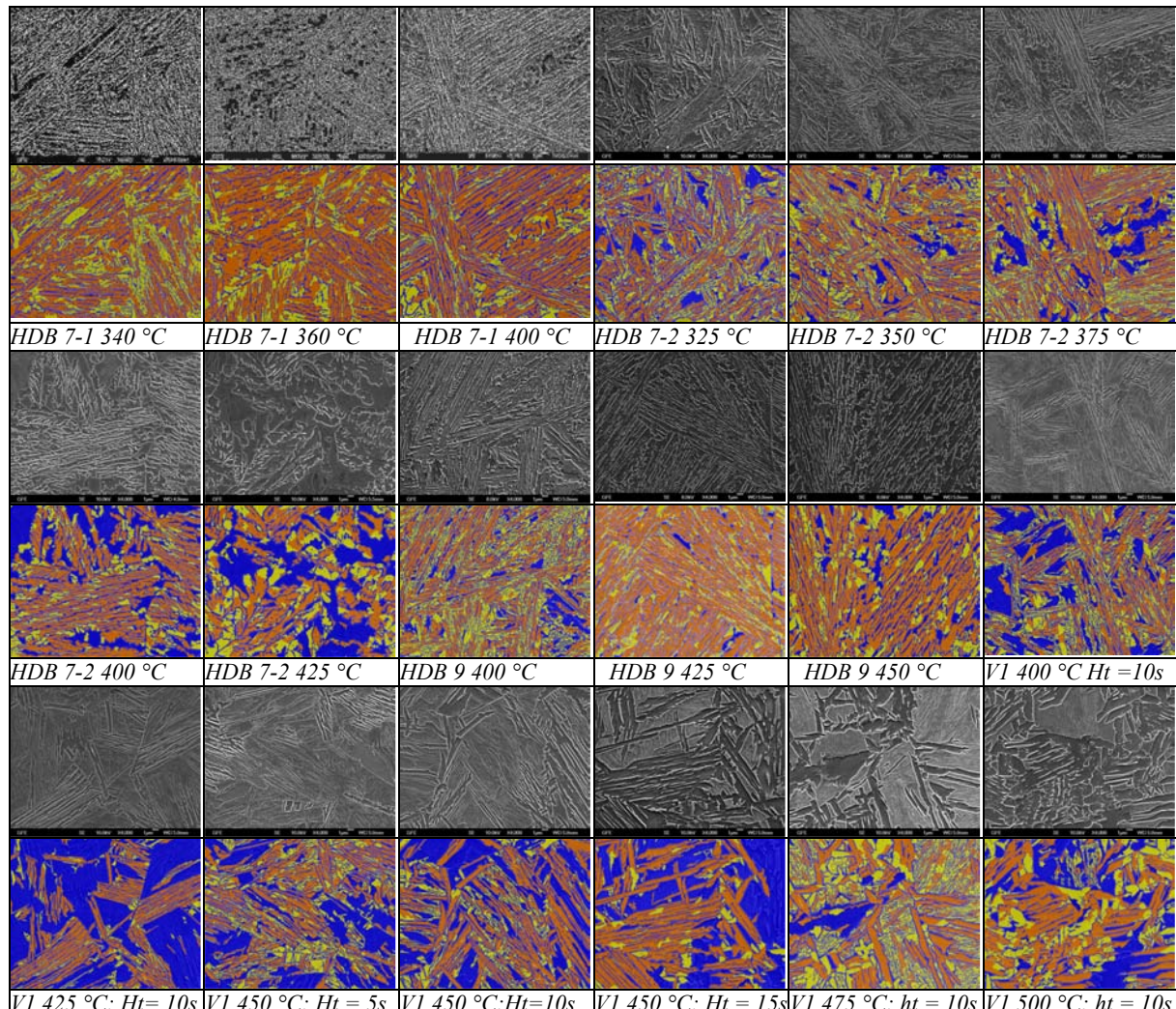


**Figure 8.18** Representative SEM images (SE, 10KV, FOW=30 $\mu\text{m}$ ) of quantified microstructures, classification results, sample codes, temperature and holding times. The identified bainite laths are coloured in orange. The other colours within the result-images show remains of the structure cognition process and not relevant in this context.

Three HDB 7-1 samples were austenitized, cooled down to different holding temperatures in range of the bainitic temperature field (at 340 °C, 360 °C and 400 °C) and held for 10 min before quenching (see Figure 8.18). Figure 8.19 shows a boxplot distribution of the lath widths of the three steel grades. The distributions show a very small increase of the 50 percentile lath width value with increasing holding temperature, accompanied with a smaller width of the distribution.

Five HDB 7-2 samples were austenitized, cooled down to different holding temperatures from 325 °C to 425 °C and held for 10 min before quenching, see Figure 8.18. Figure 8.19 shows the distribution of lath widths of the 5 steel grades. The distributions show nearly no shifting towards broader laths at increasing holding temperature (325 °C → 375 °C). However, a further increase to higher temperature shows a distinct shift in the distribution to broader laths. This is in accordance with visual observations in the SEM images.

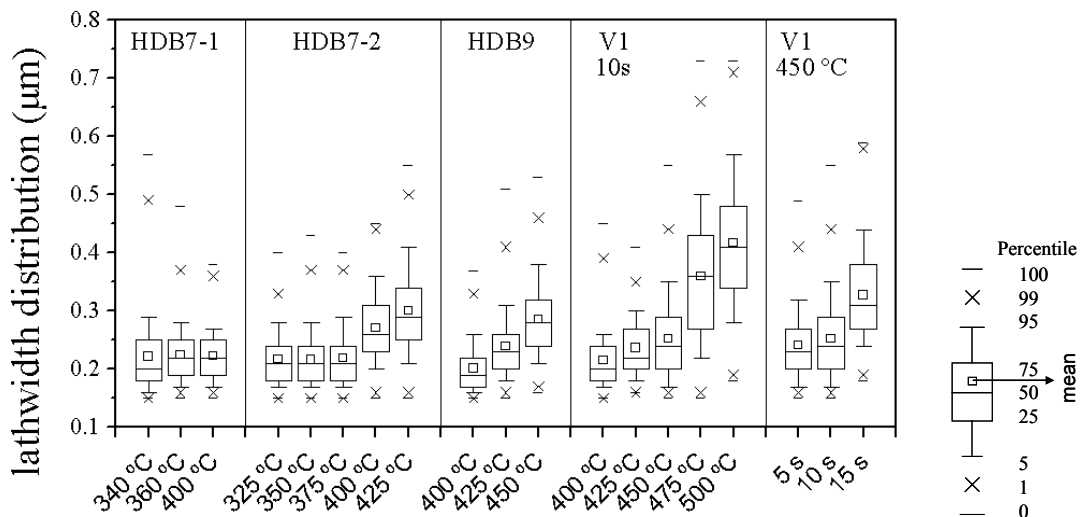


**Figure 8.19** Box plot of the lath width distribution of the microstructures shown in Figure 8.18.

Three HDB 9 samples were austenitized, cooled down to different holding temperatures from 400 °C to 450 °C and held for 10 min before quenching, see Figure 8.18. Similar to the previous distributions, the broadening of the laths with higher temperatures is clearly reflected in the box plots.

Five V1 samples were austenitized, cooled down to different holding temperatures from 400 °C to 500 °C and held for 10 s before quenching. Additional 2 samples were treated with a constant holding temperature (HT) of 450 °C and holding times (Ht) of 5 s and 15 s, see Figure 8.18. Like in the previous steel series, Figure 8.19 again shows very clearly the broadening of the ferritic laths with increasing holding temperature. Figure 8.19 also displays the effect of increased holding time at constant temperature. It is noteworthy that there seems to be nearly no effect when doubling the time from 5 to 10 s. However, increasing the time with an additional 5 s has nearly the same effect on the lath widths as raising the holding temperature by 25 °C with constant holding time.

#### Conclusions

As the analysis procedure was applied to all images without any operator intervention, it is clearly non-subjective. Being able to cope with different morphologies within the different images as well as different brightness and contrast settings of the images shows the robustness of the developed routine. The strategy of separating the analysis process into a structure cognition part and a classification part therefore leads to promising results. However, for a complete analysis including more properties and the ability to identify more different phase constituents also in other steel grades, a more sophisticated classification procedure based on a broad data-base has to be built. The discriminative power of the method was illustrated by the clear relations between lath width distributions and heat treatments.

### 8.3.7 Ferrite, martensite and bainite volume fractions in relation to mechanical properties (CP series)

To validate procedures developed in section 3.5.4 and to test the discriminating power of these procedures, TKS produced a series of complex-phase specimens with a pronounced spread in mechanical properties. The specimens were hot-rolled on a laboratory scale. The rolling schedule and

final rolling temperature were kept constant for all eight specimens, whereas the coiling temperature was varied. Typical IQ and IQ+KAM maps of these samples are shown in Figure 8.20.

Figure 8.21B shows the variation of strength and elongation with coiling temperature. The ultimate tensile strength decreases from 1073 to 843 MPa for the  $T_1 \rightarrow T_5$  temperature range and is nearly constant at higher coiling temperatures. The yield strength shows generally less variation, but presents a considerable drop for the second highest temperature. The elongation stays constant for the lower coiling temperature range and grows rapidly for the higher temperatures. To characterize the microstructure, metallographic sections were made, on which micro-hardness measurements were performed to evaluate the local strength for comparison with microstructure.

#### *EBSD characterization of CP microstructure*

On the metallographic sections EBSD measurements were performed. The IQ maps show that the average IQ value increases, i.e., the lattice distortion decreases, with temperature. Furthermore, for coiling temperature  $T_1 \rightarrow T_5$  the microstructure has an acicular character and becomes more globular with increasing temperature. For the second highest temperature ( $T_7$ ) a DP-like microstructure is present, consisting of low IQ martensite and high IQ globular bainite. It is, however, difficult to ascertain a clear threshold in temperature where the change in microstructure begins.

From the EBSD data sets the average grain size was calculated for GTA's of  $2^\circ$ ,  $5^\circ$  and  $15^\circ$ . The evolution of grain size with coiling temperature is shown in Figure 8.21C. Regardless of the threshold angle, grain size is nearly constant in the lower temperature range ( $T_1 - T_5$ ) and then shows a sharp increase for the higher temperatures ( $T_6 - T_8$ ). This increase corresponds with the change from acicular to globular structure and thus can be used to define the onset of a structural change.

The local misorientation was described by plotting the Kernel Average Misorientation (KAM) using a kernel distance of  $1\mu\text{m}$  and a cut-off angle of  $5^\circ$ . For a quantitative evaluation IQ and KAM information was combined into one map using the scheme described in §3.5.4. The combination shows a change in microstructure for the whole temperature range (Figure 8.20). The different colours were allocated to the phases martensite, bainite and ferrite (see Figure 8.21A) which allows subsequent quantitative image analysis of the microstructures.

Quantitative microstructural analysis shows a constant increase of the bainite content with temperature whereas martensite decreases, Figure 8.22A. The ferrite content is constant for the acicular structures but increases with the onset of globular microstructures. This increase is at the expense of a steeper martensite decrease content but does not influence the constant increase of bainite.

#### *Correlation of microstructure and properties*

Within the temperature range  $T_1 \rightarrow T_5$  a constant grain size was observed in combination with a 250 MPa spread in ultimate tensile strength as well as a 100 MPa drop in yield strength, which precludes any attempt at correlating grain size and tensile strength. (Figure 8.21)

However, grain size and tensile elongation, show a satisfying correlation (Figure 8.22B). This correlation can also be associated with grain shape, corresponding well to the acicular and globular structures observed. Further experiments will be necessary to distinguish clearly between these effects.

The sudden drop in yield strength at temperature  $T_7$  is associated with the unique DP-like microstructure consisting of hard martensite/bainite islands within a soft ferritic matrix.

The changes in phase content, which were established performing image analysis of combined (IQ+KAM)-maps from EBSD measurements, explain the large change in strength in the acicular regime of the microstructure. Since martensite is replaced by bainite the strength decreases with temperature even though no change in grain size is evident.

In addition, using a simple rule-of-mixture employing the volume fractions  $X_i$  and respective Vickers hardness  $HV_i$  of the single phases it was possible to fit the measured hardness quite well (equation 8-20)

$$HV_{calc} = X_{martensite} \cdot HV_{martensite} + X_{bainite} \cdot HV_{bainite} + X_{ferrite} \cdot HV_{ferrite} \quad \text{equation 8-20}$$

$$HV_{martensite} = 450 \text{ HV}; \quad HV_{bainite} = 350 \text{ HV}; \quad HV_{ferrite} = 80 \text{ HV}.$$

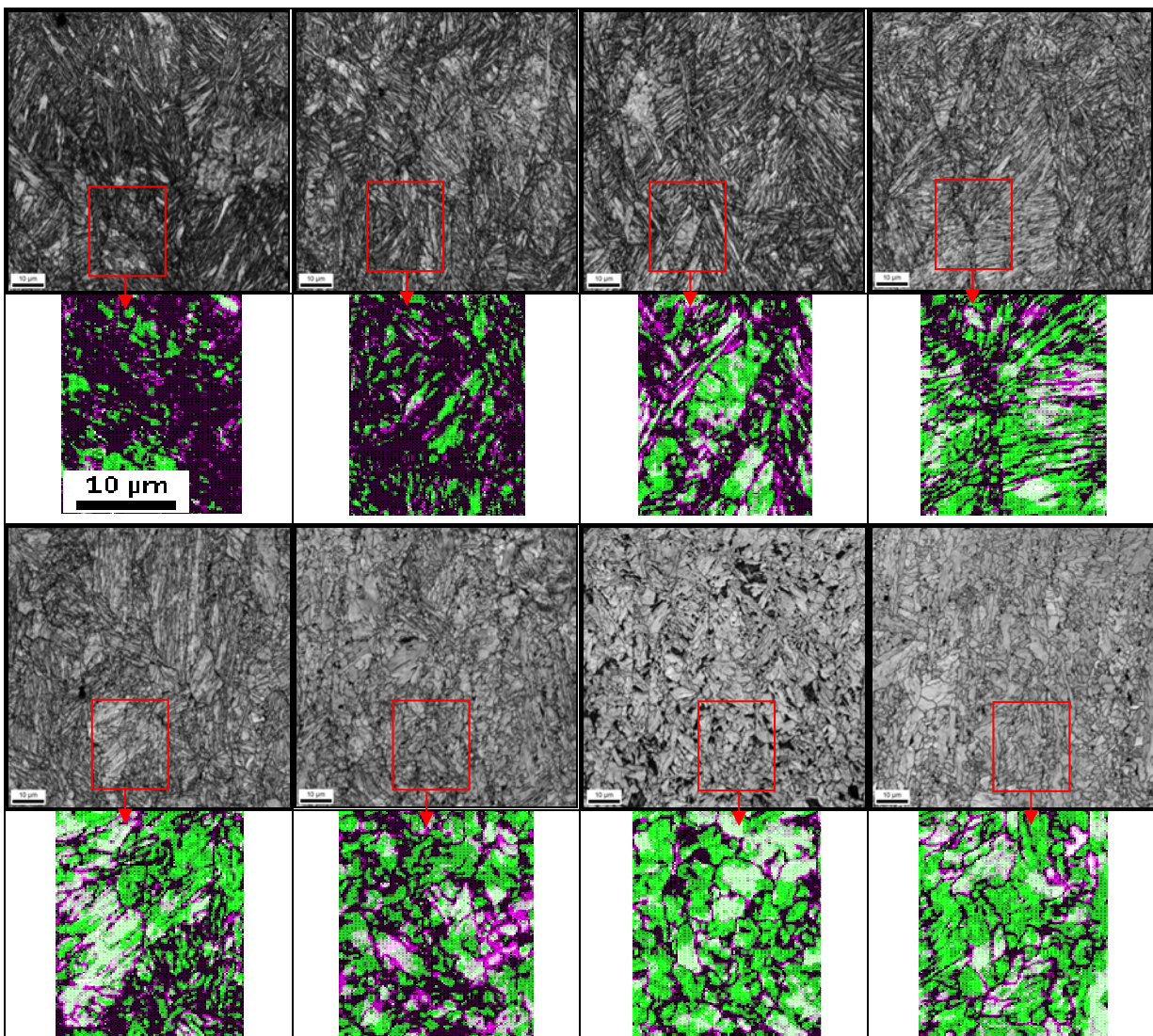


**Figure 8.20** Overview of the image Quality (IQ, FOW 90  $\mu\text{m}$ ) together with a detail of the IQ+KAM maps for CP steel coiled at eight different cooling temperatures ( $T_1 \rightarrow T_8$ ).

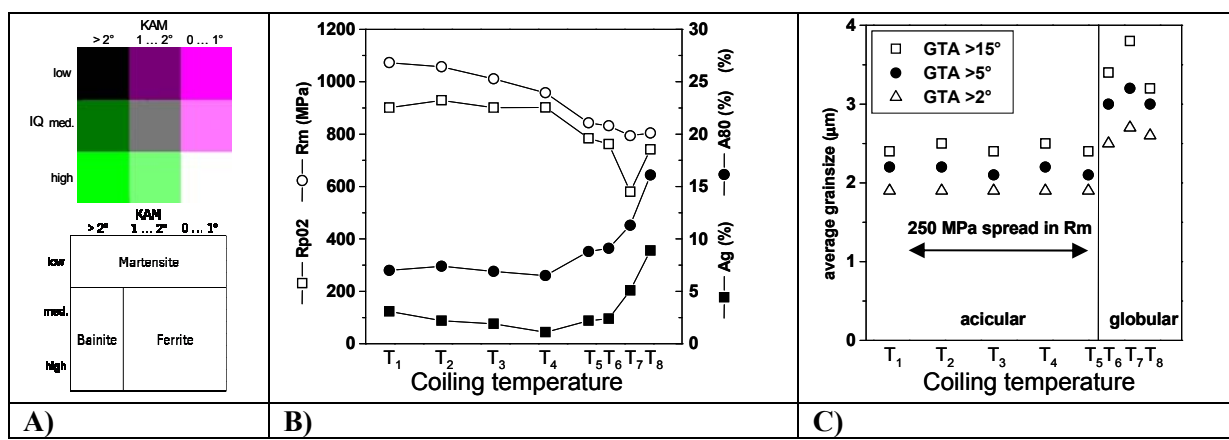


**Figure 8.21** A) Phase allocation for combined [IQ+KAM] maps. B) Mechanical properties of a hot rolled CP-grade with different cooling temperatures C) Grain size of CP800 steel as function of cooling temperature (Rm= Ultimate Tensile Strength (UTS); Rp= Yield Strength (YS); Ag = Uniform Elongation (UE); A80 = Elongation after fracture (EAF); GTA = grain tolerance angle).

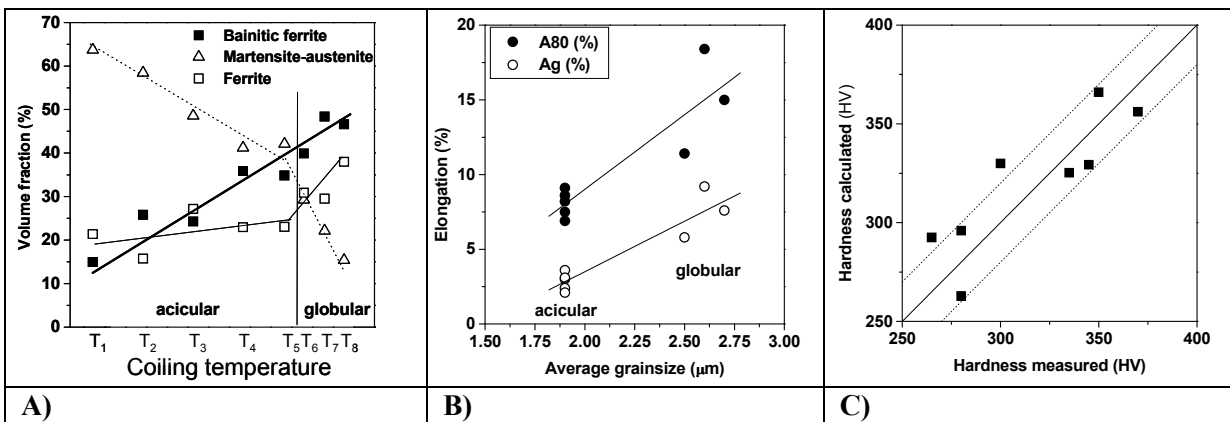


**Figure 8.22** A) Evolution of phase content with cooling temperature for CP-grade; B) Correlation between ductility and grain size for CP-grade; C) Comparison between measured and calculated hardness for CP-grade.

### 8.3.8 Effective Grain Size in relation to Strength (M series)

Kimab has tested the discriminative power of the effective grain size determined with EBSD for seven martensitic materials, in relation to Rp and Rm. Surface preparation was done following the method described in WP3 and WP5 including both silica colloidal suspension polishing and a short (1 sec) electro-polishing step. The materials and EBSD conditions are summarized in Table 8.5.

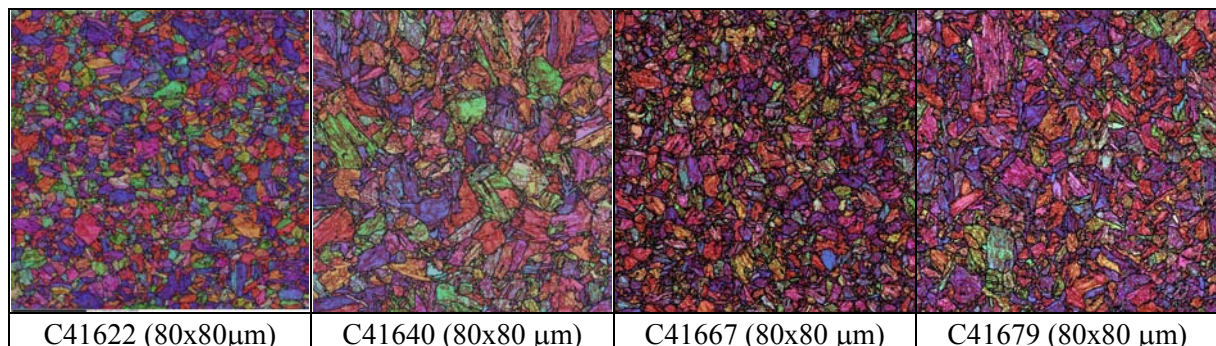
**Table 8.5** Description of martensitic materials.

Sample properties		Mechanical properties			Chemical composition (w%)					EBSD details*			
ID	Thickness mm	Rp0.2 MPa	Rm MPa	A80 %	C	Mn	Si	B $10^{-3}$	V; Nb	Zero raw data	sol. %	Zero sol. NR** %	
C41622	0.54	1210	1396	6	0.14	1.55	0.21	2.2	0.01; 0.014	23	0.95		
C41640	0.97	848	970	5	0.048	1.92	0.21	0.2	0.00; 0.001	15.5	0.6		
C41667	1.44	1161	1368	5	0.14	1.50	0.21	0.4		23.1	1.4		
C41679	1.53	1076	1269	5	0.112	1.60	0.19	0.2	0.01; 0.014	30	3.7		
C41680	1.49	1307	1533	4	0.201	0.98	0.21	0.2	0.01; 0.016	26	1.9		
C41687	1.51	1106	1292	4	0.116	1.64	0.22	2.4	0.01; 0.002	30.3	1.4		
C41749	2.05	1188	1440	6	0.167	1.28	0.22	0.3	0.01; 0.014	30.8	2.5		

\* Step size 0.1  $\mu\text{m}$ ; scan speed ca. 20 points/sec, i.e.  $\approx$ 12 hours per scan; field size ca. 0.75  $\text{mm}^2$ ;

\*\*NR = noise reduction, see text for details.

Basic noise reduction (NR) that was performed on the raw data in the HKL Tango software for all jobs before any analysis: 1) NR level 6 iteration, 2) Remove spikes, 3) NR level 5 iteration, 4) Grain Size < 0.20 delete, 5) NR level 6 iteration, 7) Remove spikes, 8) NR level 5 iteration. For the 4th step, “Grain Size < 0.20 delete”, then for the calculation of average grain size the GTA was set to 15°, and boundary completion allowed to 10°. The small grains were then ranged to a subset which was the set to zero. Subsequently the “0” pixels were replaced by the following noise reduction (NR) procedure. When Kuwahara filter was used the following settings were made: 3\*3, 5° smoothing, 1° artefact. For misorientation distribution diagram a limit on 2° for global minimum angle was used, to avoid total domination of LAGB.



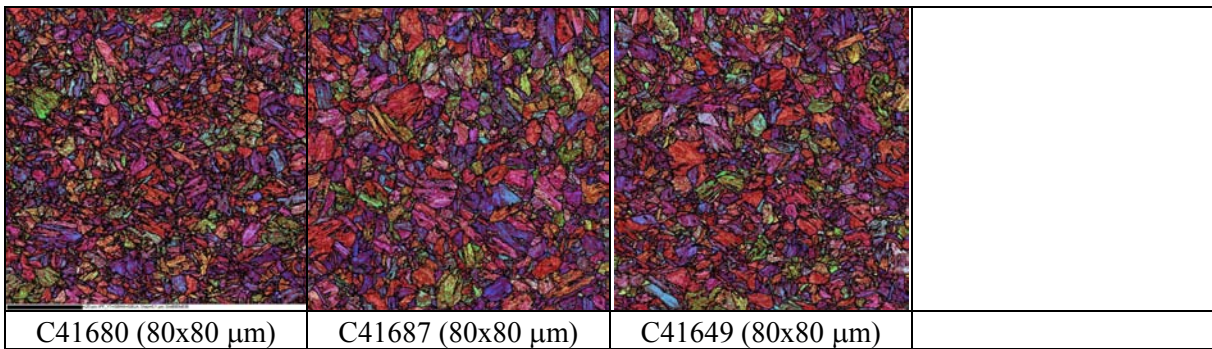


**Figure 8.23** IPF's for the series of martensitic steels. Grain boundaries ( $10^\circ$  misorientation) and sub-grain boundaries ( $1^\circ$  misorientation) are shown in black and red respectively (after Kuwahara filtering).

*Effective grain size in relation to  $R_p$  and  $R_m$ .*

For the calculation of average grain sizes for the analysis of the relation between grain size and strength, mean linear intercepts were used in the Tango software. The Grain Tolerance Angle (GTA) was set to either  $2^\circ$  or  $15^\circ$  misorientation, boundary completion allowed to  $10^\circ$ . The results are shown in Figure 8.24.

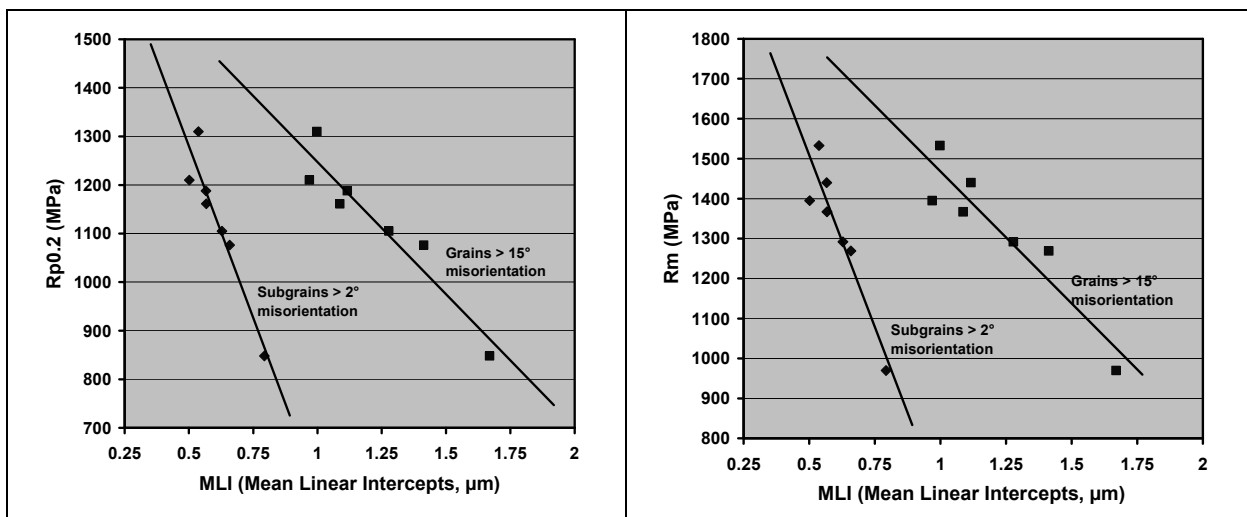


**Figure 8.24** Relation between (sub) grain size the Yield Strength ( $R_p0.2$ ) and Tensile Strength ( $R_m$ ).

In conclusion: the sample preparation and EBSD procedure derived from procedures described in WP3 and WP5 have resulted in a discriminative method for determination of correlations between the effective grain size and the  $R_p$  and  $R_m$  for a series of martensitic steels.

#### 8.4 Task 8.3 Selecting optimal procedures for microstructural quantification

In this task the overview of a number of procedures, which have been developed for quantification of specific microstructural features, is presented. Although in the original aim it was stated that a generic approach for all microstructures would be strived for, it was found during the run of the project that this is not be always realistic, since identification and partitioning of microstructural features is always related to the context of the surrounding matrix. In this section the procedures that are steelgrade or microstructure independ are presented first. In the second part steelgrade or microstructure depend procedures are summarized.

#### **8.4.1 Steelgrade or microstructure independ procedures:**

##### **8.4.1.1 Chemical quantification**

It was concluded that the quantification related to chemistry as described in detail in WP 6, was basically independent of steel grade or microstructure. The techniques used for chemical quantification are SEM/EDX, EPMA and nano-SIMS.

For *macro*-segregation EPMA was found to be an effective tool for quantification. The chemical macro-segregation of Al and Mn in DP and TRIP are presented (§6.2.1 and §6.2.2) as typical examples. Important limitation for segregation measurements by EPMA was found with respect to the measurement of carbon segregation.

For *micro*-segregation both EPMA and nano-SIMS were used and found useful for quantification. However, the lateral scales on which both techniques can operate are quite different (see §6.4). The chemical micro-segregation of C, Al, Si and Mn in DP and TRIP as presented in §6.4.5 shows typical examples of the use of EPMA as a quantification tool. Also a method for the quantification of carbon *micro*-segregation is described in (§6.4.5). This section also deals with the influence of mild topography on the carbon quantification is addressed.

As a typical example of the use of nano-SIMS on *micro*-segregation, the carbon re-partitioning during tempering of martensite in DP steel was discussed in §6.4.3.

For inclusions/precipitation measurements, it was found that inclusions >0.1 µm can be properly measured and identified using SEM/EDX (§6.3.4). For measurements of larger sample area's (25mm<sup>2</sup>) the minimum particle size has to be chosen larger (ca 1 µm) to keep measurement time within realistic limits. To some extent, including O and N in the ZAF quantification procedure can be used to distinguish between different types of O or N based inclusions.

Precipitates smaller than 0.1 µm can be measured and identified using nano-SIMS. (TEM and atom-probe were not used in this project but have also been used effectively to measure and identify precipitates in literature) and the boron state of three different steel grades in §6.4.4.

##### **8.4.1.2 nano-Hardness**

There are no actual limitations related to steel grade or microstructure for measurement of micro- and nano-hardness. However for probing individual grains or phases an important prerequisite for (nano)-indentation is that the probed volume must be homogenous. In practice this means that the minimum grain/phase size that can be accurately probed lies between 0.5 and 2µm dependent on the actual penetration depth. This means for cementite or bainite that accurate H<sub>N</sub> values are regarded as difficult or impossible to obtain. For probing of typical crystallographic orientations or probing of pre-determined phases or phase constituents based on SEM or EBSD mappings a procedure is described in §7.3 and §7.4.

#### **8.4.2 Steelgrade or microstructure depend procedures:**

Only the main quantifiable parameters are listed, derived parameters are not included in the section below.

##### **8.4.2.1 HSLA100 and HSLA31415**

Both HSLA100 and HSLA31415 matrix phases were classified as bainitic ferrite. (§2.3)

Main Quantifiable parameters:

- Grain size → mild nital or Marshall; SEM SE or InLens; *context-based* QIA (§4.3)
- Effective grain size → EBSD (§5.1)
- Bainitic ferrite fraction → quantification with IQ+KAM (§3.5.4)
- (Misorientation angle distribution (MAD) can be used to support the identification of bainitic ferrite, §2.2.1.3)
- Cementite → SEM mixed InLens/SE detection + *pixelbased* QIA (§3.5.1.3)

##### **8.4.2.2 DP600 and TRIP700**

DP600 or TRIP700 matrix phases are classified as quasi-polygonal ferrite and the second phase as M and/or RA (§2.3)

Main quantifiable parameters:

- Volume fractions: In general second phase volume fractions can be determined using tint etching and LOM. (2.2.1.4). However when the dimensions of second phase particles becomes to small, accurate volume fractions can not be determined using LOM/QIA (§8.3.3), and SEM/QIA procedures (§4.2.2) or SEM/EBSD procedures must be used (§3.5.1.1, §3.4.1, §8.3.3). When both RA and M have to be determined seperately, SEM/EBSD is preferred, although sample preparation is very critical (§3.2.5).
- Grain size ferrite (or M) → when average ferrite (or M) grain size >2 µm tint etching and LOM can be used (§1.3.4). When the average ferrite (or M) grain size < 2 µm then mild nital etching in combination with SEM and (*pixel-or context-based*) QIA can be used.
- Size distributions → possible with SEM/QIA or SEM/EBSD but strongly depends on magnification and step size (§4.3)
- Contiguity → LOM possible; SEM/EBSD preferred (§2.4.2 and §4.6)
- Banding (covariogram method §4.7.4)

When bainite is also present in a DP microstructure, it can become significantly more difficult or impossible to differentiate between various phases.

Ferrite (or M) grain size → when average ferrite (or M) grain size >2 µm tint etching and LOM can be used (§1.3.5). When the average ferrite (or M) grain size < 2 µm then mild nital etching in combination with SEM and (*pixel-or context-based*) QIA can be used.

Contiguity → LOM possible; EBSD preferred (§2.4.2 and §4.6)

#### **8.4.2.3 Complex phase CP800 and CP1000**

Both CP800 and CP1000 matrix phases were classified as granular bainitic ferrite / lath-like bainitic ferrite and secondary phase as martensite (and pearlite/cementite) (§2.3)

- Volume fractions and grain size of ferritic phases or second phase → mild nital or electro-polishing in combination with SEM and *context based*QIA (§4.2)
- Volume fractions of matrix phases ferritic/bainitic/martensite fractions → EBSD partitioning based on IQ + KAM (3.5.4 and §8.3.7)

#### **8.4.2.4 LB**

LB matrix phase was classified as lath-like bainitic ferrite. (§2.3)

Main quantifiable parameter

- Width of bainitic laths → electrolytically polished and mildly etched with HNO<sub>3</sub>; SEM SE ; *context-based* QIA (§8.3.6)

#### **8.4.2.5 MS1200**

Lath martensite (§2.3)

Main quantifiable parameter

- Effective grain size → EBSD(§8.3.8)

## Conclusions

The main objective of this project was to develop and optimize advanced metallographic quantification procedures for complex multi-phase microstructures of Advanced High Strength Steels (AHSS). These procedures rely primarily on Scanning-Electron Microscopy (SEM) and Electron BackScatter Diffraction (EBSD). The developed procedures have been evaluated via process-microstructure-property studies on steels ranging from Dual-Phase (DP) and Transformation-Induced Plasticity (TRIP) to highly challenging Complex-Phase (CP) as well as bainitic / martensitic steels. In addition, methods to determine intrinsic properties of individual phase constituents have been investigated and employed including EBSD-guided nano-indentation, Electron Probe Micro Analysis (EPMA) and high-resolution Secondary Ion Mass Spectrometry (nano-SIMS).

The set of definitions and terminology for phases and microstructural constituents which is presented in this report served as a starting point for phase identification and partitioning strategies. In the classification scheme that was developed, the description of matrix phases and secondary phases follows closely the pattern occurring in real micrographs. This approach offers the flexibility required for the description of any combination of matrix and minor phase constituents.

Guidelines for sample preparation for both SEM and EBSD are reported. In general, mild nital etching works well in combination with Secondary-Electron (SE) SEM imaging. Special attention was paid to sample preparation for EBSD. OPS polishing and electro-polishing were found to be most effective. For meta-stable retained-austenite (RA) OPS polishing followed by electro-polishing was found to be the optimal way for sample preparation for EBSD analysis.

Several approaches and procedures for advanced morphological quantification were evaluated. These include image analysis based on criteria derived from pixels, context and object. It was found that pixel-based image analysis is suitable for relatively simple multi-phase (classical DP or TRIP with a ferritic matrix) microstructures. For more complex microstructures (for example CP or bainitic/martensitic grades) context-based or object-based image analysis are required. Results from a Round Robin Test showed that the results of quantitative image analysis were found to be strongly dependent on the magnification and resolution of the images used for analysis. Finally the so called “covariogram method” was introduced to quantify the degree of microstructural banding. It was concluded that the covariogram approach is a powerful method to quantify banded microstructures.

Several, EBSD based, phase constituents partitioning procedures/guidelines in DP/TRIP/CP steels have been formulated. Next to the crystallographic based partitioning of ferrite (bcc) and austenite (fcc), image quality (IQ) and kernel average misorientation (KAM) were found the most useful parameters in partitioning strategies. Nevertheless, several specific combinations of phase constituents remain difficult to partition. Partitioning strategies have been summarized in Table 3.2. Results from an EBSD Round Robin Test showed that different laboratories, with equipment of different manufacturers, obtained similar results provided that experiments were set up in a similar way.

To quantify mechanical properties of individual phases or phase constituents a nano indentation study was conducted. Nano-indentation was found to be a promising method to determine the hardness of phase constituents in a multi-phase microstructure and to observe its dynamic response to local deformation. An empirical correlation has been formulated (equation 7.11) to establish a link between nano-hardness as measured with a Berkovich indenter and micro-Vickers. An example is presented how to use phase information obtained from EBSD measurements, as a guide to place nano-indent exactly in specific phase constituents.

For quantification of chemical segregation a range of techniques with different spatial resolution were evaluated. For sub-micron resolution, EPMA in combination with Wavelength-Dispersive X-ray (WDX) analysis was found suited to visualize chemical segregation of Mn, Al, Si, and to some extent also carbon in DP and TRIP on both macro and micro scale. Energy Dispersive X-ray (EDX) analysis in combination with SEM can be used for determining the average chemical composition of inclusion down to 100 nm. Three benchmark studies using nano-SIMS (spatial resolution 50 nm) were conducted: visualization of martensite tempering in DP, 3D analysis of bainitic structures in TRIP and identification of the boron precipitation state in boron steels.

Quantification of microstructural parameters is only relevant if the obtained quantified parameters also correlate with mechanical properties or process parameters. For several developed quantification procedures this discriminative power has been addressed in workpackage 8.

In the last work package the optimal procedures for microstructural quantification are summarized. Although in the original aim it was stated that a generic approach for all microstructures would be strived for, it was found during the run of the project that this is not realistic. Therefore, steel grade or microstructure independent procedures are presented first, and in the second part the steel grade or microstructure dependent quantifiable parameters are linked to procedures and to paragraphs in which they are described. The developed methods or approaches for quantification of AHSS microstructures can serve as a base for the European standardization of microstructural quantification of AHSS grades.

## **Exploitation and impact of the research results**

This report gives an overview of methods and strategies available for identification, classification and quantification of microstructures of Advanced High Strength Steels (AHSS). These methods can be used for understanding process-microstructure-property relationships of these steels, which is considered a prerequisite for their optimal design.

Developed methods or approaches for quantification of AHSS microstructures can serve as a base for European standardization of microstructural quantification of AHSS grades.

# List of figures and tables

## Figures

Figure 1.1	<i>Illustrative micrographs of RRT samples (ND/RD plane)</i> .....	16
Figure 2.1	<i>Light-optical micrographs of (A) Complex-phase steel (0.1 wt% C) with equiaxed ferrite and bainitic areas (B) Very-low-carbon steel (0.004 wt% C) consisting of massive ferrite.</i> .....	22
Figure 2.2	<i>Kernel Average Misorientation maps for two different bainitic microstructures: (low  high), (a) granular bainite and (b) lath bainite.</i> .....	22
Figure 2.3	<i>Characteristic histograms of experimental misorientation angle distributions of steels comprising a predominantly single-phase matrix consisting of: acicular ferrite, upper bainite, lower bainite, and martensite. Images from a study by Gourgues et al<sup>[10]</sup></i> .....	23
Figure 2.4	<i>Typical example of the VMK etching approach (sample B from Table 2.5)</i> .....	24
Figure 2.5	<i>FEG-SEM (5KV, inlens-SE) images of white outlined (A) featured martensite in a DP steel (B) featureless martensite in DP600 and (C) retained-austenite in TRIP700. Clearly, the martensite island in the DP600 microstructure (C) still shows a mild structure, corresponding to featureless martensite in LOM. The TRIP700 microstructure shows exclusively second-phase islands without hardly any visible inner structure based on FEG-SEM imaging. This is regarded as typical for retained-austenite islands, although exceptions can occur (see §3.2.4 )</i> .....	25
Figure 2.6	<i>(left) Schematic representations of low-carbon martensite with their typical intricate structure of crystallographic blocks and packets. Each individual component in this representation is defined as a block. Multiple blocks sharing a similar morphological and crystallographic orientation are defined as packets. The misorientation between neighbouring packets for low-carbon martensite is mainly 60° and occasionally 55°<sup>[10]</sup>. (right) Refinement of the martensite structure with increasing carbon content.</i> .....	25
Figure 2.7	<i>SE image (A) and corresponding EBSD maps (B-G) of the DP600 microstructure. See text for details. KAM= kernel average misorientation, IPF = inverse pole figure, IQ image quality and MAD = misorientation angle distribution.</i> .....	26
Figure 2.8	<i>Schematic model of the carbide-free bainite as put forward by Zaeffer et al.<sup>[21]</sup></i> .....	27
Figure 2.9	<i>Examples of complex microstructures. The samples were fine mechanical polished with OPS. SEM images show channelling- and atomic number contrasts in BS mode (10KV).</i> .....	28
Figure 2.10	<i>Illustrative example of a two phase (<math>\alpha</math> and <math>\beta</math>) microstructure with A) all grainboundaries, B) <math>\alpha</math>- <math>\alpha</math> grainboundaries, C) <math>\alpha</math>- <math>\beta</math> grainboundaries and D) <math>\beta</math>-<math>\beta</math> grainboundaries.</i> .....	30
Figure 2.11	<i>Illustrative example of a two phase (<math>\alpha</math> and <math>\beta</math>) microstructure with A) all phases skeletonised (<math>L_i</math>), B) <math>\alpha</math> phase skeletonised (<math>L_\alpha</math>), C) <math>\beta</math> phase skeletonised (<math>L_\beta</math>).</i> .....	30
Figure 3.1	<i>Relation between SEM morphology, EBSD phase map and IPF of the same RA island.</i> .....	36
Figure 3.2	<i>Comparison between the morphology of M islands found in TRIP700 and DP600.</i> ....	36
Figure 3.3	<i>Combined results for second-phase determination in TRIP700, measured by different partners with different (preparation) techniques. ■ (closed symbols) = retained-austenite; □ (open symbols) = retained-austenite + martensite.</i> .....	37
Figure 3.4	<i>(A) Light-optical micrograph and (B) QBSD (15KV) SEM image of DP600 based on Klemm etching of identical region. Circles indicate specific features.</i> .....	38
Figure 3.5	<i>Representative SEM images (InLens, 5KV) of the electropolished RRT materials of ND/RD.</i> .....	40
Figure 3.6	<i>Comparison of identical surface areas of TRIP700 sample, (all images FOW= 20<math>\mu</math>m).</i> .....	41
Figure 3.7	<i>Flow chart for a number of relevant parameters concerning EBSD analysis.</i> .....	42
Figure 3.9	<i>InLens+SE2 - SEM image at 25kX (left) and mean shift segmentation (right).</i> .....	45
Figure 3.10	<i>Cross-neighbourhood.</i> .....	45
Figure 3.12	<i>Method used for combined representation of image quality and kernel average misorientation (IQ+KAM), see text for a detailed method description. Colour chart (a) and phase allocation (b) for combined [IQ+KAM] maps.</i> .....	47

Figure 3.13	<i>Comparison of different steel grades using [IQ+KAM] maps.</i>	47
Figure 4.1	<i>Plots of <math>R_m</math> and <math>R_p</math> versus Area fraction (<math>A_A</math>) and boundary length (<math>L_A</math>). Symbols sizes represent the mean free distance (<math>\lambda</math>).</i>	50
Figure 4.2	<i>Progressive erosion based method and anisotropy index parameter description.</i>	55
Figure 4.3	<i>Simulated (banded) microstructures for evaluating the covariogram method.</i>	55
Figure 4.4	<i>(left top) typical covariogram obtained for a banded structure. The intensity of the banded structure (or BI index) is defined as the difference between covariance value at the first minimum and the first maximum (right top) covariograms obtained for the simulated microstructures of Figure 4.3. (left bottom) BI indexes of simulated structures.</i>	56
Figure 4.5	<i>Overview of real microstructures used to evaluate the covariogram method. For all samples heating rate is 10°C/s to reach the top temperature. (time* at top temperature; time** at 650°C).</i>	56
Figure 4.6	<i>(Left) Heat cycles used to obtain microstructures shown in Figure 4.5 (numbers in graph refer to numbers in Figure 4.5). (Right) BI index determined for the microstructures of Figure 4.5 combined with process parameters.</i>	57
Figure 4.7	<i>Simulated microstructures with, from left to right, decreasing feature sizes. The response of the C'0 parameter on the change of feature size is shown in the left graph.</i>	57
Figure 5.1	<i>HSLA steel. EBSD BC maps (FOW of 60µm) and misorientation distributions measured by VAS (left), KIMAB (middle) and Corus (right). VAS made the analysis on the RD-TD plane in this investigation compared to RD-ND which KIMAB and Corus used.</i>	65
Figure 5.2	<i>EBSD IPF map measured by CRM, using 0.5 µm step size (left) and the same microstructure measured by VAS using a step size of 0.15 µm (right) (FOW = 90 µm).</i>	65
Figure 5.3	<i>TRIP700: EBSD BC map, measured by KIMAB using 0.05 µm step size, (left) and VAS (right). Martensite (dark). (FOW = 35 µm)</i>	65
Figure 5.4	<i>CP800 EBSD map measured by Corus using 0.05 µm step size. (left) BC and (right) IPF colour map (crystal orientation). Grain boundaries larger than 2° (blue) and 15° (black) are also included in IPF map) (FOW 60 µm).</i>	66
Figure 5.5	<i>MS1200 EBSD map measured by Corus using 0.05 µm step size (left) and VAS using 0.10 µm step size (right). (FOW 60 µm)</i>	66
Figure 5.6	<i>MS1200: Misorientation distribution (cut-off at 10°) derived from EBSD data measured by: VAS (left), KIMAB (middle) and Arcelor (right).</i>	66
Figure 6.1	<i>Mn-distribution maps, Superposition of Mn map on microstructure and Mn profile in central segregation of DP steel</i>	67
Figure 6.2	<i>C and Mn distribution maps of DPsteel</i>	67
Figure 6.3	<i>LOM microstructures of TRIP samples with different holding temperatures.</i>	68
Figure 6.4	<i>Microprobe analysis of Al-Mn TRIP steel after soaking at different temperatures.</i>	68
Figure 6.5	<i>Overview of measured particles on the RRT samples left top. When, after quantification (ZAF %wt), <math>C+O+Fe&gt;85\%</math> the particle is rejected (marked with the red circles). The Ti, Nb and Ca maps represent typical elemental distributions in the samples. (note that N and O were not included in the quantification). The size of the circles is linear related to the average diameter of the particles.</i>	69
Figure 6.6	<i>Basic quantification results of the steel inclusions/precipitates found in the RRT materials as determined with EDX (■ particles &gt; 1µm; ▨ particles &gt;2µm).</i>	70
Figure 6.7	<i>Ternary graphs of Al, O, N; Ti, N, O and Mn, Ca and S.</i>	70
Figure 6.8	<i>EDX mapping of an inhomogeneous inclusion, size of the inclusion <math>\approx 4\mu m</math>.</i>	71
Figure 6.9	<i>Comparison between conventional SIMS and Nano-SIMS.</i>	73
Figure 6.10	<i>(Left) LOM image of a sample containing both lath- and granular bainite. Nano-SIMS <math>^{12}C</math> map based 3D-reconstructions of lath-shaped bainite (top-series) and granular bainite (bottom-series). The 3D reconstruction shows only the perimeter “skin” of identified islands.</i>	73
Figure 6.11	<i>Carbon re-partitioning in martensite islands for different tempering steps.</i>	74
Figure 6.12	<i>Quantitative carbon evolution in martensite islands for different tempering steps as measured by means of EELS.</i>	74

Figure 6.13 Schematic diagram showing mechanism for suppression of $Fe_{23}(B,C)_6$ formation due to combined addition of Nb and B or Mo and B, according to T. Hara et.al. <sup>[30]</sup> For all three grades a typical microstructure obtained after annealing and quenching at 600°C is shown.....	75
Figure 6.14 Location of $Fe_{23}(B,C)_6$ precipitates (green circles) in relation to the ferrite and/or austenite grains (red lines) and 2 <sup>nd</sup> phase areas (yellow line) by combination of <sup>11</sup> B, <sup>11</sup> B <sup>12</sup> C, <sup>11</sup> B <sup>16</sup> O and <sup>12</sup> C ion maps for the “alone” boron grade.....	75
Figure 6.15 Location of $Fe_{23}(B,C)_6$ precipitates with left: no addition, middle: Nb addition and right: Mo addition. Yellow (M area) red ferrite/austenite grainboundary, green $Fe_{23}(B,C)_6$ precipitates.....	76
Figure 6.16 SEM inlens images of DP600 (FOW 20 $\mu m$ ) (left) and TRIP700 (FOW 10 $\mu m$ ) (right) (electropolished). .....	76
Figure 6.17 DP600: quantitative EPMA mappings of C, Mn, Si together with the SE image (SE image was taken after the EPMA mapping (15KV, FOW 30 $\mu m$ ), ionbeam cleaning and mild electropolishing. ....	77
Figure 6.18 TRIP700: quantitative EPMA mappings (15KV, FOW 30 $\mu m$ ) of Mn, Si, and Al. ....	77
Figure 6.19 DP600 SEM image (BS, 15KV) of standard polished and after mild electropolished (SE, 5 KV) together with EPMA carbon mappings and carbon background mappings. ....	78
Figure 7.1 (left) Load-displacement curve and (right) residual impression of a Berkovich indenter. ....	79
Figure 7.2 (left) Load-displacement curves of indentations carried out in ferrite and (right) the average ferrite hardness after three different preparation modes of the surface of the same specimen (images taken from a publication by Furnémont et al. <sup>[38]</sup> ). ....	81
Figure 7.3 displacement $h_{max}$ versus nano-hardness $H_N$ based on nano-indentation mappings (7x7 indents covering 20x20 $\mu m$ ) with a maximum load of 500 $\mu N$ . ....	82
Figure 7.4 Schematic representations of typical discontinuities or gradients that may occur in a load-displacement curve during loading (a) and unloading (b and c). ....	82
Figure 7.5 Typical P-h curves for (a) ferrite and (b) martensite constituents in DP600. ....	86
Figure 7.6 TRIP700 (a) SEM image (FOW 3.5 $\mu m$ ), (b) inverse pole figure and (c) image quality maps in combination with a phase map (— twin (60°) boundaries). EBSD data has been collected prior to nano-indentation. Indents A, B and C are discussed in the text. ....	86
Figure 7.7 P-h curves of M/RA constituents in TRIP700: (a) indents A and B and (b) indent C... ....	87
Figure 7.8 TRIP700 (left) SEM image and image quality maps prior (middle) and post nano-indentation (right). (FOW 12 $\mu m$ ) Indents D, E and F are discussed in the text.....	87
Figure 7.9 P-h curves of M/RA constituent: (left) indent D and (right) indents E and F. ....	87
Figure 7.10 SEM images of (left) lath-shaped RA islands and (right) block-shaped RA islands. Triangular features correspond to the residual impression of nano-indentations labelled E, G and H. ....	88
Figure 7.11 EBSD data prior (a and c) to and post (b and d) nano-indentation analysis of lath-shaped retained-austenite islands (indents G and H). (Detail of Figure 7.10 left) Green regions correspond with retained-austenite. Triangles correspond with the position of the nano-indentations. The red arrows in the CI maps emphasize the change in confidence index due to nano-indentation. ....	89
Figure 7.12 EBSD data prior (a and c) to and post (b and d) nano-indentation analysis of a block-shaped retained-austenite island (indent E). (Detail of Figure 7.10 right) Green regions correspond with retained-austenite. Red region corresponds with mechanically transformed martensite. Triangles correspond with the position of the nano-indentations. The red arrows in the CI maps emphasize the change in confidence index due to nano-indentation. ....	89
Figure 8.1 Graphical representation of the performance of the 2D and 3D derived equations for UTS and YS (respectively equation 8-1, equation 8-3, equation 8-5 and equation 8-7). ....	93
Figure 8.2 Diagram showing necessary parameters to describe mechanical properties for DP steel-grades. ....	94

Figure 8.3	<i>Equations and statistical parameters (<math>R^2</math>, <math>\sigma</math>) of linear correlations between mechanical and microstructural parameters. <math>R^2</math> = coefficient of determination; <math>\sigma</math> = standard deviation.</i>	94
Figure 8.4	<i>Martensite, bainite and martensite+bainite area fractions vs. top temperatures (<math>T_1</math>, <math>T_2</math> and <math>T_3</math>) for DP-a (left) and DP-b (right).</i>	95
Figure 8.5	<i>Overview of DP steels for validation (etchant LePera).</i>	96
Figure 8.6	<i>Correlations between ferrite-bainite fraction and tensile strength (left) or uniform elongation (right).</i>	97
Figure 8.7	<i>Correlation of the microstructural parameters with the mechanical properties.</i>	97
Figure 8.8	<i>Diagram showing necessary parameters to describe mechanical properties of TRIP steel-grades.</i>	97
Figure 8.9	<i>Curves, equations and statistical parameters (<math>R^2</math>, <math>\sigma</math>) of linear correlations between mechanical and microstructural parameters.</i>	98
Figure 8.10	<i>Tensile strength of two TRIP series produced with 5 different top temperatures for both variants. (■ cycle 1 and □ cycle 2).</i>	98
Figure 8.11	<i>UTS vs 2<sup>nd</sup> phase area determined from LOM/Klemm images (The absolute value for area fractions are not reliable due to the very small island size) The UTS does not show a clear dependency.</i>	98
Figure 8.12	<i>UTS vs RA volume fraction determined by XRD. The UTS does not show a clear dependency to the volume fraction.</i>	98
Figure 8.13	<i>Upper images LOM (Klemm, RD/TD; RD = horizontal; Lower images EBSD based phase map red = Ferrite green = retained austenite blue = martensite yellow = grain boundaries (Scansize 15x15 <math>\mu\text{m}</math>, step size 50 nm, RD/TD RD = vertical).</i>	99
Figure 8.14	<i>Characteristic misorientation angle distributions for specific phase interactions for TRIP series.</i>	100
Figure 8.15	<i>UTS dependency of average ferrite grain size, determined with EBSD.</i>	100
Figure 8.16	<i>UTS dependency of the ferrite contiguity area.</i>	100
Figure 8.17	<i>UTS dependency of the total ferrite/martensite or ferrite / austenite grain boundary length.</i>	100
Figure 8.18	<i>Representative SEM images (SE, 10KV, FOW=30 <math>\mu\text{m}</math>) of quantified microstructures, classification results, sample codes, temperature and holding times. The identified bainite laths are coloured in orange. The other colours within the result-images show remains of the structure cognition process and not relevant in this context.</i>	101
Figure 8.19	<i>Box plot of the lath width distribution of the microstructures shown in Figure 8.18.</i>	102
Figure 8.20	<i>Overview of the image Quality (IQ, FOW 90 <math>\mu\text{m}</math>) together with a detail of the IQ+KAM maps for CP steel coiled at eight different cooling temperatures (<math>T_1 \rightarrow T_8</math>).</i>	104
Figure 8.21	<i>A) Phase allocation for combined [IQ+KAM] maps. B) Mechanical properties of a hot rolled CP-grade with different cooling temperatures C) Grain size of CP800 steel as function of cooling temperature (R<sub>m</sub>= Ultimate Tensile Strength (UTS); R<sub>p</sub>= Yield Strength (YS); A<sub>g</sub> = Uniform Elongation (UE); A<sub>80</sub> = Elongation after fracture (EAF); GTA =grain tolerance angle).</i>	104
Figure 8.22	<i>A) Evolution of phase content with cooling temperature for CP-grade; B) Correlation between ductility and grain size for CP-grade; C) Comparison between measured and calculated hardness for CP-grade.</i>	105
Figure 8.23	<i>IPF's for the series of martensitic steels. Grain boundaries (10° misorientation) and sub-grain boundaries (1° misorientation) are shown in black and red respectively (after Kuwahara filtering).</i>	106
Figure 8.24	<i>Relation between (sub) grain size the Yield Strength (R<sub>p0.2</sub>) and Tensile Strength (R<sub>m</sub>).</i>	106

## Tables

Table 1.1	<i>Inventory of materials selected for Round Robin trials.</i>	15
Table 1.2	<i>Average chemical composition (in weight-%) of the RRT materials.</i>	18
Table 1.3	<i>Mechanical properties of the RRT materials..</i>	18
Table 1.4	<i>Vickers hardness (HV0.5) of the RRT materials.</i>	18

Table 2.1	<i>Nomenclature proposed for the major matrix phase constituents and minor secondary phase components.</i>	19
Table 2.2	<i>Morphological and crystallographic features of matrix phase constituents.</i>	20
Table 2.3	<i>Morphological and crystallographic features of minor secondary phase components.</i>	21
Table 2.4	<i>Overview of the VMK etching approach.</i>	24
Table 2.5	<i>Martensite and retained-austenite fractions for several samples containing M and RA as measured by LOM-QIA based on various (tint) etchings.</i>	24
Table 2.6	<i>Classification Scheme for multi-phase steels.</i>	27
Table 2.7	<i>Classification of investigated RRT steels (carbide classification not included)</i>	29
Table 2.8	<i>EBSL based Contiguity/separation and their derived parameters of TRIP700</i>	30
Table 2.9	<i>List of parameters selected for description of phase properties.</i>	31
Table 2.10	<i>Parameters selected for description of phase properties.</i>	33
Table 3.1	<i>Overview of different specimen preparation approaches employed for EBSD measurements.</i>	37
Table 3.2	<i>Microstructural components in investigated microstructures and possible methods to identify and partition these constituents. Partition method is derived from work carried out by several partners. Abbreviations: F = ferrite, M = martensite, RA = retained-austenite, B = bainite, KAM = kernel average misorientation, IQ = image quality, GS = grain size, GAM = grain average misorientation, GROD = grain reference orientation deviation, HAB = high-angle boundary, FCC = face-centred cubic.</i>	41
Table 4.1	<i>Results of the measurement of volume fraction for individual phases and phase constituents for all the type of microstructures specified in WP1.</i>	49
Table 4.2	<i>Measurement of the average size of individual phases and phase constituents for all type of microstructures as specified in WP1 (values reported are the equivalent diameter (<math>D_{eq}</math>) values except for the line cut method)</i>	51
Table 4.3	<i>Ferrite/Second-phase boundary interface lengths (<math>\mu\text{m}^{-1}</math>)</i>	52
Table 4.4	<i>Results for the shape factor analysis. Distribution of the shape of individual phases and phase constituents for all type of microstructures as specified in WP1 are given.</i>	53
Table 4.5	<i>Short description of shape parameters that have been used.</i>	53
Table 4.6	<i>Shape factors determined for ferrite grains of RRT materials. Shape factors with similar values have the same greyscale.</i>	53
Table 4.7	<i>Results of the quantitative assessment of phase connectivity (continuity/contiguity/ separation) for relevant microstructures as specified in WP1</i>	54
Table 5.1	<i>Amount of RA and lattice</i>	59
Table 5.2	<i>Participating laboratories and their EBSD equipment (at the time of measurement)</i>	61
Table 5.3	<i>Materials and participating laboratories.</i>	61
Table 5.4	<i>EBSL parameters for HSLA steel.</i>	62
Table 5.5	<i>EBSL parameters for HSLA31415.</i>	62
Table 5.6	<i>EBSL parameters for DP600.</i>	63
Table 5.7	<i>EBSL parameters for TRIP700 steel.</i>	63
Table 5.8	<i>EBSL parameters for CP800.</i>	64
Table 5.9	<i>EBSL parameters for CP1000.</i>	64
Table 5.10	<i>EBSL parameters for MS1200.</i>	65
Table 6.1	<i>Degree of segregation of C, Mn, Al for the three analyzed TRIP samples (HT 800, 850 and 890°C).</i>	68
Table 6.2	<i>Basic statistics results for sample 1200M RD/ND section</i>	72
Table 6.3	<i>Quantified EPMA results, averaged over the total analyzed field.</i>	78
Table 7.1	<i>Reported nano-hardness values in literature for phase constituents in DP and TRIP steels (all measurements have been done with a Berkovich indenter).</i>	83
Table 7.2	<i>Reported nano-hardness values for phase constituents in DP600 and TRIP700 steels (all measurements have been done with a Berkovich indenter).</i>	84
Table 8.1	<i>Combined, mechanical and microstructural data for DP.</i>	92
Table 8.2	<i>Mean values of microstructural parameters (fractions of austenite and martensite, area of martensite + retained austenite and mean ferrite grain size) calculated using different combinations of individual measurements in various planes.</i>	92
Table 8.3	<i>Mechanical properties of a series of DP steels and microstructural parameters determined by LOM and EBSD.</i>	96

Table 8.4	<i>Results of mechanical tests, metallographic analysis and thermo-kinetic model simulation.</i> .....	97
Table 8.5	<i>Description of martensitic materials.</i> .....	105
Table 8.6	<i>List of abbreviations used in both the report and the technical annexes.</i> .....	117

## Abbreviations

**Table 8.6** List of abbreviations used in both the report and the technical annexes.

<i>A</i>	Contact Area (nano-indent.)	<i>h</i>	Displacement (nano-indent.)
A	austenite (RA = retained austenite)	<i>h<sub>c</sub></i>	Residual displacement after unloading (nano-indent.)
A <sub>80</sub>	Elongation After Fracture (EAF)	<i>h<sub>max</sub></i>	Maximum Depth of Penetration (nano-indent.)
A <sub>A</sub>	area fraction	HAB	High-Angle Boundary
AF	Acicular Ferrite	HN	Hardness Nominal
AFM	Atomic Force Microscopy	H <sub>N</sub>	Nano-Hardness
A <sub>g</sub>	Uniform Elongation (UE)	HSLA	High Strength Low Alloyed
AHS	Advanced High Strength	HV	Vickers Hardness
AHSS	Advanced High Strength Steel	IC	Image Classifier
B	Bainite	IQ	Image Quality
B, m	Empirical parameters (nano-indent.)	J	texture index
B <sub>C-free</sub>	Carbide-free bainite	KAM	Kernel Average Misorientation
BCT	Body centred tetragonal	LC	Low Carbon
B-DP	Bainitic Dual Phase	LOM	Light Optical Microscopy
B <sub>FT</sub>	full thickness Bands	M	Martensite
B <sub>L</sub>	Lower bainite	M <sub>1</sub>	Featureless martensite
BM	Boundary Misorientation	M <sub>2</sub>	Structured martensite
BSE	Back Scatter Electron	MAD	Misorientation Angle Distribution
B <sub>U</sub>	Upper bainite	MAG	Magnetic response measurement
c	contiguity	M-DP	Martensitic Dual Phase
CC	Correlation coefficient	ND	Normal direction
CCT	Continuous Cooling Transformation	OPS	Oxide Polishing suspension (Colloidal Silica (SiO <sub>2</sub> ))
CI	Confidence Index	P	perimeter
CP	Complex Phase	P <sub>D</sub>	Degenerate pearlite
CS	Classification scheme	P <sub>F</sub>	Fine colony pearlite
C <sub>sk</sub>	Continuity	Ph	Clustering (phase related)
CSM	Continuous Stiffness Measurement	P <sub>L</sub>	Lamellar pearlite
D	Clustering (dimension related)	P <sub>T</sub>	total perimeter
D <sub>eff</sub>	effective grain size	QIA	Quantitative Image Analysis
D <sub>eq</sub>	Equivalent diameter	R <sup>2</sup>	Coefficient of Determination
DP	Dual Phase	RA	Retained Austenite
EAF	Elongation After Fracture (A80)	R <sub>A</sub>	aspect ratio
EBSD	Electron Back-Scatter Diffraction	R <sub>Area</sub>	Reduction Area
EDX	Energy-Dispersive X-ray spectroscopy	RD	Rolling direction
EELS	Electron Energy Loss Spectroscopy	R <sub>F</sub>	fullness ratio
EPMA	Electron Probe Micro-Analyzer	R <sub>m</sub>	Ultimate Tensile Strength (UTS)
F	Load (nano-indent.)	R <sub>p</sub>	Yield Strength (YS)
FCC	Face Centred Cubic	RRT	Round Robin Test
FEG	Field Emission Gun	S	Stiffness (nano-indentation)
FGS	Ferrite Grain Size	s	separation
FOW	Field of Width	SE	Secondary Electron
GB	Grain Boundary	SEM	Scanning Electron Microscope
GAM	Grain Average Misorientation	SIMS	Secondary Ion Mass Spectrometry

**Table 8.6** *Continuated*

GROD	Grain Reference Orientation Deviation		
GS	Grain Size		
GTA	Grain Tolerance Angle		
TD	Transfer direction		
TEM	Transmission Electron Microscopy		
TM	Tempered/auto-tempered martensite		
TRIP	Transformation Induced Plasticity		
UE	Uniform Elongation (Ag)		
UTS	Ultimate Tensile Strength (Rm)		
VMK	Villela/Metabisulfide/Klemm		
XRD	X-Ray Diffraction		
YS	Yield Strength (Rp)		
$\sigma$	Standard Deviation		
$\Delta_B$	band gap		
$\Delta_c$	connectivity		
$\alpha_A$	Acicular ferrite		
$\alpha_B$	Bainitic ferrite – lath-like		
$\alpha_{B(G)}$	Bainitic ferrite - granular		
$\alpha_d$	Deformed ferrite		
$\alpha'_L$	Lath martensite		
$\alpha_M$	Massive ferrite		
$\alpha_P$	Polygonal ferrite		
$\alpha_Q$	Quasi-polygonal (recovered) ferrite		
$\alpha'_T$	Plate martensite		
$\alpha_W$	Widmannstätten ferrite		
$\lambda$	Mean Free Distance		
$\rho$	Number density		
$\rho_B$	Density of bands		

## **Publications**

- 1) Liesbeth Barbé and Kim Verbeken, "MICROSTRUCTURAL CHARACTERIZATION OF DUAL PHASE STEELS BY MEANS OF ELECTRON MICROSCOPY", Ceramic Transactions, Vol.200, p. 71, Conference on texture of materials (ICOTOM15), June 1-6 2008
- 2) R.A. Rijkenberg, M.P. Aarnts, F.A. Twisk, M.J. Zuijderwijk, M. Knieps and H. Pfaff, LINKING CRYSTALLOGRAPHIC, CHEMICAL AND NANO-MECHANICAL PROPERTIES OF PHASE CONSTITUENTS IN DP AND TRIP STEELS, Materials Science Forum Vols. 638-642, (2010), 3465-3472
- 3) Fischer, M.; Gerdemann, F.; Bleck, W.; Schwedt, A.: "OBJEKTBASIERTE QUANTITATIVE ANALYSE VON KOMPLEXEN MIKROSTRUKTUREN IN STÄHLEN" Tagungsband der 42. Metallographietagung, 2008, Jena
- 4) Fischer, M.; Gerdemann, F.; Bleck, W.: "OBJECT BASED QUANTITATIVE ANALYSIS OF COMPLEX MULTIPHASE MICROSTRUCTURES IN STEEL" TMS 2009 - 138th Annual Meeting & Exhibition, 2009, San Francisco
- 5) Fischer, M.; Gerdemann, F.; Bleck, W.; Schwedt, A.: "OBJEKTBASIERTE QUANTITATIVE ANALYSE VON KOMPLEXEN MIKROSTRUKTUREN IN STÄHLEN" PRAKTISCHE METALLOGRAPHIE, Band 46 (2009) Heft 5, Seite 225-235

## References

- <sup>1</sup> E. Girault, P. Jacques, Ph. Harlet, K. Mols, J. Van Humbeeck, E. Aernoudt and F. Delannay, Metallographic Methods for Revealing the Multiphase Microstructure of TRIP Assisted Steels, *Materials Characterization*, 40, 111-118, (1998).
- <sup>2</sup> A.K. De, J.G. Speer, D.K. Matlock, Color Tint-Etching for Multiphase Steels, *Advanced Materials and Processes*, 27-30, (2003)
- <sup>3</sup> S. Zajac et al.: ECSC project, "Quantitative Structure-Property Relationships for Complex Bainitic Microstructures", *Report EUR 21245EN* (2005).
- <sup>4</sup> B. L. Bramfitt and J. G. Speer; "A Perspective on the Morphology of Bainite", *Metall. Trans.*, Vol. 21A, 817, (1990).
- <sup>5</sup> *Atlas for Bainitic Microstructures*, Vol. 1, ISIJ, Tokyo, (1992).
- <sup>6</sup> Y. Ohmori, H. Ohtani, and T. Kunitake; "The Bainite in Low Carbon Low Alloy High Strength Steels", *Trans. ISIJ*, Vol. 11, 250, (1971).
- <sup>7</sup> G. Thewlis, *Mat. Sc. Techn.*, Vol. 20, 143, (2004).
- <sup>8</sup> A. Rijkenberg, M. Zuijderwijk, D. Wilcox, D. Huin, L. Barbé, S. Zajac, F. Friedel, V. Marx, E. Füreder, R. Hackl; Six-monthly Technical Report **Period 1** (01/07/06 – 31/12/06), RFCS project "Microstructural Quantification of Multi Phase Steels – MICRO-QUANT", contract number RFSR-CT-2006-00017, (March 2007).
- <sup>9</sup> A. Rijkenberg, M. Zuijderwijk, D. Wilcox, D. Huin, A. Arlazarov, L. Barbé, S. Zajac, F. Gerdemann M. Fischer, F. Friedel, V. Marx, E. Füreder, R. Hackl, C. Commenda; Six-monthly Technical Report **Period 2** (01/01/07 – 30/06/07), RFCS project "Microstructural Quantification of Multi Phase Steels – MICRO-QUANT", contract number RFSR-CT-2006-00017, (September 2007).
- <sup>10</sup> A.-F. Gourgues, H.M. Flower, and T.C. Lindley, "Electron backscattering diffraction study of acicular ferrite, bainite, and martensite steel microstructures", *Mater. Sci. Technol.*, Vol. 16, 26, (2000).
- <sup>11</sup> R. Petrov and L. Kestens, "An Orientation Microscopy Study of the Martensite Transformation in an Fe-30% Ni Alloy", publ EDAX TSL Inc, (2005)
- <sup>12</sup> G.F. van der Voort, Metallography Principles and Practice, *ASM International*, (2000).
- <sup>13</sup> J. Gurland, Transactions AIME 212 (1958) 452/455
- <sup>14</sup> Z. Fan, A.P. Miodownik, and P. Tsakirooulos, *Materials Science and Technology*, Vol. 9, 1094-1100, (1993).
- <sup>15</sup> H.E. Exner u.a., Prakt. Metallogr. 30 (1993) 393/398
- <sup>16</sup> M. H. Poech, D. Ruhr, "Quantitative Characterization of the Microstructural Arrangement", *Prakt. Metallogr.* 31 (1994), 2, pp. 70 - 77
- <sup>17</sup> G.F. Vander Voort, Microscopy Today 1995, <http://www.moremetallography.com/color/color.pdf>.
- <sup>18</sup> B. L. Bramfitt and J. G. Speer; "A Perspective on the Morphology of Bainite", *Metall. Trans.*, Vol. 21A, 817, (1990).
- <sup>19</sup> M.P. Aarnts, M. Zuijderwijk, R.A. Rijkenberg, A. Arlazarov, D. Barbier, A. Hazotte, B. Krebs, L. Germain, M. Gouné, L. Barbé, J. Komenda, O. Karlsson, J. Hagström, M. Fischer, F. Friedel, V. Marx, E. Füreder, C. Commenda; Six-monthly Technical Report **Period 6** (01/01/09 – 30/06/09), RFCS project "Microstructural Quantification of Multi Phase Steels – MICRO-QUANT", contract number RFSR-CT-2006-00017, (September 2009).
- <sup>20</sup> A. Lambert-Perlade, A.F. Gourgues, and A. Pineau, "Austenite to bainite transformation in the heat-affected zone of a high-strength low-alloy steel", *Acta Materialia* Vol. 52, 2337-2348, (2004).
- <sup>21</sup> S. Zaeferer, J. Ohlert, and W. Bleck, *Acta Materialia* Vol. 52, 2765, (2004).
- <sup>22</sup> M.P. Aarnts, M. Zuijderwijk, R.A. Rijkenberg, D. Huin, A. Arlazarov, L. Barbé, J. Komenda, O. Karlsson, J. Hagström, F. Gerdemann, M. Fischer, F. Friedel, V. Marx, E. Füreder, C. Commenda; Six-monthly Technical Report **Period 4** (01/01/08 – 30/06/08), RFCS project "Microstructural Quantification of Multi Phase Steels – MICRO-QUANT", contract number RFSR-CT-2006-00017, (March 2009).

- 23 R. van den Boomgard, “*Decomposition of the Kuwahara-Nagao operator in terms of a linear smoothing and morphological sharpening*”, Proceedings of the ISMM2002, eds. H.Talbot, R. Beasre, CSIRO Publishing, (2002).
- 24 S. Zajac et al.: ECSC project, “*Quantitative Structure-Property Relationships for Complex Bainitic Microstructures*”, Report EUR 21245EN (2005).
- 25 A. Rijkenberg, M. Zuijderwijk, D. Wilcox, D. Huin, A. Arlazarov, L. Barbé, S. Zajac, F. Gerdemann, M. Fischer, F. Friedel, V. Marx, E. Füreder, R. Hackl, C. Commenda; Mid-term Report [Technical Report Number 3] (01/07/06 – 31/12/07), RFCS project “*Microstructural Quantification of Multi Phase Steels – MICRO-QUANT*”, contract number RFSR-CT-2006-00017, (March 2008).
- 26 Definiens, Professional 5, Reference Book, 2006. (<http://www.definiens.com>)
- 27 ASTM E1268-99: Standard Practice for Assessing the Degree of Banding or Orientation of Microstructures. Published July 1999
- 28 M.P. Aarnts, M. Zuijderwijk, R.A. Rijkenberg, A. Arlazarov, D. Barbier, A.Hazotte, B. Krebs, L. Germain, M. Gouné, L. Barbé, J. Komenda, O. Karlsson, J. Hagström, M. Fischer, F. Friedel, V. Marx, E. Füreder, C. Commenda; Six-monthly Technical Report **Period 5** (01/07/08 – 01/01/09), RFCS project “*Microstructural Quantification of Multi Phase Steels – MICRO-QUANT*”, contract number RFSR-CT-2006-00017, (march 2009).
- 29 N. Valle, J. Drillet, O. Bouaziz, H.-N. Migeon; Study of the carbon distribution in multi-phase steels using the NanoSIMS 50; Applied Surface Science 252 (2006) 7051–7053.
- 30 T. Hara, H. Asahi, R. Uemori and H. Tamehiro, *ISIJ International*, vol. 44 (2004), No. 8, pp. 1431-1440.
- 31 Y. Toji, K. Hasegawa, H. Matsuda, T. Yamashita and Y. Tanaka, in: Fundamentals of Martensite and Bainite toward Future Steels with High Performance, edited by T. Furuhara and K. Tsuzaki, The Iron and Steel Institute of Japan, Tokyo, Japan (2007)
- 32 M.J. Santofimia, L. Zhao, R. Petrov and J. Sietsma: Mater. Charact. Vol. 59 (2008), p. 1758
- 33 R.A. Rijkenberg, M.P. Aarnts, F.A. Twisk, M.J. Zuijderwijk, M. Knieps and H. Pfaff, Linking Crystallographic, Chemical and Nano-Mechanical Properties of Phase Constituents in DP and TRIP Steels, Materials Science Forum Vols. 638-642, (2010), 3465-3472
- 34 W.C. Oliver and G.M. Pharr, J. Mater. Res. 7 (1992) 1564.
- 35 M.R. Begley and J.W. Hutchinson, J. Mech. Phys. Solids 46 (1998) 2049.
- 36 M. Kopernik, M. Spychaliski, K.J. Kurzydlowski and M. Pietrzyk, Mater. Sci. Technol. 24 (2008) 369.
- 37 J. Jang, M.J. Lance, S. Wen, T.Y. Tsui and G.M. Pharr, Acta Materialia 53 (2005) 1759.
- 38 Q. Furnémont, M. Kempf, P.J. Jacques, M. Göken and F. Delannay, Mater. Sci. Eng. A 328 (2002) 26.
- 39 P. M. Rice and R. E. Stoller, “*Correlation of Nanoindentation and Conventional Mechanical Property Measurements*”, Fundamentals of Nanoindentation and Nanotribology II, Vol. 649, S. P. Baker, R. F. Cook, S. G. Corcoran and N. R. Moody, Eds., Materials Research Society, Pittsburgh, PA, 2000, pp. 7.11.1-7.11.6.
- 40 C.A. Schuh, Materials Today 9 (2006) 32.
- 41 C.P. Frick, T.W. Lang, K. Spark and K. Gall, Acta Mater. 54 (2006) 2223.
- 42 J. Yan, H. Takahashi, X. Gai, H. Harada, J. Tamaki and T. Kuriyagawa, Mater. Sci. Eng. A 423 (2006) 19.
- 43 R. Rao, J.E. Bradby, S. Ruffell and J.S. Williams, Microelectron. J. 38 (2007) 722.
- 44 T.-H. Ahn, D.H. Kim, C.-S. Oh, K.-K. Um, J.-K. Choi, K.H. Oh, M. Kim and H.N. Han, “*Microstructural Characterization of high Strength Steel Using Nanoindentation*”, Thermomechanical Processing of Steels, Padua, Italy, 2008.
- 45 R. Navamathavan, S.-J. Park, J.-H Hahn and C.K. Choi, Materials Characterization 59 (2008) 359.
- 46 J. Angeli and C. Kneissl, Z. Metallkd. 95 (2004) 601.
- 47 M. Delincé, P.J. Jacques and T. Pardoen, Acta Mater. 54 (2006) 3395.
- 48 T. Ohmura, K. Tsuzaki and S. Matsuoka, Scripta Mater. 45 (2001) 889
- 49 K. Miyahara, S. Matsuoka and T. Hayashi, Metal. Trans. A 32 (2001) 761
- 50 A.F. Padilha, V. Randle and I.F. Machado: Mater. Sci. Technol. 15 (1999) 1015.

- 
- <sup>51</sup> J. Imlau, W. Bleck and S. Zaefferer, in: “*New Developments on Metallurgy and Applications of High Strength Steels*”, TMS, Warrendale, USA (2008).
- <sup>52</sup> S.H. Lee, S.H. Lee, S.H. Kang, H.N. Han, K.H. OH and H.C. Lee: *ISIJ Int.* 48 (2008) 1394.
- <sup>53</sup> P. Jacques, Q. Furnémont, T. Pardoen and F. Dellanay, *Acta Mater.* 49 (2001) 139.

European Commission

**EUR 24980 – Microstructural quantification of multi phase steels (Micro-quant)**

*M. P. Aarnts, R. A. Rijkenberg, F. A. Twisk, D. Wilcox, M. J. Zuijderwijk, A. Arlazarov, D. Barbier,  
L. Germain, M. Gouné, A. Hazotte, D. Huin, B. Krebs, L. Barbé, J. Hagström, J. Komenda,  
S. Zajac, W. Bleck, M. Fischer, F. Gerdemann, F. Friedel, V. Marx, C. Commenda, E. Füreder,  
R. Hackl*

Luxembourg: Publications Office of the European Union

2011 – 122 pp. – 21 × 29.7 cm

Research Fund for Coal and Steel series

ISBN 978-92-79-21632-9

doi:10.2777/83656

ISSN 1831-9424

## **HOW TO OBTAIN EU PUBLICATIONS**

### **Free publications:**

- via EU Bookshop (<http://bookshop.europa.eu>);
- at the European Union's representations or delegations. You can obtain their contact details on the Internet (<http://ec.europa.eu>) or by sending a fax to +352 2929-42758.

### **Priced publications:**

- via EU Bookshop (<http://bookshop.europa.eu>).

### **Priced subscriptions (e.g. annual series of the *Official Journal of the European Union* and reports of cases before the Court of Justice of the European Union):**

- via one of the sales agents of the Publications Office of the European Union ([http://publications.europa.eu/others/agents/index\\_en.htm](http://publications.europa.eu/others/agents/index_en.htm)).

Detailed understanding of process–microstructure–property relationships for high-strength steels is a prerequisite for their optimal design. This demands the ability to perform advanced microstructural quantification of their complex (multi-phase) microstructures, addressing the full range of microstructural properties that are relevant to an appreciation of their macroscopic mechanical behaviour. In turn, this requires that conventional light-optical microscopy (LOM) is complemented with high-resolution analytical techniques and image analysis to perform advanced morphological quantification of microstructures and to determine intrinsic mechanical, chemical and crystallographic properties of phase constituents.

This project has aimed to develop a range of advanced metallographic procedures to deal with morphological analysis based on scanning-electron microscopy (SEM) and electron backscatter diffraction (EBSD) together with pixel- and context-based image analysis routines. Developed procedures have been evaluated via process–microstructure–property studies on steels ranging from DP/TRIP to highly challenging complex phase (CP) and bainitic/martensitic steels. In addition, methods to determine intrinsic properties of constituents have been investigated by means of EBSD-guided nano-indentation, SEM/EDX, electron probe micro-analysis (EPMA) and high-resolution secondary ion mass spectrometry (NanoSIMS).

Highlights of this project are:

- a classification scheme with definitions of matrix and secondary phase constituents;
- procedures for advanced morphological quantification via LOM/SEM and pixel- or context-based image analysis;
- EBSD partitioning rules for phase constituents in DP/TRIP/CP steels;
- EBSD-guided nano-indentation study with evidence of indentation-induced phase transformation of retained-austenite in TRIP;
- visualisation of martensite tempering in DP steel by means of NanoSIMS;
- process–microstructure–property relationships for DP/TRIP/CP and bainitic/martensitic steels..

